Sputtering and Surface Modification of Thermoplastic Polymers with Low Energy Ion Beams

Dissertation

zur Erlandung des akademischen Grades
Doktor der Ingenieurwissenschaften
der Technischen Facultät
der Christian-Albrechts-Universität zu Kiel

Jurgita Zekonyte

Kiel 2005

1. Gutachter Prof. F. Faupel

2. Gutachter Prof. H. Föll

(ggf. 3 Gutachter)

Datum der mündlichen Prüfung 22.10.2005

Contents

1. Introduction 1

2. Polymer surfaces 4

2.1 Dynamics and glass transition temperature of polymer surfaces 5

2.2 Polymer surface properties: relevance to adhesion 8

2.2.1 Surface forces 8

2.2.2 Surface energy and surface tension 10

2.2.3 Mechanisms of adhesion 11

2.2.4 Metal-polymer interface formation 14

3. Ion Irradiation 16

3.1 Ion – polymer interaction 16

3.1.1 Energy-loss processes of ions in matter 17

3.1.2 Range and damage distributions 19

3.2 Mechanisms of Sputtering 22

3.2.1 Trends in sputtering yield 25

3.2.2 Ejection mechanisms of organic molecules 26

3.3 Molecular dynamics simulations 32

3.4 Ion irradiation effects in polymers 33

4. Analytical and experimental techniques 35

4.1 Sputtering sources 35

4.1.1 Electron bombardment ion source - ISE 10 ion source 36

4.1.2 Microwave ion gun - IonEtch sputter gun 38

4.2 X-ray photoelectron spectroscopy 40

4.2.1 The background of XPS 40

4.2.2 Instrumentation 43

4.3 Transmission electron microscopy 46

4.4 Quadrupole mass spectrometry 47

4.5 Quartz crystal microbalance 49

4.6 Atomic force microscopy 50

4.7 Profilometer 52

4.8 Contact angle measurement 52
4.9 90° peel test 53

5. Experimental 56
5.1 Preparation of polymer thin films 56
5.1.1 Polymers 57
5.1.2 Spin coating 59
5.2 Polymer metallization 61
5.2.1 Vacuum evaporation 62
5.2.2 Magnetron sputtering 64
5.3 Ion-beam irradiation 66
5.3.1 Ion chemistry 66
5.3.2 Ion energy and incident angle 67
5.3.3 Ion current and ion fluence 68
5.3.4 Sample charging 70
5.4 Polymer sputtering rate measurements 72
5.4.1 Sputter rate determination by step measurements using a stylus profilometer 72
5.4.2 XPS method 74
5.4.3 QCM method 75
5.4.4 Sputtering rate vs. temperature 76
5.5 Experiments based on X-ray photoelectron spectroscopy 77
5.5.1 Polymer surface chemical analysis 77
5.5.2 Surface glass transition temperature measurements 78
5.5.3 Condensation coefficient measurements 79
5.6 Contact angle measurements 80
5.7 Surface roughness measurements 81
5.8 90 ° peel test 82

6. Results 86
6.1 Sputtering rate of polymer thin films 87
6.1.1 Sputter rate dependence on the ion fluence and the treatment gas 88
6.1.2 Artefacts related with the region of decreased in the sputter rate 98
6.1.3 Rate dependence on ion energy and incident angle 100
6.1.4 Sputtering rate vs. sample temperature 103

6.1.5 Sputter rate dependence on polymer chemistry 108
6.2 Alterations in chemical and physical properties of polymer surfaces under ion beam irradiation 113
6.2.1 Changes in the polymer surface chemical structure 113
6.2.2 Surface glass transition temperature 130
6.2.3 Changes in surface tension 132
6.2.4 Polymer surface roughness 134
6.3 Metal-polymer interface formation: relevance to adhesion 136
6.3.1 Early stages of metal growth on treated polymer surfaces 136
6.3.2 Metal adhesion on treated polymers 142
6.3.2.1 Peel strength 143
6.3.2.2 Failure location 146

7 Discussion 152
7.1 Low energy ion beam irradiation of thermoplastic polymers 152
7.1.1 Sputter rate dependence on the ion fluence under Ar^+ irradiation 153
7.1.1.1 Polystyrene and poly-α-methylstyrene 153
7.1.1.2 Polymethylmethacrylate and polymethylacrylate 161
7.1.1.3 Polyacrylonitrile and polymethacrylonitrile 164
7.1.2 Polymer degradation under nitrogen and oxygen ions 166
7.1.3 Influence of the sample temperature on polymer ablation 172
7.1.4 Sputter rate dependence on polymer chemistry 176
7.1.5 Summary and conclusions of sputtering phenomenon of thermoplastic polymers 186
7.2 Polymer-metal interface formation and adhesion after low energy ion beam irradiation 191
7.2.1 Adhesion improvement through - mechanical interlocking 192
7.2.2 Influence of induced chemical changes on metal/polymer adhesion 193
7.2.3 Adsorption of metal on treated polymer surfaces: correlation between condensation coefficient and enhancement in adhesion 198
7.2.4 Failure location and mechanisms of adhesion 203
7.2.5 Metal/polymer interface formation: summary and conclusions 207

8 Summary and Conclusions 209

9 Outlook 214

List of References 216

Symbols and Abbreviations 228

Publication list 229

Acknowledgements 231

Chapter 1

Introduction

A growing interest in polymer applications in such fields as coatings, adhesion, composites, biomaterials, medicine, microelectronics, and thin-film technology requires special surface properties that could be tailored by flame treatment, radiation grafting, chemical treatment, photon irradiation, corona discharge and plasma treatments, as well as ion-beam modification. Up to now, corona discharge and plasma treatment are the most widely used surface modification techniques, especially in industry, and the results have been extensively published [Chan 94, Garbassi 98, Moss 86, Charbonnier 00, Friedrich 00]. Corona discharge equipment is of simple design and cost effective. But because the process takes place in ambient conditions, sample contamination becomes a problem, not every gas can be used, and the treatment is not very uniform. In contrary to this, plasma treatment is carried out in vacuum, therefore contamination of the polymer surface can be avoided, different treatment gases for different applications can be used, and the surface modification is rather uniform over the large area. On the other hand, plasma is very complicated process and it is difficult to control the treatment parameters that differ from system to system. Furthermore, the influence of electrons, neutrals, and vacuum UV photons on modification process is still not very clear.

To overcome these problems, an ion beam technique was chosen. Advantages of this treatment method compared to the widely used plasma treatments are the well defined ion fluence and a lateral space resolution that is important for thin film texturing. Together with the possibility to vary the modification depth through the variation of the ion beam energy, this technique can be used to change the physicochemical properties of the bulk polymer near surface region in a controlled way. Ions are generated by an external ion source, which means that the sample is isolated from the glow discharge generation and is held in better vacuum avoiding surface contamination, fast electron bombardment, and re-sputtering by gas phase scattering. However, in spite of the increased interest in the application of low energy ion processing for polymer surface modification, little work has been done to firmly identify the complex mechanisms of polymer surface treatment and structuring, adhesion enhancement, as well as polymer sputtering.

The fundamental motivation of this research is based on the dramatic change in the physical and chemical properties associated with ion beam bombardment of polymer surfaces using low energy ions (0.5 – 5 keV) and varying ion fluencies in the range from10^{12} to 10^{16} cm^{-2}. Irradiation with low energy ions was chosen in order to induce changes only in the polymer surface layer, leaving the bulk properties unchanged. The thickness of the altered layer ranges from 1 to 20 nm [Biersak 87] and is close to the modified layer obtained by plasma or corona treatments with which our obtained results can be compared.

When ions interact with the polymer surface, chain bonds are broken resulting in the formation of smaller molecules, many of which may be volatile and are therefore easily desorbed, i.e. sputtered, or formation of free radicals which participate in different reactions changing the chemistry of polymer surfaces easily and irreversibly. Polymer removal and modification occur simultaneously, and so it is difficult to distinguish where one process finishes and another starts, as the treated surface will be sputtered step by step. On the other hand, ions will penetrate beneath the altered layer inducing new changes there.

The objectives of the presented thesis are:

- to determine the sputter rates of polymers as a function of ion beam parameters and polymer chemistry. Recently [Zaporojtchenko 03b, Zekonyte 05], a decrease in the polymer sputter rate was observed at the beginning of the ion irradiation until constant sputtering is reached at prolonged ion fluences. Therefore, a quartz crystal microbalance was selected to monitor real time removal and kinetics of polymer sputtering as a function of ion fluence at different experimental conditions. In the following, the results and the mechanisms of polymer degradation will be explained;
- to change the physical and chemical properties of the polymer surface through the alteration of the polymer structure. Polymer chains undergo chain scissions under ion irradiation creating small mass molecules some of which can be desorbed, i.e. sputtered, and free radicals that participate in different chemical reactions creating cross-link networks, branching, and double bonds. If polymers are irradiated with oxygen or nitrogen ions, created free radicals react with reactive species inducing the formation of carbon-oxygen and/or carbon-nitrogen functional groups. To determine created functionalities, X-ray photoelectron spectroscopy (XPS) is used together with angle resolved XPS analysis that allows us to determine the uniformity of the surface modification by variation of the take-off angle. The surface glass transition temperature measurements based on the noble metal embedding method

[Zaporojtchenko 01, Erichsen 04] is used to determine the change in polymer behaviour under ion irradiation, i.e. cross-link formation and degradation;

- to determine the influence of the ion beam parameters and polymer chemistry on the metal-polymer interaction. An increased condensation coefficient and an increase in cluster density (measurements based on XPS [Zaporojtchenko 00a], or TEM) and polymer surface energy (contact angle determination) with increasing ion fluence indirectly show the improvement of metal-polymer adhesion. Practical adhesion measurements are done using 90° peel tests which indicate a strong dependence of the adhesion on the polymer chemistry. In conjunction with these results, the adhesion mechanisms of metals on the ion modified polymer surfaces are clarified.

In Chapters 2, 3 and 4 of this work backgrounds on polymer surface properties, ion-polymer interaction and analytical techniques used in the research are given. In the experimental part, Chapter 5, details for sample preparation and measurement methods are presented. The following two chapters include experimental results and discussion. The results part is divided into three large sections that present the most important obtained results of the goals mentioned above. Although experimental results are presented in three separate sections, the chapter “Discussion” is only divided into two sections: low energy ion beam irradiation of polymer surfaces; and polymer-metal interface formation and adhesion after ion treatment. After each large section, a short summary is given. Finally, the conclusions are summarized, and an outlook is presented.

Chapter 2

Polymers

A polymer is a substance composed of molecules which consist out of a long sequence of one or more species of atoms or groups of atoms linked to each other by primary, usually covalent, bonds. Polymers that consist of one type of monomers are called homopolymers. If a polymer is derived from more than one monomer, it is called a copolymer. The covalent bonds involved are characterized by high binding energies (146 to 628 kJ/mole), short bond lengths (0.11 to 0.16 nm), and relatively constant angles between successive bonds [Fink 04].

In general, polymer chains are very flexible, and therefore are coiled up with some free volume in between. The simplest chains are of linear skeletal structure which may be presented by a chain with two ends. Branched polymers have side chains, or branches, of significant length which are bonded to the main chain at branch points (junctions), and are characterized in terms of the number and size of the branches. Network polymers have three-dimensional structures in which each chain is connected to all others by a sequence of junction points and other chains. Such polymers are said to be cross-linked.

Polymers are usually classified into three groups: thermoplastics, elastomers and thermosets. Thermoplastics are linear or weakly branched polymers with negligible entanglement. They can be crystalline or amorphous. Those which crystallize do not form perfect crystalline materials but instead are semi-crystalline with both amorphous and crystalline regions. The crystalline phases of such polymers are characterized by their melting temperature (T_m). Many thermoplastics are completely amorphous polymers which exist as glassy solids. These polymers are characterized by their glass transition temperature (T_g), the temperature at which they transform from glassy state (hard) to the rubbery state (soft). Elastomers are cross-linked rubbery polymers that can be stretched easily to high extensions and which rapidly recover their original dimensions when the applied stress is released. Thermosets are rigid network polymers in which chain motion is greatly restricted by a high degree of cross-linking.

Over the last decades, polymers have been used successfully in many industrial applications, including adhesion, packaging, thin films, biomaterials, and coatings. Polymers have excellent bulk physical and chemical properties, are inexpensive and easy to process.

However, the average chemical composition and morphology of the surface of solid polymers are usually differ from those of the bulk [Elias 97], and the successful implementation of many of the above mentioned applications is determined by the surface properties.

This work concentrates on ion beam induced changes of thermoplastic polymer surfaces and/or near-surface layers. Therefore, some important surface properties will be discussed. The discussion will cover the main aspects of surface dynamics including glass transition temperature, surface forces and energy, as well as the main theories of adhesion mechanisms and metal/polymer interface formation.

2.1 Dynamics and glass transition temperature of polymer surfaces

The presence of surface dynamics comes from the observation that some polymeric systems have surface properties which are a function of the surrounding environment [Garbassi 98, Jones 99]. This means that a polymer surface can change its surface structure in terms of orientation of the surface side or end groups in response to a change in the interfacing environment. The thermodynamic driving force for surface restructuring is the minimization of the interfacial free energy between the polymer and the environment.

The studies of surface reorientation are mostly based the contact angle measurements, and in detail are reported by Garbassi et al. (1998) and Chan (1994). In vacuum and in air, the non-polar components of polymer tend to segregate to the surface, minimizing the interfacial energy. In an aqueous medium, the polar components are attracted to the interface [Chan 94]. The contact angle will decrease or increase following the changes in the concentration of the different functional groups on the surface.

Reorientation on the surface is also time and temperature dependent. At low temperatures, polymer chains have limited mobility, hence, restructuring takes longer, while the chain mobility increases for higher temperatures and reorientation occurs faster, as was shown experimentally by Morra et al. [Morra 90]. Evidence of an enhanced surface mobility is the behaviour of the glass transition temperature of thin films which show a different behaviour compared to the bulk glass transition temperature [Jones 99, Forrest 00].

The glass transition temperature T_g is the temperature at which the polymer undergoes transformation from a rubber to a glass. The transformation glass $\leftrightarrow$ rubber-like liquid resembles phenomenologically a thermodynamic second order transition since a more pronounced “jump” is observed at T_g for heat capacity and expansion coefficient [Elias 97]. However, more detailed thermodynamic measurements have shown that while the glass

transition has the appearance of a thermodynamic second order transition it cannot strictly be considered as one [Young 91; Grest 71, Krevelen 90].

Another characteristic of T_g is that the exact temperature depends upon the rate at which the temperature is changed (Figure 2.1). It is found that the lower the cooling rate the lower is the value of T_g [Elias 97, Krevelen 90]. In the regions above and below T_g there is a linear variation in specific volume of a polymer with the temperature. In the vicinity of the T_g there is a change in the slope of the curve which occurs over several degrees.

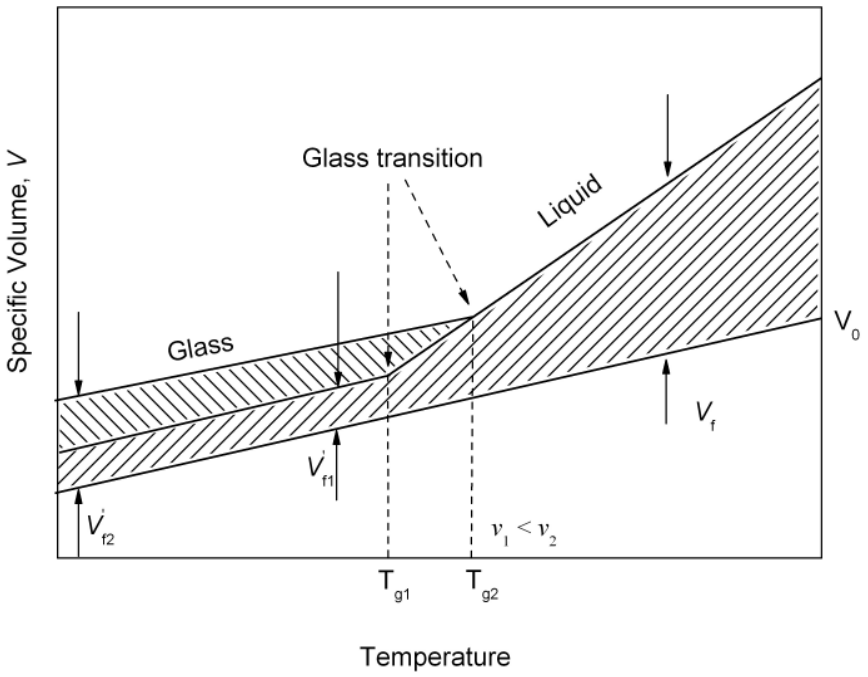

Figure 2.1 *Schematic illustration of the variation of the specific volume V and temperature of a polymer. The value of the glass transition temperature T_g depends on the cooling rate v (K/h). If $v_1 < v_2$, then $T_{g1} < T_{g2}$. The shaded area represents the variation in the free volume V_f with temperature. In the liquid state it is supposed that the free volume is high. A reduction in temperature will lower the free volume until there will be no volume to allow molecular rotation or translation. Below T_g the polymer is in the glass state, and it is assumed that the free volume V_f' remains constant. V_0 is the volume occupied by the molecules.*

In order to analyze the glass transition temperature the concept of free volume is used. The free volume is the space in the solid or the liquid not occupied by polymer molecules. In the liquid state, the free volume is high and so molecular motion takes place relatively easy. A reduction in temperature will reduce the amount of thermal energy available for the motion. The free volume will be also sensitive to the change in temperature, and most of the thermal expansion of the polymer rubber or melt can be accounted for by change in the free volume. With the decreasing temperature the free volume will be reduced until there will not be enough free space to allow molecular rotation or translation to take place. The temperature at which this happens corresponds to T_g (Figure 2.1). It is assumed that the free volume $V_f^{'}$ remains constant below T_g and increases as the temperature is raised above T_g.

The value of T_g depends upon the physical and chemical nature of the polymer molecules. The most important factor is chain flexibility. Polymers, such as polyethylene (— CH_2 — CH_2 —)$_n$, have relatively flexible chains because of easy rotation about the main chain bonds, and so the value of T_g is low. In vinyl type polymers (— CH_2 — CHX —)$_n$, the presence of the side groups, X, has the effect of increasing T_g due to the restriction of bond rotation [Young 91]. The physical characteristics of the molecules such as molar mass, branching and cross-linking also affect the glass transition temperature. The value of T_g increases as the molar mass of the polymer is increased [Young 91]. A small number of branches tend to reduce the value of T_g, while a high density of branches has the same effect as side groups in restricting chain mobility and hence raising the temperature. The presence of chemical cross-links in a polymer sample leads to an increase in the value of T_g, because of the reduced specific volume of the polymer leading to a restriction of molecular motion. If the density of cross-links is very high the temperature range of the transition is broadened and the glass transition may not occur at all.

The glass transition temperature is an interesting property rather extensively investigated for the polymer bulk, and only in 1993 a first study of glass transition in thin films was reported [Beaucage 93]. A detailed review is given by Forrest and Jones [Forrest 00]. Reiter [Reiter 94] performed experiments on the de-wetting behaviour of thin polystyrene films that were spin coated on silicon wafers. The films were heated and the temperature at which de-wetting occurred was found to decrease with the film thickness. It was stated that polymer chains in thin films have a higher mobility than corresponding chains in the bulk. Keddie et al. [Keddie 94] performed extensive studies on the polystyrene film thickness dependence of T_g. Authors reported the existence of a film thickness effect, with the glass transition temperature decreasing below the value for the glass temperature of the bulk in

films with a thickness below 100 nm, with a depression in the T_g value exceeding 20 °C. Lager temperature depression between T_g of thin films and the bulk T_g was found for free-standing films [Forrest 96]. Most of the measurements performed are based on the polymer film thickness. Recently, a noble metal nanocluster embedding method was applied to measure the surface glass transition for spin coated PS films [Zaporojtchenko 01, Erichsen 04a, Erichsen 04b]. The embedding of nanosized clusters needs long range chain mobility of the polymer, and clusters start to sink into a polymer at the glass transition temperature. Therefore, the embedding method is a probe for the glass transition temperature near the surface region. The observed depression increased with molecular weight until saturation was reached with $\Delta T_g \approx 8$ K (the difference between the bulk and surface glass transition temperature).

2.2 Polymer surface properties: relevance to adhesion

Adhesion is the surface property relevant in many applications of polymeric materials. For instance, it might be necessary to have permanent ink on polymer bags, or stable adhesion of a thin metal film on a polymer substrate. The necessary condition for the adhesion is the tight contact between the two parts. To achieve such interfacial contact, it is important to form strong and stable adhesive joints. The next stage is the generation of adhesion forces across the interface, and the nature as well as the magnitude of such forces is important. Another very important condition is how efficiently an adhesive layer wets the substrate. Before discussing adhesion theories, a short overview of surface forces and surface energies is given.

2.2.1 Surface forces

When a material interacts with another material or with the surrounding environment, it is the nature of the surface forces that determines the kind of interaction. There are long-range forces (Van der Waals' and electrostatic) and short-range forces (hydrogen, acid-base, covalent). Van der Waal's forces are always present during the interaction. However, in some cases other kinds of forces such as electrostatic ones occur at the same time. These forces arise from the interaction between charged bodies, described by the charge and the potential. The combination of van der Waals' and electrostatic effects in water (or a high dielectric constant solvent) is described by the so-called DLVO (Derjaguin, Landau, Vervey and Overbeek) theory of colloid stability. A more detailed review of all surface force theories is given by Garbassi [Garbassi 98].

Van der Waals' forces are a set of forces characterized by the same power dependence on distance. The important parameters in such a kind of interaction are the dipole moment, which arises from an uneven charge distribution in molecule, and the atomic polarizability, which indicates the tendency to redistribute the charge when the molecule is subjected to an electrical field. Owing to the process of charge redistribution, a molecule becomes a dipole and gives rise to an electrical field. An important contribution to the van der Waals' forces is the interaction between the instantaneous dipole moment arising from the instantaneous position of electrons with respect to the nucleus. The van der Waals' forces are always involved in the interaction between bodies, unlike other kinds of forces that require a particular feature [Garbassi 98].

The van der Waals' contribution to the free energy of interaction between two molecules, *w*, is inversely proportional to the sixth power of the distance,

$$w_{\mathrm{vdw}} = -C / r^6 \tag{2.1}$$

The free energy of interaction between macroscopic bodies, *W*, of different geometries can be described by a relationship of the kind:

$$W(D) \propto UA / D^{\mathrm{n}} \tag{2.2}$$

where *U* is a factor which contains numerical constants and the relevant dimensions of bodies involved, *D* is the distance between the bodies, and $A = \pi^2 C \rho_1 \rho_2$ is the Hamaker constant (ρ is the number density of molecules in the solid).

The equations above show some important features of van der Waals interactions: the free energy of interaction between macroscopic bodies depends on the dimensions of the bodies (factor *U*). Van der Waal's forces between large bodies are more long-ranged than between molecules. Finally, the effect of the chemical and physical nature of the materials involved in the interaction on the interaction itself, is described by the Hamaker constant, which contains the relevant atomic or molecular parameters in the constant *C*. Even if Van der Waal's bonds are always present, the energy of such bonds is the lowest compared to other bond types. Therefore, they are only of significance in cases where other kind of bonding is not possible.

In addition to the long-range forces, short-range forces are also present in the interactions. These are usually strong covalent, hydrogen, or acid-base forces [Garbassi 98 and references therein]. The structural feature required to form hydrogen bonds is a hydrogen

atom covalently bonded to a highly electronegative element, such as O, N, F, etc. It is expected that hydrogen bonding plays an important role in the interaction between polymer surfaces bearing hydroxyl, carboxyl, amino or similar groups. When surface atoms and molecules come very close together, very strong forces arise from the overlap of electronic clouds and sharing of valence electrons. The process when intervening atoms lose their identity and create a new species is known as covalent bonding. The details of covalent bonding depend on the chemistry and the electronic and geometrical configuration of the species involved. Most synthetic polymers do not bear surface functional groups suited for covalent bonding, as chemical inertness is a desired property for many applications. When it is necessary to join the polymer covalently with another molecule, surface activation is applied by means of surface modification introducing special functional groups suitable for covalent bonding.

2.2.2 Surface energy and surface tension

Surface atoms and molecules are in a different environment as compared to their bulk counterparts. In the bulk, a molecule is equally attracted in all directions by its neighbouring molecules [Chan94]. The surface molecules are subjected to intermolecular attraction from one side only. This tend to leave the surface region and return to the bulk until a pressure gradient, which is caused by the concentration gradient, is set up to stop further migration of the surface molecules. At the equilibrium state, the lower density of the surface layer leads to an increased intermolecular distance, putting it in a state of tension.

The origin of the surface energy of materials can be understood by thinking of the pair wise summation between the atoms of one medium with all the atoms of the other medium (Equation 2.1). If the summation is extended to all atoms, including atoms in the same medium, the energy can be determined as:

$$W = -\text{constant} + \frac{A}{12\pi D_0^2} \tag{2.3}$$

where the constant is the bulk or cohesive energy of the atoms of a given phase in their equilibrium position. The second term arises from the existence of two surfaces which atoms have fewer neighbours than those in the bulk. For two isolated surfaces, free energy is given by:

$$W = \frac{A}{12\pi D_0^2} = 2\gamma \tag{2.4}$$

or

$$\gamma = \frac{A}{24\pi D_0^2} \tag{2.5}$$

where γ is the surface tension. The main problem with equation (2.6) is that it is not clear how the interfacial contact separation D_0 should be determined. Israelachvili [Israelachvili 91] found that the universal cut-off distance is 0.165 nm.

The simplest way to measure surface tension is to use contact angle measurements (for a detailed explanation see Chapter 4.3.2). If a drop of a liquid is placed on a solid surface, three interfacial tensions exist: liquid-solid γ_{sl}; liquid-vapour γ_{v}; and solid-vapour γ_{sv}. Contact angles θ, of liquids on solids are summarized in the Young's equation:

$$\gamma_{sv} = \gamma_{sl} + \gamma_{lv} \cos\theta \tag{2.6}$$

Using various liquids, it is possible to determine the critical surface tension γ_{crit}, of a polymer. Most polymers have a value of γ_{crit} lower than the surface tension of water (72 mN/m) but higher than the surface tension of oils and fats (20 – 30 mN/m) [Elias97].

2.2.3 Mechanisms of adhesion

There are four main adhesion theories: mechanical interlocking, diffusion theory, electrostatic attraction, and adsorption theory, Figure 2.2. The theories work on different distance scales between two materials: from the atomic scale for chemical bonds to an undetermined scale in the case of mechanical interlocking. All theories are given in detail in reviews by Fourche [Fourche 95], Kinlock [Kinlock 94], Leeden and Frens [Leeden 02].

The theory of ***mechanical interlocking*** originates from rough empirical observations. It was observed that sticking is more successful on rough and irregular surfaces. However, it was possible to establish good adhesion between perfectly smooth surfaces [Garbassi 98]. In any case, the question remains open, whether production of a particular morphology activates a new adhesion mechanism, or if it increases the effectiveness of other adhesion mechanisms due to an increased area or removal of a contamination layer.

The ***diffusion*** theory proposed by [Voyutskii 49] explains the adhesion between two surfaces of identical polymers. According to this model, adhesion of two macromolecules in intimate contact results from the diffusion of the molecules of the superficial layers. The model has limited applications, because interdiffusion is obtained when adherates are mutually soluble, and macromolecules are very mobile which is achieved above the glass

transition temperature. The model is unlikely to describe the behaviour of polymers which are not or only slightly soluble in one another, or if the polymer surface is crystalline or highly crosslinked [Leeden 02]. Attempts to extend this theory to polymer/metal systems were not successful [Kinloch 94, Fourche 95].

The ***electrostatic attraction*** theory was developed for the occurrence of an electrical double layer at the interface between two solids, therefore justifying the adhesion force with the establishment of an electric attraction [Derjaguin 55]. However, it appears that for typical adhesive/substrate interfaces any electrical double layer does not contribute significantly to the intrinsic adhesion, and observed electrical phenomena during the joint fracture process probably arise from the failure events, rather than to cause the adhesion between the materials [Kinloch 94, Garbassi 98].

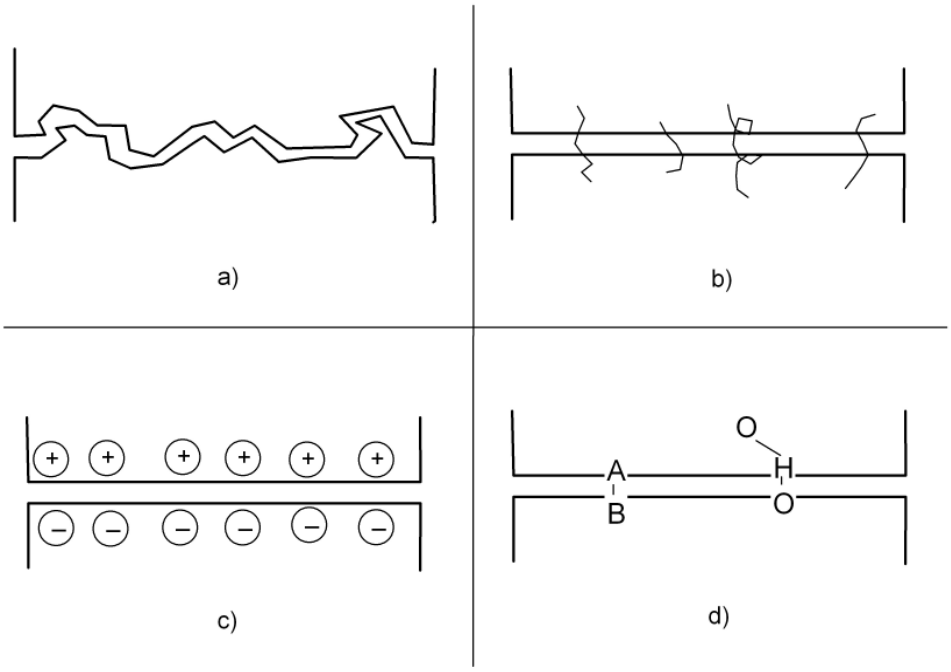

Figure 2.2 *Mechanisms of adhesion: a) mechanical interlocking; b) interdiffusion of chains; c) electrical interactions; d) chemical interactions (adsorption theory), [Garbassi 98].*

The ***adsorption theory*** is the most widely applicable theory. It proposes that, when sufficiently intimate molecular contact is achieved at the interface, the material will adhere because of the interatomic and intermolecular forces which are established between the atoms and molecules in the surface of adhesive and substrate [Kinloch 94, Leeden 02]. This theory

includes all the explanations which involve chemical bonding, acid-base and van der Waals interactions. An essential condition required for this adhesion model is a close and intimate contact between the substrate and the adhesive. For this reason the adhesive must wet the substrate surface. Above, polymer surface tension and energy was shortly discussed. Qualitatively, the rule holds true that the higher the surface energy of the solid is relative to the surface energy of a liquid, the better is the wettability of the solid and the smaller is the contact angle and the greater is the adhesion between two materials.

After wetting and spreading of the liquid, physical adhesion must take place before any other bonding process occurs. A measure of the attraction of two solids S_1 and S_2 across an interface is the reversible work of adhesion W_{adh} given by the relationship of Dupre [Kinloch 94, Fourche 95, Leeden 02]:

$$W_{adh} = 2(\gamma_{s1}^{d}\gamma_{s2}^{d})^{1/2} + 2(\gamma_{s1}^{p}\gamma_{s2}^{p})^{1/2} \tag{2.7}$$

where γ^d and γ^p are dispersion and polar (dipole, hydrogen, acid-base interactions) components of the surface tension. W_{adh} is the work required to separate S_1 and S_2 creating a unit of surface area of S_1 and S_2 at the expense of a unit area of S_1 - S_2 interface, [Krevelen 90, Kinloch 94, Fourche 95].

However, it was shown that the fracture energy of and assembly of few hundred J/m^2 is considerably higher than the reversible work of adhesion (Equation 2.7) [Kinloch 94, Fourche 95]. The values of the adhesion work assume that only secondary bonds act at the interface which have a much lower bond energy compared to primary chemical bonds (covalent, ionic, metallic) or acid-base interactions. Adhesion by chemical bonding takes place rather frequently in the case of polymer-metal interfaces [Fourche 95]. The formation of such bonds is based on a charge transfer from the metal to the polymer. An increase in adhesion through the connection by primary bonds is obtained when special side or functional groups are introduced along the polymer chain or new adsorption sites containing radicals, unsaturation, etc. are created.

Before finishing this chapter, it is worth mentioning the model based on the ***weak boundary layer***, proposed by Bikerman [Bikerman 61]. The author showed that failure is very unlikely to propagate exactly along the interface. The fracture cohesively propagates in one of the solid contacts. Thus, whatever mechanisms govern the assembly formation, the strength itself depends on the bulk properties of the adherates [Fourche 95]. Nevertheless, Bikerman [Bikerman 61] indicates that another failure mechanism can occur when the fracture moves

towards a weak interfacial layer located between two materials. Most surface treatments are used to enhance adhesion by introducing functional groups or creation of a heavily cross-linked layer. At this point, the concept of a weak boundary layer becomes important because it introduces the idea of an "interface" which´s properties determine the joint strength [Fourche 95].

The examination of various theories made on the basis of adhesion specifically referred to polymers, has shown that only those based on chemical interactions have a general character and a wide application. Electrostatic and interdiffusion theories are important in some specific systems and mechanical interlocking may cause other mechanisms to take part in the adhesion phenomenon. The theories were referred to the adhesion enhancement at the interface of the adherent and the substrate. However, the cohesive failure suggests the formation of some weak boundary layer in one of the solids.

2.2.4 Metal-polymer interface formation

Metallized plastics are used extensively in applications ranging from food packing to microelectronics [Mittal 98, Lee 91]. Whatever the intended purpose of metallization may be, a metallized polymer will not perform its function unless the metal adheres strongly to the polymer substrate. Reliable adhesion between metal and polymer will depend on the nature of interaction between these two materials. A strong chemical reaction involving metal/polymer bond formation is expected to result in strong adhesion, whereas a purely physical interaction via van der Waals or electrostatic forces is supposed to result in weak adhesion [Mittal 76]. Consensus exists that noble metals, such as Au, Ag and Cu, interact weakly with polymers. However, it was shown that due to the strong aggregation tendency of noble metals on polymers, the chemical interaction at room temperature and above occurs between metal clusters and the polymer [Strunskus 98]. For highly reactive metals, Cr, Ti, Al, Co, the available experimental data show strong chemical interactions with polymers, involving the formation of new compounds [Faupel 02].

Droulas et al. [Droulas 92] reported the interaction of evaporated Au and Al with different polymers. Evaporated Al atoms were shown to interact by adsorption onto some specific sites present on polymer surfaces: phenyl rings, ketones and carboxyl ester moieties. The adsorption results in electron transfer from Al to the electrophilic sites and formation of a $[CO]^{-\delta}Al^{+\delta}$ complex, which's stability depends on the competition between the metal-polymer interaction and the metal-metal interaction [Droulas 92]. No interaction and formation of interfacial compounds was found for evaporated Al and Au on PE and PP. Metal atoms possess a large mobility on the surfaces of these two polymers and due to strong metal-metal

interaction a growth involving formation of large clusters followed by coalescence takes place. Low interaction with formation of unstable metal atom-arene complexes was reported for Au on PS and PET. In the case of the Au/PS system, the complex between metal and substrate was observed for low metal coverage, while with continuing metal coverage Au-arene interaction is weakened. Strong interaction with formation of a stable charge transfer complex was demonstrated for Al on PS, PEEK, PET.

When Cr is deposited onto a polymer surface, the metal reacts strongly with functional groups of the polymer surfaces causing disorientation of macromolecules. Arene-Cr sandwich complexes were favoured for the Cr/PS system, metastable Cr-C species with four membered rings were formed for the Cr/PC system, and C-O-Cr complex formation was observed when Cr reacted with C=O or C-O-C functional groups present in PC, PMMA, PET [Friedrich 99, Friedrich 00]. The formation of stronger Ag-O-C and somewhat weaker Ag-π species were observed for the Ag/PET system [Gerenser 92, Burger 92]. When nitrogen was present in the polymer rather strong silver-nitrogen-carbon bonds (C-NH-Ag, C=N-Ag) were observed [Gerenser 92].

Summarizing the available experimental results, complex metal-oxygen-polymer or metal-nitrogen-polymer species will result in stable and rather strong metal/polymer interactions. Complex formation of metal atoms with π electron containing bonds or ring systems often result in weak and unstable bonds that have the tendency to rearrange [Friedrich 00]. If no functional groups are present in the polymer, as in the case of PE or PP, the physical interaction between the metal and the polymer leads to poor interaction between these materials, and therefore to very weak adhesion. The strength of interaction also depends on the nature of the metal: reactive metals (Al, Cr) easily oxidise, thus they preferentially will react with oxygen functional groups; noble metals (Ag, Cu, Au) are more reactive with nitrogen [Burger 92].

Even if Al or Cr interaction with polymers is stronger compared to the interface formation between noble metals and polymer surfaces, the addition of oxygen and nitrogen functional groups or other kind of adsorption sites can improve the adhesion between metal and polymer. Out of this reason surface modification is required. There are a number of modification techniques that in one way or another change the polymer surface chemistry. An overview is given by Chan [Chan 94]. This research concentrates on the ion-beam induced physical and chemical alterations of the polymer surface properties. One of the topics concentrates on the incorporation of oxygen and nitrogen functional groups into the polymer surface layer in order to improve the adhesion of noble metal on polymers.

Chapter 3

Ion Irradiation

Sputtering is the removal of material from objects by energy transfer in collisions of energetic atomic projectiles. It occurs in nature, where it causes erosion of the surface of airless astronomical bodies. The first documented sputtering in the laboratory was done by Grove in 1852 [Grove 52]. He indicated the formation of a deposit at the anode of a gaseous discharge tube and its removal when the polarity of the electrodes was reversed. After Grove's discovery, most observations on sputtering were made using gas discharges for almost a century. Isolation and characterization of the process using controlled ion beams in vacuum and characterization of materials started only in the second half of the twentieth century.

In this chapter, the basic physical processes of the sputter phenomenon will be presented. Particle/polymer interactions including the mechanisms of energy deposition, penetration depth and damage distribution, theoretical ejection models of organic molecules, as well as ion induced effects in polymers are discussed in this chapter.

3.1 Ion – polymer interaction

Ion interaction with a solid induces great damage resulting from bond breakage, which becomes more important in organic films, since recovery of the damage by annealing becomes difficult [Venkatesan 87]. Bond breakage in organic materials generally results in the formation of smaller molecules, many of which may be volatile and are easily desorbed, changing the chemistry of polymers easily and irreversibly.

Most of the phenomena observed during ion bombardment of polymers are related to the energy deposition from the incoming ions to the target. The basic quantity characterizing ion-to-target energy transfer is the projectile's energy loss per unit length, dE/dx. Depending on the ion velocity, energy loss mechanisms can be divided into nuclear stopping power and electronic stopping power. Another important parameter is the ion penetration depths and therefore the damage distribution. These parameters will be shortly discussed below. For

detailed overviews the reader is referred to a number of literature references [Fink 04, Berisch 81, Berisch 91, Biersak 80, Ziegler 88].

3.1.1 Energy-loss processes of ions in matter

The total amount of energy deposition depends upon the target mass and electronic structure, as well as upon the mass, energy and fluence of the projectiles. The dominant energy-loss mechanisms are very different for low and high velocities, as shown schematically in the Figure 3.1. At low incident velocities the projectile losses its energy predominantly via inelastic binary collisions with the atoms in the solid. The energy transfer may suffice to remove an atom from its lattice site, which later can cause other atoms to recoil resulting in a collision cascade. At high velocities (or very high energy ranges), the energy loss of ions penetrating matter is dominated by electronic collisions, mainly target excitation and ionization. In insulators, the lifetimes of excited electronic states may be long enough to allow the excitation energy to be transformed into atomic motion and sputtering (electronic sputtering) [Fink 04, Sundquist 91].

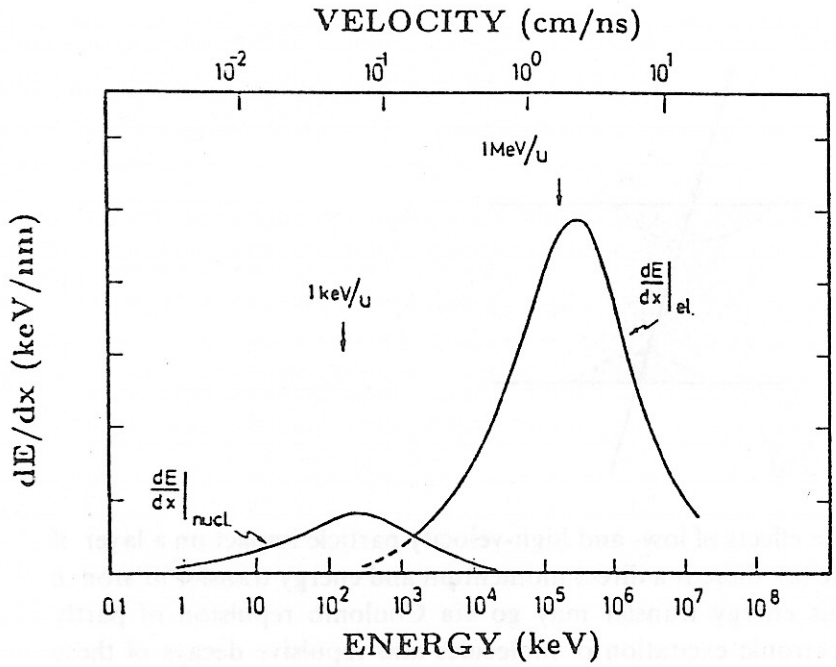

Figure 3.1 *Nuclear and electronic energy loss per unit length,* [Sundquist 91].

The *nuclear stopping* power is related to the kinetic energy transfer from the incoming ion to the target atoms. The calculations of the nuclear stopping power have been performed by considering the fact that due to their low mass electrons can transfer only little momentum during elastic collisions at high impact energies [Fink 04, Sundquist 91]. At low energies, the cross-section for inelastic collisions vanishes with decreasing ion energy. The energy loss of an incident ion is usually characterized by the stopping power cross section S_n, which depends on the parameters of a binary collision. The energy loss per unit path due to elastic collisions is expressed as a product of the cross section and the number density of target atoms (n_t) [Mahan 00, Fink 04]:

$$\left(\frac{dE}{dx}\right)_n = n_t S_n \tag{3.1}$$

At high velocities the energy loss of ions penetrating matter is dominated by electronic collisions, mainly target excitation and ionization. For gases or insulators, the *electronic stopping* power falls off [Golser 91] faster at low ion velocities, since there is a non-vanishing minimum energy transfer. Semi-empirical calculations of the electronic stopping power are based on the concept of effective charge Z_p^{eff} and are obtained from scaled proton stopping power data [Fink 04]:

$$S_e(Z_p, \upsilon_p) = Z_p^{eff\,2} S_e(\text{proton}, \upsilon_p) \tag{3.2}$$

where the electronic stopping for heavy ions with nuclear charge Z_p and the proton stopping power are evaluated at the same velocity. This rule is accurate for high ion energies for bare projectiles ($Z_p^{eff} = Z_p$). For lower energies, the ions may lose or capture electrons and the stopping power problem is transferred to the definition of the effective charge.

According to Bragg's rule [Bragg 05], the stopping power of ions in a compound material may be estimated by the linear combination of the stopping powers of the individual elements. However, this rule has limited accuracy because the energy loss to the electrons in any material depends on the exact orbital and excitation structure of the target matter. The deviations from Brag's rule refer to bonding changes that might alter the mean charge state of the ion, and hence the projectile energy loss [Fink 04]. The stopping power of hydrocarbons (can also be applied to polymers) can be derived using linear superposition of atom "cores" and "bonds", with the cores resembling the stopping contribution from the closed shells of atoms, and the different bond contributions resulting from bond electrons [Fink 04]. The

technique, called the "*cores and bonds*" (CAB) approach, was derived by Ziegler and Manoyan [Ziegler 88]. In general, the stopping power is expressed as following:

$$S(Z_1) = (\gamma Z_1)^2 \left[\sum \text{cores} + \sum \text{bonds} \right] \tag{3.3}$$

where γ is the fractional effective charge of the ion and Z_1 is the atomic charge of the projectile.

The amount of deposited ion energy used in our experiments (ion energy 1- 5 keV) falls into the nuclear energy loss regime. In this case, the slowing down of an ion in the matter can be described as a sequence of binary collisions with the target atoms. The ejection of a large molecule due to impact of a slow particle is difficult to understand within the sputtering events like single-knock-on, linear cascade or the spike regime (sputtering events will be discussed in some detail in the following sections) [Sundquist 91]. A single-collision ejection mechanism may work for small molecules. However, for large molecules, a collective momentum-transfer mechanism via surrounding atoms and molecules is needed to explain how the intact molecules leave the surface. In this case, linear cascade or spike regimes are believed to be involved [Sundquist 91]. Even if low energy ions deposit energy via nuclear collisions, the electronic stopping is also present, due to both the primary particle and the recoils [Marleta 90b, Sundquist 91]. The calculated nuclear stopping power for 1 keV Ar^+ ions for polymer samples is of the order of 25 – 45 eV/Å, and, correspondingly, 15 – 18 % of the energy loss is due to the electronic type (4 – 5 eV/Å) [Biersak 87].

3.1.2 Range and damage distributions

Due to interactions with nuclei and electrons of the target, and incident ion will be slowed down along a randomly shaped path. The projectiles come to rest at some depth in the target (Figure 3.2). The range is the total path length of the projectile within the target. The mean projected range, R_p^p, along the initial direction of the projectile is equal to the average depth of penetration for normal incidence only. The range is given by:

$$R_p = \int_{E_f}^{E_0} \left(\frac{dE}{dx} \right)^{-1} dE \tag{3.4}$$

where E_0 and E_f are the starting and the final energy of the incoming projectile, respectively. The final energy corresponds to the energy at which the projectile ion cannot overcome the potential barrier between the target atoms and hence comes to rest.

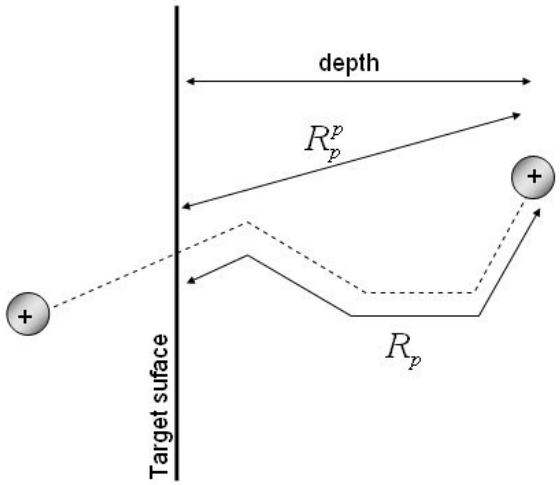

Figure 3.2 *The total range R_p, projected range R_p^p, and depth of penetration of a projectile.*

For negligible electronic stopping and low energy heavy ions in matter, the relationship between total range and projected range is a function of the mass ratio (M_1 and M_2 are masses of a projectile and a target material, respectively) [Fink 04a, Mahan 00]:

$$R_p^p = \frac{R_p}{1+\frac{M_2}{3M_1}} \tag{3.5}$$

The ion total range and projected range highly depend upon the energy of the primary projectiles and on the energy deposition mechanism. In the nuclear energy loss region, i.e. for low ion energies (0.1 – 100 keV), direct momentum and energy transfer from incident particles to target atoms occurs. A number of large angle scattering processes leads to a broad, nearly spherical range distribution. The penetration range of such ions is up to several hundreds of nanometres [Biersak 87]. On the other hand, fast particles (ion energy > 100 keV) transfer their energy via electronic excitation of molecules with the ion range exceeding several micrometers. High energy projectiles usually have straight particle trajectories nearly up to the end of their flight path, leading to sharp range distributions. Table 3.1 gives some results for projected and total ion ranges in polymers obtained from Monte Carlo range calculations [Biersak 87] for low energy ions. The ion range was also checked experimentally and showed a good agreement with the calculated values [Wilson 93a, Wilson 93b, Adesida84, Hnatowicz 93]. However, the lowest ion energy used in experimental range calculations was 50 keV, which is still much higher than our experimental energies. It should

be noted once more, that we were interested in the near surface layer modification which is achieved using ion energies up to 10 keV. The damage range for low ion energies is determined by molecular dynamics simulations, and up to date was not proved experimentally. Nevertheless, the ion depth distribution is comparable to the one of plasma and corona treatments, with which we would like to compare our results.

Table 3.1 *Total ion range R_p and projected ion range R_p^p for some polymers at different ion energies and ions [Biersak 87].*

Element	E, keV	Polymer	R_p, nm	R_p^p , nm
Ar	1	PMMA	5.42	4.36
	10	"	23.31	19.84
	100	"	158.01	143.56
	1	PE	5.89	4.89
	10	"	25.32	22.23
	100	"	169.07	156.83
O	1	PMMA	7.33	5.19
	1	PE	7.53	5.71
	1	PI	6.51	4.45
	1	Teflon	6.44	3.78

Irradiation effects are a consequence of energy transfer from the projectiles to matter. If the energy transferred to an atom in a nuclear collision is lower than the bonding energy to its environment, the hit atom starts to oscillate around its equilibrium position. If the transfer energy is equal to the bonding energy, then the atom may be released from its initial site, but will return to form a bond but as highly excited atom [Fink 04]. When the energy transferred to the atom is higher than bonding energy, atoms are kicked out from their original position, they move longer distances, may hit other atoms resulting in a collision cascade or may even be removed from the target. The mechanisms of sputtering and main parameters describing the phenomena are discussed in the next section.

3.2 Mechanisms of sputtering

When ions with energies exceeding a few tens of eV impinge on the surface several processes are initiated (Figure 3.3):

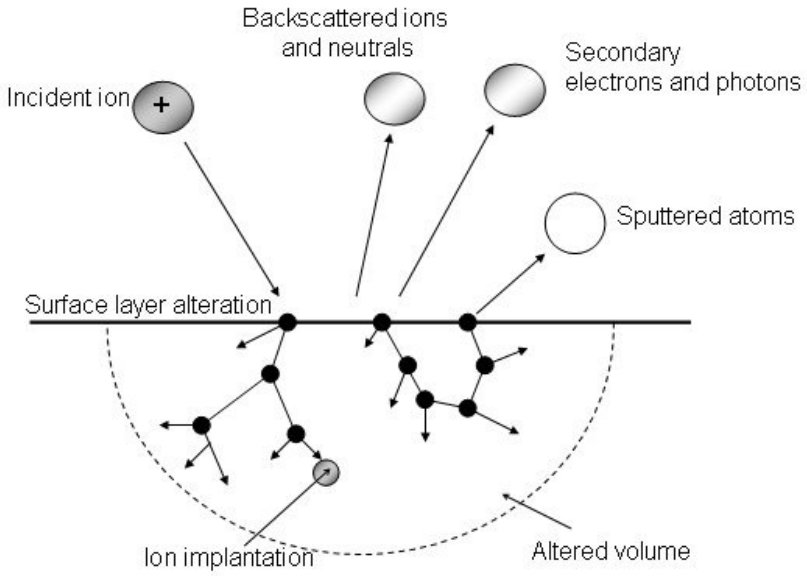

Figure 3.3 *Interaction of ions with a surface.*

- A small fraction of the incident ions is backscattered by the collision with the surface and near surface atoms. The backscattered particles are mostly neutral atoms with a broad energy distribution.
- Ion impact at the surface of a solid may also give rise to the emission of electrons (usually referred as secondary electrons) and photons. The electrons may be affected by potential emission, kinetic emission, or Auger emission from excited sputtered particles. Photons originate from backscattered or sputtered particles, excited in collisions with a surface atom before emission, or directly from excitations in the near-surface region of the solid.
- At the end of their range, the injected projectiles are trapped and accumulate in the solid. This phenomenon is called ion implantation, and is extensively used in integrated circuit technology. Nevertheless, implanted gaseous ions may induce unwanted results, such as formation of bubbles and blistering of the surface layer.

- The major fraction of the incident ions is slowed down in collisions with atoms and electrons of the target. The energy transferred to the target atoms may initiate a collision cascade, possibly leading to the ejection of surface atoms or clusters of target atoms, i.e. sputtering.
- The ion impact may also cause some structural rearrangements in the surface of a target material like the formation of vacancies and interstitials, changes in the stoichiometry, etc. [Chapman 80].

Incident ions slow down during the collision with atoms and electrons of the solid. During the collisions, energy in excess of the lattice binding energy may be transferred to an atom of the solid. The energy transfer mostly occurs in direct collisions with target atoms. However, energy may be also transferred by local electronic excitation and ionization. In any case, atoms are removed from their original sites. Knock-on atoms may also remove other atoms from their lattice sites, creating a collision cascade. Surface or near-surface atoms will be emitted if they receive a momentum in the direction of vacuum with an energy enough to overcome the surface binding energy. It is a matter of chance whether the cascade leads to the sputter ejection of an atom from the surface, or whether the cascade propagates into the interior of the target, gradually dissipating the energy of the primary ion impact. Usually more than 60 % of the ejected atoms originate form the first atomic layer, while the rest comes from the layers underneath [Behrisch 91].

The traditional concepts of sputtering can be divided into chemical and physical sputtering. Chemical sputtering takes place if incident ions and the atoms of the solid interact chemically and volatile molecules are formed. The erosion rate may increase beyond the value corresponding to knock-on sputtering. Physical sputtering invokes a transfer of kinetic energy from the incident particle to target atoms and subsequent ejection of those atoms which have enough kinetic energy to overcome the surface binding forces. Depending on the energy and mass of the incident ions, different collision cascade regimes can be distinguished (Figure 3.4) [Sigmund 81] as discussed below:

- *Single-knock-on regime* (ion energies up to 1 keV). The collision cascades are dilute and involve only a few atoms. Recoil atoms from ion-target collision receive sufficient energy to leave the surface, but it is not enough to generate cascades.
- *Linear-cascade regime* (ion energy several keV). Recoil atoms receive sufficient energy to generate recoil cascades. The density of recoil atoms is

sufficiently low so that collisions between moving atoms are infrequent, i.e. there is larger probability that the moving atom will collide with a non-moving atom.

- *Collision-spike regime* (heavy ions with energies above 100 keV). The density of recoil atoms is so high that the majority of atoms within a certain volume is in motion.

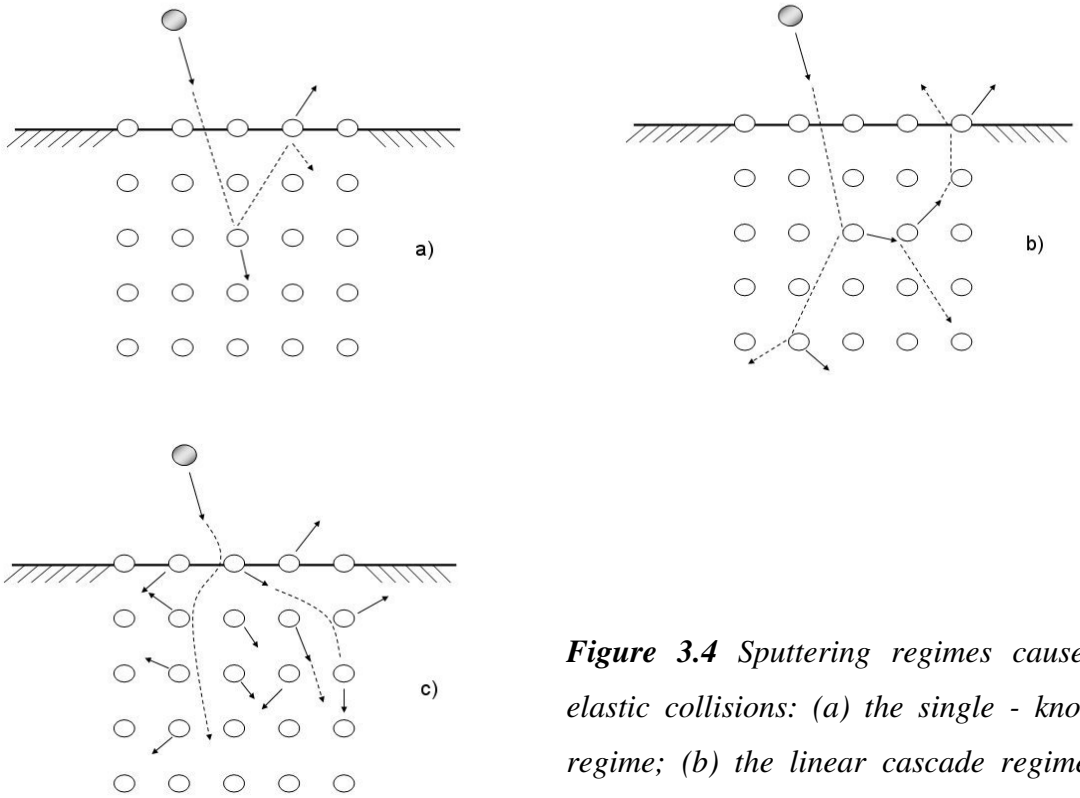

Figure 3.4 *Sputtering regimes caused by elastic collisions: (a) the single - knock-on regime; (b) the linear cascade regime; (c) the spike regime [Sigmund 81].*

Classical sputtering regimes, as well as the dependence of the yield (number of atoms removed from the target per incident particle) on experimental conditions were successfully applied to elemental materials. However, for organic molecules and polymers new models describing the emission of large material clusters and biomolecules had to be developed. In the following subsections, the trends in sputter yields of elemental targets, and the ejection mechanisms of organic molecules are discussed.

3.2.1 Trends in sputtering yield

The erosion of material under ion impact is measured by the sputtering yield *Y*, defined as the mean number of atoms removed from the surface of a solid per incident particle. The yield values depend on different parameters such as (i) the projectile energy, mass and angle of incidence; (ii) the mass of the target atoms; (iii) the surface binding energy of the target; and (iv) the crystallinity and the crystal orientation of the solid.

With respect to the incident ion's kinetic energy, there is a sharp yield threshold, followed by a rapid increase in yield with increasing energy. There is a broad maximum in the energy region of 2 to 50 keV, and a decline in yield at higher energies. The decline is related to the deeper penetration of ions into the solid and lower energy deposition in the surface layers. The threshold (for metallic targets the energy is 20 - 40 eV) exists because there is a minimum energy (the surface binding energy) that must be provided for a particle to escape from the target [Mahan 00].

Higher mass projectiles give larger sputtering yields compared to lighter ions. For heavy target atoms, the yield increases with the kind of projectile in the order Ne → Ar → Kr → Xe [Mahan 00]. The maximum yield for light targets is obtained at intermediate projectile masses (argon or krypton).

The yield increases for off-normal incidence up to a point, and then decreases for cases of glancing incidence. The increase in yield values may be due to an increased probability to escape for the recoil atoms for off-normal incidence. The decrease in yield is because of an increased probability of reflection or escape of a still-energetic incident particle. In this case, the number of recoils created during the ion interaction with the target is reduced. The maximum sputter yield is observed near 55 to 70 degrees, which depends on the projectile energy and mass, and the surface topography [Behrisch 81].

The particles removed from a solid surface are emitted with a broad energy distribution, with different excitation and charge states and in all exit angles. At high emerging energies, the number of sputtered particles decreases proportional to $1/(E_o)^2$, where E_o is the energy of sputtered particle, [Behrisch 81]. The angular distribution of the sputtered particles may be described by the ideal cosine emission law [Behrisch 81, Mahan 00]:

$$j_\Omega(\theta) = Yz^+ \cos\theta / \pi \tag{3.1}$$

where j_Ω is the emission flux angular distribution, z^+ is the impingement flux of the projectiles, θ is the emission angle, measured normal to the surface. For low ion energies, an "undercosine" distribution, in which fewer particles are ejected in the direction of the surface

normal, has been observed. For light projectiles, most particles are emitted in the direction of the surface normal, an “overcosine” distribution, [Behrisch 81, Mahan 00].

Up to now all trends in sputter yield were related to those obtained for metals. In the case of polymers, the determination of the yield is a rather complicated task. Polymers are composed of molecules which have long sequence of one or more species of atoms or groups of atoms, and the usual definition of sputtering yield for elemental targets cannot be applied to the sputtering of polymers, unless the identities of all sputtered particles (usually determined by secondary ion mass spectrometry (SIMS)) are known. In the case of polymers, ejected species are usually molecules of different sizes [Brigs 82, Delcorte 99], and the sputter yields are referred to the yields of molecules. However, the yield of each molecule decreases with the exposure time [Briggs 82], and each fragment is removed at a different rate. Therefore, in literature, yields for separate molecules are given. When the type of the emitted molecules is not known, the amount of material removed per unit time is used for the definition of sputtering rate.

Important observations were made for the molecule yield dependence on ion nature, energy, and angle. The fragmentation of polyethylene-terephthalate into low-mass molecular ions increased with decreasing primary ion mass but with increasing ion energy (from 2 to 22 keV) [Delcorte 99]. A yield dependence on incident angle was not observed in the case of polymer sputtering [Delcorte 99], even though the yield for elemental materials increases in the range of 50 to 70 degrees. However, the detailed experimental observations, as data for kinetic energy and angular distributions are scarce, and theoretical predictions are not perfectly valid in the case of low-energy particle induced desorption.

3.2.2 Ejection mechanisms of organic molecules

As it was already mentioned, irradiation effects are a consequence of the energy transfer of the projectiles to the material. Close to the projectile´s path through the solid, the deposited energy is extremely high and causes extensive fragmentation of target molecules. Over time, locally deposited energy diffuses away from the initially excited region towards the material bulk. If the energy transferred from the incident particle to the target atom is higher than the binding energy of the atom, the recoil atom is free to move and eventually to knock-on other target atoms forming a cascade. Several different kinds of species are desorbed from the target including neutral and charged fragments and whole molecules.

A desorption event in response to the impact of an energetic projectile is the end result of a large number of processes, all of which are in principle amenable to theoretical treatment.

In contrast to elemental materials, where sputtering mechanisms are widely investigated and reported in a number of papers in literature [Behrisch 81, Behrisch 91, Mahan 00], the studies on polymer molecule emission by energetic particle bombardment are very limited. Nevertheless, it was shown [Delcorte 99, Sundquist 91] that ejection mechanisms of organic materials differ from those of metals. The main desorption theories of organics are extensively discussed in a review by Reimann [Reimann 93]. Here, only the main aspects of each desorption model (collision cascade; hit theory; thermal models; shock wave; and pressure pulse) will be presented.

Collision cascade desorption

The collision cascade model is considered for cases in which solid matter is irradiated (or bombarded) by keV ions. In this "low velocity" regime, the velocity of the projectile is less than the Bohr velocity, and the incident ion sets target atoms in motion by direct elastic nuclear collisions. Target atoms which are set in motion, undergo subsequent collisions, setting a second generation of atoms into motion and so form an atomic collision cascade, as mentioned above. A schematic diagram of an atomic collision cascade is once more shown in Figure 3.5 (a).

Generalization of the collision cascade theory in the case of a molecular solid is rather complex. Hoogebrugge and Kistemaker [Hoogebrugge 87] have pointed out that the initial, more energetic part of the collision cascade can be described by the atomic collision cascade model, Figure 3.5 (b). Later, in the low energy regime, the complete molecule takes part in the collisions because of the presence of strong bonds, Figure 3.5 (c). In this model, a molecule at the surface is removed by the impact of a number of atoms from below, Figure 3.5 (d).

Haring et.al. [Haring 87] proposed statistical model for larger polyatomic molecules. The theory states, that a polyatomic molecule consisting of m atoms, each of which is hit by one recoil atom from a collision cascade in the substrate, Figure 3.5 (e).

Hoogebrugge and Kistemaker [Hoogebrugge 87] have extended the model of Haring in a sense that a polyatomic molecule containing $m > 2$ atoms has to be hit by exactly two atoms originating from a collision cascade in order to be ejected. According to the authors, each atom from below is assumed to collide with a part of a molecule to be desorbed, Figure 3.5 (e).

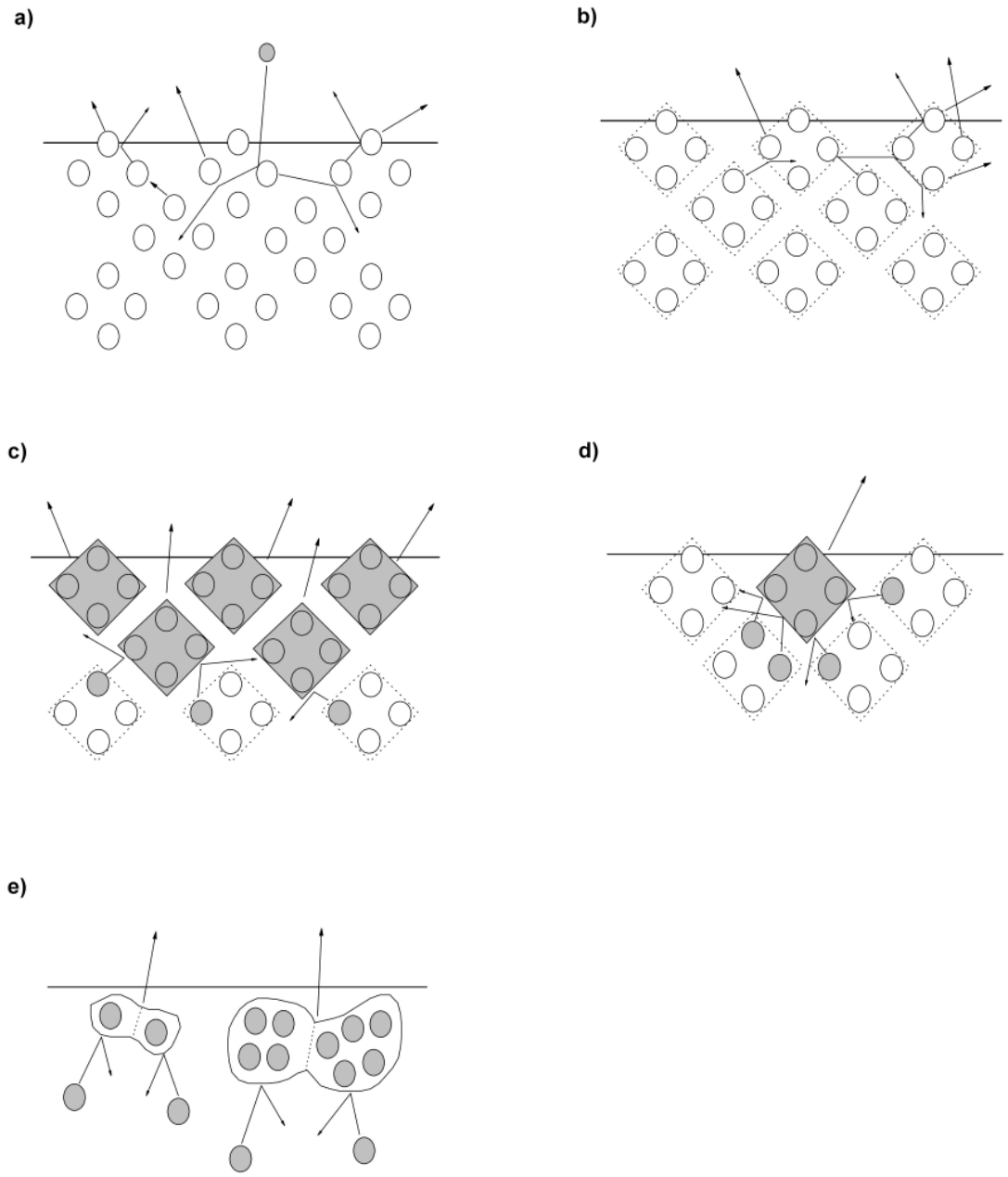

Figure 3.5 *Schematic diagrams of a collision cascade induced sputtering of atoms and molecules. a) Collisional cascade in an atomic solid. b) - d) Collision cascades in an organic solid. b) At early times, the cascade has an atomic character. c) For later times, the cascade has a molecular character. d) One molecule being ejected by several atoms impacting from below. e) A schematic diagram of statistical models: left - model of Haring: to eject molecules each atom should be hit by one recoil atom; right - model of Hoogebrugge and Kistemaker:* a *molecule containing m > 2 atoms is hit by exactly two atoms originating in a collision cascade.*

A general principal of the collision cascade theory for organic materials would be: desorption of a large molecule with sufficiently low internal energy to avoid fragmentation that requires some kind of "collective" desorption process, i.e. a push in the same direction by several atoms colliding from below, [Reimann 87].

Hit theory of desorption

The main idea of the hit theory, introduced by Katz [Katz 68] is that if a molecule near the surface receives at least i_{min} hits, then the molecule is desorbed. The theory is designed for cases in which incident MeV ions are responsible for the initial excitation. In this case, target particles are set in motion indirectly through relaxation of electronically deposited energy.

A schematic diagram of an organic molecule bond to a surface is shown in figure 3.6. The molecule is assumed to be hit by a flux of secondary electrons due to the nearby passage of a MeV ion through the material. Desorption of the intact molecule under these conditions requires the preservation of all internal bonds and the breaking (excitation to an anti-bonding state) of some of the external bonds. The charge of the removed species depends on some additional adjustments in bonding.

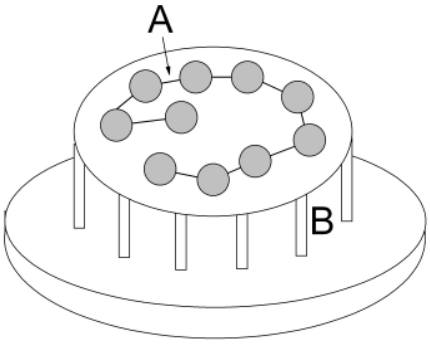

Figure 3.6 *Schematic diagram of an organic molecule showing internal bonds* **A** *and bonds to surrounding molecules in the surface* **B**. *Successful desorption requires breaking of all bonds* **B** *while leaving all of bonds* **A** intact.

Thermal models of desorption

Thermal models of desorption may be described as following: after impact of an ion energy is deposited locally within a small volume. As a result of either collisions or coupling of electronic energy into the nuclear coordinates, target particles receive a certain amount of kinetic energy. If nearly every particle in the energized region receives a significant amount of kinetic energy, then the energized region is referred to as a "thermal spike" and may be characterised by its temperature. The created thermal spike evolves spatially over time

because of heat conduction. The excited region becomes larger but at the same time it cools down, finally diluting completely.

There are two mechanisms by which desorption occurs (see Figure 3.7):

1. *Activated desorption* or evaporation from a heated region on a molecule-by-molecule basis. Lucchese [Luccheses 87] stated that for each ion impact, there will be a relatively sharp boundary between the region in which nearly all surface molecules have been desorbed and the region in which almost no surface molecules have been desorbed. According the model (Figure 3.7 (a)), only molecules from the first monolayers are assumed to be desorbed.
2. *Bulk desorption* refers to events in which locally deposited energy causes an abrupt transition of a small volume from the solid or liquid phase to the gas phase, after which the material which is in the gas phase is emitted at once. This desorption mechanism is sometimes referred to as "gas-flow" or "phase explosion" desorption, and different approaches were used to model the bulk desorption process [Sunner 88, Urbassek 91, Kelly 90].

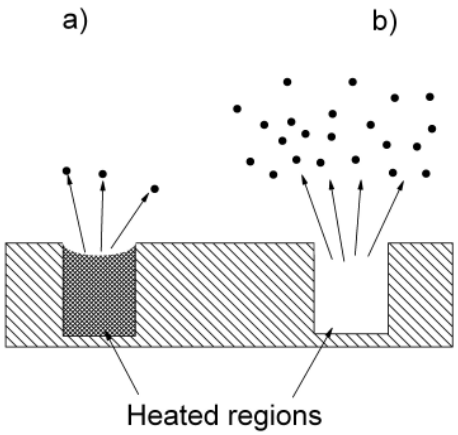

Figure 3.7 *Schematic diagrams of the thermal desorption mechanisms. a) Activated desorption. b) Bulk desorption.*

Shock-wave models of desorption

The incidence of energetic particles onto surfaces can lead to extremely high deposited energy densities. One possible consequence of a high energy density and a high energy density gradient is that a "shock wave" may be created which propagates outward from the region of excitation. If a shock wave is reflected by the surface from below, material may be "mechanically ablated" by being in effect left behind during the unloading wave. It is also possible that the shock wave energy may be focused into defects or narrow protrusions

sticking out of the surface, also leading to direct removal of a part of the solid. Finally, after a shock wave passes through a region of a material, this region is left in heated state. The excess thermal energy may cause desorption through evaporation or bulk desorption due to the energy density gradient [Zel'dovich 67, Landau 59].

A qualitative definition of a shock wave could be as following: a shock wave is a relatively narrow mechanical disturbance propagating through a material causing distinct changes in thermodynamic parameters like pressure, temperature, and material density in its wake.

Pressure-pulse model of desorption

The theory of a pressure pulse model of organic molecules has been presented by Johnson et al. [Johnson 89]. In this model, an ion traversing a solid is assumed to deposit kinetic energy ΔE_i in a small spherical volume of radius r_0. The kinetic energy could either be the result of a collision interaction or of an electronic interaction with partial conversion of the electronically deposited energy into kinetic energy. The assumed geometry is shown in Figure 3.8. The energy is assumed to propagate by diffusion. As energy reaches the surface, desorption of molecules may occur by evaporation, or when a molecule receives a critical momentum in direction of the surface normal.

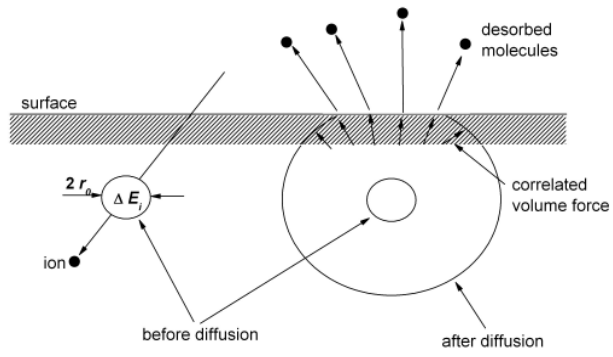

Figure 3.8 *Left: an incident ion creates a localized region of kinetic energy excitation. Right: the energy diffuses by collisions. As the energy reaches the surface, desorption occurs either by evaporation or in response to the correlated volume force.*

To sum up the discussion, the theories discussed above were developed and experimentally tested under very different conditions with respect to the target state (liquid or solid), the bombardment energy, and the ion type (atomic or cluster). Because of these

differences, none of the models can be applied to describe processes that take place in a polymer under ion bombardment, and it is quite reasonable to apply two or more models.

Desorption of a large organic molecule without significant fragmentation requires a considerable impulse without large influence of the internal energy. “Volume forces” and collective motion of the lattice can satisfy these requirements and lead to the emission of intact molecules relatively far away from the area of the initial excitation [Reimann 93]. Consequently, the bulk desorption, shock wave and pressure pulse models are the main candidates to describe the removal of large molecules. Even if bulk desorption and the pressure pulse/shock wave models are most suitable to describe the ejection of large molecules under particle impact, there are cases for which the collision cascade, ion track (hit theory), and evaporation models can by applied [Reimann 93]. For example, evaporative models can provide a good explanation for MeV ion-induced desorption of small molecules. The collision cascade model describes the high kinetic energy component of molecules desorbed under keV ion bombardment.

3.3 Molecular dynamic simulations

Molecular dynamics (MD) simulations can provide important results regarding ion penetration ranges and damage distributions, and for molecular desorption mechanisms and processes that occur in irradiated polymers.

Up till now, a number of Monte-Carlo calculations were done to determine the ion range in different materials as a function of the primary ion energy [Fink 04, Biersak 87]. One of the most often used simulation codes for range and stopping power determination is TRIM (transport of ions in matter) [Biersak 80, Biersak 87]. Since the first calculations and simulation codes for polymers were developed, the topic is a matter of interest in research. There are a number of different codes (SRIM, CasP1.2, BT, MSTAR) that are equally good when compared with each other, and most importantly theoretical results agree well with the experimental data [Fink 04].

In the past decade, MD simulations were performed for the molecular desorption from organic overlayers on inorganic substrates [Garrison 00, Delcorte 00b, Delcorte 01]. In such simulations, separate PS molecules were placed on a silver substrate, therefore the molecule ejection mechanisms depended highly on the ion interaction position. If a low energy (1 – 5 keV) argon ion hit the Ag substrate, silver atoms are set in motion due to the successive collisions between the atoms. In the case that the primary energy is quickly dissipated among Ag atoms belonging to the top layer, high yields of substrate atoms as well as intact PS

molecules were observed [Delcorte 00b]. During the 500 eV Ar ion interaction with a PS cube (1000 $Å^3$), small polymer molecules were removed during the first femtoseconds. The whole PS cube was fragmented because of the collision cascades inside the polymer coils, and large molecules were emitted [Delcorte 01]. The obtained results did not reflect the exact desorption mechanisms of thick polymer samples, as simulations were done for organic layers with a thickness much smaller than the penetration depth of incident ions with energies of 0.5 – 1 keV.

Beardmore and Smith [Beardmore 95] were the first who modelled a polyethylene crystal under 1 keV Ar ion bombardment. They identified the induced damage in the solid (chain scission, cross-linking, carbonization) and the ejection process was attributed to a quick sputtering of atoms and radicals, followed by slower large molecule desorption. The most recent paper by Delcorte and Garrison [Delcorte 04] reported the kinetic energy distributions of PS fragments desorbed from a polystyrene matrix (organic sample of 250 nm^3 containing 232 PS tetramer molecules) under 500 eV Ar ion irradiation. Performed calculations showed the emission of some large molecules as well as a large yield of small fragments like H_2 or C_2H_2. The entire emission event takes up to 10 ps, which is much slower than molecule emission from the Ag substrate [Delcorte 01, Garrison 00]. Fragmentation of large molecules was not excluded, as emitted molecules possessed internal energies between 0 and 40 eV and species leaving the surface with energies larger than 30 eV are expected to decompose in vacuum. Another important observation was that energy dissipation and molecular ejection were localized, and a large fraction of the energy was stored in the vibrational modes of the excited molecules.

Up till now, there are no MD simulations done for polymer systems in which post-chemical reactions are taken into account. The calculations are usually performed for very first ion interaction with a target. What ejection mechanisms and energy dissipation mechanisms occur at later ion bombardment times when the whole polymer surface chemistry is changed is still under question.

3.4 Ion irradiation effects in polymers

Ion irradiation leads to irreversible changes in organic materials. Many polymers, when exposed to radiation, suffer main-chain scission leading to the formation of low molecular weight molecules and loss of their mechanical properties [Charlesby 87]. If there is no external supply of some reactive elements, and in the case of a higher concentration of primary radicals, the open polymeric bonds occurring during the scission have time to react

with each other, thus initiating cross-linking, branching, or creation of double bonds. In such cases, the molecular weight increases. Both ion-induced chain scissions and cross-linking lead to irreversible changes in the polymer and its elastic properties. Scission ultimately degrades the polymer itself and the irradiated layer fails; if cross-linking dominates, adhesion failure occurs between the strongly cross-linked polymer regions and the underlying unirradiated polymer. Calcagno and Foti [Clacagno 91], Puglisi [Puglisi 88], and Fragala [Fragala 98] measured molecular weight distributions after polymer irradiation at energies in the range of 100 keV to several MeV.

Some of the excited states may survive for very long times. These states are known as radicals. The lifetimes of such radicals are long enough to undergo chemical reactions. If a polymer is positioned in some reactive environment after irradiation, like treatment with reactive gases such as O_2, N_2, or placed in ambient atmosphere, long lived radicals may also react with reactive species forming special functional groups. For example, polymers treated with oxygen plasmas [Moss 86, Charbonnier 00, Friedrich 00] have oxygen-containing functional groups which lead to an increase in the polymer surface energy. Nitrogen-containing plasmas introduce carbon nitrogen functionalities required mostly for the improvement of wettability, printability, and bondability.

In fact, chemical changes caused by the irradiation of polymers are relatively small [Charlesby 87], but these changes produce major physical modifications. Interest in ion-induced polymer modification has grown significantly due to reports of large improvements in metal/polymer adhesion. These have been obtained using ion stitching with MeV ions, ion beam mixing and ion beam assisted deposition (IBAD) [Galuska 92]. In the case of ion mixing, a thin metal film is placed on a substrate and ~ 100 keV ions are implanted into the specimen such that the resulting collisional mixing occurs in the interfacial region. According to the ideal surface modification idea, low energy ions are most suitable for surface modification. In the case of IBAD, the polymer surface is bombarded with low energy (100 – 1000 eV) ions during metal film deposition. Adhesion enhancement in this case has been attributed to a variety of mechanisms, such as chemical bond formation, contamination removal and interfacial mixing. An increase in the peel strength was also observed for polymer surface modification before metal deposition [Flitsch 90].

The morphology of polymer surfaces may also be changed during the irradiation forming cones or spike-like features. Especially great effect was observed on the surface of fluoropolymers [Michael 86]. In addition, optical [Elman 83], electrical [Venkatesan 83, Wang 93], and mechanical [Carlson 85] properties of polymers are changed.

Chapter 4

Experimental and analytical techniques

In this chapter, an overview of the instrumentation of the analytical and experimental techniques used for the sample preparation and characterization is given. Experimental parameters and detailed procedures will be presented in Chapter 5.

4.1 Ion-beam sources

The development of ion sources started with the investigation of the canal rays by Goldstein in 1886 [Goldstein 96]. Later, electron-atom collisions were used to design low current ion sources. Higher ion current sources became available with the investigation of arc discharge ion sources in the 1930s. In the 1940s the rf- and microwave plasma ion sources came into production.

The characteristics of an ion beam are determined by the plasma and the extractor. For example, the ion beam current is determined by the plasma density, plasma electron temperature, the extraction voltage, and the extractor geometry. The beam emission is determined by the plasma density distribution, the plasma ion temperature, and the extractor geometry. Ions are formed from neutrals by different ionization mechanisms. The various ways in which ionization can be achieved include electron impact ionization, photoionization, field ionization, and surface ionization. Often the type of ionization determines the type of the ion source. The physics of an ion source is principally plasma physics [Chapman 80, Wolf 95, Brown 04]. Nevertheless, this work is dealing with the ion interaction with polymer surfaces, and not with the plasma itself. Therefore, a detailed analysis of the plasma and ionization effects is beyond the scope of this research.

There is a large number of ion sources with respect to the parameters such as beam current (the total current extracted from the exit aperture of the ion source), ion energy and energy spread (half-width value of the energy distribution), and beam purity [Fuchs 90]. An overview of different types of ion sources can be found in the books by Wolf [Wolf 95] and Brown [Brown 04]. As mentioned above, low energy ion sources were selected for this research in order to perform surface modification of polymers, which leads to the alterations in various physical and chemical properties, while leaving the polymer bulk properties

unchanged. The working principle and instrumentation of the electron bombardment and microwave ion-beam sources, which were used in the present study, is given below.

4.1.1 Electron bombardment ion source - ISE 10 ion source

Such a type of ion source is mainly used in areas where a well defined electron energy is required and a moderate ion current is sufficient. Advantages of this ion gun design are the low energy spread of the ions, and the easy and cheap design. The largest disadvantage is the low filament lifetime in presence of reactive gases.

The working principle is the following: electrons are emitted by a cathode, usually by thermionic emission, and accelerated towards an anode. Some of the primary electrons collide with the gas atoms and ionize them. Secondary electrons from these collisions are accelerated towards the anode to energies depending on the potential distribution and the starting point of the electron. The potential distribution depends on the electron current density and the gas pressure. If the anode potential is increased to the value of the ionization potential of the gas used, ions are created in an increasing number until the energy reaches the maximum of the ionization cross section. With increasing potential, more and more secondary electrons can gain energies above the threshold energy required for ionization and contribute to the ion production. The ion energy spread can be as large as the potential difference between the threshold energy and the anode potential, depending on the point of ionization and the position of the extraction aperture. The ion energy spread in the low-pressure regime can be reduced by introducing a grid close to the cathode, which will act as anode, and the extraction aperture, which is kept at a few volts above or at grid potential. The cathode design also influences the energy spread of the primary electrons through the potential difference along the directly heated cathodes. This leads to low-voltage high-current cathodes.

The *ISE 10 ion source (OMICRON)* is designed to clean the samples for surface analysis. This ion beam source was used for the polymer surface modification with inert and reactive gases, as well as for determination of the sputter rate of the polymer. Ionization in the ion source is done by electron bombardment in order to allow a continuous variable beam current in the nA to μA regime. Figure 4.1 shows the schematics of the exterior and interior of the ion gun. The ion generation takes place inside a collision chamber which has a special shape (Figure 4.1 (b)). Electrons are emitted from a circular Yttrium oxide coated ribbon filament and subsequently accelerated by an anode grid which has a potential of +120 V with respect to the filament. While travelling to the anode, the electrons ionize the neutral particles (atoms and molecules) present in the volume between the cathode (filament) and anode. The

anode is shaped in such a way that the electrons cross the anode volume many times. This increases the collision probability while at the same time avoiding the presence of an additional magnetic field.

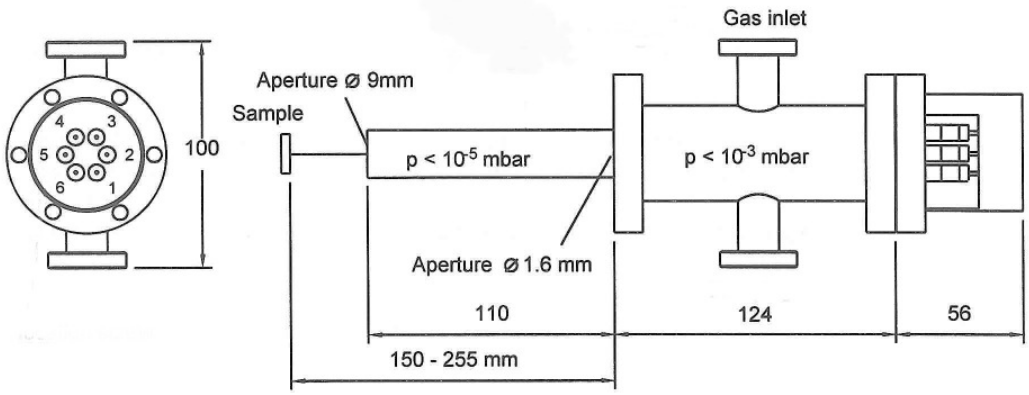

Figure 4.1 *a) The ion gun exterior with the outer dimensions, and the pin connections (1-repeller, 2-focus, 3-extractor, 4-anode, 5-filament (-), 6-filament (+)). b) The interior of the ion gun.*

The ions are mainly produced in the filament plane and subsequently extracted from the source volume while being accelerated to a pre-selected kinetic energy. The final ion energy can be selected in the region of 0.1 to 5 keV. An ion-optic lens is placed behind the

extractor electrode and focuses the ions into a beam with a diameter (FWHM) in the range of 3 to 12 mm.

4.1.2 Microwave ion gun - IonEtch sputter gun

Ion sources using plasma generated by a microwave discharge in a magnetic field have many advantageous features. There is no hot filament, this allows to run the source using aggressive gases, provides long lifetime, it is easy to operate, and large areas can be treated uniformly. The main disadvantage is the limited lifetime of the microwave window because of electron bombardment and metal vapour deposition.

A microwave ion source consists of a single or multimode cavity, or contains a separate vessel made of insulating material. In most microwave ion sources, a magnetic field is superimposed to improve the microwave heating of the plasma electrons. Microwaves are coupled into the discharge chamber with an antenna or microwave window. Ions are extracted from the microwave-generated plasma in the usual way through the single- or multiple-aperture or slit extraction systems. Microwaves entering the discharge chamber can propagate through the plasma and transfer their energy to free electrons, which further ionize the gas atoms. If electron density in the plasma ($n_{ep} = 6.66 \times 10^{10}$ cm^{-3} for 2.45 GHz) reaches its maximum value, microwaves cannot enter the plasma any more and can only be weakly absorbed at the plasma surface. In the presence of a high magnetic field ($B_c = 87.5$ mT for 2.45 GHz), electron cyclotron heating occurs and the right-hand circular polarized fraction of the microwave can enter the plasma. If the magnetic field exceeds the electron cyclotron resonance (ECR) value and the neutral particle density is sufficiently high, the energy of the microwave is effectively absorbed by off-resonance heating process. In this way electron densities of 10^{13} cm^{-3} can be generated and high ion currents can be extracted from the plasma [Wolf 95, Brown 04].

Figure 4.2 shows the external and interior schematics of the *IonEtch sputter gun (Tectra)*, which was used mainly for determination of the polymer sputter rate for different gases, and large surface area modification. Plasma for this gun is generated in a quartz cup with inner diameter of 53 mm, Figure 4.2 (a). The cup is surrounded by four water cooled magnets made of neodymium-iron-boron, which produce ECR zones in a multi-cusp field. The magnetron is operating at a frequency of 2.45 GHz, and is mounted at the end plate. The cylindrical resonator of fixed dimensions is constructed with sliding end plate.

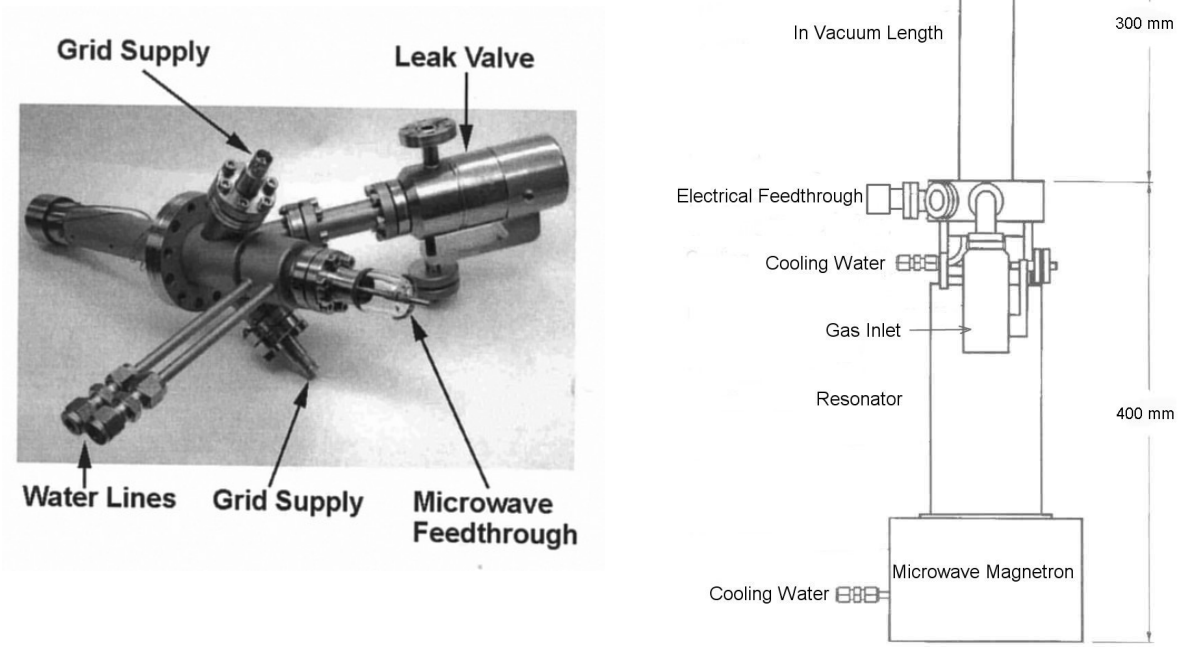

a)

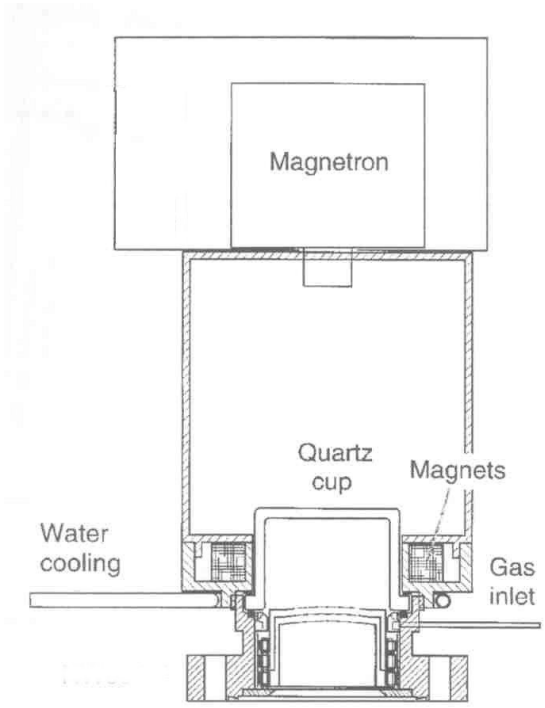

b)

Figure 4.2 *a) The IonEtch sputter gun. b) The interior of the ion gun. [Anton 00]*

Microwaves are generated by a microwave magnetron and coupled through a resonant coupler into a coaxial feedthrough structure which guides the microwaves into the vacuum and up to the boron nitride (BN) plasma chamber. Plasma is excited in the chamber and the microwaves are absorbed. The plasma is physically confined to the chamber by BN and occurs there preferentially due to the higher local gas pressure and the assistance of the ECR effect. Further enhancement of the plasma density is provided by an axial magnetic field arranged around the discharge chamber. This generates a magnetic field of 87 mT strength inside the plasma at which electrons in a 2.54 GHz microwave field will undergo ECR motion. This spiralling motion greatly increases the electron path length and therefore the probability of collisions with other molecules and subsequent ionization. The open end of the plasma chamber is closed with an aperture containing a single hole. The aperture is made from molybdenum, with the hole diameter being 1.5 mm. A positive voltage applied to this aperture accelerates ions from the plasma into the chamber. A second aperture is provided to assist ion extraction and beam current control.

4.2 X-ray photoelectron spectroscopy

4.2.1 The background of XPS

X-ray photoelectron spectroscopy (XPS) involves irradiation of a sample with soft X-rays and the energy analysis of emitted photoelectrons which are generated close to the sample surface. XPS has its origins in the investigation of the photoelectric effect, discovered by Hertz in 1887 [Hertz 87], in which X-rays were used as exciting photons. The X-ray irradiation causes photoionization of atoms in the specimen and the response of the specimen is observed by measuring the energy spectrum of the emitted electrons. The kinetic energy E_k of the emitted photoelectrons is related to the X-ray energy ($h\nu$) and the binding energy E_b of the core electrons of the element by the Einstein relation [Einstein 05]:

$$E_k = h\nu - E_b \tag{4.1}$$

The photoemission and relaxation processes (X-ray fluorescence (XRF) and Auger electron emission (AES)) that occur during X-ray irradiation are presented in Figure 4.3. The left hand side of the figure shows a schematic energy level diagram of a solid at an initial state. Energy is measured downwards from an assumed zero level taken at Fermi level. Normally, vacuum level should be chosen as zero level energy, but in XPS and AES binding energies are measured with respect to the Fermi level.

If the core level (for example the K level, as given in the Figure 4.3) is ionized by an incident photon, whose energy hv is greater than the binding energy E_b of an electron in the K level, the emitted electron leaves a hole in the core level. If the photoelectrons have sufficient kinetic energy, they are able to escape from the surface by overcoming the work function Φ_s of the specimen, and photoemission is said to occur. The kinetic energy E_k at which electrons are emitted is given by:

$$E_k = hv - E_b - \Phi_s \tag{4.2}$$

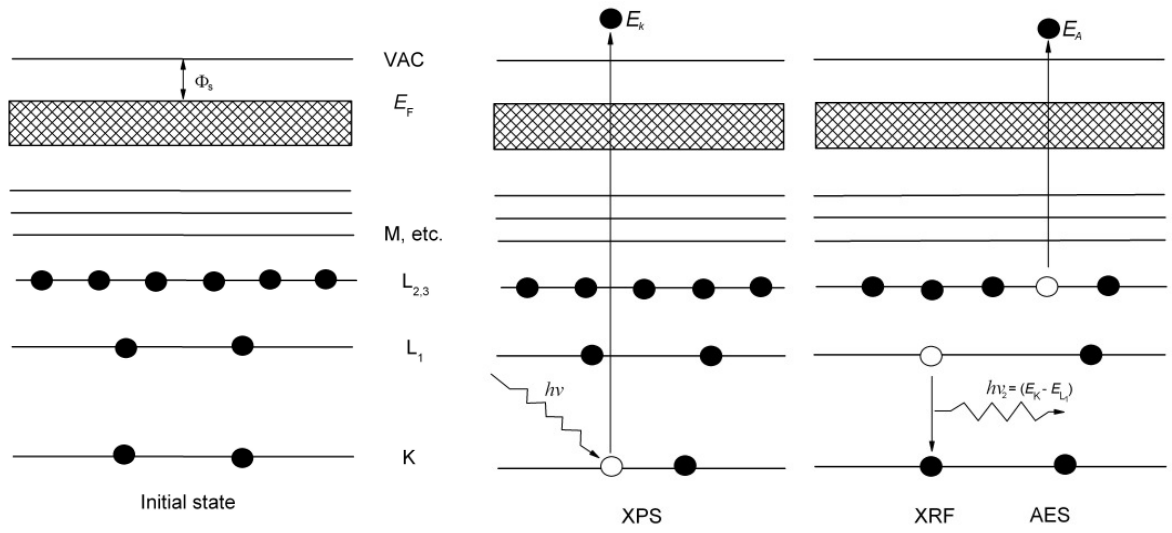

Figure 4.3 *Photoemission and subsequent relaxation processes, XRF and AES.*

Auger series are the result of one of the decay mechanisms of the core-hole created during photoemission. Following the creation of the hole in the K level, the atom relaxes by filling the hole with an electron via transfer (or transition) from an outer level (for example level L_1 as shown in the Figure 4.3). The excess kinetic energy hv_2 becomes available during the transition. If this energy is emitted as an X-ray photon, X-ray fluorescence occurs. If the excess energy is transferred to another electron either in the same or in a higher level, emission of an Auger electron with an energy E_A takes place after the electron, e.g. in level $L_{2,3}$, gains the remaining excess energy. After the AES effect took place, the atom is in a doubly ionized final state. For nearly all elements associated with polymers AES dominates over X-ray fluorescence [Briggs 98].

In every XPS spectrum, the peaks can be divided into three classes: peaks due to photoemission from core levels, from valence levels, and Auger series due to Auger emission. With Mg K_α and Al K_α photons (Section 4.2.2) at least one core level is excited for any element in the periodic table (except hydrogen) and the characteristic binding energy values allow elemental identification. The core level spectra consist of separate, sharp, clearly identifiable peaks.

Valence levels are those occupied by electrons of low binding energies (0 – 20 eV) which are involved in delocalization or bonding orbitals. Here, the spectrum consists of many closely spaced levels giving rise to a band structure. Auger series result from the decay mechanism for core hole states. Because some of the levels involved can be quite close in energy, there are several competing processes which give rise to a series of peaks in a particular region of the XPS spectrum.

The soft X-rays penetrate many microns deep into the sample. But only surface photoelectrons leave the sample without inelastic collisions retaining their original kinetic energy and so that they contribute to the peaks. Other electrons suffer inelastic collisions resulting in energy loss during the movement through the solid. These losses usually give rise to the step-like increase in the background on the low kinetic energy side of the spectra. The probability of an inelastic scattering event to occur is determined by both the kinetic energy of the electron and the material through which it is travelling. For the photoelectrons emitted with a certain angular distribution from a depth z below the surface, the intensity can be written as:

$$I_z = I_0 \exp(-z / \lambda \sin\theta) \tag{4.3}$$

where I_z is the intensity originating from the atoms at depth z, I_0 is the intensity from the surface atoms and θ is the electron take-off angle with respect to the surface. In this case, λ is the inelastic mean free path of the detected electrons, defined as the average distance that an electron with a given energy travels between successive inelastic collisions. Because values for λ are derived from 'attenuation' experiments, λ is also called attenuation length. The dependence of λ on kinetic energy is expressed as a power relationship $\lambda = E_k^x$, where x lies between 0.5 -0.7 for a wide range of materials, for organic materials $x > 1$ [Briggs 98].

Due to the exponential decay behaviour (Equation 4.3), it is not possible to derive a unique value for the sampling depth d that varies with the take-off angle and it is the basis of angle-resolved XPS. Commonly 3λ (95% detection) is taken to be the 'sampling depth'. The maximum information depth possible to measure is up to 3 – 10 nm [Sabbatini 93, Briggs 90,

Briggs 98], which is approximately the same as the ion range of low energy ions (1 – 5 keV) in a polymer substrate (Section 3.1.2) [Biersak 87]. This is the reason, why XPS is such a surface sensitive technique. It is able to perform elemental analysis because no two atoms of the periodic table have the same set of binding energies. Moreover, XPS can be used to collect information on the electronic structure and the chemical environment, since for the same kind of atom the energy levels change with their oxidation states or with their net charge.

4.2.2 Instrumentation

A schematic diagram of the XPS (Omicron FullLab) instrument is shown in Figure 4.4. The spectrometer consists of a vacuum chamber, an X-ray source, an electron energy analyzer, a detection system, and a data acquisition system controlled by a PC.

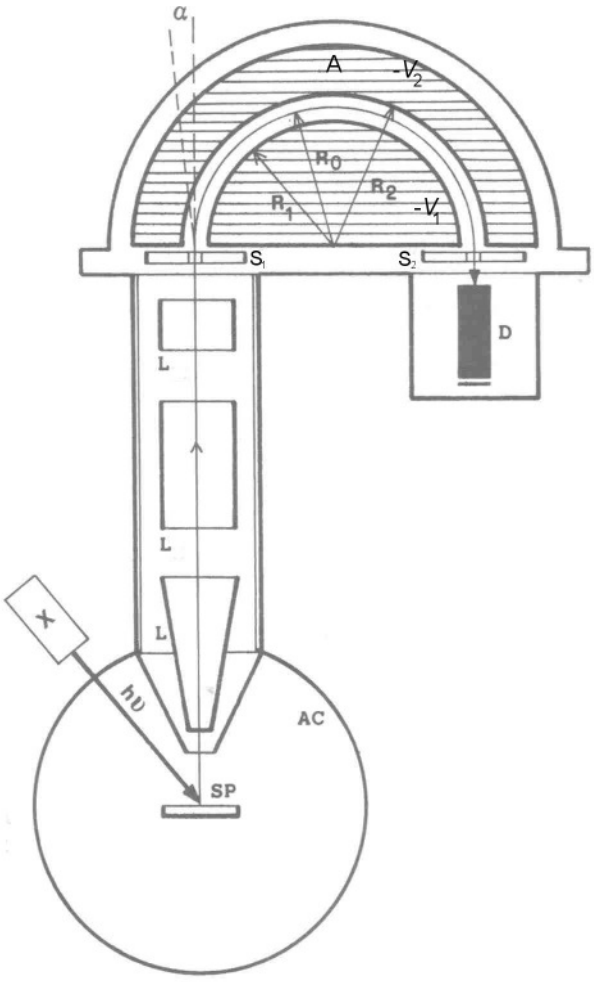

Figure 4.4 *Schematic diagram of an XPS instrument. A - analyser, AC – analysis chamber, L – focus and retardation lenses, D – detector, S – slits, SP – specimen, X – X-ray source.*

It is necessary to have good vacuum in order for the photoelectrons to reach the analyser without being scattered by residual gas molecules. In our laboratory, the vacuum in the analysis chamber is in the range of 10^{-9} – 10^{-10} mbar. This ultra-high vacuum condition is enough to avoid electron scattering, and to reduce the contamination (or increase the time for adsorption of a monolayer of contaminants) of the sample surfaces with the residual gas molecules.

X-rays are generated in the X-ray source by bombarding an anode with high energy electrons from a heated filament. The emission spectrum consists of characteristic lines, emitted due to electronic transitions of outer shell electrons into the core-holes created by the impact of the electrons. The X-ray source used in our experiments contains a double anode system featuring aluminium and a magnesium anode, from which Kα X-rays having energies of 1486.6 eV for Al, and 1253.6 eV for Mg are emitted. These types of X-rays have sufficient energy to excite core-level electrons of all elements. The characteristic linewidths are relatively narrow (Al 0.85 eV, Mg 0.7 eV, [Briggs 90]) minimizing the contribution to the photoelectron linewidth.

Emitted electrons are collected, retarded and analysed in the analyser in which the energy distribution of the electrons emitted from the sample is measured and the photoelectron spectrum is plotted as intensity versus kinetic energy. The EA 125 concentric hemispherical analyser (CHA), connected to our XPS system, is composed of two concentric hemispheres. The inner and outer hemispheres are biased negatively and positively with respect to the pass energy of the analyser. The analyser disperses electrons according to their energy across the exit plane and focuses them in the angular dimension, from the entrance to the exit plane.

The input lens collects the electrons from the source or target and focuses them onto the entrance of the analyser simultaneously adjusting their kinetic energy to match the pass energy of the analyser. The lens is also designed to define the analysed area and angular acceptance of electrons which pass through the hemispherical analyser. The length design employs a double length concept, where the first length selects the spot size and the angular acceptance, while the second lens retards or accelerates the electrons to match the pass energy of the analyser.

The detector consists of a five channel electron multiplier (channeltrons), placed across the exit plane of the analyser, amplify the current of a single electron. The transmitted electrons are dispersed in energy across the analyser slit by $2R_0/E_p$ mm eV^{-1} (E_p is the pass energy). The small current pulse present at the output of the channeltron is passed through a

vacuum feedthrough to a preamplifier. From here the signal is passed on to pulse counter for processing and production of an electron energy spectrum.

As it was already mentioned above, emitted photoelectrons leave the sample with a kinetic energy given by the Equation 4.2. A schematic energy diagram of a sample and analyser is shown in Figure 4.5.

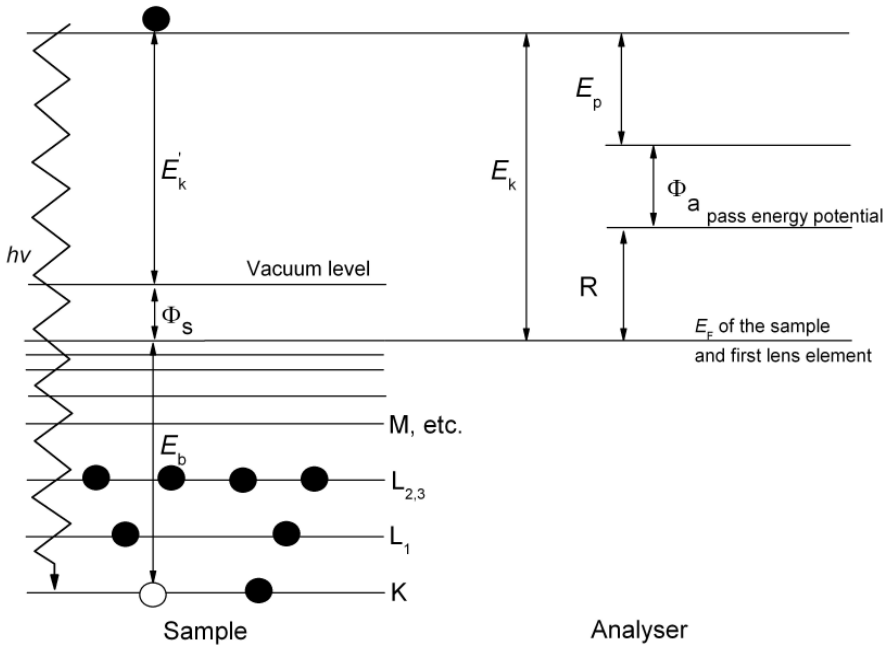

Figure 4.5 *Schematic energy diagrams of a sample and analyser. Even if the true kinetic (E_k') energy of the electron leaving the sample depends on the work function of the sample Φ_s, the measured kinetic energy E_k depends on the work function of the analyser Φ_a*

The true kinetic energy scale cannot be measured directly because Φ_s varies from sample to sample and it is not known. The offset of the spectrum by Φ_s is not important since the kinetic energy measured with the analyser is important. The ejected electrons pass through the first length element and then are retarded by an amount R, determined by the lens voltages, before entering the analyser. The analyser is a band pass filter only transmitting electrons with an energy very near to the pass energy E_p. Therefore electrons have a measured kinetic energy $E_k = R + E_p$. But the analyser has its own work function Φ_a. Therefore

electrons which have been transmitted by the analyser with a retardation of E_p would have a kinetic energy that is independent of the work functions of the sample:

$$E_k = hv - E_b - \Phi_a \tag{4.4}$$

In the hemispherical analyser two concentric hemispheres with the outer radius R_2, inner radius R_1 have a mean equipotential surface between them of radius R_0. Potentials V_1 and V_2 ($V_2 > V_1$) are applied to the hemispheres. If electrons with an energy E_p are ejected at S_1 tangentially to the equipotential surface, they will be brought to a focus at S_2, (Figure 4.4), irrespective to the plane of their circular trajectory. The relationship between the pass energy and the potential difference is given by:

$$e\Delta V = e(V_2 - V_1) = E_p\left(\frac{R_2}{R_1} - \frac{R_1}{R_2}\right) \tag{4.5}$$

The analyser is a band pass energy filter for electrons with a specific constant pass energy yielding a constant energy resolution ΔE throughout the spectrum. The finite energy resolution depends on the electron pass energy, the slit width and the acceptance angle of the lens system. The energy resolution of the analyser is given approximately by:

$$\Delta E = E_p\left(\frac{d}{2R_0} + \alpha^2\right) \tag{4.6}$$

where d is the slit width and α is the half angle of the electrons entering the analyser at the entrance slit. For the EA 125, where R_0 = 125 mm, d = 1mm, and $\alpha \approx 3°$, the ΔE can be set 0.5 - 1 eV.

An extensive quantitative analysis of XPS can be found in the literature among which are those by Seah (1980), Briggs (1990), etc. The equations used to determine elemental concentration and film thickness will be given in the chapter “Experimental” where particular experiments (surface chemical analysis, sputter rate determination by means of XPS, polymer film thickness calculation on the peeled off metal side) will be described.

4.3 Transmission electron microscopy

In transmission electron microscopy (TEM) high energy electrons are used to irradiate thin specimens about 100 nm or less in thickness. The transmitted electrons form an image of

the specimen magnified in several steps with the aid of electro-optical lenses. The entire image can be observed directly on a fluorescent screen. A detailed description of this technique can be found in books by Fuchs [Fuchs 90] and Reimer [Reimer 84]. TEM offers a high resolution which extends to atomic dimensions and microscopy of thin film specimens yields information about the material structure.

The electrons emitted from the electron gun are accelerated to an energy of 100 – 300 keV. The condenser lens then shapes them into an approximately parallel beam which illuminates the specimen uniformly. The objective lens produces a first image, which then is further magnified by intermediate and projector lenses and is finally projected onto the fluorescent screen. The image can be recorded on a plate by exposing the photographic emulsion, or as in our case by CCD camera, which allows further digital picture processing.

The image contrast is generated by the incident electrons that are elastically scattered or diffracted in the specimen by small angles. In most cases, only electrons penetrating the specimen without scattering are used for image formation. The adjustable objective aperture limits the scattering angle of the electrons to the order of 1mrad and allows only the direct beam to pass through. Since the scattered or diffracted electrons are excluded, any changes in the intensity of the transmitted beam due to inhomogeneities in the specimen with respect to density, thickness, and orientation create an image contrast.

In this work, a Philips CM30 electron microscope with a maximum acceleration energy of 300 keV was used to analyze the form, size and distribution of metal clusters on the surface of thin polymer film. In this case, the quality of the TEM images is influenced by the scattering contrast, which is produced in the specimen when different regions differ in thickness, density or mean atomic number [Fuchs 90].

4.4 Quadrupole mass spectrometry

When a solid surface is bombarded with ions, components of this surface are sputtered, and some of the sputtered particles are emitted as ions. Analytical information can then be obtained in a mass spectrometer that operates on the basis of first storing ions and then facilitating their detection according their mass/charge (*m/e*) ratio. The extensive quadrupole mass spectrometry (QMS) reviews with a detailed review of the theory are given by Dawson [Dawson 76], March and Todd [March 95], and Fuchs [Fuchs 90].

In QMS, mass separation takes place by the excitation of ion oscillations in an electric quadrupole field, which consists of the sum of a static and a high-frequency component. The field is generated by three cylindrically symmetric electrodes (two end caps and a ring) with a

circular or in the ideal case hyperbolic cross section. The principle layout of the QMS is shown in Figure 4.6. A direct voltage U_a and a high-frequency voltage $U_b \cos \omega t$ are applied to the electrodes. Ions injected at point 0 in the z direction perform lateral oscillations in the high-frequency quadrupole field. For specified field parameters and ions of uniform charge, the shape of these oscillations depends on the mass. The quadrupole ion trap uses the filtering action to maintain ions of the chosen *m/e* range within a closed volume, rejecting all others. Ions of a specific mass move along a stable path (1) and can leave the spectrometer in the direction of the detector. Ions of deviating mass perform instable oscillations with increasing amplitude (2), finally striking the electrodes and thus being eliminated. The chosen ions are accumulated within the volume and then their number is measured after a suitable storage period.

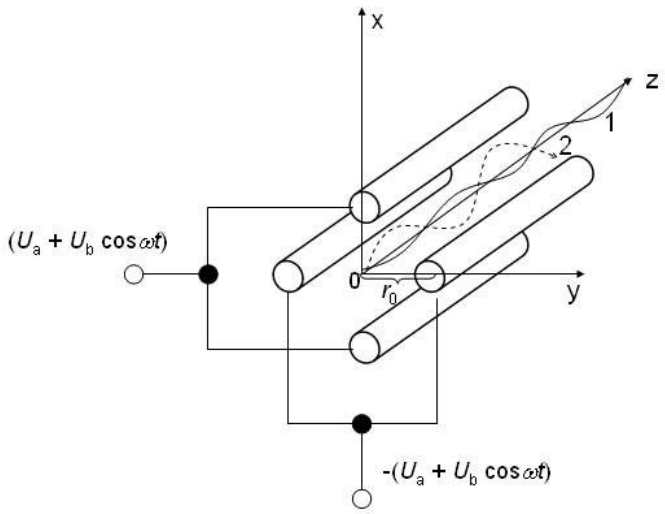

Figure 4.6 *The principle of the quadrupole mass spectrometer. An explanation given in text.*

A QMS 200 (Blazers) was used to determine the type of the bombarding ions and to detect the molecular species emitted during ion irradiation at different sample temperatures. The QMS allowed us to determine the sputtered polymer species and to observe the change of particular mass molecules as a function of time or temperature, depending on the experimental conditions. Spectra were recorded and processed using the Quadstar 421 software (Blazers).

4.5 Quartz crystal microbalance

A quartz crystal microbalance (QCM) consists of a thin quartz crystal sandwiched between two metal electrodes through which an alternating electric field is applied across the crystal, causing vibrational motion of the crystal at its resonant frequency. For many years, QCMs were used as gas-phase mass detectors. Recently, their application has been extended to liquids and viscoelastic deposits leading to applications in electrochemistry and micro-rheology [Buttry 92]. The QCM in our experiments was used to monitor the metal deposition rate and metal film thickness, as well as to determine the polymer sputtering rate.

The basis working principle of the QCM is the converse piezoelectric effect in which application of a voltage across the crystal results in a corresponding mechanical strain. The crystal symmetry dictates that strain induced in a piezoelectric material by an applied potential of one polarity will be equal and opposite in direction to that resulting from the opposite polarity. Application of an electric field across the crystal produces a shear strain proportional to the applied potential. To summarize, an alternating potential across the crystal causes vibrational motion in the quartz crystal with amplitude parallel to the surface of the crystal, [Buttry 92].

Sauerbey [Sauerbey 59] was the first to demonstrate the extremely sensitive nature of the piezoelectric devices towards mass changes at the surface of the QCM electrodes. According to Sauerbey's equation, the mass change per unit area Δm at the QCM electrode surface causes a change in the oscillation frequency Δf of the crystal:

$$\Delta f = -C_{\mathrm{f}} \Delta m \tag{4.7}$$

where C_{f} is the sensitivity factor for the crystal used. Equation 4.7 relies on a linear sensitivity factor that is the fundamental property of the QCM crystal. It is assumed that the incremental change in mass from foreign film is treated as though it was really increasing the thickness of the underlying quartz. The deposited film is considered to be rigid and so thin that it does not experience any shear forces during vibration. The thickness is the parameter of interest in gas-phase thin film deposition, and it can be calculated by:

$$d_{\mathrm{f}} = \Delta m / \rho_{\mathrm{f}} \tag{4.8}$$

where d_{f} is the thickness of the deposited film and ρ_{f} is the bulk density of deposited material. However, vacuum and gas phase thin film depositions fail to fulfil any of these conditions, and exhibit more complicated frequency-mass correlations.

It was accepted, that when the mass of the deposit causes a change in frequency of less that 2% of the frequency of the pristine crystal, Sauerbey's equation can be applied in the thin film calculations [Denison 73, Behrndt 71]. As the film thickness increases, the elasticity of the deposit has to be considered. Lu and Lewis [Lu 72, Lu 75] extended equation 4.7, which is currently applied by most QCM softwares to calculate rigid thin film thickness in gas phase deposition:

$$d_{\mathrm{f}} = \frac{N_{\mathrm{q}}\rho_{\mathrm{q}}}{\pi\rho_{\mathrm{f}}Zf_{\mathrm{l}}}\tan^{-1}\left[Z\tan\left(\frac{\pi(f_{\mathrm{u}}f_{\mathrm{l}})}{f_{\mathrm{u}}}\right)\right] \tag{4.9}$$

where N_{q} is the frequency constant of a quartz crystal, ρ_{q} is the density of the quartz (2.684 g/cm^3), f_{l} and f_{u} are frequencies of loaded and unloaded crystals, respectively and Z is the Z-factor of the film material which is calculated as follows:

$$Z = \sqrt{\frac{\rho_{\mathrm{q}}G_{\mathrm{q}}}{\rho_{\mathrm{f}}G_{\mathrm{f}}}} \tag{4.10}$$

where G_{q} and G_{f} are the shear moduli of the quartz and the film material (usually bulk values are taken for calculations), respectively. The accuracy of the mass load and thickness calculation mainly depends on how accurate the Z-factor and material density is known. The equation 4.9 can be applied for frequency changes up to 40 %. Crystal failures are observed above this value.

4.6 Atomic force microscopy

The atomic force microscopy (AFM) was invented by Binning, Quate and Gerber [Binning 86]. The advantage of AFM over scanning tunnelling microscopy is that AFM is able to image insulating surfaces. In atomic force microscopy commonly the repulsive force between the tip and the sample is measured on the basis of the cantilever deflection.

A typical AFM (AutoProbe, from Park Scientific Instruments) consists of a piezoelectric scanner, an optical head, and a base, which supports the scanner with the head and includes a circuit for measuring the deflection signal, Figure 4.7. It operates by scanning across the surface with a sharp tip mounted on a soft cantilever spring. Features on the sample surface cause the cantilever to be deflected as the sample moves under the tip. An optical system is used to sense the position of the tip relative to the sample. The laser beam of a laser diode is focused onto the back of the cantilever. The beam is reflected off the cantilever onto

a split photodiode. The differential signal from the spit photodiode provides a sensitive measure for the cantilever deflection. The feedback signal is used to control the height of the piezoelectric crystal as the sample is scanned. The height of the piezoelectric crystal is related directly to the topography of the sample surface.

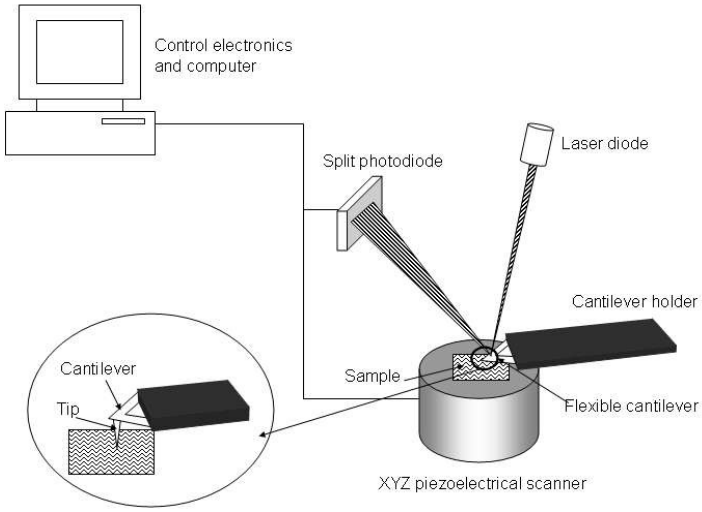

Figure 4.7 *A schematic representation of the main components of the AFM. The instrument incorporates an electronic unit and a computer station equipped with image and command monitor.*

The contact-mode AFM was initially introduced for high-resolution surface profiling. In contact-mode AFM, the atomic-scale image contrast originates from the variation of the repulsive force between tip-sample and therefore contains local information due to the short-range character of the force. The repulsive force experienced by the tip is measured by recording the cantilever deflection. The later is controlled by the cantilever spring constant k and the magnitude of the force. The vertical displacement of the cantilever is proportional to the differential signal from the vertical segments of the photodetector. The lateral force applied in the contact mode on the tip causes buckling or torsion of the cantilever depending upon whether the fast-scanning is along or perpendicular to the cantilever beam. The cantilever twisting gives rise to the differential signal from the horizontal segments of the photodetector. The special variation of these signals is converted into an image.

With the progress in microscopy, it was realized that for many materials the tip-sample force has to be minimized to achieve high resolution images. In new modes (non-contact,

tapping and force modulation) either the cantilever is vibrating with its resonance frequency or the vertical sample position is modulated. The tip-sample force interaction causes a change in the amplitude, the phase, and the resonance frequency of the vibrating cantilever. The special variations of the changes can be presented in height or interaction images. In general, the surface topography is better represented by height images, whereas the nanostructures and the fine morphological features are better distinguished in amplitude or phase images [Magonov 96].

4.7 Profilometer

Surfaces are generally not flat but exhibit small-scale peaks and valleys. In addition, to AFM surface roughness can also be measured by a profilometer. This technique is suitable for measuring macroscopic surface structures, whereas AFM has a very high special resolution and is more suitable for determining microstructures. A profilometer is a mechanical sensing system. When in use, a sharp stylus rests slightly on the surface, carefully crossing it. The up and down movements of the stylus are magnified and recorded, creating surface profiles.

The Dektak 8000 profilometer (Veeco) was used mostly to measure the amount of removed material and the film thickness.

4.8 Contact angle measurement

In the Section 2.2.2, it was mentioned that surface atoms and molecules are in a different environment compared with their bulk counterparts. In the bulk, a molecule is attracted equally in all directions by its neighbouring molecules, while the surface molecules are subjected to intermolecular attraction from one side only. At the equilibrium state, the lower density in the surface layer increased the intermolecular distance, putting it in a state of tension.

The simplest and most common way to measure the surface tension is to use contact angle measurements. The two types of the contact angle are static and dynamic contact angle. Static contact angles are measured when the system is stationary, while dynamic contact angles are determined when the system is moving. In our experiments, we used static contact angle measurements, using the contact angle system OCA from Dataphysics with pre-installed software.

When a drop of liquid is placed on a solid surface and the surface tension of the liquid is larger than the surface tension of the solid, it will cause a definite angle of contact between the liquid and the solid phases. In such cases, the contact angle θ (Figure 4.8) will have values

greater than 90 degrees, and the surface is said to be non-wetting. When the same liquid is placed on a surface with increasing tension, the contact angle decreases as the surface tension of the solid increases (Figure 4.8, going from right to left). If $\theta = 0°$, total wetting occurs. When a drop of a liquid is put onto a solid surface, three interfacial tensions exist: liquid-solid γ_{sl}, liquid-vapour γ_{lv}, and solid-vapour γ_{sv}, Figure 4.8. The contact angle θ, is defined by the force balance at the three-phase boundary and is defined by the Young's equation: $\gamma_{sv} = \gamma_{sl} + \gamma_{lv} \cos\theta$.

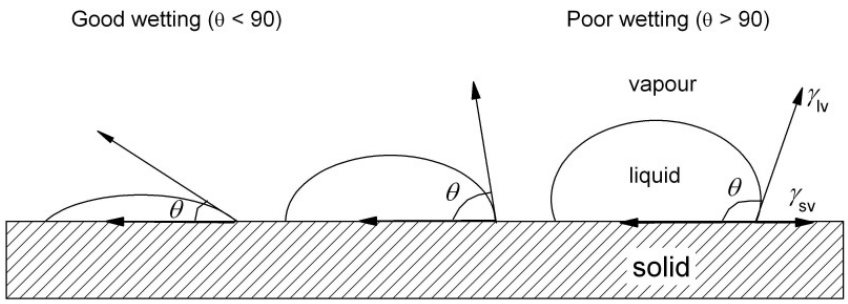

Figure 4.8 *Small and large contact angles representing good and poor surface wetting. On the right side interfacial tension components γ_{sl}, γ_{lv}, γ_{sv} (as described in the text) are shown.*

Contact angle measurements are affected by a number of factors, including surface preparation, contamination, environment, temperature, and drop size. Inhomogeneous solid surfaces created by roughness, or contamination, or the sample preparation method can give different contact angle values for the same material. The effect of the environment on contact angle is usually caused by the adsorption of vapour onto a polymer surface reducing the tension of the polymer surface, and again giving different results in different environmental conditions. It is also important to pay attention to the experimental temperature and the drop size. The increase in the values of these two parameters will result in a decrease in the contact angle, [Chan 94].

4.9 90° peel test

Methods for measuring the adhesion properties strongly depend on the nature of the system under examination. The adhesion properties can be measured by an adhesion cross test, pull, shear, scotch tape, and peel tests. In the adhesion strength measurements, 90° peel

tests (quickTest QTS 3 from Prüfpartner GmbH) were used, which's schematic diagram is presented in Figure 4.10. The peel test involves attaching a grip to the coating and peeling the coating off the substrate.

The test machine contains table, which can be moved in all tree directions, force measuring cell, and computer where peel strength values (in N) and peel curves are recorded. Force measuring cell is connected to the table through a steel cable. Polymer substrate with deposited metal film is fixed on the table with special plates, so that the substrate does not move during the experiment, and only the adhesion force between the metal film and polymer surface is measured. When the metal film is peeled up at constant rate, table moves to the right at the same rate because of the connecting cable. The angle between the metal film and the measuring cell remains constant, 90°.

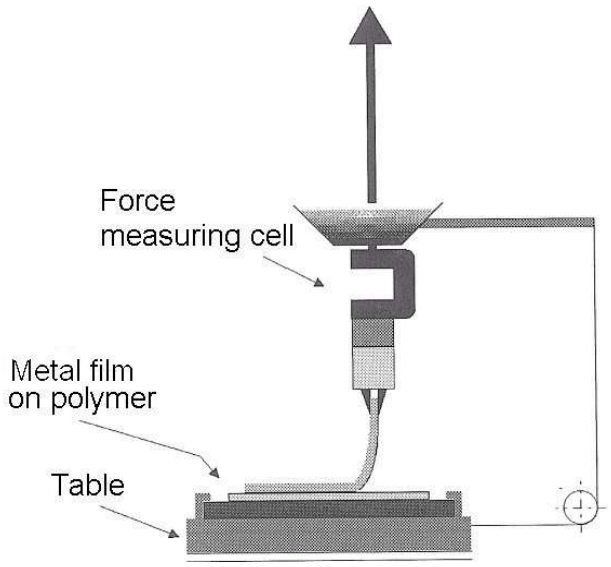

Figure 4.10 *A schematic diagram of the 90° peel test.*

The peel test technique measures the experimental or practical adhesion strength in terms of force per unit length. It is important to note that the practical adhesion is a function of the basic adhesion (or intermolecular interaction) and other factors such as stress in the films, the preparation conditions or the measurement technique itself [Mittal 76]. Kinloch [Kinloch 94] gave a detailed overview of the dependence of adhesive fracture on the geometry of the adhesive layer and the measurement conditions. Here, some points will be briefly mentioned. It was shown that the peel strength (P) depends on the thickness of the adhesive layer. The value of P and the fracture energy, G_c, increase and reach a plateau for relatively thick adhesive layers in the case of flexible peel joints (i.e. polymer on polymer)

[Gent 77, Kinloch 94]. A similar fracture dependence on the joint width was observed [Kinloch 81]. The adhesive fracture energy passed through a maximum value with increasing adhesive layer thickness when joints consisted of steel bonded to the sample with a rubber-toughened epoxy [Kinloch 94]. The maximum value was reached for thinner layers if the peel rate was high. This shows that the practical strength values also depend strongly on the displacement rate, as well as on the test temperature. Preparation of the adherent film, in our case a metal layer, may also influence the measured adhesion strength, as well as other mechanical properties, because of different grain sizes, columnar structures and film densities [Ohring 92].

Taking this into account, the changes in the basic adhesion, caused by changing the properties of the polymer–metal interface, may not be reflected in the measured adhesion, if the external factors are not kept the same. Therefore, the adhesive layer (metal film) preparation and the peel test conditions should be kept constant, in order to be able to compare the obtained results.

Chapter 5

Experimental

The goal of this research is to determine polymer sputter rates, to alter physical and chemical properties of polymer surfaces, and to improve the metal/polymer interface formation. In order to understand the mechanisms that occur during ion irradiation of polymers, or how induced changes influence the adhesion between metal and polymer, a large number of experiments was required. Before describing each particular experiment, details about the different polymers and the polymer thin film preparation (organic film deposition, polymer surface metallization) will be given. Later, parameters of ion-beams, as well as sputter rate measurements obtained using three different methods will be described. Experiments based on X-ray photoelectron spectroscopy like chemical analysis, determination of the surface glass transition temperature and metal adsorption probability are explained. The details of the sample preparation and the experimental procedures for the 90° peel test performed to measure the adhesion force of metal on modified polymer surfaces are given. Finally, contact angle and surface roughness measurements are presented at the end of this chapter.

5.1 Preparation of polymer thin films

Thermoplastic polymers containing aromatic rings, oxygen, nitrogen, and fluorine functional groups were used for this research. The polymer thin films were prepared by spin coating, solution casting, vapour deposition, or RF magnetron sputtering. Fluorine containing polymer films were obtained by vapour deposition that involves thermal decomposition of the polymer granulate and repolymerization on the substrate [Biswas 03]. Resputterred PTFE thin films were prepared by RF magnetron sputtering [Biederman 00, Schürmann 05]. Evaporated and resputtered polymer films were prepared by my colleagues, or obtained from other sources. Therefore, no details will be given in this work and the reader is referred to the above mentioned literature. The polymers mainly used in the experiments described below were prepared by the spin coating technique, the details of which are given in the Section 5.1.2. It should be noted, that polymer sheets or polymer foils with thicknesses of 1 mm and 0.25 mm respectively were used for the peel test experiments instead of thin ~ 10 – 200 nm films.

Before describing the film preparation steps, details about the polymers used in the research are given.

5.1.1 Polymers

In this work, simple hydrocarbon polymers or polymers containing aromatic rings, oxygen, nitrogen or fluoro groups were investigated. Table 5.1 summarizes the polymers used in the experiments together with the source they were purchased from and the form of use.

Table 5.1 *Polymers used in this work. For some polymers the molecular weight M_w and molecular weight distribution M_w/M_n are given.*

Polymer	Chemical formula	Source	Form of use
Polystyrene (PS) M_w = 220.9 kg/mol M_w/M_n =1.03	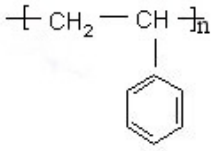	Polymer Source GoodFellow	Spin coated film Sheets
Poly-α-methylstyrene (PαMS) M_w = 9 kg/mol	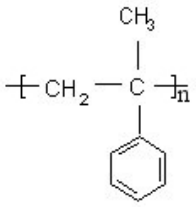	Aldrich	Spin coated film
Polymethyl-methacrylate (PMMA) M_w = 161.5 kg/mol M_w/M_n =1.06	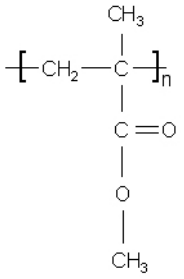	Polymer Source GoodFellow	Spin coated film Sheets
Polymethylacrylate (PMA) M_w = 150 kg/mol M_w/M_n =1.13	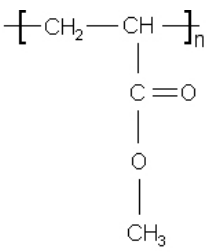	Polymer Source	Spin coated film

Table 5.1 *Continued.*

Polymer	Chemical formula	Source	Form of use
Polyacrylonitrile (PAN) M_w = 150 kg/mol	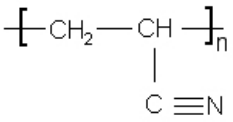	Scientific Polymer Products	Spin coated film
Polymethylacrylo-nitrile (PMAN) M_w = 20 kg/mol	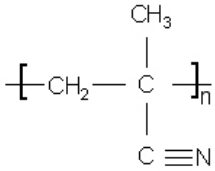	Scientific Polymer Products	Spin coated film
Bisphenol-A-polycarbonate (BPA-PC)	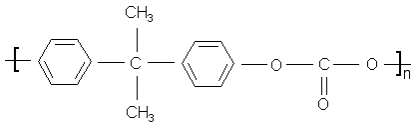	Bayer GoodFellow	Spin coated film Sheets
Polypropylene (PP)	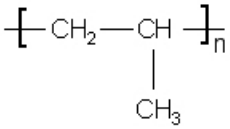	Renolit Saltzgitter	Foils
Polyisobutylene (PIB) M_w = 400 kg/mol	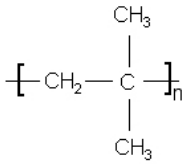	Scientific Polymer Products	Spin coated film
Polytetrafluoro-ethylene (PTFE)	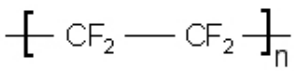	GoodFellow	Vapour deposited film
Teflon AF 1600	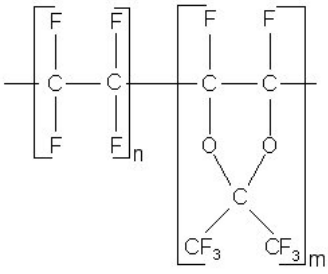	DuPont	Vapour deposited film

5.1.2 Spin coating

The polymers prepared by spin coating were received in form of powder, pellets, sheets or foils. Thin films were obtained using a spincoater P-6708D from Specially Coating Systems (USA). The principles of spin coating are following: a drop of a solution is deposited on the centre of a substrate spinning at high speeds (1000 - 4000 rpm).

Solution preparation

To spin polymers on some substrate, polymer powder or pellets had to be solved in particular solvents: water free toluene (99.8 %, Aldrich) for PS, PαMS, PMMA, PMA, PIB; dichlormethane (99.9 %, Aldrich) was used to desolve BPA-PC; N,N-Dimethylformamide (99.9+ %, Aldrich) - PMAN, PAN. These solvents were selected because they desolve the particular polymers, and did not evaporate too fast during the spin coating leading to smooth films as desired for further experiments. Acetone is another solvent suitable to desolve most polymers. Nevertheless, during the spin coating process, it evaporates too fast causing the formation of polymer films with rather rough surfaces.

Polymer solutions with different concentrations were prepared. This resulted in different film thicknesses, measured with the profilometer (Section 4.7), which varied from 10 to 200 nm (Figure 5.1), although there is also some dependence of the film thickness on the rotation speed, which will be discussed later. It should be pointed out, that for different solutions different concentrations are required in order to obtain a similar film thickness.

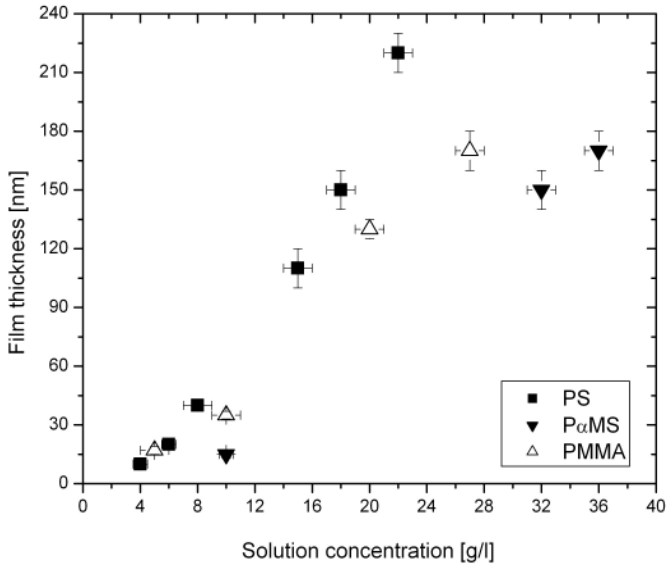

Figure 5.1 *The dependence of the polymer film thickness on the solution concentration (given in g/l). The films were prepared at a constant rotational speed (1000 rpm).*

Spin coating process

As it was mentioned in the beginning of this chapter, a drop of solution should be deposited on the substrate which should be spinning at high a speed in order to obtain uniform films. Mainly there are four stages in the spin coating process:

Stage one: *deposition of the coating fluid onto the wafer and substrate*. The solution can be deposited using a nozzle or it can be sprayed. In our case, the polymer solution was poured onto the sample through a syringe with a sub micron sized Teflon filter (Eydam) on top of the injector. The filter was used to eliminate particles that were not desolved by the solvent. Si wafers with a native oxide layer, quartz crystals (Caburn), or gold covered Si wafers were taken as substrates. Pure Si wafers and quartz crystals were cleaned with acetone before deposition of the polymer films. PS thin films were also prepared on Cu TEM grids for TEM measurements. This preparation with be explained in all details later in this chapter.

Solutions can be deposited in two ways. In the so called static dispense process, the fluid is poured on a stationary substrate, and only afterwards the stage is starting to rotate. This deposition technique was used if the solution had a high viscosity (solution concentration > 20 g/l) or if the substrate had a rectangular shape. The substrate was completely covered with the solution in order to ensure full coverage of the substrate surface during high speed spinning.

In the dynamic dispense process, the solution is deposited while the substrate is turning at low speed in order to spread the fluid across the substrate decreasing the amount of resin material wasted since it is usually not necessary to deposit as much material to wet the entire surface. The dynamic dispense deposition technique was used to cover substrates with polymer films using solutions with low concentrations (up to 20 g/l). The fluid was deposited on the rotating wafers at speeds ranging from 100 to 500 rpm.

Stage two: *the substrate is accelerated up to its final rotation speed*. In this stage, the fluid is expelled from the wafer surface by the rotation motion. Because of the initial depth of the fluid on the wafer surface, spiral vortices are shortly present. Rings will form as a result of a twisting motion caused by the inertia that the top of the fluid layer exerts while the wafer below rotates faster and faster. After some time, the fluid is thin enough to rotate together with the substrate and any differences in thickness are gone. The final speed of 1000 rpm, used for the thin film deposition, was reached after 10 s.

Stage three: *the substrate is spinning at a constant speed in order to achieve the final film thickness.* This stage is characterized by gradual fluid thinning. Fluid thinning is quite uniform, though with solutions containing volatile solvents, it is possible to see interference

colours. The combination of spinning speed and spinning time will define the final film thickness. In general, higher spinning speeds and longer spinning times create thinner films.

As this work does not concentrate on the detailed investigation of thin film preparation by spin coating, polymer films with different thicknesses were prepared at a constant rotation speed (1000 rpm) and time (200 s), changing just the concentration of the solution, (Figure 5.1).

Stage four: *the substrate is spinning at a constant rate in order for the solvent to evaporate*. As stage three advances, the fluid thickness reaches a point where the viscosity effects yield rather minor net fluid flow. At this point, the evaporation of any volatile solvent species will become the dominant process occurring in the coating. In fact, at this point the coating effectively "gels", because as these solvents are removed, the viscosity of the remaining solution will likely rise effectively freezing the coating [Meyerhofer 78].

Stages three and four occur simultaneously and so it is difficult to exactly define the border between two stages. However, at the engineering level the viscous flow effects dominate early, while the evaporation process dominates later.

PS film preparation for TEM

It is required to have thin specimens for the TEM in order to allow electron transmission. In order to investigate polymer films they need to be placed on supporting grids. Cu grids with a diameter of 3 mm were used in this case. PS thin films on Cu grids were prepared as described by Erichsen [Erichsen 04a, Erichsen 04b]. PS films of 40 – 50 nm in thickness were deposited by spin coating on cleaned glass substrates. After the films were dried, they were divided into small squares (9 mm^2) using a scalpel. Then small pieces of PS were rinsed with distilled water. The PS films do not desolve in the distilled water, but float on the water surface. This made it easy to lift the film on the grid from below.

The prepared films were annealed in a vacuum oven at a temperature $T = T_g + 30°C$ for 3 hours in order to remove the rest of the solution and the water. High resolution XPS spectra (see Section 5.4.1) were taken in order to confirm the chemical composition of the polymer. The spectra were compared with the spectra given in the polymer handbook [Beamson 92].

5.2 Polymer metallization

Polymer metallization was done by physical vapour deposition (PVD), a term that includes both metal evaporation from the vapour phase and sputtering (in our case, magnetron

sputtering (MS)). Gold (Good Fellow) and copper (Aldrich) wires of the 99.99 % purity were used for the metal layer deposition by evaporation. For magnetron sputter deposition Cu sputter targets having 99.9 % purity (workshop of the Technical Faculty) were used.

In this Section, the above mentioned deposition methods will be discussed. Metallization parameters for special experiments like condensation coefficient measurements, surface glass transition temperature determination and peel tests will be given in following sections where these experiments will be described.

5.2.1 Vacuum evaporation

Vacuum evaporation is a PVD process in which the atoms or molecules evaporated from a thermal vaporization source reach the substrate without collisions with residual gas molecules in the deposition chamber [Mattox 98]. As this type of evaporation process requires a relatively good vacuum, the deposition took place in an ultrahigh vacuum chamber where the pressure was maintained at 10^{-9} – 10^{-8} mbar, while it usually increased to 10^{-7} mbar during evaporation.

Thermal evaporation requires that the surface and generally a large volume of the materials must be heated to a temperature where the vapour pressure exceeds the chamber pressure. The saturation or equilibrium vapour pressure of a material is defined as the vapour pressure of the material in equilibrium with the solid or liquid surface in a closed container. The vapour pressure is measured using a Knudsen cell which consists of a closed volume with a small orifice of known conductance. When the container is held at a constant temperature, the material that escapes through the hole depends on the pressure differential.

Resistively heated evaporation sources were used in most of the experiments where moderate metal deposition was required. The source must contain a molten liquid without extensive reaction, and the molten liquid must be prevented from falling off from the heated surface. This was accomplished by using cylindrical cups made out of the high melting point materials molybdenum, aluminium oxide or boron nitride. The crucible with the metal was heated by external tungsten wire heating elements wound to fit around the container, Figure 5.2. Additional aperture systems allowed to evaporate metal only onto the desired surfaces while avoiding metallization of the manipulator and the other vacuum devices in the chamber. In order to obtain an optimum treatment and evaporation position, the manipulator could be moved and rotated in all directions. It also contains electrical contacts and thermo elements allowing it to heat the sample and to monitor the sample temperature. The Omicron full lab

vacuum chamber system allowed the transfer of the prepared samples into the analytical chamber for further investigations without exposing them to air.

In order to heat the evaporation source, the evaporator was connected to an AC power supply. The current, passing through the copper connectors and the crucible, was increased slowly to prevent evaporator from damage due to thermal shock. The values for the heating current differed for each material as each metal starts to evaporate at different temperatures. Au, Cu, Al evaporate from melts, while Cr has a vapour pressure that is below its melting point and therefore sublimates, but all metals used evaporate as single atoms [Ohring 92, Mattox 98].

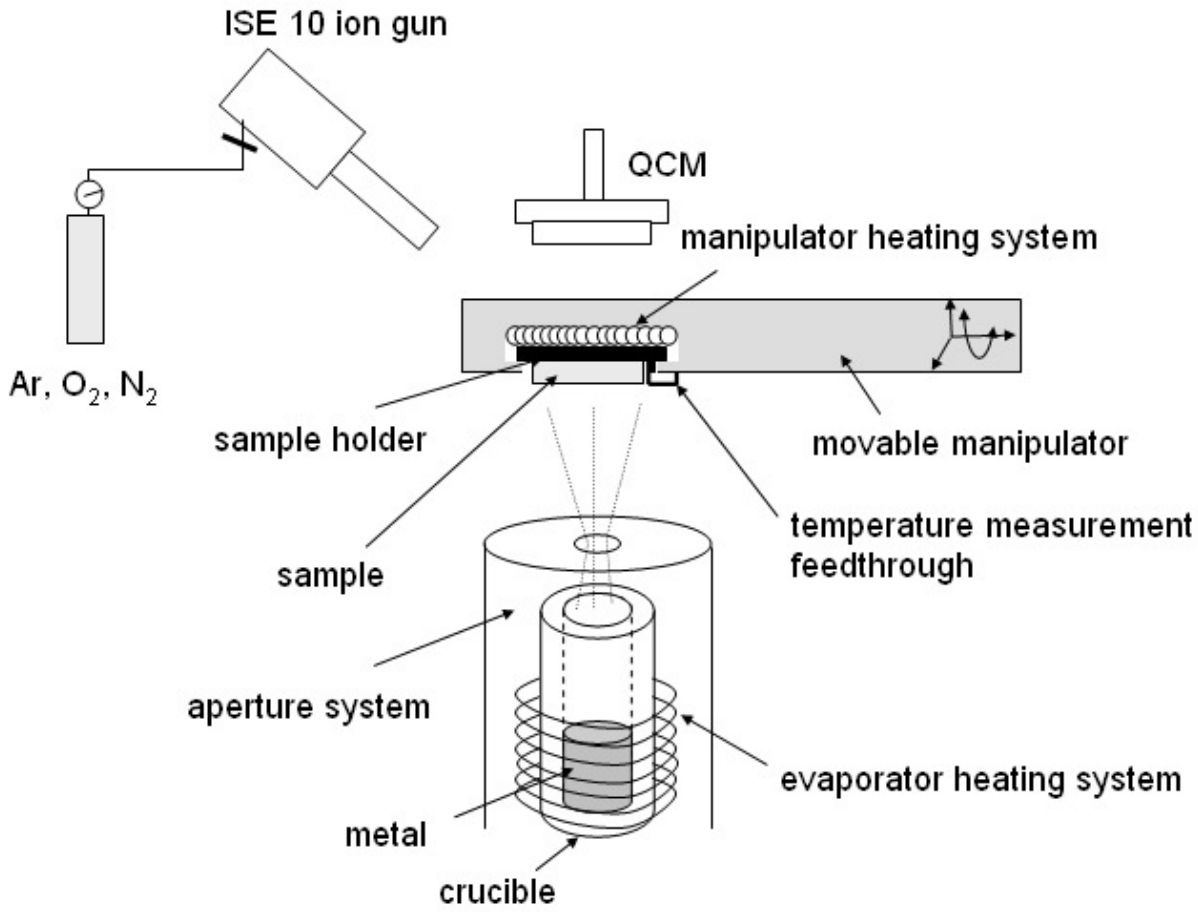

Figure 5.2 *Schematic diagram of the sample preparation for condensation coefficient and surface glass transition measurements.*

Metal evaporation was used for the condensation coefficient and surface glass transition temperature measurements, as only small amounts (~ 0.25 – 10 Å) of metal had to be deposited. A schematic diagram of the sample preparation for these experiments is given in

the Figure 5.2. Evaporation was also used to deposit thin films with a thickness of ~ 10 - 20 nm onto the polymer surfaces before thick (several μm) metal layers for the peel test were deposited.

5.2.2 Magnetron Sputtering

For the peel test experiments, large surface areas had to be covered with metal, the films had to be 5 – 6 μm in thickness, and because of the large number of required samples, the deposition time had to be as short as possible. For these reasons, metal deposition by magnetron sputtering was used which is another PVD process where the bombarding particle creates a collision cascade in the surface-near-region of the target and some of the momentum is transferred to surface atoms which can be ejected as atoms or clusters if they have enough kinetic energy to overcome the surface binding forces.

The purpose of using a magnetic field in a sputtering system is to make more efficient use of the ionizing electrons causing them to produce more ions. When a magnetic field of strength **B** is superimposed on the electric field $\mathcal{E}$ between the target and the substrate, electrons within the dual field environment experience the Lorentz force in addition to the force of the electric field:

$$\mathbf{F}=\frac{mdv}{dt}=-q\left(\mathcal{E}+\mathbf{v}\times\mathbf{B}\right) \tag{5.1}$$

where q, m and v are the electron charge, mass and velocity, respectively. If **B** and $\mathcal{E}$ are parallel to each other, and an electron is emitted normal to the target surface but parallel to both fields, then the expression $\mathbf{v} \times \mathbf{B}$ vanishes. Electrons are then only influenced by the electrical field. In the case, when $\mathcal{E}$ is neglected, and an electron is emitted from the cathode with a velocity v at angle θ with respect to **B**, then the electron experiences a force $qv\mathbf{B}\sin\theta$ in the direction perpendicular to **B**. The electron starts a circular motion with radius r by a balance of the centrifugal and Lorenz forces involved, $r = mv/q\mathbf{B}\sin\theta$, [Chapman 80, Ohring 92]. The general motion will be helical.

In magnetrons, electrons are trapped near the target, enhancing the ionizing effect there. This is achieved by employing magnetic and electric fields perpendicular to each other, as shown schematically in Figure 5.3 (a). Electrons are normally emitted with a velocity v from a surface into a region with a magnetic field **B** which is parallel to the target surface, and a strong electrical field $\mathcal{E}$ perpendicular to the surface and therefore to the direction of **B**. These electrons will be rapidly accelerated, initially away from the target by the strong

electrical field normal to the surface, which decreases linearly with increasing distance to the surface. Executing a helical motion, electrons reach the region of the parallel magnetic field, where they are deflected into an orbit back towards the target. The parametric equations of motion are [Chapman 80, Ohring 92]:

$$y = \frac{q\mathcal{E}}{m\omega_c^2}\left(1-\cos\omega_c t\right) \tag{5.2 a}$$

$$x = \frac{\mathcal{E}t}{B}\left(1-\frac{\sin\omega_c t}{\omega_c t}\right) \tag{5.2 b}$$

where y and x are the distances above and along the target, and $\omega_c = qB/m$. These equations describe a cycloidal motion that the electrons execute within the cathode dark space where both fields are present. By suitable orientation of the target magnets, a 'race track' can be defined where electrons move around at high speeds. Target erosion by sputtering occurs within this track because the ionization of the working gas is most intense around it, as shown in the Figure 5.3 (b).

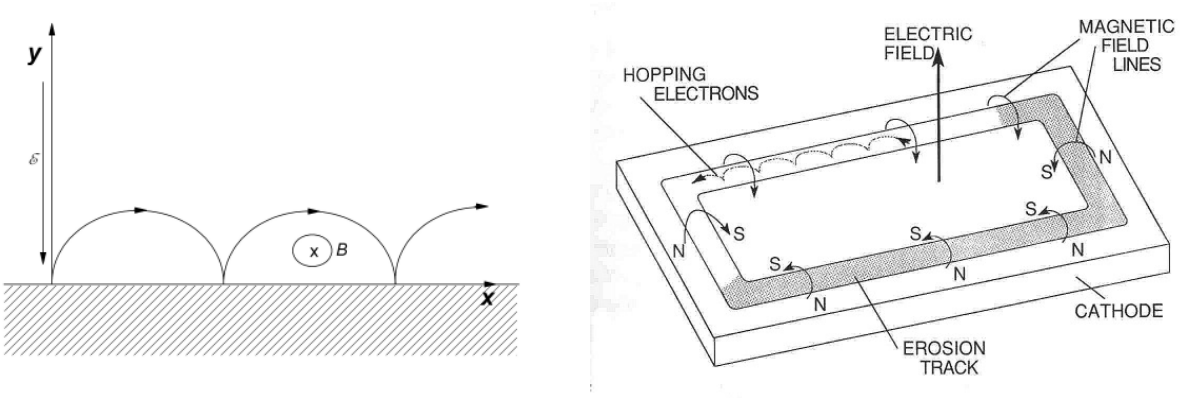

a) b)

Figure 5.3 *a) Motion of an electron ejected from a surface with velocity v into a region of a magnetic field B parallel to the surface (i.e. perpendicular to the plane of paper), and with the electrical field & linearly decreasing away from the surface. (b) A schematic diagram of a planar magnetron sputtering configuration with applied fields and electron motion.*

The geometry of a planar magnetron can be rectangular, as shown in the Figure 5.3, or of circular configuration as it was used in the experimental setup. Despite the large

advantages of the magnetron sputter source, there is still one big disadvantage of the planar magnetron. Because of the localized erosion of the target, the deposition rate varies with time and the target is not sputtered uniformly making it necessary to replace it regularly.

A planar magnetron ION'X-2''UHV 9102 (Thin Film Consulting) was used to deposit thick Cu films on thin Cu or Au layers which were previously evaporated onto the modified polymer surfaces. Metallization was done in a vacuum chamber which was initially evacuated to 10^{-7} mbar. For sputtering, an Advanced Energy MDX 500 power supply was coupled to the magnetron sputter source. Metal targets with a diameter of two inches were mounted onto the cooled holder. Depending on the experiment and the metal target, deposition rates were varied in the range from 10 nm/min to 25 nm/min by changing the DC power from 50 to 140 W. The sputter rate was monitored with a quartz crystal microbalance. The thickness of the metal film was measured with the profilometer.

5.3 Ion-beam irradiation

Ion beams were used to determine the sputter rates of polymers and to modify polymer surfaces with low ion fluences using different gases and ion energies. The irradiation was performed prior to any experiment that were carried out in a preparation chamber (Omicron Full Lab) or in a home made vacuum chamber for metal deposition. The working principles and instrumentation of the sputter guns used in the experiments are given in Section 4.1. Before describing the experiments, important ion beam parameters like ion chemistry, current, energy, incident angle, as well as sample charging should be explained.

5.3.1 Ion chemistry

In the experiments, mainly three types of gases were used: argon, nitrogen and oxygen. Quadrupole mass spectrometry (Section 4.4) was used to determine with what kind of ions the polymer surface was bombarded. The preparation chamber was filled with the gas under investigation (the pressure in the gas-filled chamber was $3 \times 10^{-6} – 6 \times 10^{-6}$ mbar), the ion guns were turned on using the power supplies, and the QMS was programmed to record cycles of mass spectra (schematic diagram of the ion gun, the QMS and the sample position in the chamber is given in Figure 5.9). Later, the spectra were compared with the mass spectra taken in the clean chamber. In the case of argon, only Ar^+ ions were produced but different spectra were obtained for nitrogen and oxygen. The mass spectra showed peaks at relative masses of 14 and 28 for N_2, and 16 and 32 for O_2. These correspond to N^+ and N_2^+ ions for

nitrogen gas, and O^+ and O_2^+ for oxygen gas. Calculated fractions (Table 5.2) of these masses showed that for these gases N_2^+ and O_2^+ are the main ions interacting with the surfaces.

Table 5.2 *The fraction of ions (in %) for different gases. The values in brackets are the mass/charge ratio recorded in the mass spectra.*

Gas	Ar	N_2		O_2	
Ion	Ar^+ (40 m/e)	N^+ (14 m/e)	N_2^+ (28 m/e)	O^+ (16 m/e)	O_2^+ (32 m/e)
%	100	6 ± 1	94 ± 1	8 ± 1	92 ± 1

5.3.2 Ion energies and incident angles

In Section 4.1.1, it was mentioned that for the ion gun ISE 10, ions are mainly produced in the filament plane and are subsequently extracted from the source volume and accelerated to a pre-selected kinetic energy. The final ion energy was selected to be in the region of 0.5 to 5 keV. In the case of the IonEtch microwave sputter gun (Section 4.1.2), the final energy selected for the experiments was in the range of 0.6 to 1 keV.

The incident energy was measured with the energy analyzer, a schematic diagram is shown in Figure 5.4(a). The analyzer consists of a Faraday cup (discussed below) and retarding grids. The positive retarding voltage V_R, applied to the grid, was increased from zero to the value of the selected kinetic energy of the ions, and the ion current, j, was recorded. Only ions with energies higher than the value of V_R contribute to the collector current, those ions which have a lower kinetic energy will be stopped repelled. When the grid potential approached the incident ion energy value, the current dropped to zero. The derivative dj/dV_R shows the ion energy distribution. As an example, Figure 5.4(b) shows the ion energy distribution determined for the IonEtch gun for a pre-selected energy of 1 keV. Obtained results show that the incident energy of the ions is 1 keV ± 0.1 keV.

In the experiments, the ion guns were fixed so that the ions interacted with the surface at fixed angles. In the preparation chamber (Figure 5.2), the angle between the surface normal and the ion incident trajectory was 36°, in the metal deposition chamber the angle was 35°. A number of sputtering rate measurements were done using the QCM method where ion guns were positioned normal to the sample. When it was required to perform experiments as a function of the incident angle, samples were tilted to achieve the desired angle.

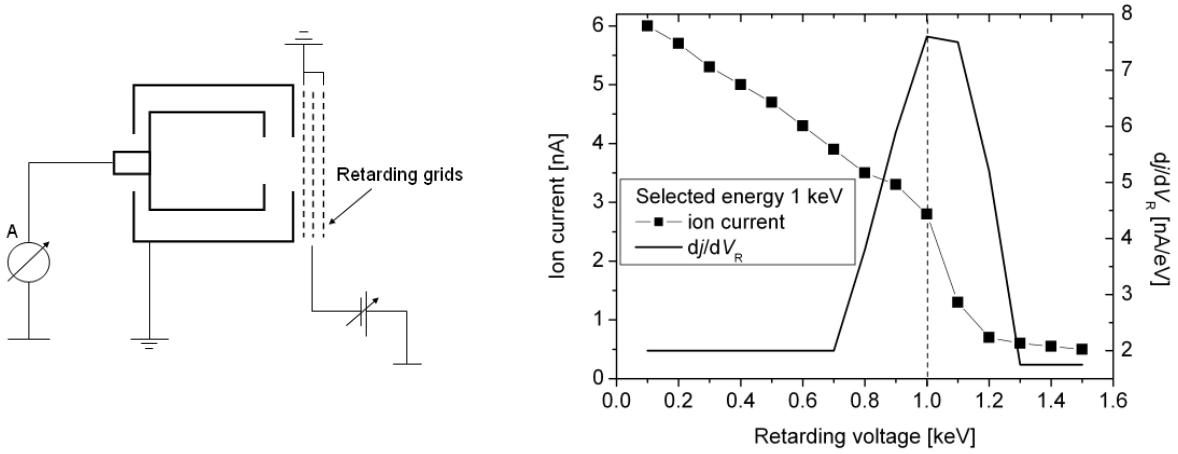

a) b)

Figure 5.4 *a) Schematic diagram of the energy analyzer. b) Ion energy distribution for the IonEtch gun. Pre-selected energy was 1 keV.*

5.3.3 Ion current and ion fluence

The ion current is an important parameter for determination of the ion fluence and the beam distribution. The ion fluence is the number of incident ions per square centimetre and is calculated as follows:

$$\text{ion fluence} = \frac{jt_s}{A_F e} \tag{5.3}$$

where j is the ion current (in A), t_s the sputtering time (in s) , A_F is the aperture area (in cm^2) of the Faraday cup (diameter of the aperture is 2.5 mm), and e is charge of an electron.

In order to measure the ion current, a Faraday cup was placed on one level with the sample on the movable manipulator. A Faraday cup is an electrode with which the electrical current is measured while a charged particle beam impinges on it. The schematic diagram of the Faraday cup that was used in the current measurements is illustrated in the Figure 5.5. The cup consists of two isolated coaxial cylinders: a grounded outer screening cylinder and an inner collecting one (or collector). In between them there is an additional negatively biased secondary electron retarding aperture which minimizes the electron loss. The cup absorbs all charged particles that pass into the collector and significantly decreases the escape of

secondary particles created due to interaction of primary particles with the collector surface. The collector has a feedthrough that is connected to a Picoammeter 6485 (Keithley).

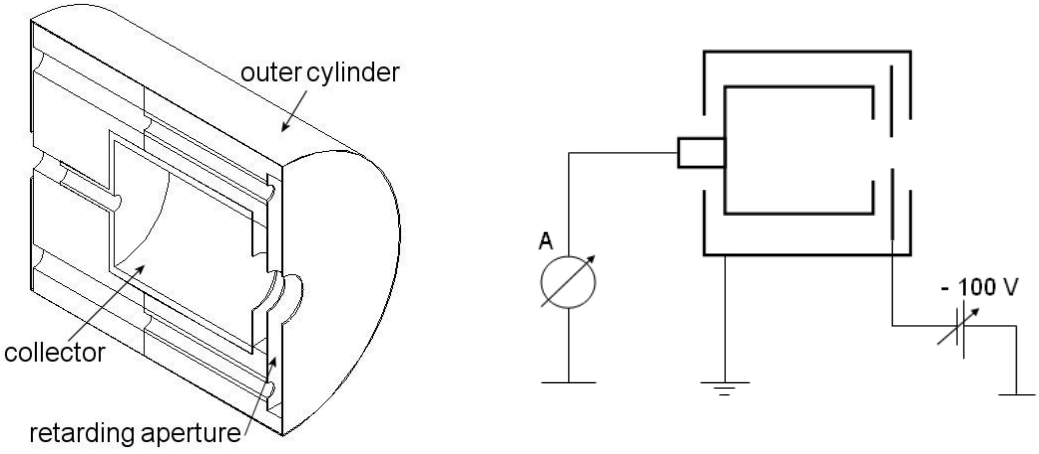

Figure 5.5 *Schematic diagram of a Faraday cup.*

It was necessary that the ion beam was as wide as possible in order to assure uniform surface modification over a large area. As the Faraday cup was placed on the movable manipulator, it was possible to determine the optimum treatment position and ion beam diameter. By changing the focus and the extraction voltage, the beam diameter could be varied. The maximum beam diameter allowing uniform surface modification was found by measuring the ion current while moving the Faraday cup in the x-z plane. The ion current was measured at a constant height (coordinate y was not changed), this means that the ion gun ISE 10 was 140 mm away from the sample and the sample holder was moved in z and x directions, and the current was measured, as shown in Figure 5.6. The left graph shows the ion current distribution for fixed y and z coordinates, as only the x coordinate was varied. Here, a value for z was chosen where the ion current had a maximum value as shown in the right figure. Similar measurements were done for fixed y and x coordinates changing just the position on the z-axis. The full width at half maximum (FWHM) varied between 7 and 8 mm where ion current changed ~ 10 to 15 %. This was enough to allow uniform treatment in an area with a diameter of about 8 mm. The samples which were to be modified were positioned in the middle of the region of maximum ion current.

In a similar way, the ion current distribution for the IonEtch sputter gun was measured. This ion gun is able to modify even larger areas uniformly having a maximum radius of 20

mm. This is important in the case of polymer surface modification for peel test measurements where the sample size was 22 × 30 mm.

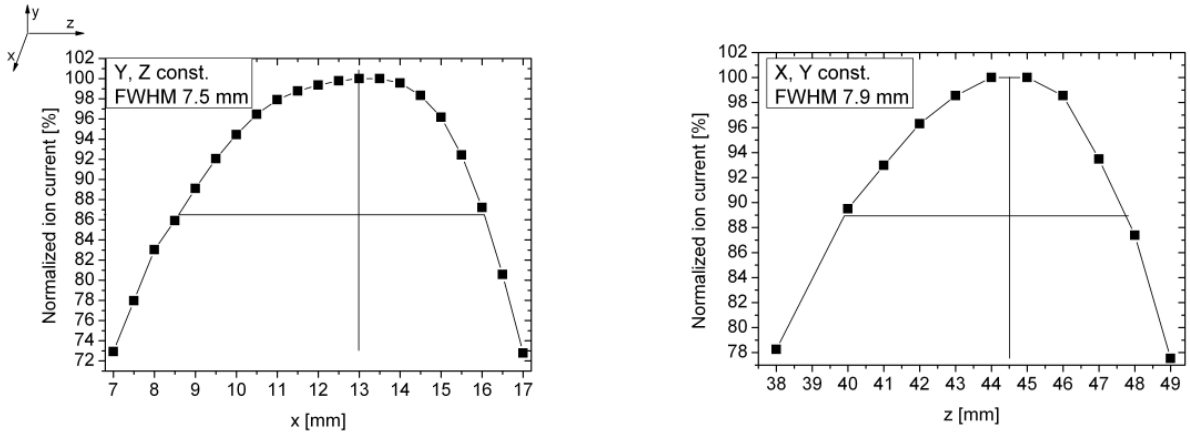

Figure 5.6 *Normalized ion current (given in %) distribution. The insert on the upper left shows the manipulator axis. Left: the ion current measured at fixed y and z coordinates, z was chosen at the position of the maximum ion current as shown in the right (z = 44.5). Right: measurements performed at fixed y and x coordinates, x = 13 (left).*

5.3.4 Sample charging

When an insulator is bombarded with a positive ion beam the surface potential rises due to the impact of the positively charged ions and the emission of secondary electrons [Sabatini 93]. The result is a barrier electric field on the surface retarding the arriving ions. It was found, that in thin polymer films the practical breakdown field is in the order of 10^7 V/m [Fischer 82, Dissado 92]. For thin polymer films of 100 - 200 nm in thickness, the breakdown voltage is in the order of several Volts (10 – 20 V). So ions with ion energies of several keV will pass through the barrier without extensive loss of energy. In order to check the influence of surface charging, an ion gun was used with and without neutralizator. In both cases, removed film thickness (determined with a profilometer) differed by 2 nm which is in the range of experimental uncertainty.

A large charge is built up when polymer sheets with a thickness of 1 mm and foils of 0.25 mm are irradiated with low energy ions. In this case, the breakdown voltage is ~ 10^4 V, and an energy of 1 keV is not high enough for ions to pass through the charge barrier. The influence of charging on the ion modification is demonstrated in Figure 5.7(a). A PS sheet

was irradiated with Ar^+ ions with an energy of 1 keV. XPS spectra of the carbon C1s peak and shake-up satellite (a characteristic feature of PS, see in Chapter 6) were recorded for different fluences. Comparing them to the same ratio obtained for a thin PS film (120 nm) (solid squares), it is obvious, that changes are induced very slowly and only at above an ion fluence of 10^{14} cm^{-2}.

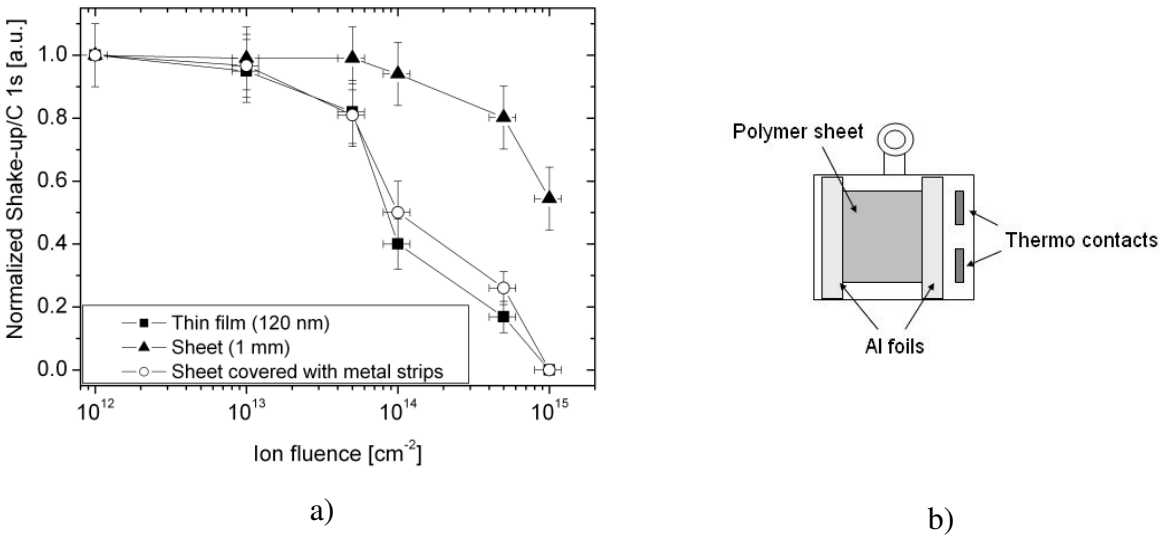

Figure 5.7*. a) Normalized ratio of Shake-up/C1s for PS thin films and sheets vs the fluence of 1 keV Ar^+ ions. b) Schematic diagram of a sample holder with a polymer sheet (1 mm in thickness) covered with Al foil. The foils are in contact with the sample holder, which is grounded through the thermo contacts*

To eliminate this problem, it is necessary to prepare samples in such a way that the built-up charge can flow away from the surface, leaving an uncharged irradiation area for incoming ions. For this reason a PS sheet was partly covered with an Al foil, which was in contact with the grounded sample holder, Figure 5.7(b). XPS analysis was repeated for this sample, and recorded changes were in good agreement with the results for the thin polystyrene film, which is very important for our investigations, Figure 5.7(a) open circles. Because of the space charge formation on thick polymer samples, ion modification of sheets or foils was done when such samples were partly covered with a metal mask that was in

contact with the grounded sample holder. This is also important for the sample preparation for the peel test (Section 5.8), as only thick polymer sheets were used for this experiment.

5.4 Polymer sputtering rate measurements

The sputtering rate measurements are one part of the research. It was already mentioned that the common definition of the sputter yield for elemental targets (atoms sputtered per incident ion, Section 3.2.1) cannot be applied to the sputtering of polymers, except for the case that the identity of all sputtered particles and their distributions are known. For this reason the sputter rate *SR* of the polymers was calculated. *SR* can be defined as the ratio of the amount of material removed to sputter time, t_s, normalized to the ion current density, *j*',:

$$SR = \frac{d}{t_s}\frac{1}{j'} \tag{5.4}$$

where *d* is the amount of removed material in nm, $j' = j/A_F$ where *j* is the ion current measured with the Faraday cup and A_F is the aperture area of the Faraday cup. In the following sections, the sputter rate will be given in nm/min for defined ion currents. The sputtering or sputter rate is also called the removal rate, and ablation rate is a term used in the cases where temperature is involved. The three methods described below were used to measure the rate.

5.4.1 Sputter rate determination by step measurements using a stylus profilometer

The most simple sputter rate determination method is to measure the step between the bombarded and unsputtered parts, which are obtained when a part of a sample surface under investigation is covered with some thin metal wire or foil. To shorten the name of this method, the term “step method” will appear in the text.

For this type of experiments, a special sample holder was manufactured as shown in the Figure 5.8(a). The sample holder consists of a background plate with thermal contacts allowing to record the temperature during temperature dependant experiments. The special mask contains a Ta wire fixed onto the surface with screws. The height of the mask was slightly higher than that of the Si substrate, so that the wires did not touch the sample surface. In such a way, the surface was protected from external damage. This particular system was used for the rate calculations using the ISE 10 ion gun with the incident angle of 36° and an ion energy in the range of 1 to 5 keV. In order to minimize shadowing effects, the sample was positioned in the middle of the beam area. When polymers were bombarded at different

angles of incidence with the ISE 10 and IonEtch sputter guns, it was impossible to use this sample holder because of the manipulator geometry, which was different from the one used in the preparation chamber. In such cases, 2 to 4 narrow strips of Al foil were used instead of the Ta wire. Since the strips were in close contact with the polymer surface, it was necessary to fix and remove them with care trying to avoid surface scratching. Several unsputtered lines remained on the polymer sample after ion bombardment (Figure 5.8(b)). These later were measured with the profilometer. The profile is shown in Figure 5.8(c). The profiling was done for each strip every millimetre in order to have an average removal value which was used for the sputtering rate calculations.

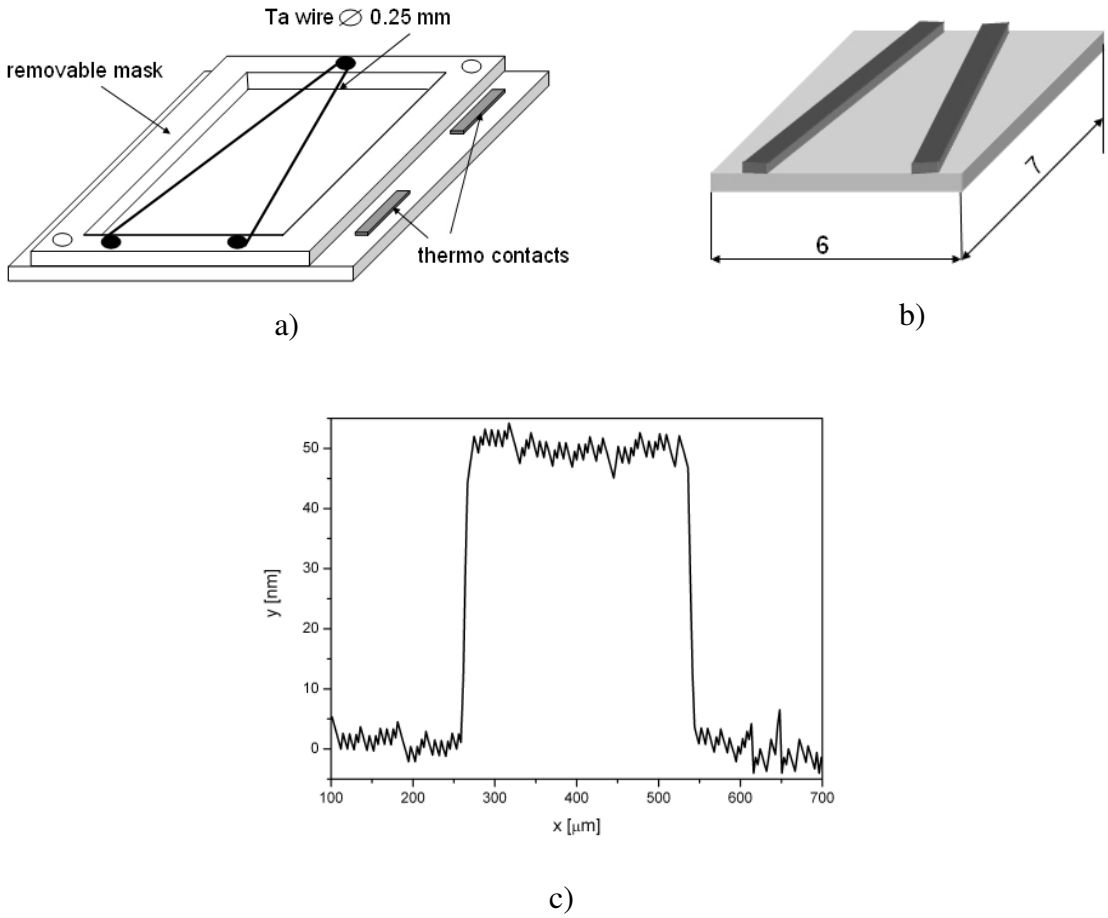

Figure 5.8 *a) Schematic diagram of a sample holder for sputter rate determination. A Ta wire with a diameter of 0.25 mm is fixed with screws onto a removable mask. b) An example for a polymer film after sputtering through the mask. Two unsputtered lines remain on the surface after the sputter process. Sample dimensions are given in mm. c) Typical sputtering profile measured with a profilometer.*

A typical sputtering time was about 3 to 60 min (depending on the polymer, ion current and gas) which corresponds to an ion fluence of 1×10^{15} cm^{-2} and higher. It was important to use these high fluences, because with the profilometer it was only possible to measure height differences of at least 5 nm on smooth sample surfaces.

5.4.2 XPS method

X-ray photoelectron spectroscopy (XPS) is a technique that allows to determine the thickness of very thin films and was applied to measure the change in thickness of thin polymer films after ion beam bombardment [Zaporojtchenko 03b].

In order to measure polymer sputter rates with XPS sputtering was performed in a preparation chamber (Omicron Full Lab) using the ISE 10 sputter ion gun. The polymer samples were bombarded with argon ions with a kinetic energy of 1 keV at an angle of incidence of 36. The ion fluence was in the range of 10^{12} to 10^{16} cm^{-2}. In this case, polymer samples with of a size 10×10 mm were fixed in the centre of the sample holder shown in the Figure 5.8a, without the mask being attached. The beam was defocused, and the diameter of the area that was uniformly modified was ≈ 8 mm. After sputtering, the samples were transferred to an analytical chamber where the XPS measurements were performed using an electron spectrometer (Omicron) equipped with a non-monochromated Al $K\alpha$ source at 0° take off angle. Thin polymer films (~ 10 - 12 nm) prepared by spin coating were used in order to detect the XPS signal of the Si substrate through the polymer film. The intensities of the C 1s, Si 2s and Si 2p peaks were recorded and used for further calculations.

The thickness measurements are based on the relative peak intensities of the film and substrate. If a sample consists out of a layer (thickness d) of material A, and a bulk material B (where A and B are of uniform composition), then equation 4.3 (Section 4.2.1) for the thin layer and bulk can be written as:

$$I_A = I_A^{\infty}\left[1-\exp\left(-d / \lambda_{A,A}\cos\theta\right)\right] \tag{5.5 a}$$

$$I_B = I_B^{\infty}\left[\exp\left(-d / \lambda_{B,A}\cos\theta\right)\right] \tag{5.5 b}$$

where I_A and I_B are measured intensities, I_A^{∞} and I_B^{∞} are the intensities of bulk A and B samples under identical conditions, $\lambda_{A,A}$ and $\lambda_{B,A}$ are the attenuation lengths of the electrons of the measured core-electrons A and B travelling through material A. In special cases, $\lambda_{A,A} \approx$

$\lambda_{B,A}$, and so we can denote it as λ_A. Then from the Equations 5.5, the layer thickness can be calculated by:

$$d = \lambda_A \cos\theta \ln\left(\frac{I_B I_A^{\infty}}{I_A I_B^{\infty}} + 1\right) = \lambda \cos\theta \ln\left(\frac{I_f I_{Si}^0}{I_{Si} I_f^0}\right) \quad (5.6).$$

where I_{Si}^0 and I_f^0 are the intensities of bulk Si and the polymer film, respectively, I_{Si} and I_f are the intensities of Si through the polymer film and of polymer film itself, and λ is attenuation length of Si electrons in the polymer film. The values of λ were taken as 3.72 nm for PS and PαMS, and 3.88 nm for PMMA [Tanuma 93]. Knowing the value for *d*, the sputter rate can be calculated using the Equation 5.4.

5.4.3 QCM method

The third method is based on the quartz crystal microbalance (QCM) (Section 4.5) [Zekonyte 05]. The advantage of this technique is that it allows to do real time sputter rate measurements and to study the kinetics of sputtering.

Sputter rate measurements using the QCM were performed in the home made ultra-high vacuum chamber using the ISE 10 ion gun (Omicron) or the IonEtch sputter Gun (Tectra). The bombardment with Ar^+, N_2^+ and O_2^+ ions was done at beam energy of 0.5 to 3 keV for different ion fluences, and at normal angle to the quartz crystal. The pressure in the chamber during sputtering was 5×10^{-6} mbar using the ISE 10 ion gun, and 10^{-4} mbar using the IonEtch sputter gun. The ion current density in both cases was 1μA/cm^2. The QCM crystals covered with spin coated polymer films (100 - 200 nm) were mounted onto a special sensing that was water-cooled. The oscillation circuit used to drive the QCM was mounted directly at the end of the feedthrough on the atmospheric side. The STM-100/MF thickness/rate monitor (Sycon Instruments) was used to determine the thickness of the removed film by the frequency change due to the reduced mass. The crystals used were AT cut gold coated sensing crystals with a diameter of 13 mm having an oscillating frequency of 6 MHz (Caburn). The crystal area affected by the ion treatment was 7.5 mm in diameter. A defocused ion beam was used to uniformly sputter the polymer from the crystal. The thickness/rate monitor was connected to a computer which was used to measure the data (t_s, total *d*,) every second.

5.4.4 Sputter rate vs. temperature

Temperature dependent sputter rate measurements were performed using the step method and quadrupole mass spectrometry (Section 4.4). The holder shown in Figures 5.7(a) and 5.8(a) contains thermocontacts which connected to a thermoelements located in the manipulator in order to measure the temperature of the sample holder when heated (Figure 5.9). The temperature difference between the sample holder and the sample surface is up to 1.5 K for a heating rate of 1 K/min, as demonstrated by Erichsen [Erichsen 04a]. In order to obtain good thermal contact between the sample and sample holder, Si free graphite (Plano) was used as fixing glue. The ion bombardment was performed in the preparation chamber with 1 keV Ar^+ ions for 10 – 20 min (ion fluence 10^{16} cm^{-2}). The sputtering was performed at a constant temperature reached by the slow heating (1 K/min). At the same time, the QMS recorded mass spectra as a function of time. Later, the spectra were analysed and particular masses were plotted as a function of the ion fluence (see Section 6.1.4). The sputter rate was calculated after the thickness was determined using the profilometer.

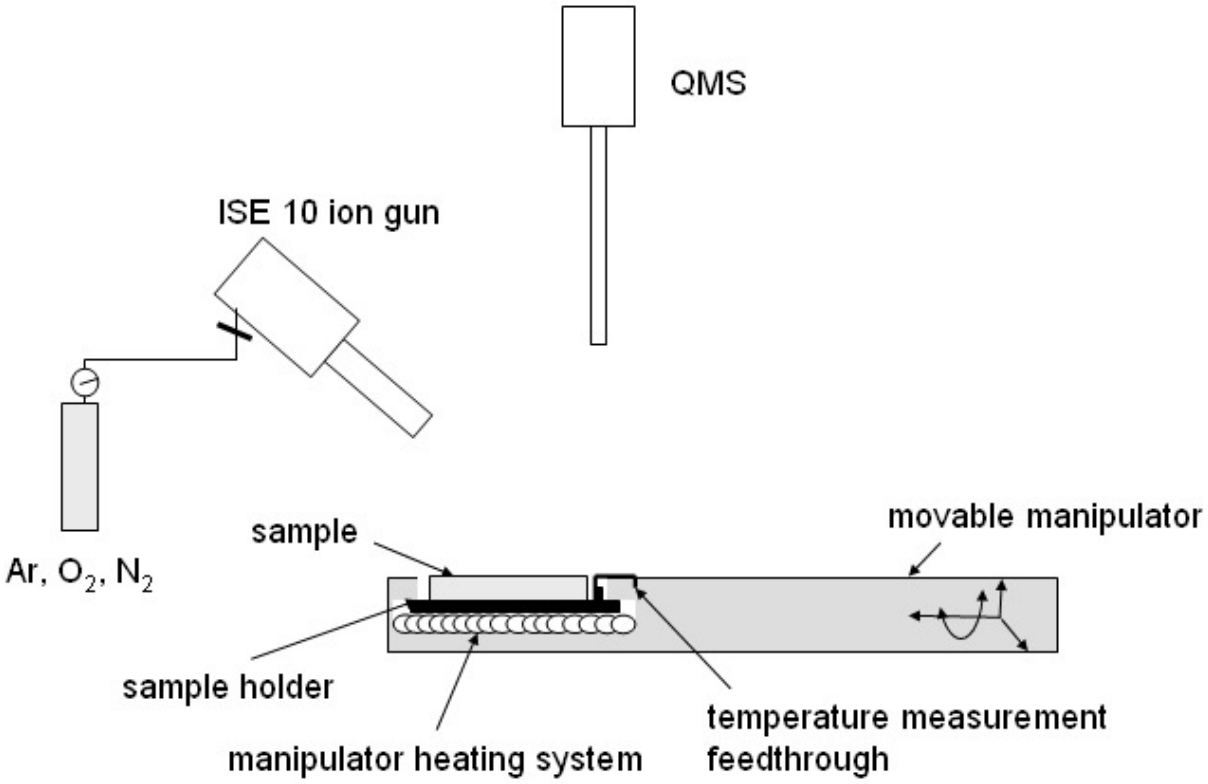

Figure 5.9 *Schematic diagram of the sputter rate measurements as a function of the sample temperature*

5.5 Investigations based on X-ray photoelectron spectroscopy

5.5.1 Polymer surface chemical analysis

In order to explain most of the results, it was important to understand which chemical changes take place on the polymer surface. The polymer samples were moved to analytical chamber (Omicron Full Lab) where XPS analysis was performed after treatment with different gases and different energies and ion fluences. The samples were transferred through the transfer chamber keeping them ion UHV and avoiding exposure to atmosphere (unless it was necessary for the experiments).

XPS measurements were performed using an electron spectrometer (Omicron) equipped with a non-monochromated Al $K\alpha$ (1486.6 eV) or Mg $K\alpha$ (1253.6 eV) source. The pass energy was chosen to be 20 eV in order to obtain high resolution elemental spectra of the C1s, O1s and N1s peaks. The atomic concentration (expressed as at.%) of each element was calculated as follows:

$$C_{\mathrm{a}} = \frac{I_{\mathrm{i}} / S_{\mathrm{i}}}{\sum I_{\mathrm{n}} / S_{\mathrm{n}}} \tag{5.7}$$

where I is the intensity of each element, S is the relative sensitivity factor of an element. The relative sensitivity factors S were taken from the handbook of XPS [Moulder 92]: C1s = 0.296, O1s = 0.711, N1s = 0.477.

A high magnification X-ray beam was used to assure that the recorded signal came only from the polymer sample avoiding signals from the manipulator or the sample holder. It was also important to use the high magnification beam because it was important to record the signal from the modified area only. High resolution spectra were analysed and peak fitting performed using the CASA XPS software.

As it was discussed before, the sampling depth in XPS is a function of the emission angle of the photoelectrons. The technique based on variation of the vertical sampling depth with photoelectron take-off angle is referred to as angle-resolved XPS (ARXPS). It is a particularly important technique for polymer surface studies because destructive depth profiling (sputter depth profiling) causes rapid polymer degradation, changes in the polymer chemical structure, etc. Unfortunately, the depth regime which can be studied is limited to 10 nm [Briggs 98].

A schematic diagram of the surface sensitivity enhancement by variation of the electron take-off angle θ which is the angle between the electron emission trajectory and the surface normal is given in Figure 5.10. The major requirement for surface sensitivity

enhancement is that the surface must be flat, as the surface roughness leads to an averaging of electron exit angles and also to shadowing effects such that the surface enhancement becomes impossible [Briggs 90]. For the overlayer thickness calculation Equations 5.5 – 5.6 can be applied.

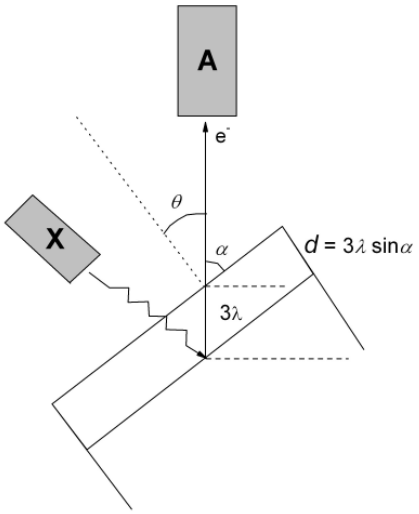

Figure 5.10 *Schematic diagram of the surface sensitivity enhancement by variation of the electron take-off angle θ which is the angle between the electron emission trajectory and the surface normal. X – X-ray source, A – analyser.*

The take-off angles were 0, 15, 30, 45, 60 and 75 degrees. This analysis revealed the polymer modification depth and whether functional groups preferably formed on near the surface or deeper in the polymer.

5.5.2 Surface glass transition measurements

It is assumed that the surface glass transition temperature differs from the one of the bulk, but differential scanning calorimetry (DSC) usually applied to determine bulk T_g cannot be used for the surface measurements. A surface sensitive method based on the embedding of noble metal nanoclusters into polymers showed to be one of best techniques to determine the surface T_{gs} [Zaporojtchenko 01, Erichsen 04a, Erichsen 04b].

Polymer films prepared by spin coating, were tempered in UHV above the bulk glass transition temperature, and prior to metal deposition samples of the size of 11 × 11 mm were treated in the preparation chamber with 1 keV ions with an ion fluence of 10^{12} – 10^{14} cm^{-2}. Au deposited by thermal evaporation with metal deposition rate of 0.2 – 0.26 Å /min at room temperature forms clusters on the polymer surface at a nominal Au thickness of 0.26 Å. The evaporation rate and nominal thickness were measured with a QCM which was in one line with the evaporator. A schematic diagram of the sample preparation is given in Figure 5.2.

The prepared samples were transferred into the analytical chamber where they were heated at 1 K/min rate and the XPS spectra of the C1s and Au4f peaks were recorded. The difference between the temperature of the sample holder and the actual temperature on the polymer surface was not larger than 1.5 K [Erichsen 04a]. The metal intensity was normalized to the carbon intensity in order to eliminate time-dependent changes in the intensity of the XPS spectra. The ratio of I(C1s)/I(Au4f) vs. temperature was plotted. In the vicinity of T_{gs} there is a change in slope of the curve which occurs over several degrees. The value of T_{gs} was taken as the point at which the fitting lines intersect each other, Figure 5.11.

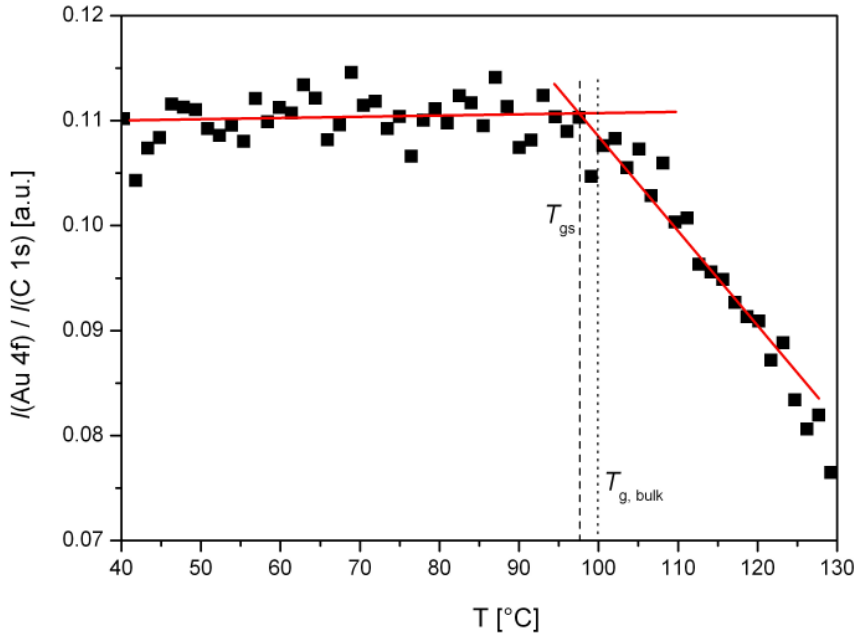

Figure 5.11 *Typical embedding profile for untreated PS. The point at which fitted lines (in dark grey) intersect each other is taken as the surface glass transition temperature T_{gs} (dashed line). The bulk T_g for this PS is shown by the dotted line.*

5.5.3 Condensation coefficient measurements

After evaporation, noble metal atoms adsorb on the polymer, remain and diffuse on the polymer surface for a certain time, and then desorb into the vacuum or are trapped somewhere on or beneath the polymer surface. Metal atoms remaining on or in the polymer contribute to the condensation coefficient C defined as the ratio of the number of adsorbed

metal atoms to the total number of metal atoms arriving at the surface. A detail description of condensation coefficient measurements and meal-polymer interaction, as well as metal cluster growth on inert organic surfaces is given in a number of publications [Faupel 02, Behnke 00, Zaporojtchenko 03a, Zaporojtchenko 02, Kanzow 04].

Metal was deposited by thermal evaporation with a deposition rate of 0.3 Å/min and nominal thickness of ~ 1nm, as discussed above (Section 5.2.1), onto treated polymer surfaces at room temperature. The metal evaporation rate and thickness were monitored with a QCM. The nominal thickness is a measure of the total amount of metal evaporated, which is not necessarily identical to the actual metal layer covering the polymer. The real thickness had to be determined experimentally as only the amount of remaining metal on the organic surface was taken into account for the condensation coefficient calculations. XPS is a surface sensitive technique that allows to determine the actual amount of metal deposited onto the polymer. In the experiments, an X-ray gun (Omicron) with a non-monochromatized Al $K\alpha$ source and high magnification beam was used.

For calculation of C, XPS peak intensities of metals (for Au: Au 4f and Au 4d peaks, Cu: Cu 2p and Cu 3d peaks) were recorded on the substrates for which $C = 1$. Deposited metal on PS treated at an ion fluence of 10^{16} cm^{-2} completely condensates was taken as a standard. Recorded metal intensities were taken as a point of reference linked to the nominal thickness measured with a QCM. The cluster density N_c was calculated as the ratio of the metal thickness d_m on the polymers to the cluster volume:

$$N_c = \frac{d_m}{4\pi r_c^3 / 3} \tag{5.8}$$

where, r_c is the average cluster radius determined by the metal peak intensity ratio of Cu3p/2p [Zaporojtchenko 00a], or from TEM images.

5.6 Contact angle measurements

For the contact angle measurements (Section 4.8), the contact angle system OCA from Dataphysics with preinstalled software was used. A drop of water was placed onto the treated polymer surface by a microsyringe. At equilibrium, the angle was measured by a camera equipped with a goniometric eyepiece.

Polymer treatment was performed with the ISE 10 ion gun using 1 keV Ar^+ ions and a defocused ion beam. After treatment, the samples had to be removed from the vacuum chamber as the contact angle measurements were performed in air. At least two samples were

prepared for each ion fluence ($5 \times 10^{12} - 10^{16}$ cm^{-2}) under the same conditions to have as many data as possible. The average contact angle was taken as an angle for particular ion fluence. The contact angles θ were calculated by the program using the Young-Laplace function. The software allows to take photographic images of the drop which will be shown in the results part.

Contac angle measurements depend strongly on the environmental conditions as was briefly mentioned in the Section 4.8 (details are given in Ref. [Chan 94]). The surface preparation, environmental temperature, drop size were kept constant, and the whole experiment was performed in one day in order to be able to compare results.

5.7 Surface roughness

The AutoProbe atomic force microscope (Section 4.6) from Park Scientific Instruments was used to measure the influence of the ion beam on the surface roughness of the polymer film. Polymer samples were irradiated with Ar^+ ions with an energy of 1 keV in the ion fluence range of $10^{14} - 10^{16}$ cm^{-2}.

Region analysis, that includes all of the region measurement options refer to the induced areas within a mask, was used to calculate the roughness. Two types of roughness, average and root-mean-squared, are reported.

The *average roughness*, R_{ave}, is given by the average deviation of the data, referred to as the average of the data within a specified region:

$$R_{ave} = \sum_{n=1}^{N} \frac{|z_n - \bar{z}|}{N} \tag{5.9}$$

where $\bar{z}$ is the mean z height (given by the average height within the specified region of a mask), N – number of data points in the included mask. Average roughness refers to the included areas within a mask.

Root-mean-squared roughness, R_{rms}, is given by the standard deviation of the data, which refers only to the included areas within a mask:

$$R_{rms} = \sqrt{\frac{\sum_{n=1}^{N} (z_n - \bar{z})^2}{N-1}} \tag{5.10}$$

The measurements are referred to as the mean height of the data within the mask.

5.8 90° peel test

90° peel tests gave a possibility to measure the adhesion force with which metal adheres to a polymer. The schematic diagram of the technique and working principle were presented in Section 4.9. Before explaining the experimental procedure, details of the sample preparation will be given.

In order to perform peel test measurements, it was necessary to use a metal film with a thickness of at least 6 μm. Polymer metallization for these measurements was performed in a custom made vacuum chamber (Figure 5.12a), where the pressure of the evacuated chamber was maintained in the range of 10^{-8} – 10^{-7} mbar. Samples were prepared in several steps.

Prior to metal deposition, the surfaces of polymer sheets (PS, PMMA, BPA-PC), or thin (200 nm) PαMS film that were spin coated on BPA-PC sheets (BPA-PC was selected because of the good adhesion obtained between these two polymers, and because toluene, a special solvent for PαMS, does not solve polycarbonate) were treated with 1 keV ions (Ar, O_2, N_2) in the fluence range of 10^{13} – 10^{16} cm^{-2} using a microwave ion gun (Section 4.1.2). In order to avoid sample charging, treatments were done through the metal mask, as discussed in Section 5.3.4. The mask and sample parameters, as well as their position on the sample holder are shown in the Figure 5.12(b). After treatment, a 20-30 nm thick metal film was immediately evaporated. And finally, a 6 μm Cu film was sputtered onto the sample.

The two step metallization process was necessary because sputtered atoms have a high kinetic energy (2-30 eV) compared to evaporated atoms which have a kinetic energy of 0.1 eV [Ohring 92]. The energy of the sputtered atoms is high enough to break polymer bonds or to induce additional changes not desired in the experiments. Moreover, the adhesion strength was measured between the polymers and different metals, i.e. Au and Cu. As copper targets were the produced by the mechanical workshop of the faculty, it was the easiest way to deposit the required Cu layer on top of the evaporated gold, aluminium or copper film. Another reason is that after metallization by thermal evaporation, the metal chamber was opened and all vacuum devices like the ion gun, evaporators and the second magnetron containing different metal targets were covered with aluminium foil to protect them from Cu contamination. For this reason, the evaporated metal film had to have formed a completely closed layer to avoid polymer reaction with air. With one exception: if reaction with atmospheric oxygen was desired in the experiments, metallization was done after the treated polymer was subjected to the laboratory environment.

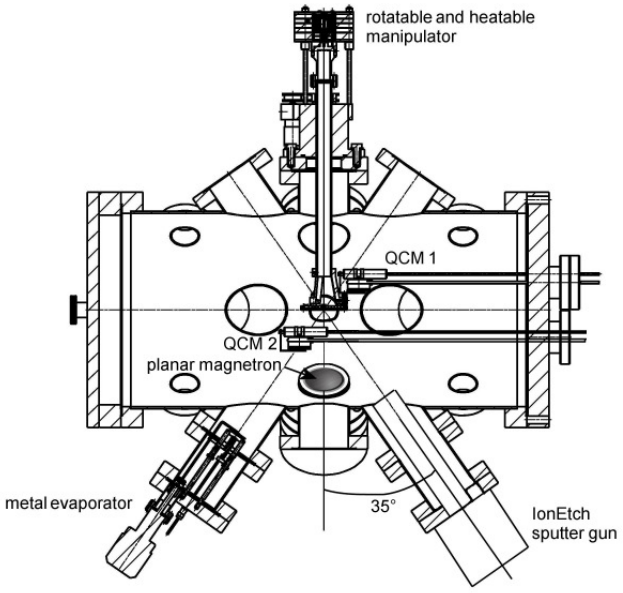

a)

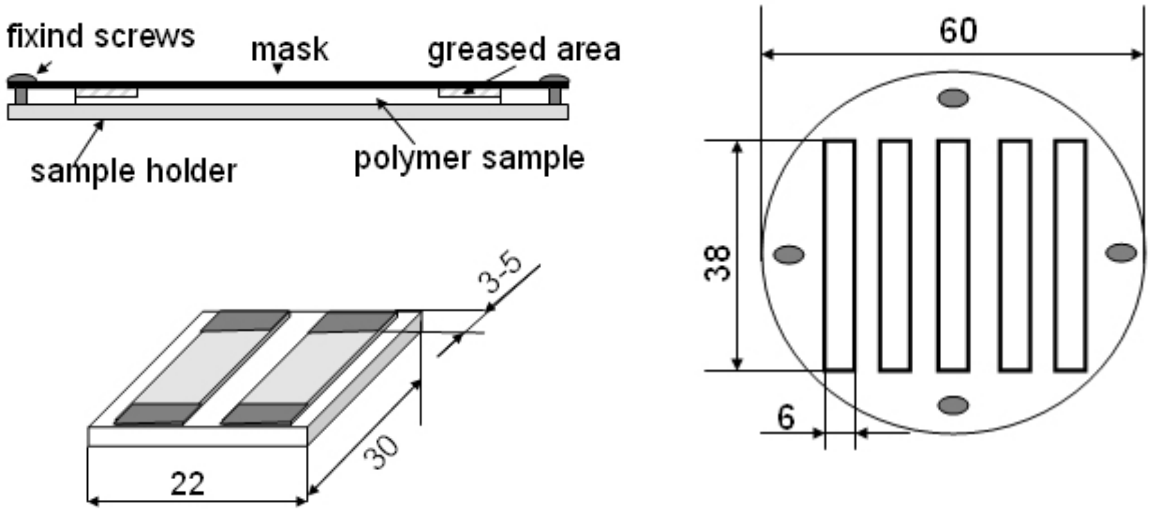

b)

Figure 5.12 *a) Cross section of the custom home made vacuum chamber for metal deposition. QCM 1 is placed in a way so that it measures the deposition rate of the metal sputtered by the magnetron, QCM 2 measure the evaporation rate of the metal evaporator. The angle between the ion gun (or evaporator) and the sample holder normal is 35°, between the magnetron and the sample holder normal the angle is 40° . b) Schematic diagram of the sample preparation. Top left: a polymer sample with greased ends is placed on the sample holder; a special mask is placed on top and fixed with screws. Bottom left: the polymer sample after metal deposition (dark areas – metal deposited on grease). Right: mask. Dimensions are in mm.*

The schematic diagram of the sample preparation is shown in the Figure 5.12(b). Two polymer samples (each 22 × 30 mm) were placed onto the round sample holder (with a diameter of 60 mm). Both sample ends (3 – 5 mm) were covered with a thin layer of ultra high vacuum grease (silicone and halogen free) in order to provide a starting point for the adhesion strength measurements. Finally, a special mask was fixed with screws. The mask was necessary, because of the limitation of the peel test device which allows to peel off stripes with a width of 6 mm. Each polymer sample contained two metal stripes as shown in the figure.

The ion gun, evaporator and magnetron source were fixed at some angles. For this reason, the sample holder was connected to a motor which slowly rotated the holder together with the fixed sample in order to obtain a uniform treatment and metallization.

The main problem in the peel test is to obtain the starting point. For this reason, the both ends of the polymer samples were covered with grease which was later covered with metal just as the rest of polymer sheets or foils (Figures 5.12(a) and 5.13(a). Metal deposited onto the greased part had very poor adhesion to the polymer surface which allowed to fix this end to the measuring device. A packing tape was cut into strips 6mm in width and 8 mm in length which were later bent resulting in a length of 4 mm. One end of the tape was fixed to the force measuring cell of the machine (Figures 4.10 and 5.13(a)), another end was fixed to the metal film by scotch tape (Tesa®) which had good adhesion to the metal and the tape (Figure 5.13(a)). It was important to use tapes, which under tension do not extend or elongate. Peeling was done starting from both sample sides, i.e. the metal strip was peeled up to the middle of the sample, where it was cut, new tape was fixed from the other side, and the peeling procedure continued. The peeling parameters were: peeling length 2 mm, the rate - 5 mm/min. A computer was connected to the device containing the measuring software which recorded the peel force vs. peeling distance, as shown in the Figure 5.13(b). Later, the obtained data were analysed and the peel strength (in N/m) was calculated by dividing the force (in N) by the metal film width (6 mm = 6×10^{-3} m). Before each peel test, the fixing tape and metal strips were relaxed by lowering the measuring cell some one tenth of a millimetre down. That is why there is some slope in each measuring curve until the adhesion force plateau was reached.

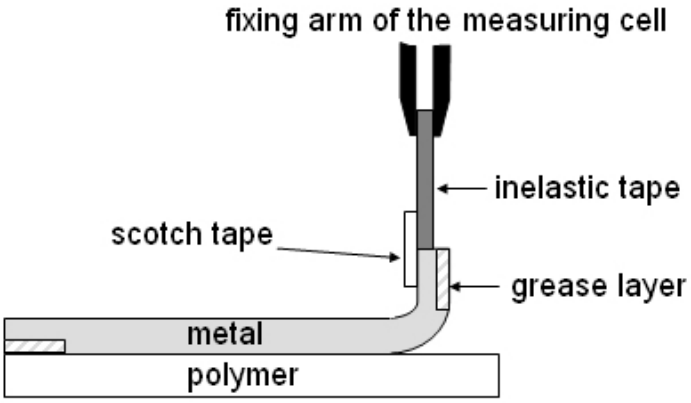

a)

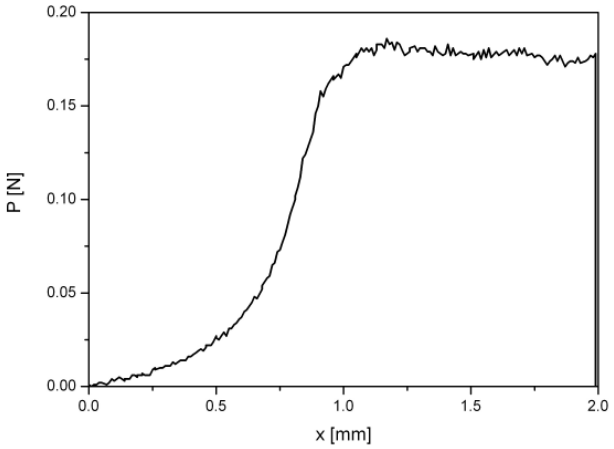

b)

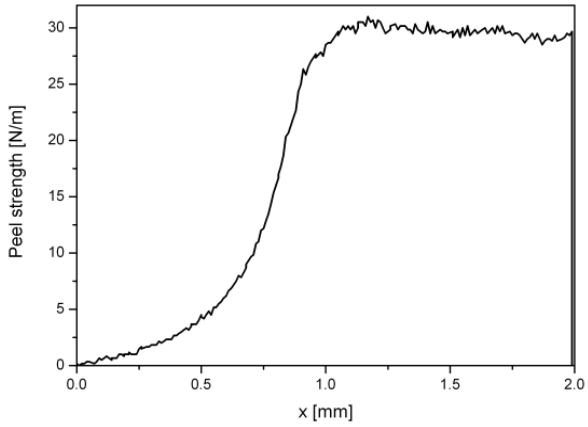

Figure 5.13 *a) Schematic diagram of the sample preparation for the peel test. b) Typical peel curves. Top: the curve recorded by the computer, the force P is given in N (P ~ 0.18 N). Bottom: the same curve only with recalculated peel strength, which is equal to ~30 N/m.*

Chapter 6

Results

The obtained results can be divided into three main parts, namely, (i) dependence of the polymer sputter rate on the ion beam parameters and polymer chemistry, (ii) alteration of the chemical and physical properties of the polymer surfaces under low energy ion beam irradiation, and (iii) metal-polymer interface formation after ion irradiation of polymer surfaces.

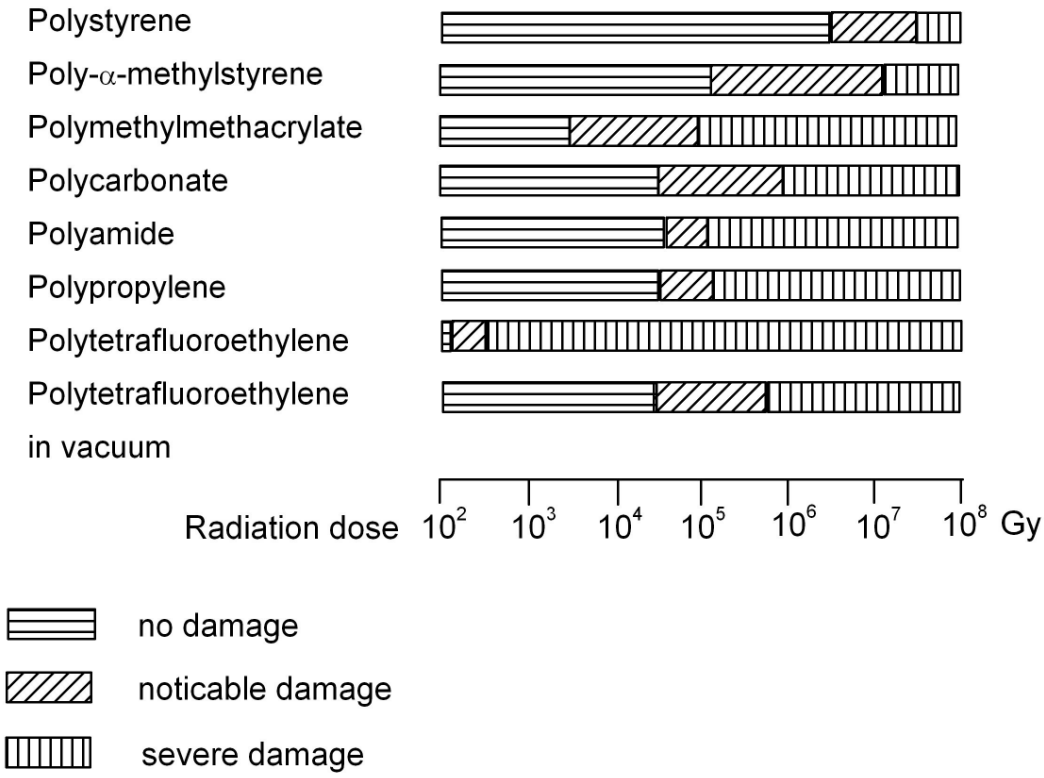

Figure 6.1 *Schematic diagram of thermoplastic polymer stability under γ irradiation, according to [Menges 90, Woods 94].*

When energetic ions hit the surface, surface atoms, clusters or, in the case of polymers, molecules of different sizes are ejected from the target. In addition to the material sputtering, structural rearrangements take place leading to changes in the chemical and physical

properties of the polymer surface. The rate at which these changes are induced differ from polymer to polymer. As an example, Figure 6.1 gives a schematic diagram presenting the radiation stability of some thermoplastics under γ-ray irradiation as a function of the radiation dose.

Following this schematic diagram, different thermoplastic polymers (containing aromatic rings, oxygen, nitrogen and fluorine in their structure, Tables 5.1 and 6.2) that undergo fast or slow degradation under irradiation were selected for further investigation. PS, which has a high stability and prefers to cross-link, PαMS and PMMA with a rather low resistance to radiation and preferential degradation by main chain scission where selected as model systems. Therefore, most experiments were performed only with these three polymers.

Surface modification and sputtering occur simultaneously and cannot be treated separately. To make things less complicated, the results presented in this chapter will be divided into three sections. The sputtering rates of different polymers are given in Section 6.1. The next section deals with ion induced changes in the polymer surface chemistry. Finally, results obtained for metal-polymer interface formation are presented in Section 6.3.

6.1 Sputtering rate of polymer thin films

Sputtering of polymers is a rather complicated mechanism and their sputter rates differ largely from the sputter rates of metals, alloys or semiconductors, which were extensively investigated and are well understood. In contrast to rigid materials, where ejected particles consist of atoms or clusters, and where the surface chemical structure is not dramatically affected, sputtering of organic materials is accompanied by a complete loss of the pristine structure and the emitted species changes with the duration of the ion bombardment. Therefore, it is necessary to investigate the sputter rate dependence on the ion fluence and the ion type, the projectile energy and the incident angle, as well as on the sample temperature and the polymer chemistry. The rate was determined using three measuring methods (XPS, QCM and “Step”) described in Section 5.4.

Before presenting the first results, the terminology used in the text should be introduced. The term “sputter rate” will be used in the text instead of sputter yield, for the reasons given in Section 5.4. The removal rate will be used as a synonym for the sputter (or sputtering) rate. The term of ablation rate is used in the cases where the sample temperature is involved in the experiments.

The *differential rate* (*dSR*) that is defined as the ratio between the change in the thickness Δd obtained in a time interval Δt_s and the time interval Δt_s, ($\Delta d/\Delta t_s$). The rates were

obtained using different methods and sputtering conditions, which complicates the comparison of the data. Therefore, all rate results were normalized to the ion current density, j':

$$dSR = \frac{\Delta d}{\Delta t_s} \frac{1}{j'} \tag{6.1}$$

where, j' is the ion current density, $j' = j/A_F$, where j is ion current (in A), A_F is the aperture area (in cm^2) of a Faraday cup. When the ratio of the total amount of removed thickness and the total sputter time is normalized to the ion current density, the term of *total rate* (Equation 5.4) is used. The difference between *dSR* and total *SR* is that the first term shows the results that may be obtained at intervals of the whole sputtering process, while the total rate gives the final result after a defined bombardment time or ion fluence.

The sputter rate results for different polymers will be presented as a function of the ion fluence, the ion type, the projectile energy and the angle of incidence, as well as of the sample temperature and the polymer chemistry.

6.1.1 Sputter rate dependence on the ion fluence and the treatment gas

The method based on the quartz crystal microbalance (Section 5.4.3) gives the possibility to measure the real time removal rate and to study the kinetics of sputtering. With the QCM the sputter time t_s, the removed thickness d, and the total sputter rate d/t_s were recorded every 3 to 15 seconds. In order to obtain the differential rate, the derivative was taken by averaging the slopes of two adjacent data points:

$$\frac{\Delta y}{\Delta x} = \frac{1}{2}\left(\frac{y_{i+1} - y_i}{x_{i+1} - x_i} + \frac{y_i - y_{i-1}}{x_i - x_{i-1}} \right) \tag{6.2}$$

where y was taken as the recorded film thickness d, and x was the time t_s. Figure 6.2 shows an example for the derivative calculation for PS. Figure 6.2(a) gives the dependence of the removed thickness on the sputter time. The plot of $\Delta d/\Delta t_s$ vs. t_s in Figure 6.2(b) presents the derivative of the curve shown in the left, where the ratio $\Delta d/\Delta t_s$ is the differential sputter rate.

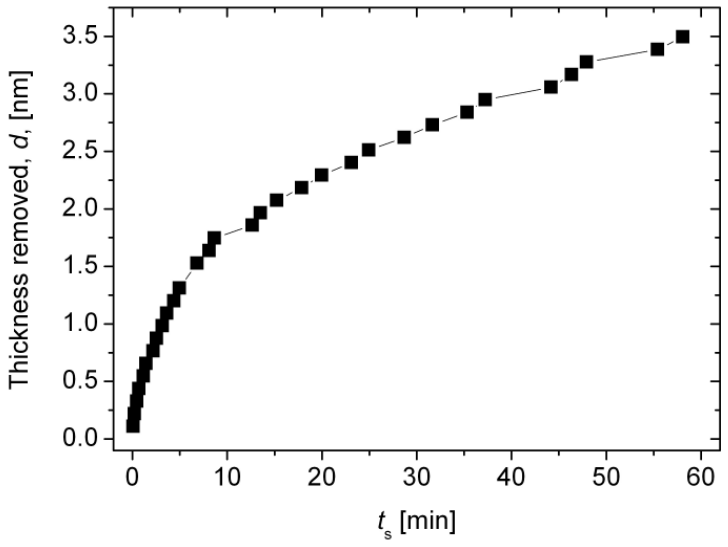

a)

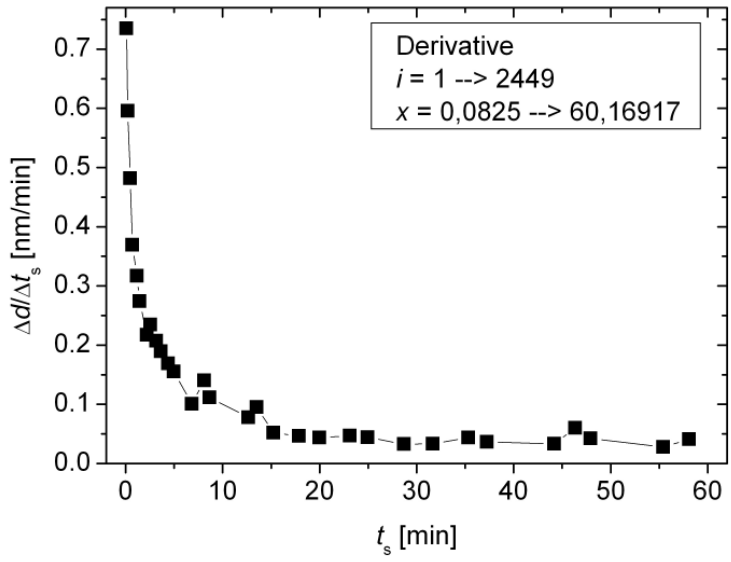

b)

Figure 6.2 *Derivative calculation example for PS treated with Ar^+ ions at energy of 1 keV. a) Dependence of the removed thickness dependence on the. sputter time. b) The derivative was obtained by averaging the slopes of two adjacent data points of the graph shown in the left. The ration $\Delta d/\Delta t_s$ is the differential sputter rate.*

The thickness of the removed film, the differential and the total sputter rates vs. the ion fluence for PS are given in the Figure 6.3. In each figure, the dependence on the treatment

gas is shown. The results shown in the figure are obtained for the IonEtch sputter gun (Tectra) using ions with an energy of 1 keV at an angle of incidence being normal to the sample surface. PS is sputtered fast at the beginning of the sputtering in the time region of 70 to 90 s at an ion current of 1.6 μA which corresponds to an ion fluence of $1 \times 10^{15} - 3 \times 10^{15}$ cm^{-2}. Polymer removal rate at prolonged ion radiation becomes constant.

Polymer sputtering with oxygen ions takes place much faster compared to nitrogen and argon ions. During the bombardment with oxygen ions ~ 40 nm of PS film were sputtered, while only ~ 11 nm and 5 nm were removed by treatment with nitrogen and argon gas, respectively, for the given final ion fluences, Figure 6.3(a). Therefore, the final sputter rate for O_2^+ ions is higher by a factor of five, Figure 6.3(b) and (c). Little difference was observed in the sputter rate for argon and nitrogen ion irradiation. PS sputters faster during the bombardments with nitrogen only at the beginning. Later, the values for the final rate (total *SR* and *dSR*) for argon and nitrogen ion bombardment are close to one another.

The tendency for the total and the differential sputter rate is the same, with the exception of the degradation behaviour under oxygen bombardment. For the latter case, calculated *dSR* values show a sharp minimum at an ion fluence of about 10^{15} cm^{-2} (Figure 6.3(b)). It should be noted, that such behaviour of the differential sputter rate was observed only for PS under the irradiation with 1 keV oxygen ions.

Below, the removed thickness, the differential and total sputter rates of PαMS and PMMA are given as a function of the ion fluence at ion energy of 1 keV with different ions using the IonEtch sputter gun (Tectra), Figure 6.4. On the left hand side, results for PαMS are shown (Figure 6.4(a, b, c)), and on the right for PMMA (Figure 6.4(d, e, f)). For both polymers the tendency of the sputter rate is the same as for PS. Sputtering with oxygen causes the polymers to be sputtered several times faster that under the influence of argon or nitrogen. Removal rates for Ar^+ and N_2^+ differ only at the beginning of sputtering, while at the end the rates are similar.

In Figure 6.5 the rates of the three polymers (PS, PαMS and PMMA) obtained for irradiation with different ions are compared. In Table 6.1, the results for the total sputter rate of three polymers at defined ion fluencies and for different treatment gases are summarized. PMMA has the fastest sputter rate under the bombardment of any gas. Styrene polymers show similar removal rates for Ar and N_2 ions with slightly higher rates for PαMS. During treatment with oxygen ions, the initial sputter rate for PS is two times lower compared to the rate of PαMS, but at the end they become similar.

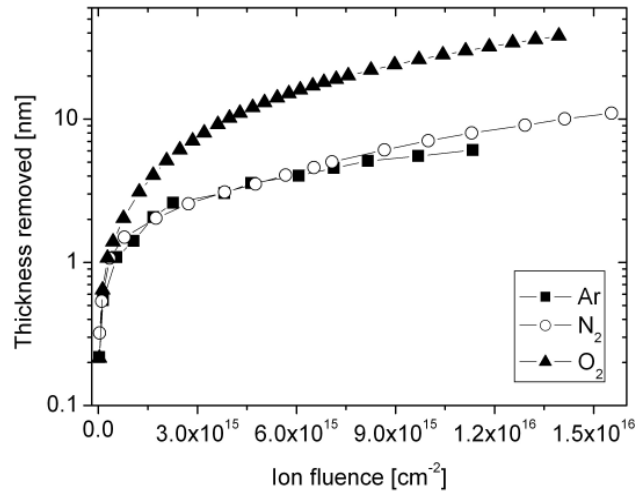

a)

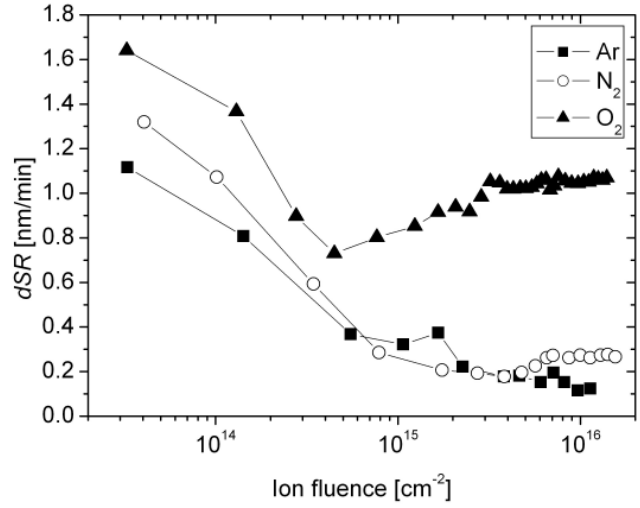

b)

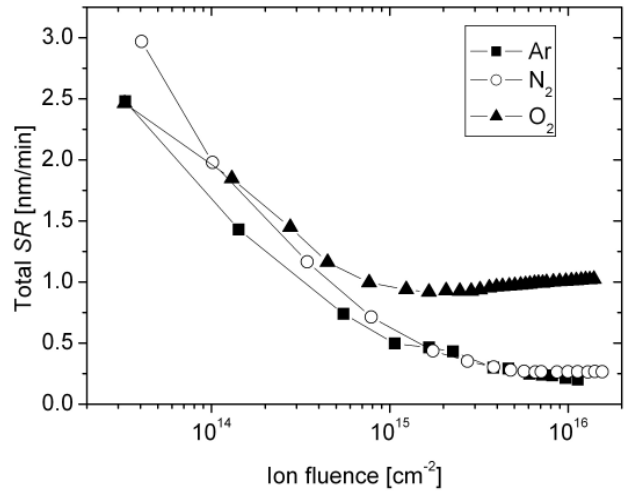

c)

Figure 6.3 *a) Removed thickness, b) differential sputter rate dSR, and c) total SR vs. ion fluence for* ***PS*** *treated with 1 keV Ar^+, N_2^+ and O_2^+ ions, the ion current ~1.6 μA.*

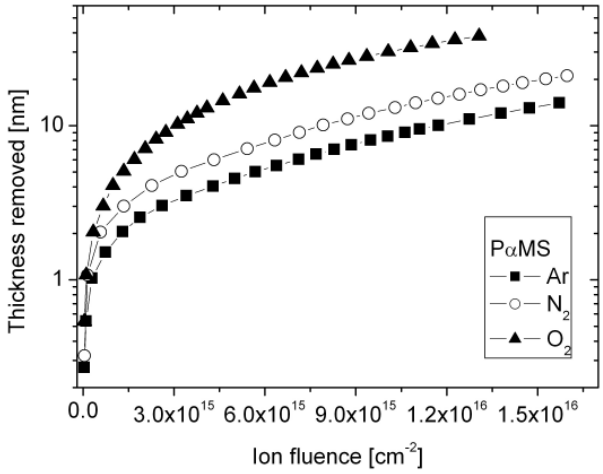

a)

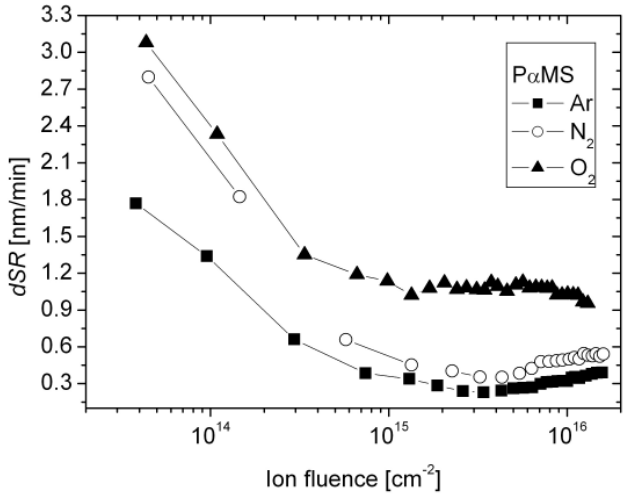

b)

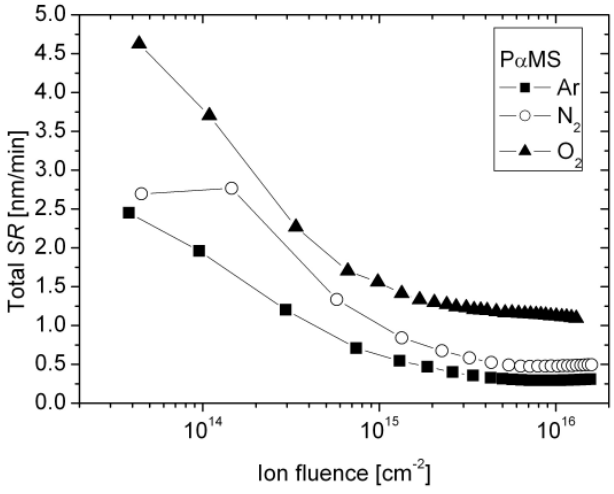

c)

Figure 6.4

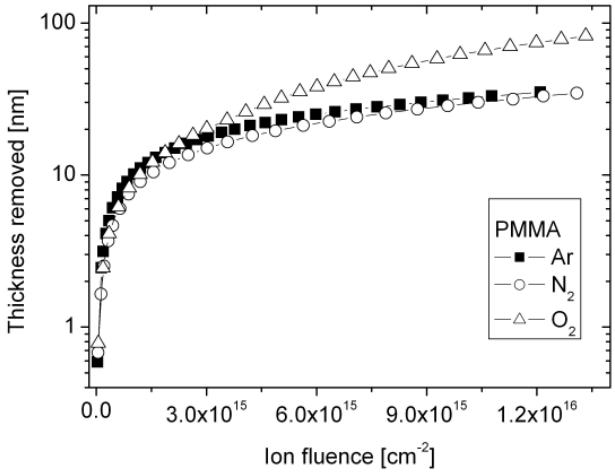

d)

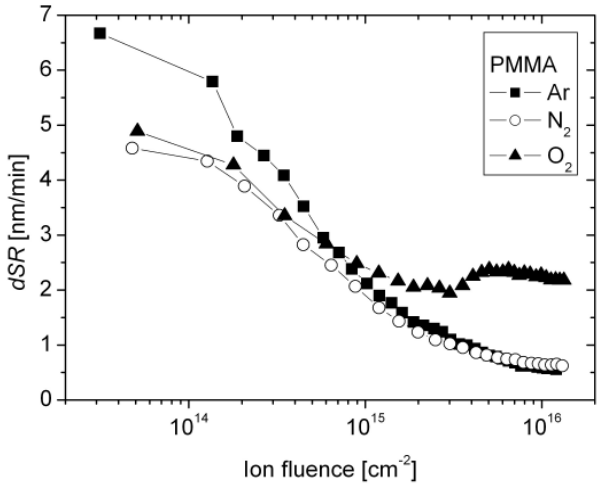

e)

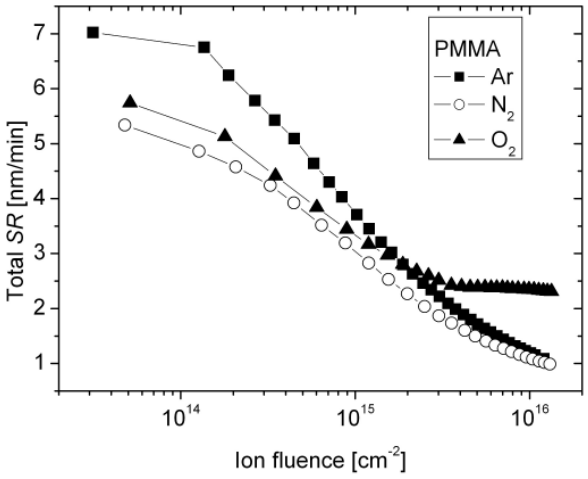

f)

Figure 6.4 (continued) *a), d) Removed thickness, b), e) differential sputter rate dSR, and c), f) total sputter rate, SR, vs. ion fluence for* ***PαMS*** *(a, b, c) and* ***PMMA*** *(d, e, f) treated with 1 keV Ar^+, N_2^+ and O_2^+ ions, the ion current ~1.6 μA.*

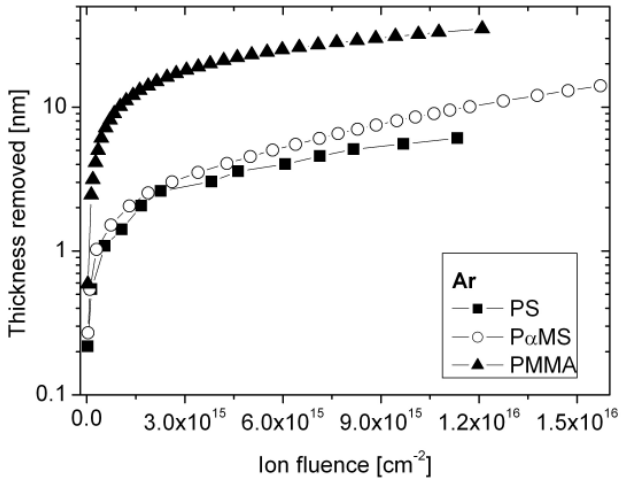

a)

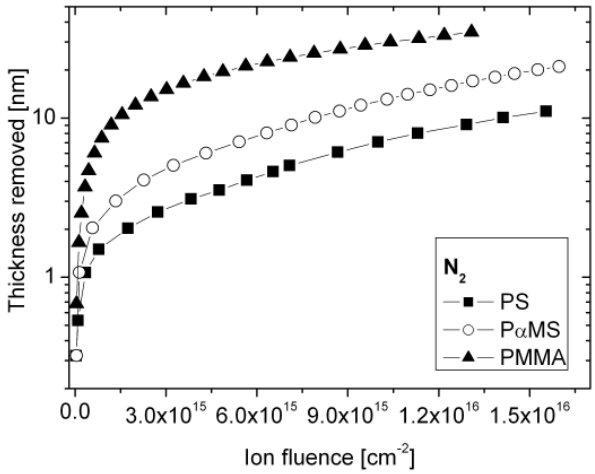

c)

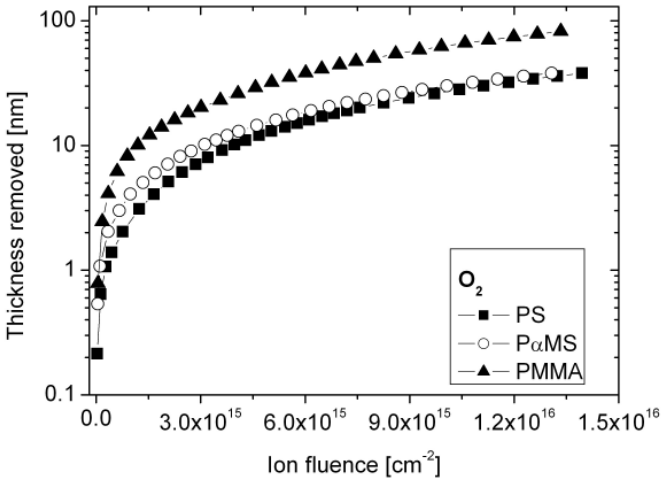

e)

Figure 6.5

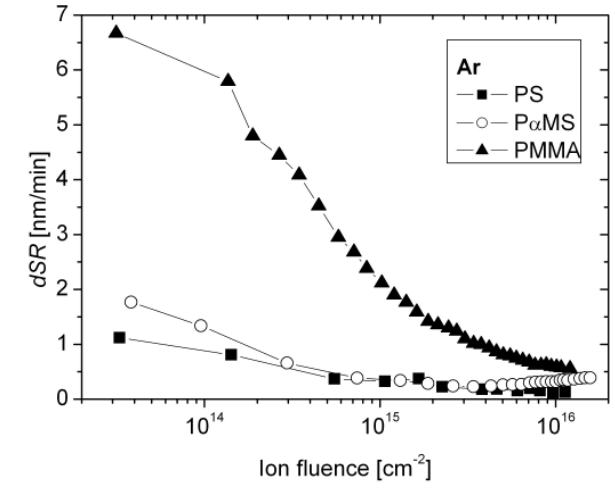

b)

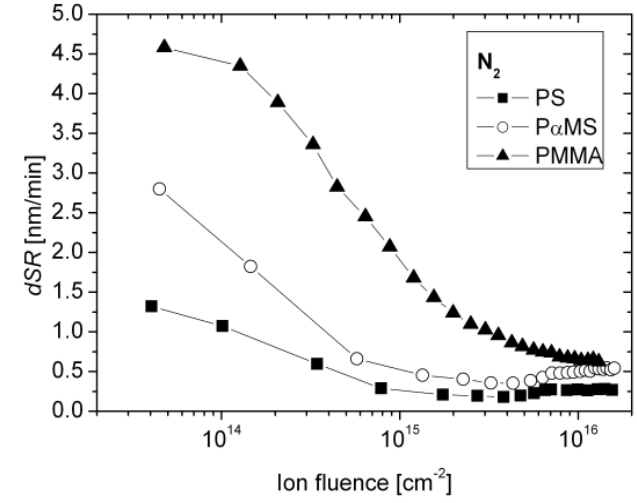

d)

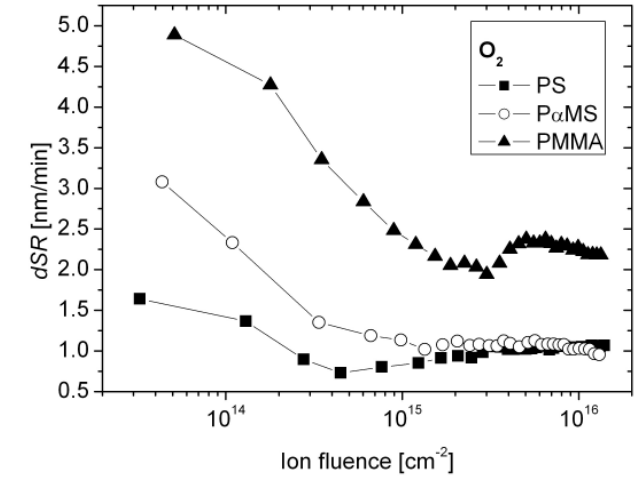

f)

Figure 6.5 (continued) *a), c), e) Removed thickness, b), d), f) differential sputter rate, dSR, vs. ion fluence for* ***PS***, ***PαMS*** *and* ***PMMA*** *treated with Ar^+ (a, b), N_2^+ (c, d) and O_2^+ (e, f) ions, the ion current ~1.6 μA.*

Table 6.1 *Total sputter rates (in nm/min) of PS, PαMS and PMMA after the bombardment with different ions. Rate results are given for a fixed ion fluence.*

Ions	PS	PαMS	PMMA	Ion fluence, cm^{-2}
	1.430	1.959	6.751	10^{14}
Ar^+	0.495	0.543	3.704	10^{15}
	0.201	0.296	1.086	10^{16}
	1.980	2.765	4.862	10^{14}
N_2^+	0.436	0.840	2.829	10^{15}
	0.266	0.481	1.017	10^{16}
	1.846	3.70	5.126	10^{14}
O_2^+	0.938	1.411	3.166	10^{15}
	1.012	1.108	2.315	10^{16}

Differential sputter rate measurements were also obtained using XPS (Section 5.4.2). Figure 6.6(a) shows the *dSR* as a function of the ion fluence for PS, PαMS and PMMA. All three polymer films (~ 10 -12 nm in thickness) were bombarded at room temperature with 1 keV Ar^+ ions in the preparation chamber. The angle of incidence was 36° off the sample surface normal. The tendency of the polymer removal rate is the same as observed with the QCM: the rate decreases rapidly up to an ion fluence of $10^{14} – 10^{15}$ cm^{-2} (depending on the polymer), afterwards the polymer removal rate is constant. Again, PMMA shows the highest rate at the beginning of sputtering. Note, that an ion fluence of 5×10^{15} cm^{-2} is the limit in these measurements for polymethylmethacrylate because further sputtering completely removed the polymer leaving the pure Si wafer. The difference in the rate for PS and PαMS is only observed in the beginning of the bombardment, later, in the constant ablation regime, the differential rate is almost the same for these two polymers.

The total rate was determined by taking the defined integral from a baseline of zero using the trapezoidal rule. Figure 6.6(b) shows an example of the integral calculation for PS. The insert in the right corner gives the integral parameters, where *i* is the number of measuring points, *x* is the limit of integration, and *A* is the total integral area. The removal rate was calculated by dividing the area by the total ion fluence. The total sputter rates of PS and PαMS at an ion fluence of $10^{16}cm^{-2}$ are 0.2 and 0.3 nm/min, respectively. PMMA is sputtered

with a rate of 2.0 nm/min at an ion fluence of 5×10^{15} cm^{-2}. These data agree well with those obtained by the QCM (Table 6.1, Figures 6.3, 6.4).

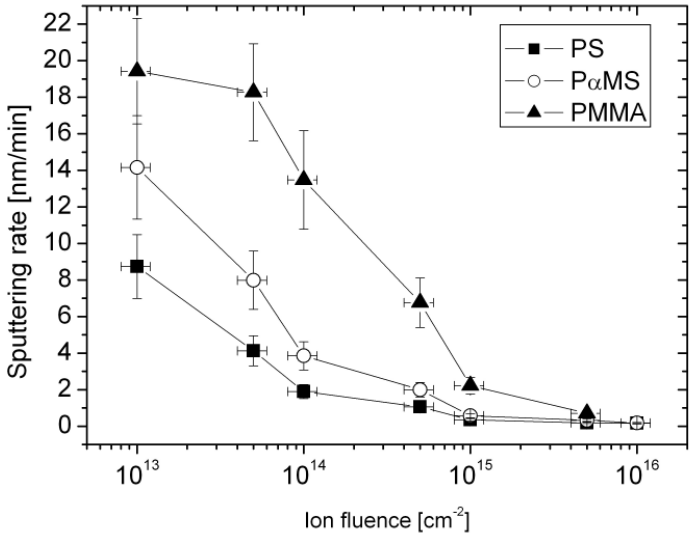

a)

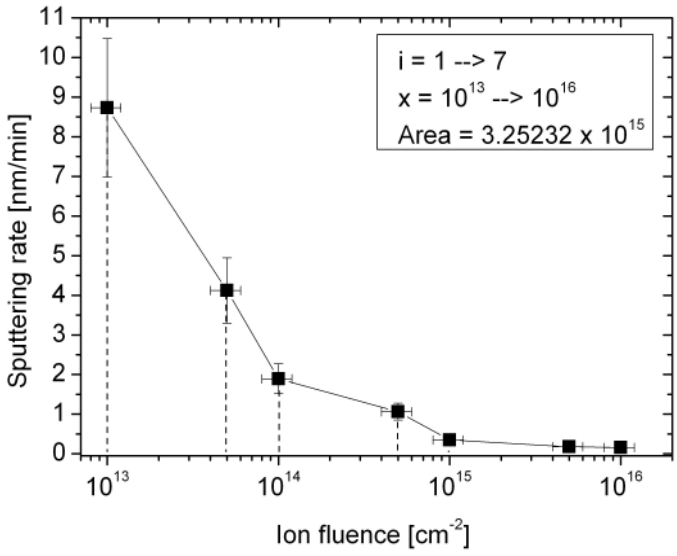

b)

Figure 6.6 *a) Differential sputtering rate of PS, PαMS and PMMA vs. Ar^+ ion fluence. b) Integral calculation for PS (i - the number of measuring points, x – the limit of integration, A – total integral area).*

6.1.2 Artefacts related with the region of decreased sputter rate

The sputter rates of different polymer films determined with XPS and QCM showed the same behaviour. The rates decreased drastically at the beginning of the ion bombardment until steady state sputtering was reached. The decrease in the rate can be attributed to several reasons: (i) the steady-state sputtering takes place in the substrate, and the decrease in the rate occurred due to the complete removal of the polymer film; (ii) an adsorption layer forms on top of the polymer film leading to the decay during the ion bombardment; (iii) major chemical changes in the polymer occur in the low ion fluence region causing the change in the rate.

In the case of the sputter rate measurements using the XPS method, the prepared polymer films were very thin (~ 10 - 12 nm). With increasing ion fluence, the intensity of the carbon C1s line decreased showing that the polymer film thickness decreased, and that the substrate, a Si wafer, was approached as the intensity of the Si2p line increased. In contrast to this, the polymer films prepared on the quartz crystals were of 100 - 200 nm in thickness. During the ion sputtering, the films were reduced by 5 – 80 nm, depending on the ion energy and chemistry as well as the polymer itself. The remaining film still covered the quartz crystal even if the sputter rate decreased in the ion fluence region of 10^{12} to 10^{15} cm^{-2}. Taking this into account, the observed trend is not due to a transition from sputtering of the polymer sputtering of the substrate (Si wafers or gold quartz crystals).

An influence of the absorbed species on the polymer surfaces on the sputter rate of the organic films cannot be excluded, as the samples were removed from the furnace and transferred into the preparation chamber after annealing. If this is the case, then the observed trend in the removal rate might be the transition from the contamination layer to the polymer film. In order to understand the influence of the contamination layer on the polymer sputter rate, films were sputtered in two steps. An example for PMMA bombarded with argon and nitrogen ions is shown in Figure 6.7. During the first sputtering treatment the sputter rate decreases up to an ion fluence of about 4×10^{15} cm^{-2}, followed by the constant polymer removal. After the first sputtering treatment, the modified PMMA film was exposed to air for at least 1 hour. During this time surface oxidation and contamination took place. Afterwards, the same sample was sputtered a second time. This time, the rate reaches the value, measured in the steady-state region of the first sputtering treatment, at an ion fluence of 10^{13} cm^{-2}, as marked with the dashed line in the figure.

The two-step sputter procedure was repeated for the other polymers. In all cases, the absorbed layer was removed till the ion fluence given above. Even if the contaminants are removed till an ion fluence of 10^{13} cm^{-2}, the sputter rate of pure organic films still decrease up

to ion fluences of 5×10^{14} - 5×10^{15} cm^{-2}, showing that other processes than removal of absorbed species take place.

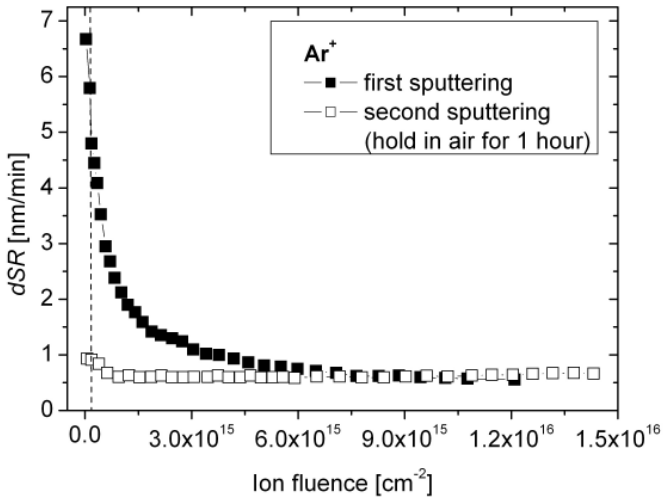

a)

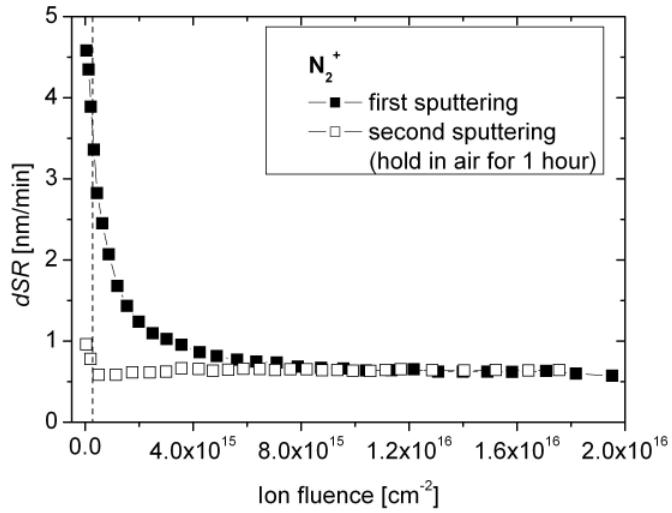

b)

Figure 6.7 *Two-step sputtering of PMMA with (a) argon and (b) nitrogen ions was used to measure the influence of the adsorption layer on the polymer sputter rate. The dashed line indicates the ion fluence of* 10^{13} cm^{-2} *at which the contamination layer is removed.*

A large influence of the adsorbed species is excluded also by the rate measurements using the X-ray photoelectron spectroscopy method which has several advantages. Firstly, the polymer samples were annealed under UHV conditions for several hours in order to remove the rest of the solvent and the adsorbed species before performing the measurements. Sputtering followed by spectra acquisition was done without removing films the films from the chamber and exposing them to atmosphere, thereby avoiding new contamination. Secondly, the XPS spectra showing the chemical composition of the polymer were recorded together with the change in the film thickness. It was noted that major changes in the polymer surface chemistry were induced in the ion fluence region where the decrease in the rate was recorded. From these observations, it can be concluded that chemical changes occurring up to a fluence of 10^{15} cm^{-2} should be one of the most important reasons leading to the drastic decrease in the sputter rate. Results for surface modification are presented in Section 6.2, where structural alterations will be given as a function of the ion fluence.

6.1.3 Rate dependence on ion energy and incident angle

The dependence of the sputter rate and the removed thickness on the ion energy is given in Figure 6.8. Figure 6.8(a) shows the total rate obtained during the bombardment with Ar^+ ions at energies of 1 and 3 keV with ISE 10 ion gun using the QCM balance method. With increasing projectile energy, the polymer thickness decreases faster resulting in larger rates under bombardment with high energy ions.

The tendency of the sputter rate for different ion energies remains the same, i.e. the removal rate decreases up to a particular ion fluence followed by a constant rate. It was observed, that the steady state region is shifted to higher fluences for higher projectile energies. Figure 6.8(b) shows the total *SR* for PS, PαMS and PMMA as a function of the energy obtained at constant an ion fluence of 4×10^{15} cm^{-2}. In the energy region from 0.5 to 5 keV, the sputter rates of the different polymers increase. PMMA is removed with the fastest rate. PαMS is sputtered with a rate similar to PS at the lowest energies (0.5 and 1 keV), and only at higher energies the difference in the rate of these two polymers increases.

According to the practical observations of the sputter yields of metals, the maximum yield was observed at angles near 50° to 75° [Berisch 81]. This could be also valid for polymers because of the increased probability for particles to escape for off-normal incidence. Comparing the *dSR* results obtained by the QCM and XPS, it is found that a difference in the sputter rates is observed at the beginning of ion sputtering (Figure 6.9(a)). The removal rate is higher under the bombardment at an angle of incidence of 36° off the sample surface normal.

In the constant sputter region, the angle of incidence has no influence on the removal rate. The difference in the sputter rates at low ion fluences can be caused by the projectile's angle of incidence. On the other hand, sputter rate determination methods like the QCM and XPS are rather different. Therefore, the rate dependence on the angle of incidence was done using one method at a constant ion fluence.

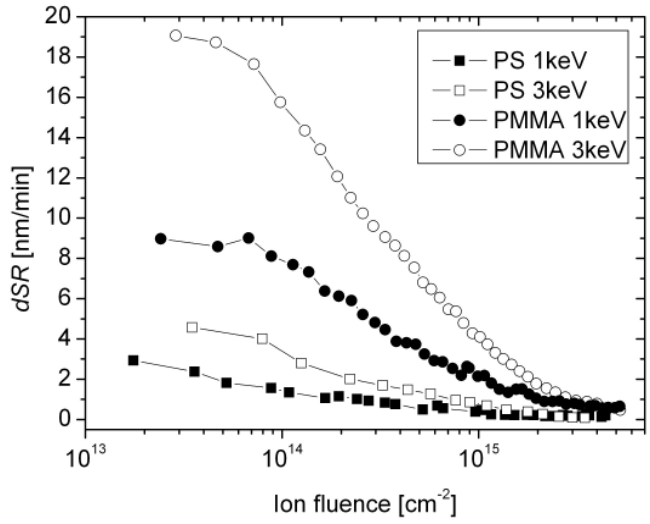

a)

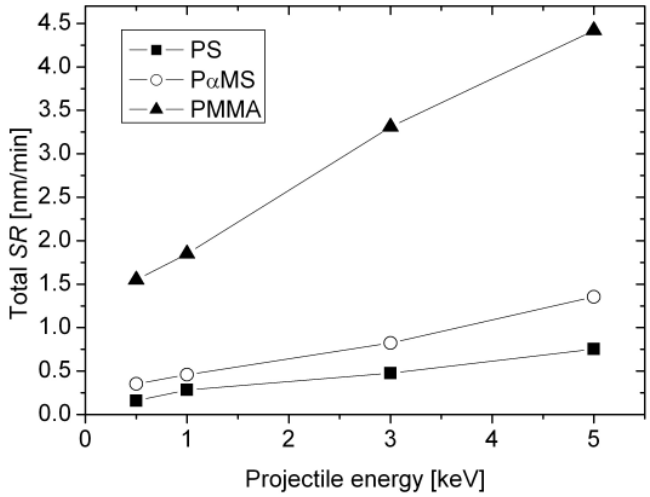

b)

Figure 6.8 *a) Total sputter rate (SR) vs. ion fluence as a function of the ion energy for PS and PMMA. Solid squares present the polymer rate received during the bombardment with* Ar^+ *ions with an energy of 1 keV, open squares – 3 keV. b) Sputter rates of different polymers as a function of the projectile energy at a constant ion fluence of* 4×10^{15} cm^{-2}.

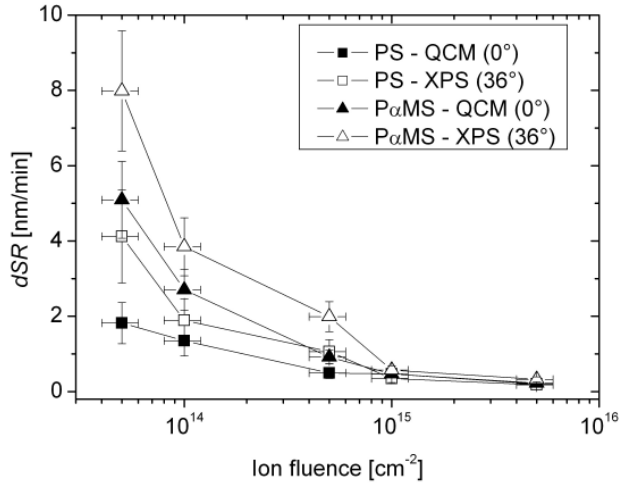

a)

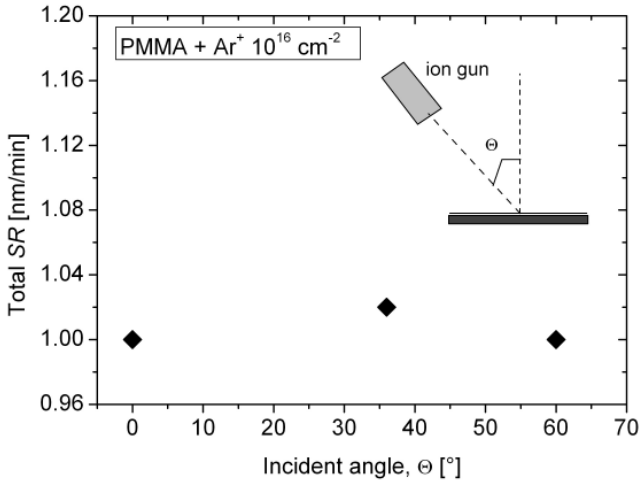

b)

Figure 6.9 *a) Differential sputter rates (dSR) of PS, and PαMS vs. ion fluence for two angles of incidence (0° and 36°). Rates at an angle of 0° were measured with the QCM, 36° off-normal – XPS. b) The total sputter rate of PMMA as a function of the incident angle of the ions for an argon ion fluence of* 10^{16} *cm*$^{-2}$*. The insert in the graph schematically presents the angle of incidence.*

PMMA was sputtered with 1 keV Ar^+ ions at an ion fluence of 10^{16} cm^{-2} with a projectile angle of incidence 0°, 36° and 60° off the sample surface normal. In all three cases, the ion bombardment time and ion current were kept constant which resulted in an ion fluence equal to 10^{16} cm^{-2}. The removed thickness was measured with a stylus profilometer ("step"

method, Section 5.4.1). The change in polymer thickness was the same for all three angles, 30 ± 2 nm, therefore the calculated total *SR* for this ion fluence and incidence angles of 0°, 36° and 60° was the same, ~ 1 nm/min, Figure 6.9(b).

6.1.4 Sputtering rate vs. sample temperature

In order to understand the mechanisms that take place in polymers during the ion bombardment it was necessary to determine the dependence of the removal rate on the substrate temperature (measurements are described in Section 5.4.4). The polymers were sputtered with argon ions with an energy of 1 keV at an angle of incidence of 36° off the surface normal using the ISE 10 ion gun. The thickness of the removed polymer was measured with the profilometer and the rate was calculated using Equation 5.4. The results for the determined ablation rate of PS and PαMS are given in Figure 6.10. The sputter rate of polystyrene remains constant with increasing temperature for a large temperature range and an increase was observed beginning at $T = 437$ K. The sputter rate of PαMS steadily increases with increasing temperature. In both cases, the increase in the ablation rate starts at temperatures much lower than the thermal degradation temperatures of these polymers. For PS, thermal degradation sets in around 573 K, and for PαMS volatile product evolution begins at 523 K [McNeill 89] (thermal degradation temperatures were determined by pyrolysis).

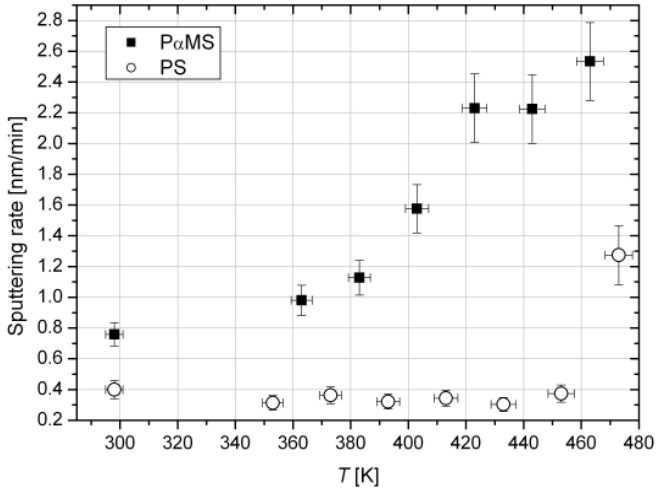

Figure 6.10 *Sputtering rate dependence on the sample temperature. The rate measurements were done at Ar^+ ion fluences of $9.2 \times 10^{15} \pm 2 \times 10^{15}$ cm^{-2} for PS, and $5 \times 10^{15} \pm 2 \times 10^{15}$ cm^{-2} for PαMS.*

During sputtering, mass spectra were recorded as a function of time at defined temperatures with a quadrupole mass spectrometer. The technique allowed to record the sputtered polymer species and to observe the change in the number of these species as a function of the ion fluence. Figure 6.11 shows the influence of the Ar^+ ion fluence on the intensity of removed molecules with masses of 51 m/e (C_4H_3) and 77 m/e (C_6H_5 – phenyl ring). These are characteristic masses for PS and PαMS polymers [Briggs 82].

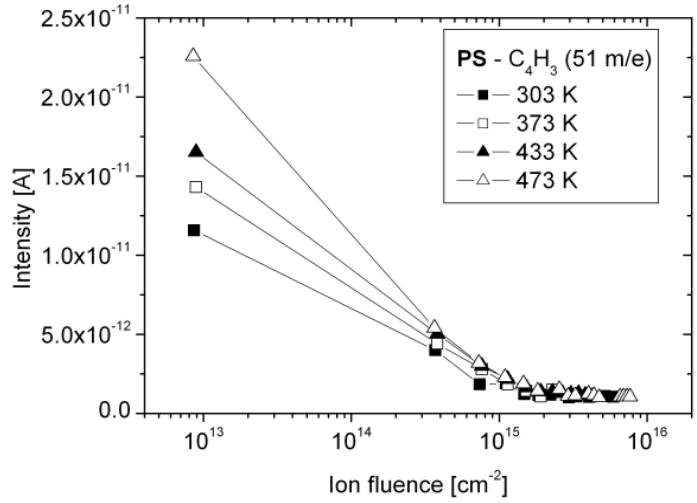

a)

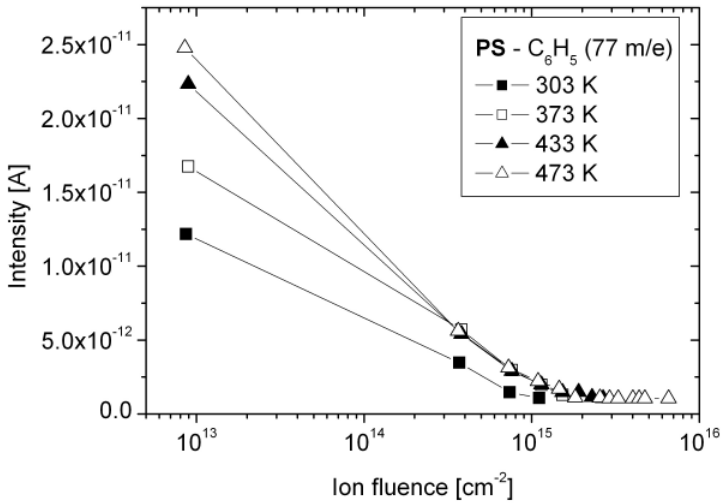

b)

Figure 6.11

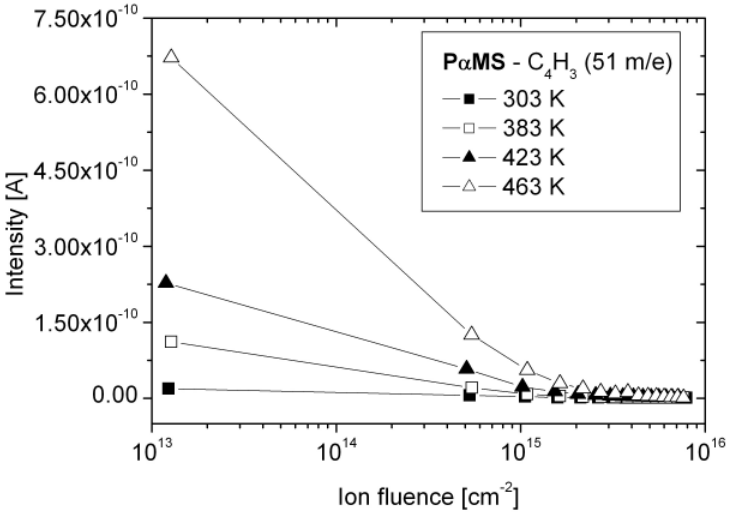

c)

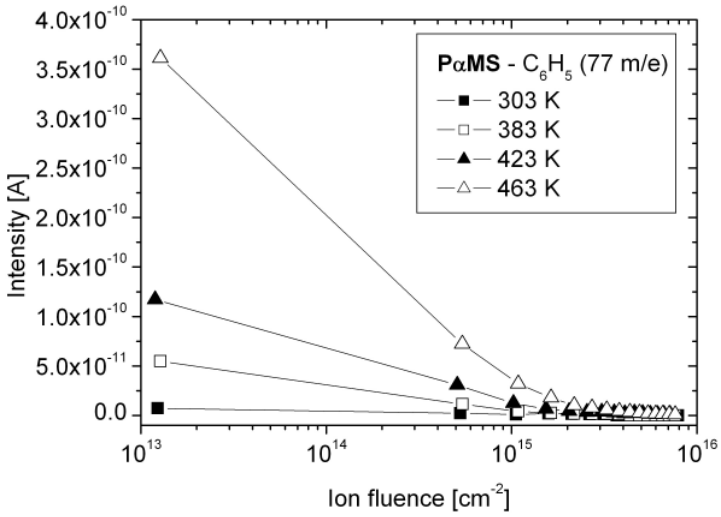

d)

Figure 6.11 (continued) *Change in intensity of 51 m/e (a, c) and 77 m/e (b, d) for PS and PαMS as a function of the* Ar^+ *ion fluence for defined sample temperatures.*

Species with masses of 51 m/e and 77 m/e, as well as other recorded with the spectrometer (not shown here), decrease with increasing ion fluence for all sample temperatures. On the other hand, the intensity of sputtered molecules increases with the increasing temperature at the beginning of the polymer irradiation. This enhancement is very distinct for PαMS and is less pronounced for PS (note: given polymers do not thermally degrade at the temperatures given in the Figure 6.11, and the mass dependence on the ion fluence is only because of the sputtering, with exception of the mass 51 m/e (C_4H_3) at T = 463 K for PαMS). In the case of poly-α-methylstyrene, the C_4H_3 molecule, was already detected

at T = 453 K when the PαMS sample was heated only without sputtering. Therefore, the current intensity of this particular fragment at T = 463 K was normalized to the intensity of this mass that was recorded before the ion bombardment.

Figure 6.12 compares the results of two masses vs. heating temperature at a defined ion fluences. Figures (a) and (b) present data obtained for PS and PαMS, respectively. In these graphs, the results are compared with those received when sample was only heated (open and solid squares, respectively). During the heating (without ion beam sputtering), first volatile species were recorded above 473 K for PS, while PαMS starts to decompose above 443 K. It was observed, that the characteristic masses for polystyrene, in contrast to PαMS, have a maximum intensity at about 550 K followed by a decrease at high temperatures.

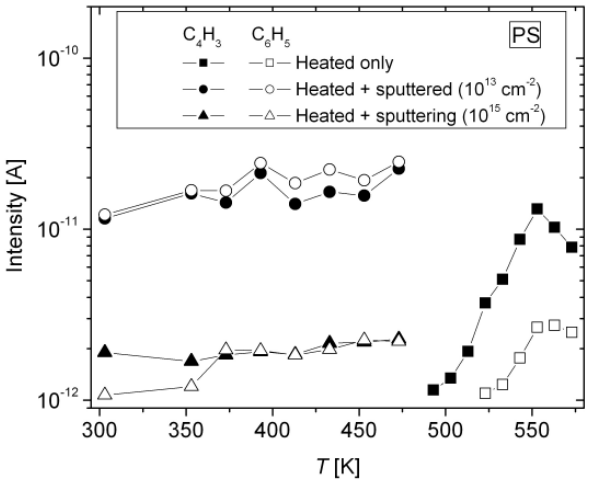

a)

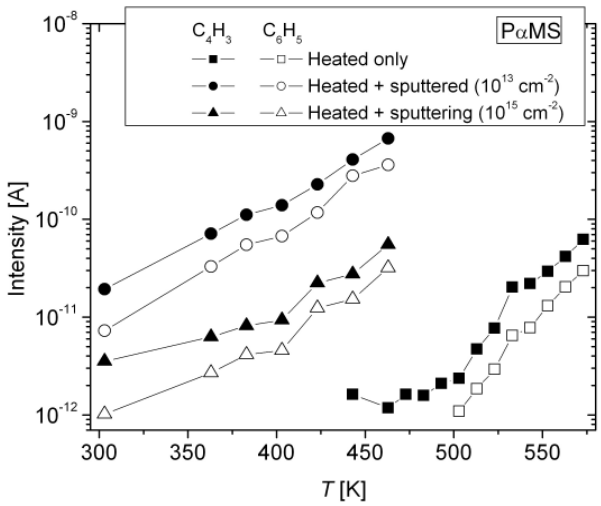

b)

Figure 6.12

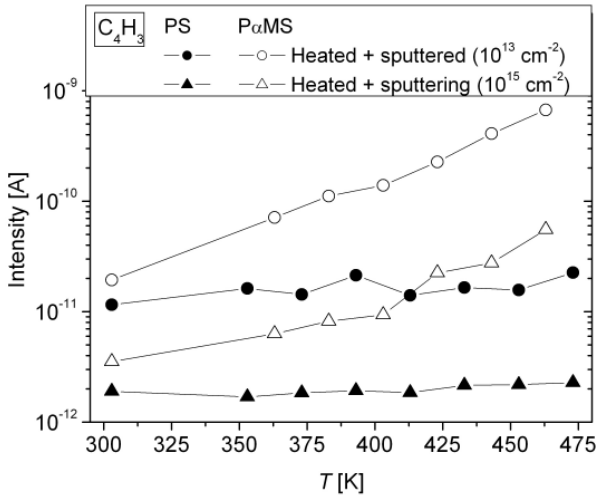

c)

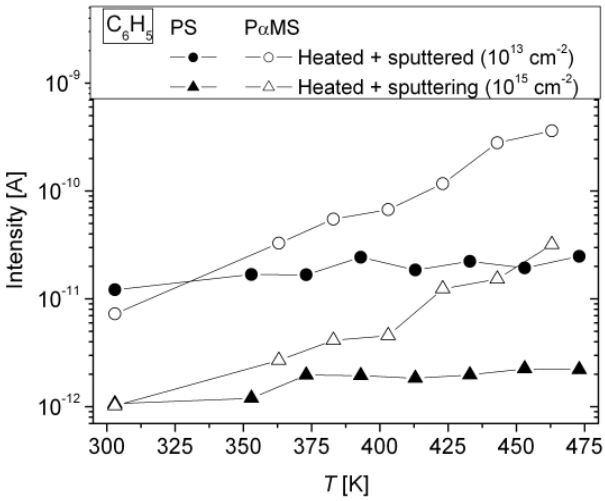

d)

Figure 6.12 (continued) *The dependence of number/intensity of the sputtered molecules with masses of 51 m/e and 77m/e on sample temperature at fixed ion fluences for (a) PS and (b) PαMS. Solid and open squares represent the intensities of these molecules recorded during heating only. (c) C_4H_3 and (d) C_6H_5 molecule intensities vs. sample temperature at two ion fluences for PS and PαMS.*

For both polymers degradation can be shifted to lower temperatures if ion irradiation is applied. The intensities of the C_4H_3 and C_6H_5 molecules increase with temperature under ion bombardment at an ion fluence of 10^{13} cm^{-2}. In the constant sputtering regime at an ion fluence of 10^{15} cm^{-2}, the intensities are lower compared to the first seconds of ion irradiation, but still higher than those obtained by pure thermal degradation. Figure 6.12 (c) and (d)

compares the intensities of the C_4H_3 and C_6H_5 species, respectively, as a function of temperature for PS and PαMS at fixed Ar^+ ion fluences. When PαMS is bombarded at high temperatures the total amount of ejected molecules from the polymer increases with the ion fluence, while for PS the intensity of emitted species remains almost constant in the whole experimental temperature range.

6.1.5 Sputter rate dependence on polymer chemistry

The above results were mostly given only for three polymers: PS, PαMS and PMMA. Figure 6.13 shows the thickness and total rate vs. ion fluence for three additional polymers obtained for 1 keV Ar^+ ion bombardment. The polymers listed in the figure have very similar chemical structures and differ only by one additional group. These polymers can by grouped as follows: PS and PαMS; PAN and PMAN; PMA and PMMA. The difference between these paired organic materials is that the second mentioned polymer in the pair contains an additional methyl group, (chemical structures are shown in Table 5.1, Section 5.1.1). Methyl containing polymers (in the figure represented by open symbols) sputter faster than polymers that have no such group in their chemical formula. An exception is the pair of acrylates (PMA and PMMA). Both polymers approach the same final sputter rate of ~ 1.5 nm/min at an ion fluence of 5×10^{15} cm^{-2}.

More sputter rate results for polymers containing oxygen, nitrogen, aromatic rings, fluorine, and pure hydrocarbons are given in Table 6.2. The rates were determined by the "step" method (Section 5.4.1) at a defined ion fluence. For this particular rate determination method, it is desirable to bombard material surfaces with relatively high fluences in order to obtain a sharp step between sputtered and unsputtered parts. For a sharp step, a better profile is obtained. Therefore the errors are small. Because of the long treatment times (large ion fluences), the rate is calculated in the constant sputtering region, giving no information as to what happens at the beginning of the ion bombardment.

The sputter rate dependence on the polymer chemistry shows that polymers containing aromatic rings (PS, PαMS, BPA-PC, PMDA-ODA and PBO) have the lowest removal rates. When polymer have oxygen or/and nitrogen groups (acrylates, acrylonitriles, nylon) their sputter rates increase by one order of magnitude. The exceptions in these cases are organic films that contain both polar groups and aromatic rings, like BPA-PC, PMDA-ODA and PBO. As mentioned above, such polymers are removed rather slowly. The reason is the property of the aromatic ring that acts as the energy sink, protecting the organic material from degradation. Polymers containing fluorine in their structure, such as PTFE, FEP and Teflon

AF, have very high sputtering rates. Here again, the exception is PBO with one of the slowest removal rates.

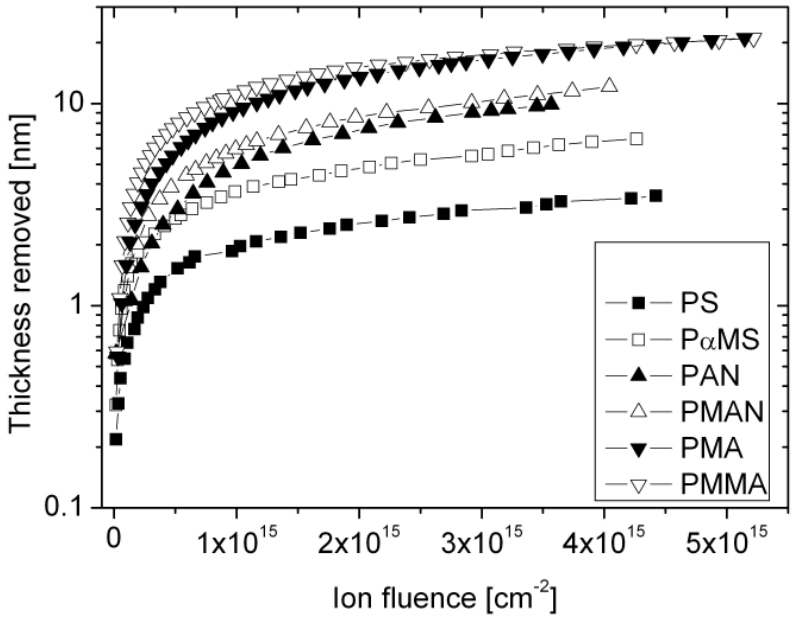

a)

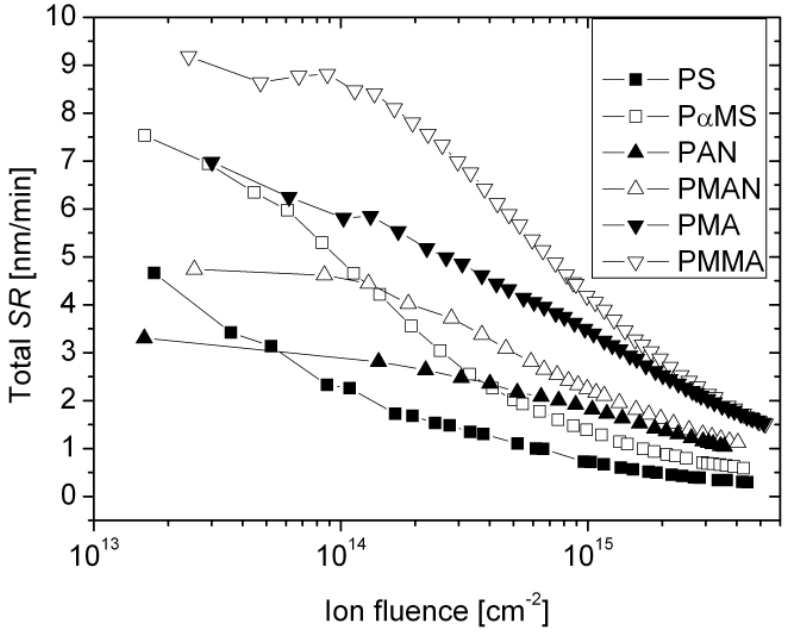

b)

Figure 6.13 *a) Removed thickness, and b) total sputter rate vs. ion fluence for different polymers. Results were obtained during the bombardment with 1 keV* Ar^+ *ions.*

Table 6.2 *Total sputtering rate (SR) of different polymers bombarded with 1 keV argon ions at a defined ion fluence (IF).*

Polymer	**Chemical structure**	***SR*, nm/min**	***IF*, cm^{-2}**
PS	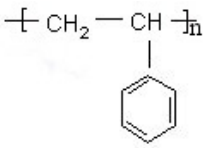	0.296	5×10^{15}
PaMS	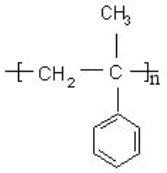	0.587	5×10^{15}
PAN	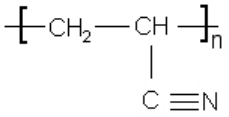	1.039	5×10^{15}
PMAN	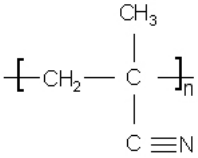	1.122	5×10^{15}
Nylon 11	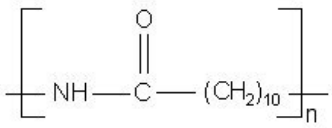	2.511	1×10^{16}
PMA	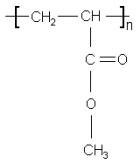	1.532	5×10^{15}
PMMA	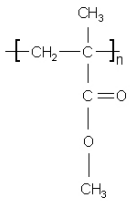	1.563	5×10^{15}
PIB	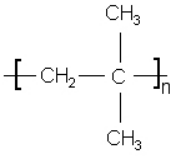	1.591	5×10^{15}

Table 6.2 *continued*

Polymer	Chemical structure	*SR*, nm/min	*IF*, cm^{-2}
BPA-PC	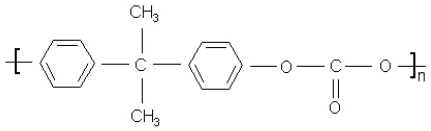	0.395	5×10^{15}
PMDA-ODA	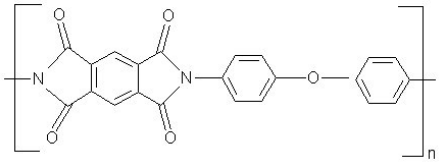	0.128	1×10^{16}
PBO [a]	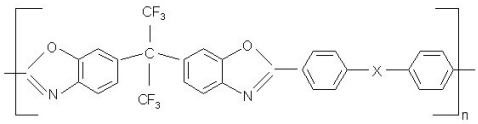	0.072	1×10^{16}
FEP	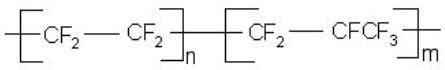	4.278	5×10^{15}
PTFE	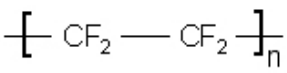	7.359	1×10^{15}
Teflon AF	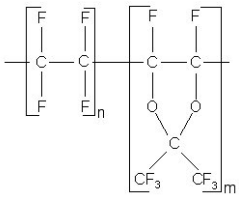	18.566	1×10^{15}

a) X in chemical formula was not given by the manufacturer.

In order to summarize the results of Section 6.1 several conclusions can be drawn:

1) The sputter rates of polymers depend on the ion fluence. The rates decrease up to a particular ion fluence followed by a steady-state sputtering region. This tendency is observed for every investigated polymer bombarded with different ion energies, gases and at different sample temperatures.

2) The decrease in the sputter rate is attributed to the induced chemical changes that occur exactly in the fluence range where the rate declines. Alterations in the polymer structure will be presented in the Section 6.2.

3) The more reactive the ions used are for polymer sputtering, the faster the polymers are removed. Oxygen being the most reactive gas (at least of the gases used in these experiments) leads to the highest polymer sputter rates compared with the rates obtained after bombardment with argon or nitrogen ions.

4) In the energy range from 0.5 to 5 keV sputter rates of the polymers increased.

5) No dependence of the sputter rate on the different incident angles of the projectiles at ion fluences above 10^{15} cm^{-2} was observed.

6) The ablation rate measurements at different sample temperatures showed different tendencies for different polymer types. The PS rates showed no influence on the increasing temperature, and only above 473 K the rate increased by one order of magnitude. PαMS, on the other hand, sputtered faster with increasing sample temperature. Mass spectrum analysis showed that the ion beam induced depolymerization at temperatures lower than for heating only.

7) Polymer sputter rates depend highly on the polymer chemistry itself. Organic films containing aromatic rings are sputtered with the lowest rates, while Teflon-like polymers (PTFE, FEP, Teflon AF) have the highest removal rates.

6.2 Alterations in chemical and physical properties of polymer surfaces under ion beam irradiation

Polymers either suffer main chain scissions when exposed to radiation leading to the formation of low molecular weight species which later can be sputtered, or different chemical reactions can occur because of formed free radicals leading to cross-linking, branching, and double bond formation. If a sample is treated with gases like oxygen or nitrogen, radicals reacting with the different species form new functional groups not present in the original/pristine polymer. Post-chemical reactions take place when treated polymer surfaces are subjected to atmosphere or other reactive environment because of the presence of long-lived free radicals. Incorporation of new functionalities may occur also due to treatment with inert gases like argon. This happens because of the post-chemical reactions with the residual gases (usually oxygen containing ones) in the treatment chamber. Formation of cross-link networks or increased concentration of low molecular weight species in one or another way changes the polymer properties. The influence of the both is perfectly reflected in the glass transition temperature measurements, which either increases or decreases depending on the preference of polymer to cross-link or degrade. The surface morphology and tension may also be changed during the ion bombardment. The increase in polymer surface roughness and energy may contribute to the improved adhesion of metals on polymers.

6.2.1 Changes in the polymer chemical structure

Alterations of chemical structure of polymers was studied after ion bombardments with Ar^+, O_2^+ and N_2^+ ions, as well as after the exposure of modified polymers to atmosphere. Depending on the treatment conditions, it was possible to incorporate oxygen or nitrogen containing functional groups. Figure 6.14 (a) and (b) show XPS survey spectra for PS and PMMA after different treatments performed using 1 keV ion irradiation at an ion fluence of 10^{16} cm^{-2}. Pure PS, which in its chemical structure contains only carbon and hydrogen, is free from other elements; however, it easily accepts oxygen and nitrogen, when this polymer is treated with O_2^+ or N_2^+, or if it is subjected to air after the argon modification, Figure 6.14(a). XPS analysis of PMMA shows that this polymer also reacts with nitrogen, when it is bombarded with N_2^+ ions. The oxygen peak (O1s) intensity indicates that during different treatments O_2 is removed from the polymer rather intensively, even when bombarded with O_2^+ ions, Figure 6.14(b).

Figures 6.14 (c) and (d) show the atomic weight concentrations (in %) of oxygen and nitrogen on modified PS and PMMA surfaces. The treatments were done Ar^+, N_2^+ and O_2^+

ions with an energy of 1 keV using the ISE 10 (Omicron) ion gun. The atomic concentrations were calculated using Equation 5.7 (Section 5.5.1) for a take-off angle of 0°. In all cases, saturation in incorporated or removed species is observed.

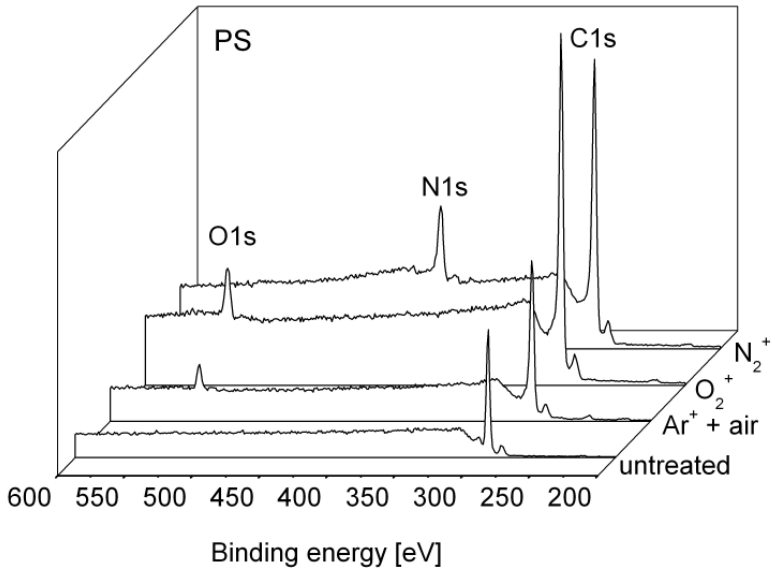

a)

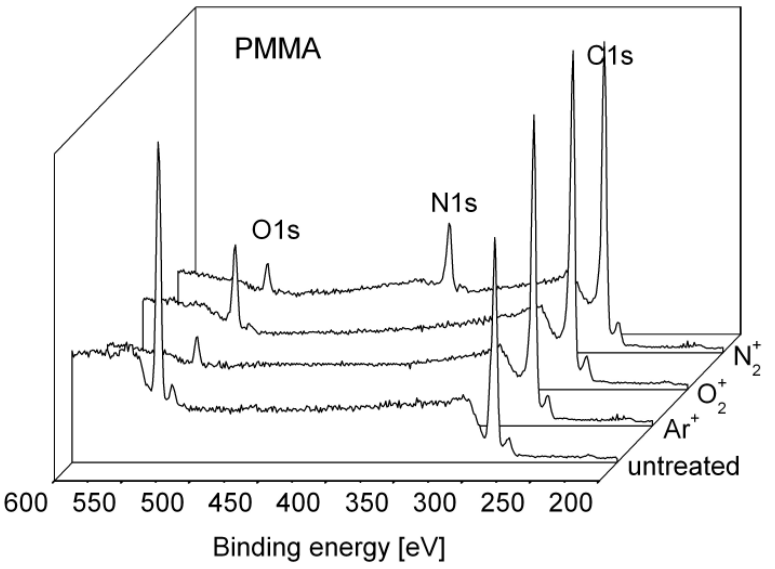

b)

Figure 6.14

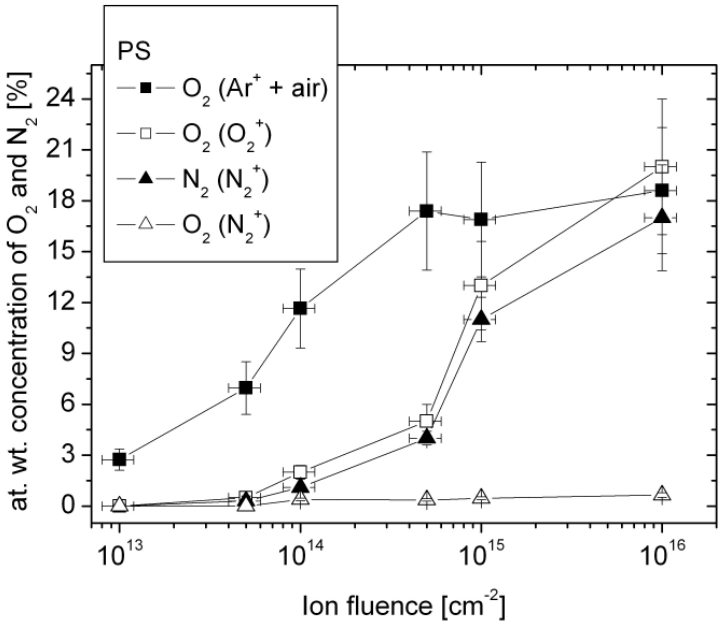

c)

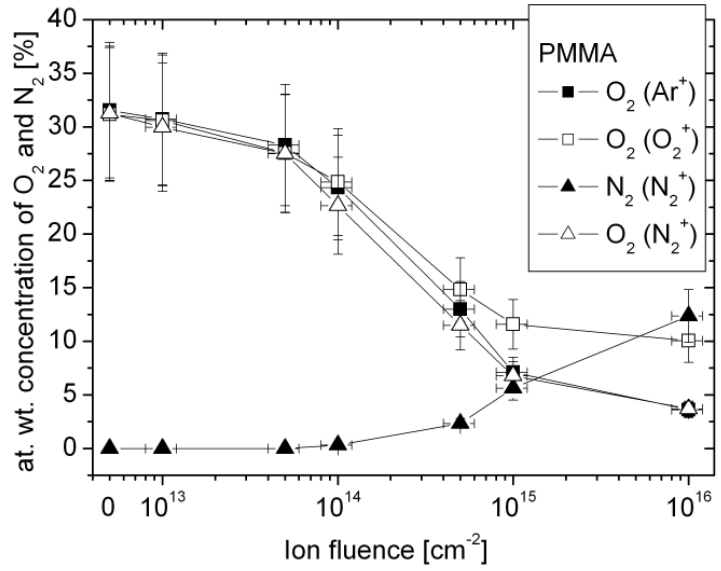

d)

Figure 6.14 (continued) *XPS survey spectra for (a) PS and (b) PMMA treated under different conditions. The atomic weight concentration of oxygen and nitrogen vs. ion fluence for (c) PS and (d) PMMA. The type of ions used is given in brackets. The data shown was obtained using the ISE 10 ion gun.*

Oxygen and nitrogen concentration in PS increases with the ion fluence. Treatment with argon gas only usually does not introduce additional functionalities, if the ion bombardment was performed under high vacuum conditions. If the modified samples were taken to air, the oxygen content increased drastically, Figure 6.14 (c). However, incorporation

of oxygen (of much lower concentration, compared to that obtained after the exposure to atmosphere) was also observed after modification of PS with Ar^+ ions under good vacuum conditions. Oxygen species are present in the residual gas of the preparation chambers, and react easily with the activated polymer surfaces. It should be noted, that under N_2^+ irradiation, a little amount of O_2 (~ 1%) is also introduced into the polymer surface together with nitrogen. The reason is the same as for the argon treated PS surfaces. When polymer modification was done with the IonEtch sputter gun, oxygen and nitrogen contents also increased. Under O_2^+ bombardment, the atomic weight concentration of oxygen was 9, 17, 22 and 26 % for ion fluences of 10^{13}, 10^{14}, 10^{15} and 10^{16}, respectively. Irradiation with N_2^+ ions introduced 2, 5, 11, 15 and 17 % of nitrogen for ion fluences of 10^{13}, 10^{14}, 5×10^{14}, 10^{15} and10^{16}, respectively.

In the case of PMMA, the amount of oxygen decreases up to an ion fluence of 5×10^{14} cm^{-2} and reaches saturation under the irradiation of different ions, Figure 6.14 (d). When treated with O_2^+ ions, oxygen degradation occurs slower above an ion fluence of 5×10^{14} cm^{-2}, and reaches saturation at a value of ~10 % which is higher compared with argon or nitrogen treatments. Under N_2^+ ion bombardment, the oxygen concentration decreases and reaches the same saturation value as for Ar^+ ion bombardment, while the nitrogen content increases.

XPS analysis was done using angle resolved X-ray photoelectron spectroscopy (AR-XPS, Section 5.5.1). This technique allows us to enhance surface sensitivity by variation of the electron take-off angle. Figure 6.15 shows the results for PS treated with 1 keV argon (Figure 6.15 (a), (b)), oxygen ((c), (d)) or nitrogen ((e), (f)) ions. The graphs on the left show the ratios vs. take-off angle for defined ion fluences, on the right, the same ratios are normalized to the value obtained at an emission angle of 0°.

When PS is treated only with argon ions (Figure 6.15 (a) and (b)), the only change observable in the XPS spectra is the reduction of π–π^* shake-up satellite which indicates polymer aromaticity, and little oxygen incorporation (~ 2 %), which is not discussed here. Plot (a) shows how the ratio shake-up/C1s decreases with the ion fluence (the percentage values of the satellite only are given in brackets (insert in graph (a)). A shake-up was not detected above an ion fluence of 5×10^{14} cm^{-2}. Normalizing the given ratio to the value received under an angle of 0°, it is possible to see where the modification starts at first. At a take-off angle of 0° photoemitted electrons carry information about the largest sampling depth, and it is assumed that the normalized ratio is equal to unity. With increasing take-off angle, the information comes from lower depth and so the spectra become more surface sensitive. Phenyl rings start to degrade in the upper-most surface layer (emission angle 75°)

for a very low ion fluence (5×10^{13} cm^{-2}). After prolonged bombardment with ions, polymer destruction occurs deeper within the polymer.

Treatments with reactive ions such as N_2^+ and O_2^+ cause phenyl rings to degrade in the same way as for argon bombardment. Additional to this, nitrogen or oxygen species are introduced into the polymer. The amount of these elements incorporated into PS increases with the ion fluence, Figure 6.15 (c) and (e). From the normalized O1s/C1s and N1s/C1s ratios, it is obvious that first O_2 or N_2 containing functional groups form on the top of the surface. With increasing ion fluence the functional groups start to form deeper in the polymer. During modification with N_2^+ ions, a small amount of oxygen (~ 1 %) is introduced into the polymer together with nitrogen itself.

AR-XPS analysis was also done for the polymer containing oxygen groups in their chemical structure such as PMMA, Figure 6.16. Treatment conditions were the same as for PS. The atomic weight concentration is given in the Figure 6.14 (d). Ion irradiation with different gases results in O_2 loss with increasing the ion fluence. The strongest degradation of oxygen containing groups observed occurred under argon bombardment ((a) and (b)). Treatment with O_2^+ ions ((c) and (d)) slows down degradation of these functionalities, especially for large ion fluences. PMMA modification with N_2^+ ions ((e) and (f)) removes carbon-oxygen groups and introduces additional nitrogen. The loss of oxygen during nitrogen treatment is similar to that observed for Ar^+ ion bombardment, therefore, only N_2 incorporation is shown in the figure. The formation of new nitrogen functional groups starts on the surface at an ion fluence of 10^{14} cm^{-2}. At 10^{16} cm^{-2}, the modified surface layer is saturated with N_2, as the difference in the normalized ratio remains constant with increasing take-off angle.

The atomic concentrations of different elements present in the polymer provide only general information about the surface chemical structure. In order to gain a better understanding about the type of functional groups formed, peak fittings are required. The carbon C1s line is the most informative peak which is sensitive to all changes in the polymer and therefore details of the incorporated species can be obtained. Peak fittings were done using the CASA-XPS software in order to determine the formation of new functional groups, and the loss or rearrangements of the ones originally present. Figures 6.17 and 6.18 show C1s XPS spectra with fitted features for PS and PMMA treated with argon, nitrogen and oxygen ions. The XPS spectra presented in the figures were recorded at 0° take-off angle. Graph (a) in both figures gives the carbon spectra of the pristine polymer. Chemical formulas of PS and PMMA are given in the inserts of the graphs. Which carbon bond corresponds to the fitted

feature in the main C1s peak is indicated by numbers in the formula: 1 and 2 for PS; 1 to 4 for PMMA.

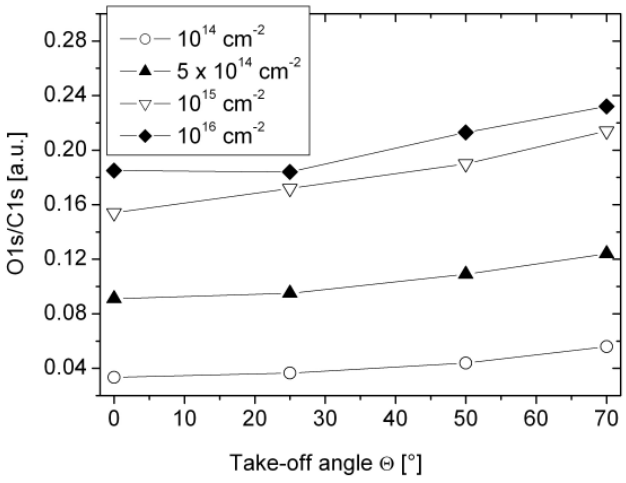

a)

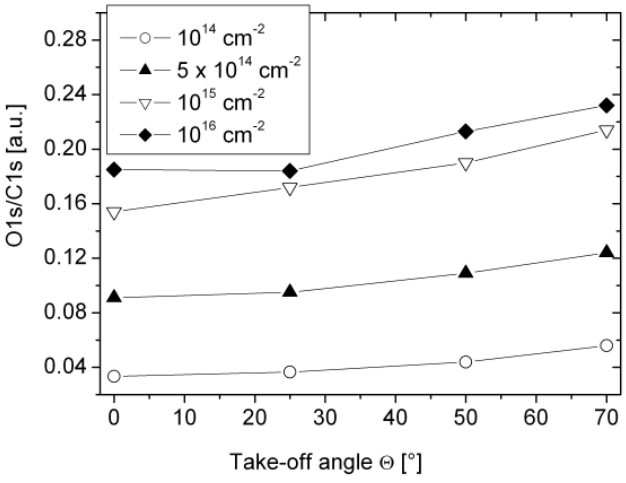

c)

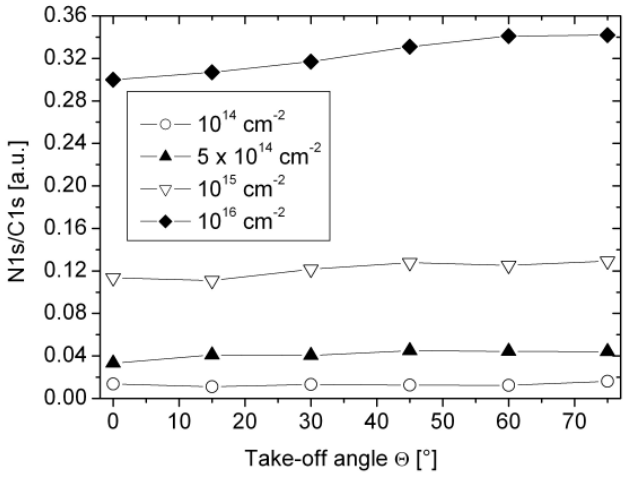

e)

Figure 6.15

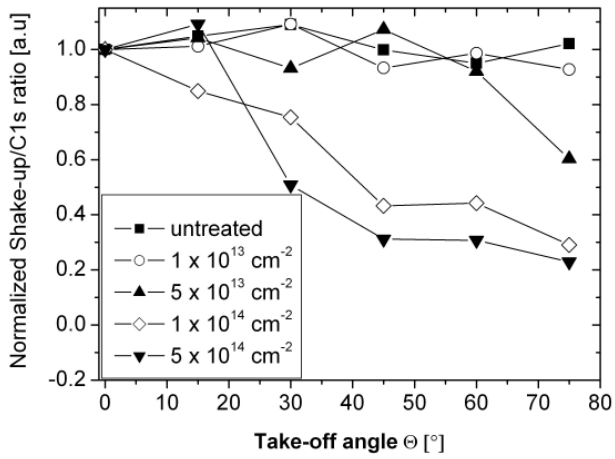

b)

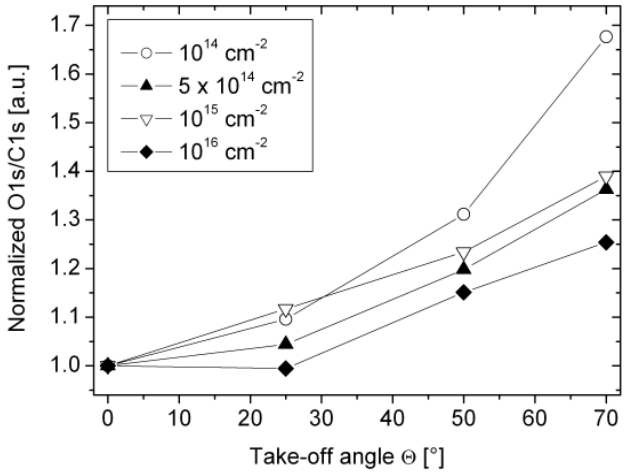

d)

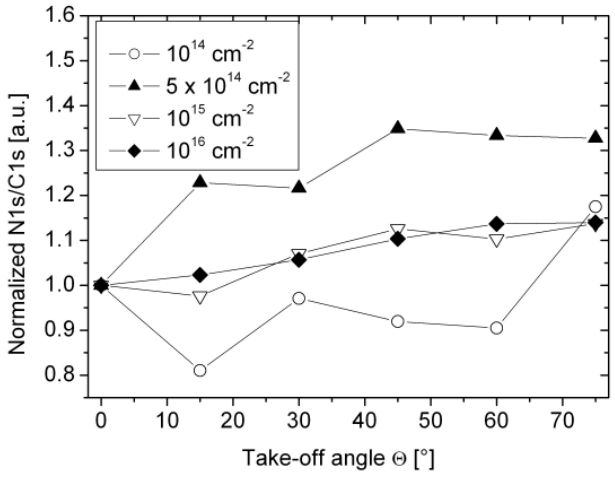

f)

Figure 6.15 (continued) *AR-XPS for treated PS. (a) and (b) PS modified with Ar^+. Percentage values of the π–π^* shake-up satellite (calculated for a take-off angle of 0°) are given in the brackets. (c) and (d) modification with O_2^+ ions. (e) and (f) treatment with N_2^+ ions. Modifications were done using the ISE 10 ion gun.*

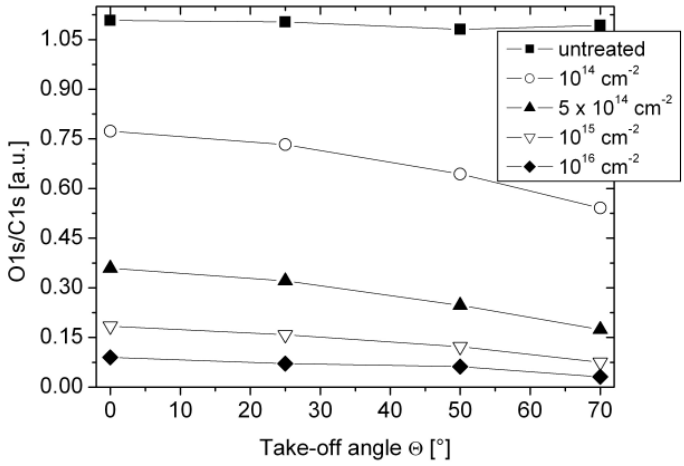

a)

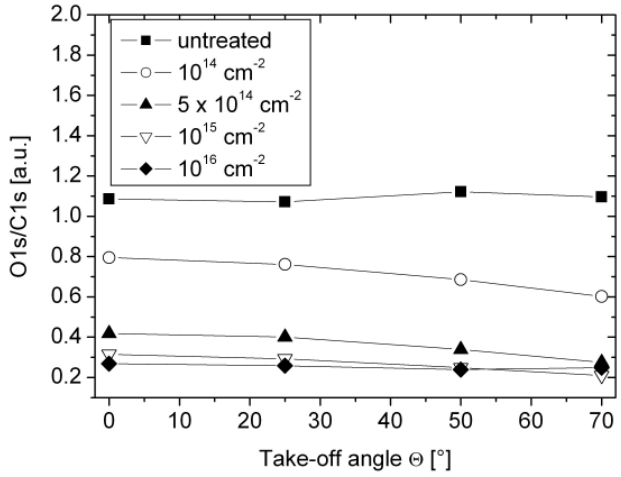

c)

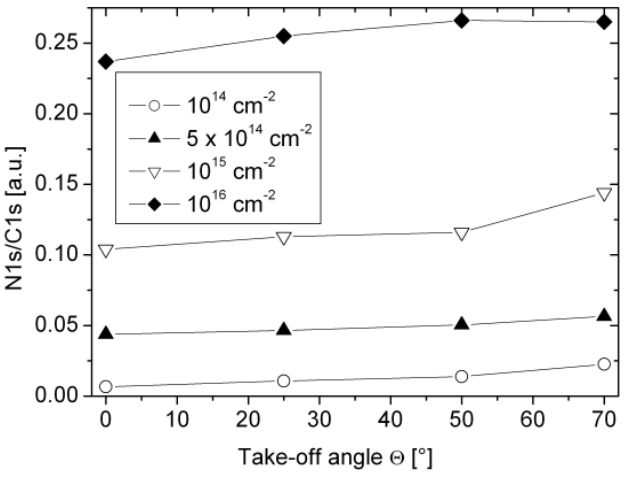

d)

Figure 6.16

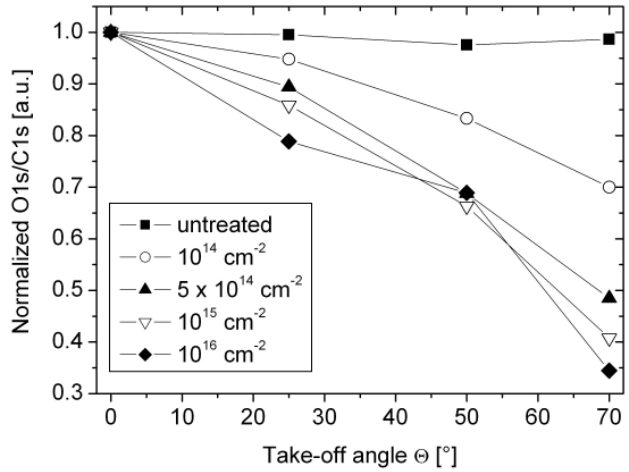

b)

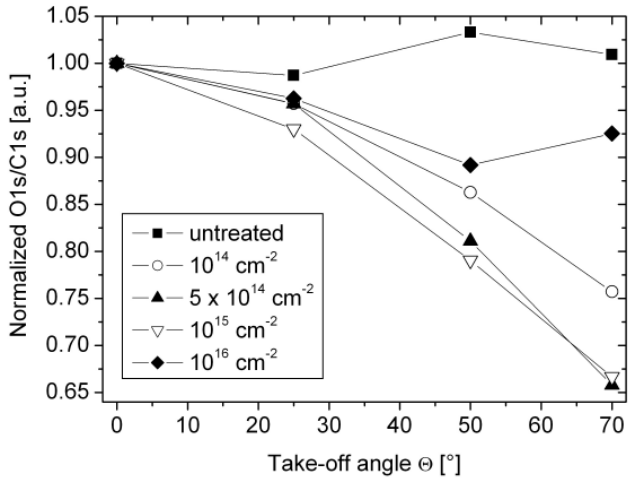

d)

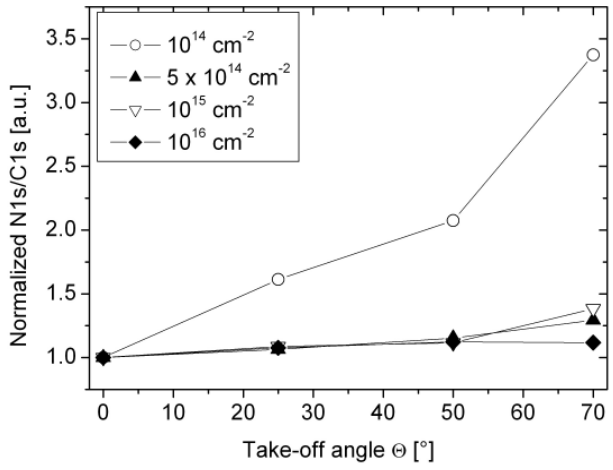

f)

Figure 6.16 (continued) *AR-XPS for treated PMMA. Polymer modified with Ar^+ ions (a) and (b); O_2^+ ions (c) and (d); N_2^+ ions (e), (f). In the case of nitrogen treatment, only N_2 incorporation is shown, as the decrease in oxygen is similar to that observed for argon treatment. Modifications were performed using the ISE 10 ion gun.*

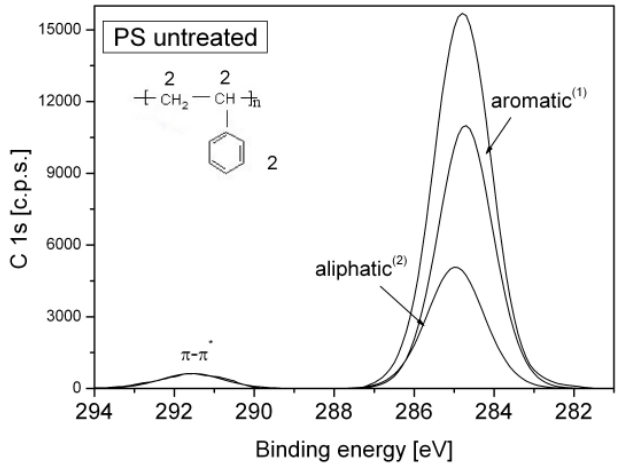

a)

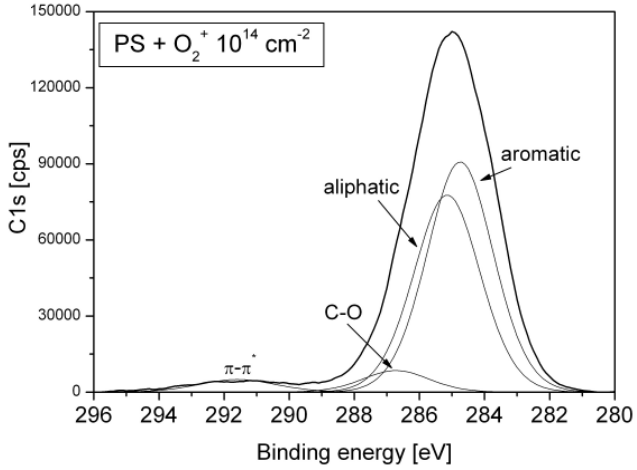

c)

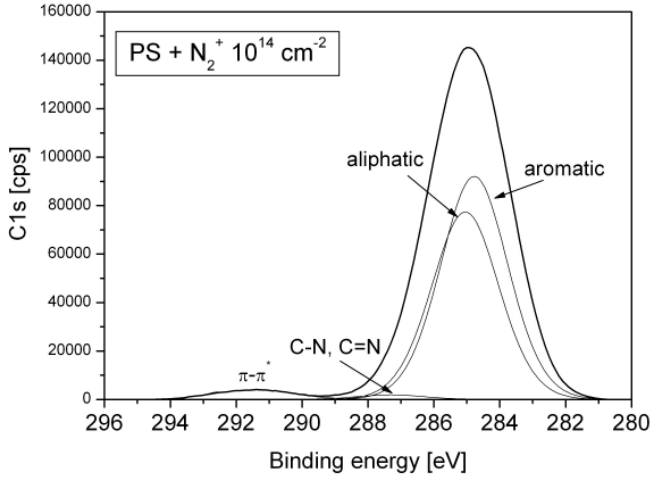

e)

Figure 6.17 *Carbon C1s XPS spectra for PS. (a) Untreated PS. Insert on the top left shows the chemical formula. The carbon bonds corresponding to the fitted features in the main C1s peak are indicated by numbers (1 and 2) in the formula.*

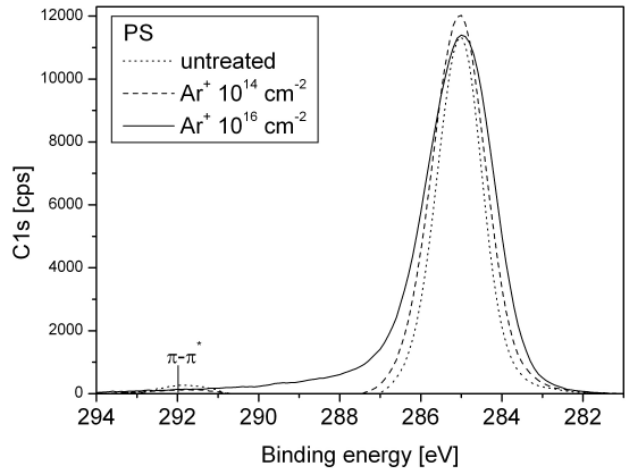

b)

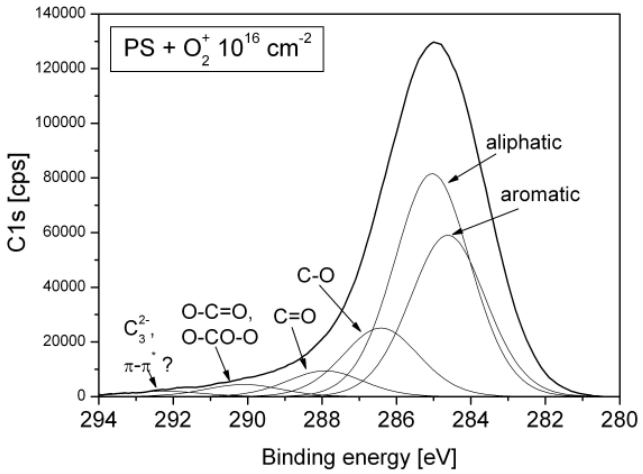

d)

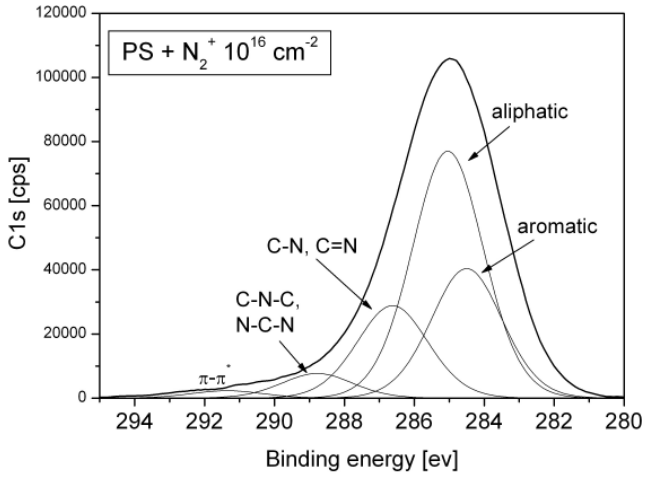

f)

Figure 6.17(continued) *(b) Comparison of C1s spectra of pristine and modified (Ar^+ ions) PS. Peak fitting in the C1s spectra after the treatment with O_2^+ ions (c) 10^{14} cm^{-2}, (d) 10^{16} cm^{-2}; and N_2^+ ions (e) 10^{14} cm^{-2}, (f) 10^{16} cm^{-2}.*

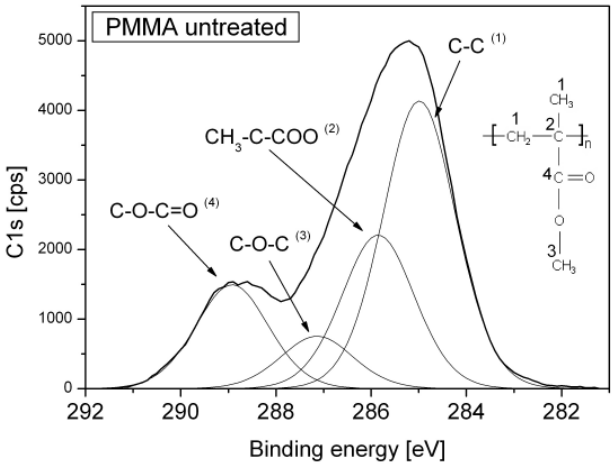

a)

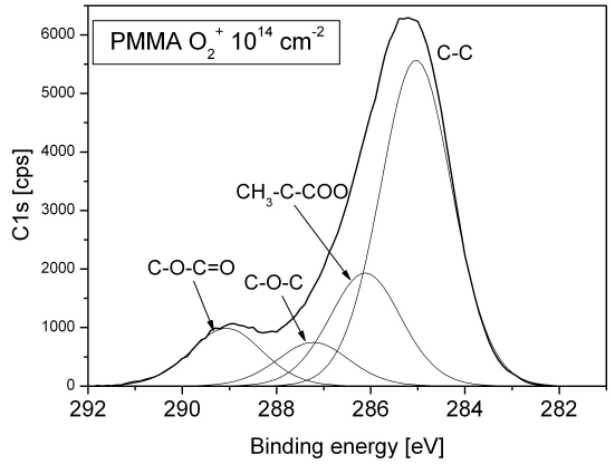

c)

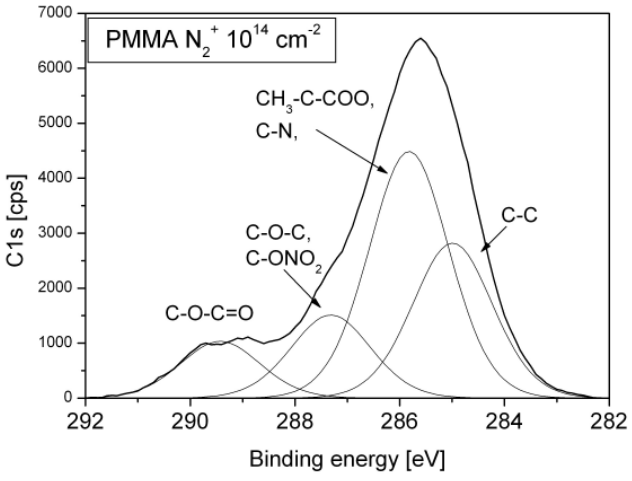

e)

Figure 6.18 *Carbon C1s XPS spectra of PMMA. (a) Untreated PMMA. Insert on the top right shows the chemical formula with the numbers (1 to 4) indicating fitted features in the main C 1s peak.*

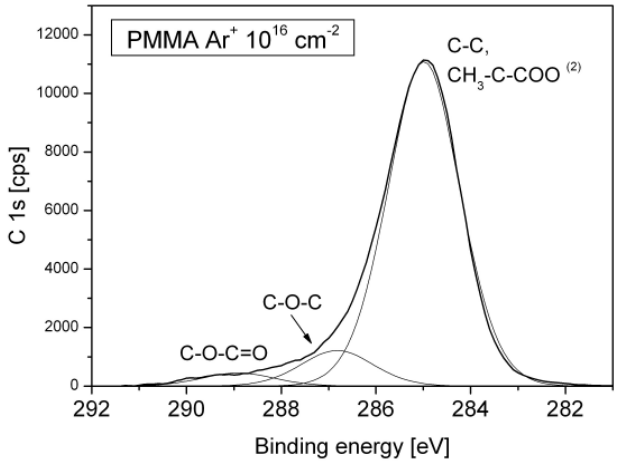

b)

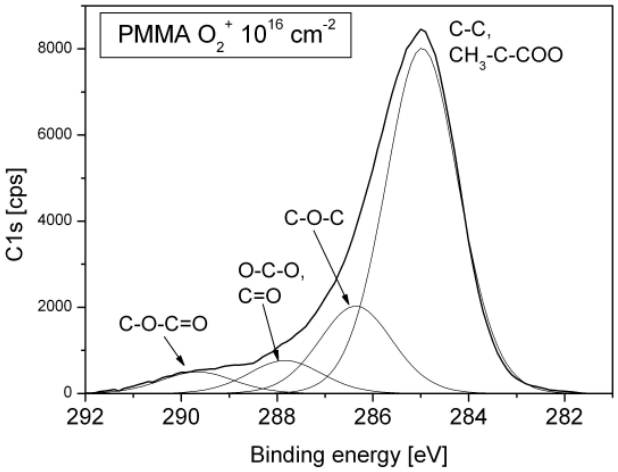

d)

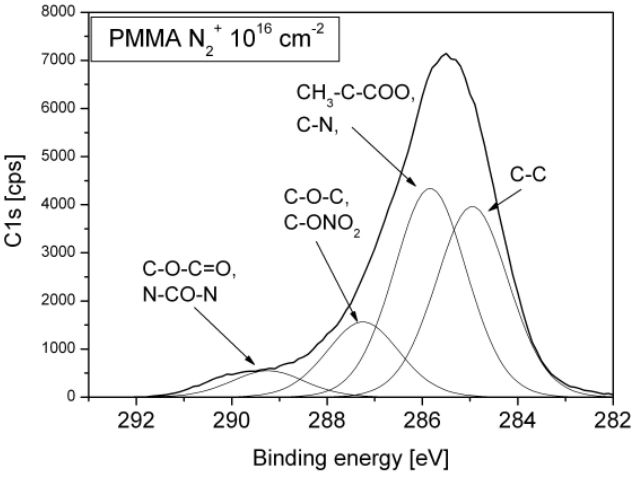

f)

Figure 6.18 (continued) *(b) PMMA modified with Ar^+ ions at an ion fluence of 10^{16} cm^{-2}. Peak fitting in the C1s spectra after treatment with O_2^+ ions (c) 10^{14} cm^{-2}, (d) 10^{16} cm^{-2}; and with N_2^+ ions (e) 10^{14} cm^{-2}, (f) 10^{16} cm^{-2}.*

Figure 6.17 shows the fitted carbon features for PS. Untreated PS contains aliphatic (C-C) and aromatic (C=C in the ring) carbon functionalities in its structure. Graph (a) shows the C1s peak with fitted features, as well as the π-π^* shake-up satellite indicating polymer aromaticity. In figure (b) the carbon C1s peaks of untreated and Ar^+ treated PS are compared. With increasing ion fluence, the peaks become broader with a long tail in the direction of the high binding energy. The π-π^* satellite loses its shape until it disappears or is covered by the tail. During the bombardment, the aliphatic carbon feature increases while the aromatic one decreases. Such behaviour is observed also for treatment with oxygen and nitrogen ions, see figures graphs (c) to (f). Oxygen containing functional groups are incorporated during the treatment with O_2^+ ions (Figure 6.17 (c) and (d)); nitrogen are detected/present after treatment with N_2^+ ions, see figures (e) and (f). The oxygen functional groups shown given in figures (c) and (d) for oxygen modified PS were also formed when the treated polymer was exposed to atmosphere.

Figure 6.18 shows the fitted carbon C1s peaks for PMMA. Untreated PMMA contains different oxygen-carbon groups shown in figure (a). During treatment with argon ions the intensities of these features become smaller with the increasing ion fluence, see figure (b). Similar behaviour is observed when PMMA is treated with oxygen or nitrogen. In the case of oxygen modification (graphs (c) and (d)), the number of functional groups initially present in the polymer decreases with the duration of the bombardment up to an ion fluence of about 10^{15} cm^{-2}. Afterwards, the amount of oxygen remains constant (Figure 6.14 (b)) resulting in a larger final number of carbon-oxygen functionalities compared to argon treated PMMA surfaces (figures (b) and (d)). A different behaviour is observed when the polymer is bombarded with N_2^+ ions (see figures (e) and (f)). The amount of those features increased in the case of nitrogen bombardment, however the same features usually decreased in number or vanished completely under argon or oxygen treatments. This resulted in the formation of nitrogen containing functional groups bonded directly to C or O_2.

From Figures 6.17 and 6.18, it is obvious that some features appear at very low ion fluences, while other requires longer treatments. To confirm this, AR-XPS analysis was performed, and peak fittings were done for all carbon features recorded at different angles. Figure 6.19 shows the concentrations of some special functional groups observed in the C1s line of treated PS and PMMA. Percentage values of selected functional groups are plotted vs. the take-off angle as a function of the ion fluence. The position of these groups in the carbon peak is shown in Figures 6.17 and 6.18 for PS and PMMA, respectively.

The number of aromatic and aliphatic carbon groups in the untreated PS (Figure 6.17 (a)) fits with the ratio aromatic/aliphatic = 3/1, in percents that is ~ 70 % for aromatic, ~ 25 % for aliphatic, and ~ 5 % for the shake-up transition. To see how the ratio changes with the ion fluence, fitting was done for all AR-XPS spectra. The intensity of the aromatic feature decreases with ongoing ion bombardment down to a final value of 20 %, (Figure 6.19 (a)), resulting in the increase percentage of the aliphatic feature and the vanishing of the π-π^* satellite. When analyzing the dependence of the aromatic group on the take-off angle, the degradation in the upper-most surface layer (θ = 50 - 75°) is observed after the treatment with an ion fluence of 5×10^{13} cm^{-2}, Figure 6.15(b). A small amount of oxygen functionalities formed during the argon modification of the PS surface was also formed in the upper most polymer surface layer.

Graphs (c) to (f) in the Figure 6.17 showed the formation of new functional groups after PS was treated with oxygen and nitrogen ions. C-O functionalities started to form already at an ion fluence of 10^{14} cm^{-2}, preferably on the surface (Figure 6.19 (b) solid symbols). At an ion fluence of 10^{15} cm^{-2} saturation in the amount of this group is achieved, and the formation of the C=O feature (open symbols in the graph) begins. Other carbon-oxygen functional groups appear in the O_2^+ treated PS after treatment with the highest ion fluence. Similar behaviour of the carbon-oxygen functionalities was observed for polymers exposed to air after modification. A difference was only observed in the concentrations of the features formed. The observations were the same for C-N and N-C-O groups that were formed in nitrogen treated PS, Figure 6.19 (c). Note that the N-C-O feature is detectable already at an ion fluence of 5×10^{14} cm^{-2} (open up-triangles) but only at the surface, as the XPS feature of this group vanishes when analysis is done for larger depths.

The same fitting procedure was done for PMMA. The C-O-C=O characteristic feature, marked as number 4 in Figure 6.18 (a), was selected to describe the behaviour of PMMA under ion irradiation. The intensity of this functional group decreases with increasing ion fluence when the polymer is treated with Ar^+ ions, Figure 6.19 (d). AR-XPS analysis shows that C-O-C=O degrades starting from the outer-most surface layer at an ion fluence of 10^{14} cm^{-2}, and the surface concentration of this feature became lower as the concentration recorded deeper in the sample. When PMMA is treated with oxygen or nitrogen ions, this the intensity of the functional group decreases at first up to an ion fluence of 5×10^{14} cm^{-2}. Then at an ion fluence of 10^{15} cm^{-2}, an increase is observed, Figure 6.19 (e) and (f). At this point, O_2 or N_2 is incorporated into the polymer leading to the formation of new functional groups in addition to the ones already present or formed by the rearrangement of the old bonds.

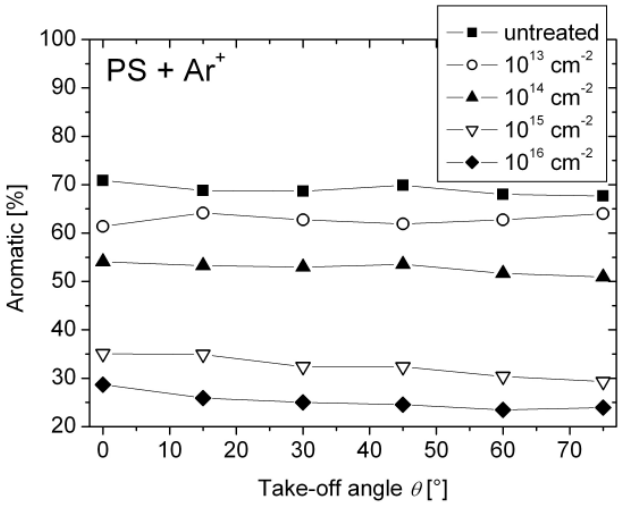

a)

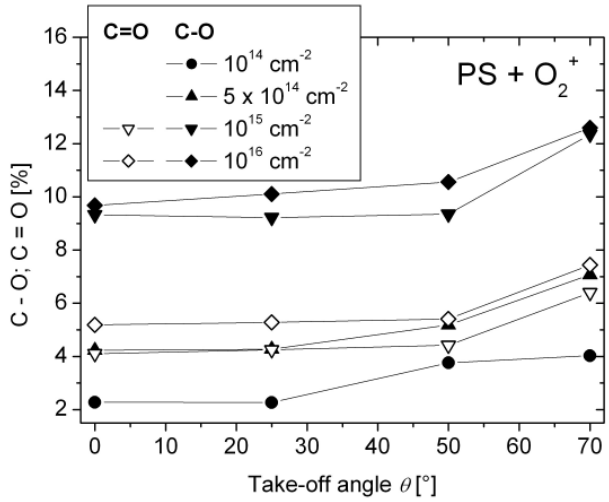

b)

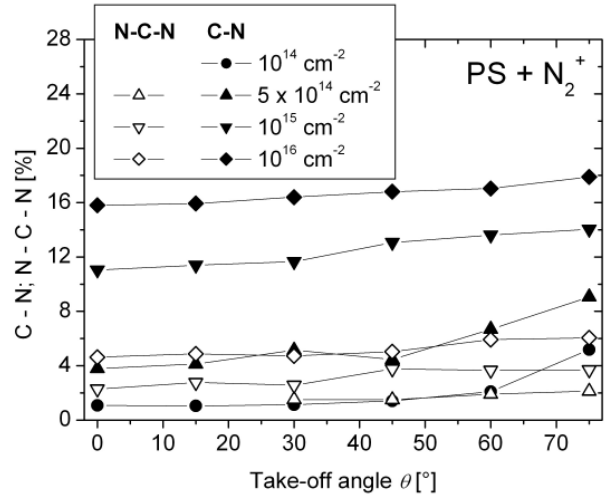

c)

Figure 6.19

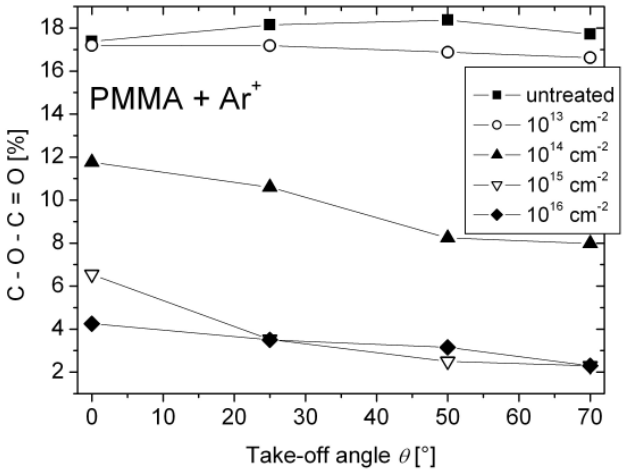

d)

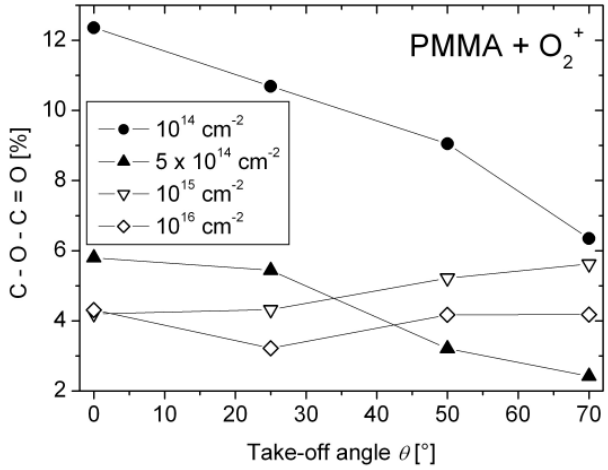

e)

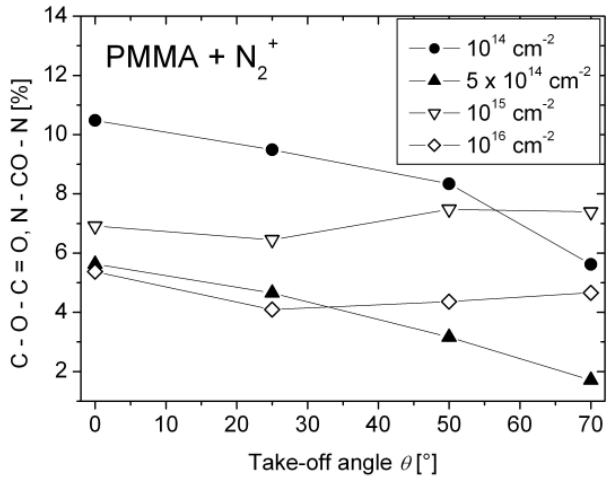

f)

Figure 6.19 (continued) *Percentages of special functional groups obtained by AR-XPS for PS and PMMA treated with 1 keV Ar^{+}(a) and (d)), O_2^{+}(b) and (e)), and N_2^{+} (c) and (f)) ions. Selected functionalities are given in Figures 6.17 and 6.18 for PS and PMMA, respectively.*

6.2.2 Surface glass transition temperature

In the introduction of this chapter it was mentioned that ion irradiation can result in cross-linking or in the formation of low molecular weight (LMW) species. Depending on the polymer's tendency to create cross-link network or to form small mass molecules through chain scissions, the properties of the polymer may be improved or become worse. By measuring the glass transition temperature, it is possible to determine if formation of cross-links or degradation products is preferred. In the first case, the glass transition temperature should increase and in the second case it should decrease.

In order to measure the glass transition temperature of thin modified layers (thickness up to 5-6 nm [Biersak 87]), none of the conventional techniques used to measure the glass transition temperature can be applied, as the temperature has to be measured for a thin surface layer only. The method based on the embedding of noble metal clusters [Zaporojtchenko 01, Erichsen 04], described in Section 5.5.2, is surface sensitive and, therefore, was adopted.

Figure 6.20 shows a plot of the difference in the surface glass transition temperature T_{gs}, ($\Delta T_{gs} = T_{gs}^{tr} - T_{gs}^{untr}$, where T_{gs}^{tr} is the measured temperature after the polymer treatment, T_{gs}^{untr} is the temperature for the untreated polymer) vs. the ion fluence for three polymers treated with 1 keV argon ions. ΔT_{gs} for PS increases monotonically with exposure, while the change for PαMS and PMMA is very small and almost constant in the measured ion fluence range.

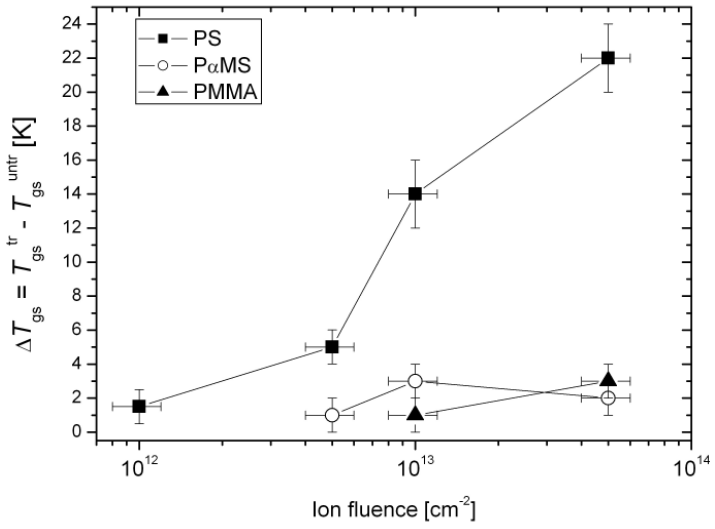

Figure 6.20 *The change in surface glass transition temperature, ΔT_{gs}, vs. ion fluence for PS, PαMS and PMMA treated with Ar^+ ions with an energy of 1 keV.*

The small change in the ΔT_{gs} for poly-α-methylstyrene and polymethylmethacrylate shows that formation of degrading products is preferred. PS, on the other hand, is a polymer which preferentially cross-links. The degree of cross-linking, x, was calculated for PS treated with Ar^+ ions using the well known relation given in the Ref. [Krevelen 90]:

$$T_{g,\,crl} - T_{g,\,0} = 1.2\, T_{g,\,0}\, (x / (1 - x)) \qquad (6.3)$$

where x is the number of cross-links per number of backbone atoms, $T_{g,0}$ and $T_{g,crl}$ are the surface glass transition temperatures of the uncross-linked and cross-linked polymer, or in our case, temperatures determined for the untreated and treated polymers, respectively. The calculated cross-linking density for PS is given in Table 6.3. It should be noted that Equation 6.3 attributes the increase in the surface glass transition temperature completely to cross-linking and does not take into account the increase in the chain stiffness resulting from new functional groups formed after polymer treatment with reactive gas.

Table 6.3 *Change in surface glass transition temperature and calculated degree of cross-linking for PS treated with argon ions.*

IF, cm^{-2}	10^{12}	5×10^{12}	10^{13}	5×10^{13}
ΔT_{gs}, K	1.5	5.01	14	22
Degree of cross-linking, %	3.5	6.2	16	18.5

The surface glass transition temperature for PS increases also when it is treated with oxygen or nitrogen ions. At lower fluences the temperature difference is the same as for argon treated PS, and only starting at an fluence of 10^{13} cm^{-2} ΔT_{gs} it rises further for PS containing N_2 and O_2 functional groups. Table 6.4 presents values for ΔT_{gs} for PS treated with argon, nitrogen and oxygen ions at an ion fluence of 5×10^{13} cm^{-2}. The increase in the temperature change for the oxygen and nitrogen treated PS surfaces may be due to the enhanced cross-linking through the new functionalities, and due to the formation of carbon-oxygen and carbon-nitrogen functional groups which may restrict chain rotation resulting in higher glass transition temperature values [Young 91].

Table 6.4 *Change in the surface glass transition temperature for PS treated with argon, nitrogen and oxygen ions at an ion fluence of* 5×10^{13} cm^{-2}.

Ions	Ar^+	N_2^+	O_2^+
ΔT_{gs}, K	22	31	35

No influence of the modification gas on the glass transition temperature was observed in the case of PαMS and PMMA. The differences in temperature remained the same as those recorded for argon treatment (ΔT_{gs} = 2 - 4 K).

6.2.3 Changes in surface tension

Water contact angle measurements (Section 5.6) were done in order to measure the surface tension. Figure 6.21 shows images of water drops on untreated and Ar^+ treated PS. Grey lines in the images indicate the interface between liquid and the polymer surface. The water drop on untreated PS is of the form of a bead with the angle $\theta > 90°$. With increasing ion fluence, the liquid spreads on the treated surface, showing that the hydrophobic PS surface becomes hydrophilic, when the polymer is irradiated with ions. Similar images were taken for other polymers.

Contact angle measurements were done in air. It means that the treated polymers were removed from vacuum and reacted with atmospheric O_2. During these reactions oxygen containing functional groups were formed that influenced the experimental measurements.

Figure 6.22 shows the dependence of the water contact angle on the ion fluence for PS and PMMA. Values of θ were calculated with the software using the Young-Laplace function. Liquid spread more across the surface with increasing ion fluence resulting in smaller contact angles. For PMMA, the value of θ remains constant up to an ion fluence of 10^{14} cm^{-2} and it starts decreasing above an ion fluence of 10^{14} cm^{-2}. Untreated polymethylmetharcylate has a lower angle than pristine PS because of oxygen functional groups present in PMMA which in contact with water turn from the bulk towards the surface.

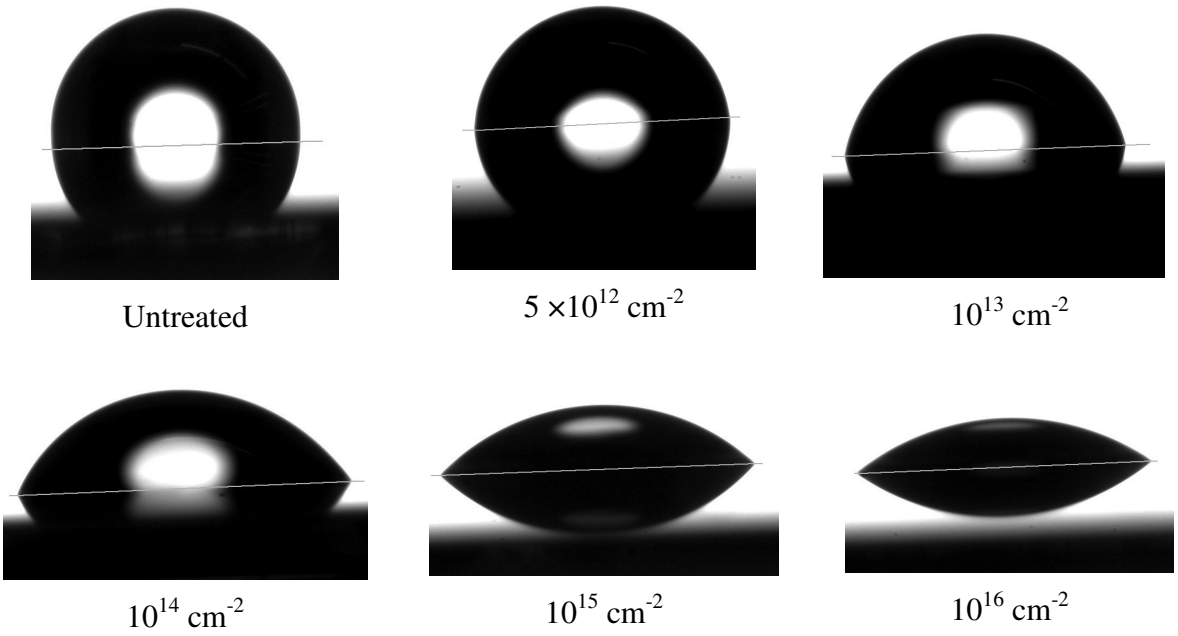

Figure 6.21 *Water drops on a PS surface before and after argon treatment. Contact angle measurements were done in air. The grey line in the middle of the drop indicates the interface between water and polymer surface*

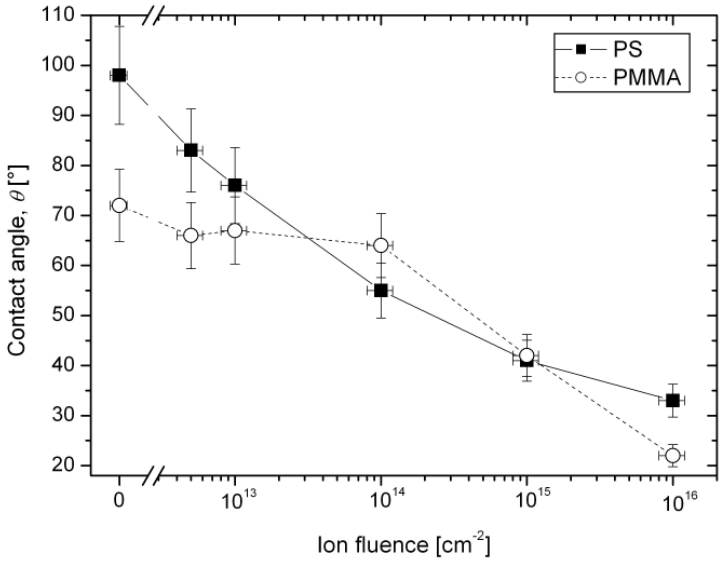

Figure 6.22 *Contact angle of water on Ar^+ treated PS and PMMA surfaces. Measurements were done in air.*

6.2.4 Polymer surface roughness

The influence of the ion beam on the surface roughness of the polymer film was measured with AFM. At low ion fluences, the change in surface roughness was negligible and only above an ion fluence of 10^{15} cm^{-2} a difference (2-3 times) was observed. The values of the polymer surface roughness are given in the Table 6.5. All polymers were treated with 1 keV Ar^+ ions. For comparison, the values for pristine films are given. When the ion fluence reaches values 10^{15} and 10^{16} cm^{-2}, R_{ave} or R_{rms} do not differ with the treatment time.

Table 6.5 *Average, root-mean-squared roughness of different polymers treated with 1 keV Ar^+ ions.*

Polymer	Ion fluence, cm^{-2}	R_{rms}, nm	R_{ave}, nm
PS	0	0.333	0.257
	10^{15}	1.095	0.852
	10^{16}	0.983	0.771
PαMS	0	0.412	0.307
	10^{15}	0.848	0.652
	10^{16}	1.02	0.792
PMMA	0	0.565	0.438
	10^{15}	1.495	1.217
	10^{16}	1.18	0.911

Summarizing Section 6.2, it was shown that:

1) polymer surface treatments with different gases induce chemical changes forming new functional groups, and rearranging or removing old bonds. Exposure of the modified samples to air causes free radicals to react with the atmosphere resulting in additional oxygen incorporation;
2) nitrogen and oxygen incorporation into PS increases with the ion fluence until saturation is reached at an fluence of about 10^{15} cm^{-2}. The intensity of the shake-up satellite, the characteristic feature of this polymer, decreases with increasing fluence.

In the case of PMMA, the amount of oxygen was observed to decrease under irradiation with different gases. Nitrogen was also introduced into this polymer under N_2^+ ion bombardment. The concentration of nitrogen increased with the fluence, while the concentration of O_2 decreased;

3) AR-XPS showed that the very first changes under ion irradiation occur in the outer most surface layer, and only after prolonged ion bombardment the modification is uniformly distributed in the whole treated layer;

4) different features were fitted to the carbon C1s peak, showing the formation of different functional groups. AR-XPS of the characteristic features showed that these functional groups started to form on the surface, and some of them formed even at lower ion fluences as compared to the results observed for normal take-off angle;

5) through the surface glass transition temperature measurements it was observed that PαMS and PMMA preferably form degradation products, because of the constant T_{gs}. For PS, the surface T_{gs} increases with increasing ion fluence, and the largest calculated cross-linking density reaches almost 20 %. An influence of different ions on T_{gs} was observed only for PS, with ΔT_{gs} being higher for nitrogen and oxygen modification compared to argon treatment. No influence of the ion type was recorded for the two other polymers;

6) contact angle measurements showed that polymer surfaces change from hydrophobic to hydrophilic after argon ion irradiation and exposure to air. A decrease in the water angle on treated polymer surfaces indicates an increase in polymer surface energy, which may be important in the case of metal/polymer adhesion (see next section);

7) changes in the surface roughness were negligible at low ion fluences. Larger differences were observed at fluences above 10^{15} cm^{-2}. One of the adhesion theories claims that the increase in the surface roughness should improve the adhesion between two materials, Section 2.2.3. However, observed changes in roughness for PS, PαMS and PMMA are not very large, and the influence on the adhesion is expected to be small.

6.3 Metal-polymer interface formation: relevance to adhesion

Polymers and metals are very dissimilar materials, and interaction between them is weak. In the initial metal deposition stage, small metal clusters are formed on the untreated polymer surfaces. With increasing metal fraction, clusters become larger, start to coalesce and continuous metal films are obtained with rather poor adhesion strength between two materials. When a polymer is treated with various ions, new adsorption sites are created resulting in an increased density of metal clusters and a larger condensation coefficient, as well as improved metal-polymer adhesion. However, treatment of some polymers did not increase the adhesion strength even if the condensation coefficient approached unity. Analysis of the peeled-off side of removed metal films showed that the failure location changed from interfacial for untreated to cohesive failure in the polymer substrate for treated surfaces.

6.3.1 Early stages of metal growth on treated polymer surfaces

The early stages of metallization are far from thermodynamic equilibrium conditions since isolated metal atoms impinge on the polymer surface. Therefore, various competing processes (adsorption, surface diffusion and nucleation after encountering other metal adatoms, metal atom reemission into vacuum, etc.) have to be taken into account to understand how the metal-polymer interface is formed. Metals of low reactivity, especially noble metals like Cu or Au, do not wet polymer surfaces but form 3D clusters, as shown in Figure 6.23 for Au cluster formation on untreated and treated PS surfaces.

There are two possibilities for metal nucleation on polymer surfaces: the so called random and preferred nucleation. Nucleation is preferred, when metal atoms are trapped at some defect sites, and random where nuclei are formed by metal atom encounters. Both cases are distinguished by examining the maximum cluster density as a function of the deposition rate. It was shown [Thran 99, Zaporojtchenko 00a, Zaporojtchenko 03a], that noble metal atoms underwent random nucleation and complete condensation at RT on polymers with high concentrations of polar groups like PMDA-ODA polyimide. Preferred nucleation and, correspondingly, incomplete condensation was observed on untreated PS.

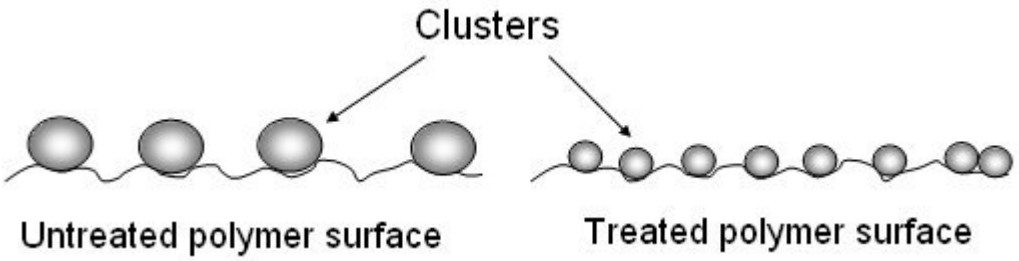

a)

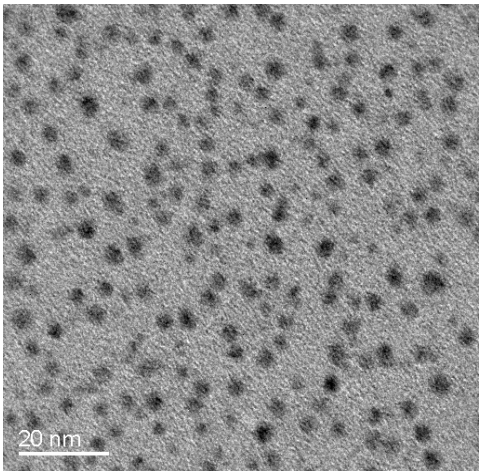

b) *untreated*

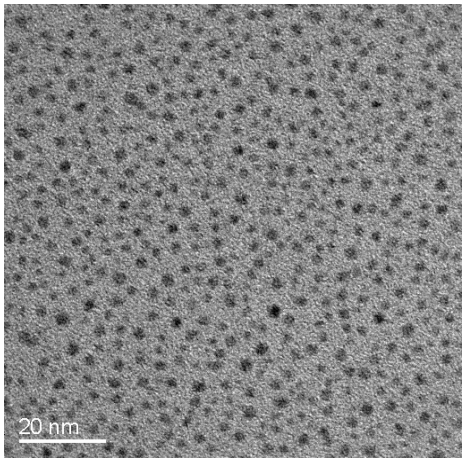

c) Ar^+ 5×10^{12} cm^{-2}

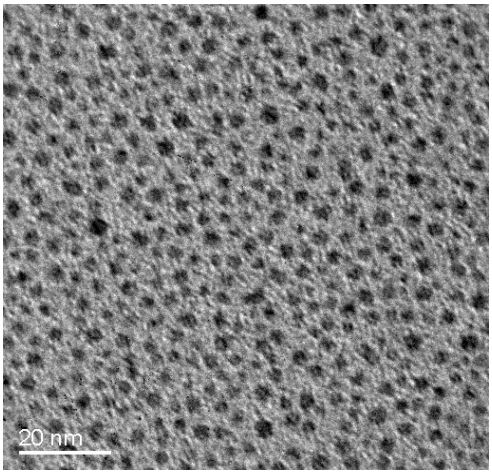

d) Ar^+ 10^{13} cm^{-2}

Figure 6.23 *(a) Schematic diagram of noble metal cluster formation on untreated and treated polymer surfaces. (b-d) TEM images of Au clusters on PS films. PS was treated with* Ar^+ *ions with an energy of 1 keV. The nominal thickness of the deposited Au was 0.3 nm.*

A description of condensation coefficient C and the cluster density N_c measurements and calculations is given in the Section 5.5.3. The condensation coefficient is defined as the ratio of the number of adsorbed metal atoms to the total number of metal atoms arriving at the surface. C is related with the probability to find a preferred site for adsorption that is related to the mean distance between these sites and the diffusion length of the adatoms on the polymer surface. If the distance between the nucleation centres is larger than the diffusion length of metal adatoms, most of all approaching metal atoms are not able to find a nucleation site resulting in a low value of C. A schematic diagram of cluster formation on pristine and modified polymer surfaces is given in Figure 6.23(a). On the untreated surface only few nucleation centres are present, leading to smaller cluster densities with large clusters as shown in the TEM image (Figure 6.23(b)). The cluster density of Au on an untreated PS surface is 10^{12} clusters/cm^2 and the condensation coefficient is about 0.45, Figure 6.24(a). Using ion-beam treatment, additional adsorption sites (defects, polar groups, unsaturations, etc.) can be created on the polymer surface. Metal atoms arriving on the treated surface easily find preferred adsorption sites and form clusters, with a distance comparable to or even smaller than the surface diffusion length, leading to the formation of evenly distributed small clusters with a high cluster density and, consequently, to an higher condensation coefficient. The density increased up to 4.56×10^{12} clusters/cm^2 and 8×10^{12} clusters/cm^2 for ion fluences of 5×10^{12} cm^{-2} and 10^{13} cm^{-2}, respectively, Figure 6.23. The condensation coefficient of Au also increased with increasing ion fluence and reached unity, Figure 6.24(a).

As the condensation coefficient increases with increasing density of adsorption sites, there is possibility that adhesion between metal and polymer can be also enhanced with increasing ion fluence. The improvement may be due to the increased number of nucleation sites, or because of the formation of strong chemical bonds between metal and ion beam induced functionalities. The peel strength (measured with the peel test (Section 5.8)) for the Au/PS system is given in Figure 6.24(b). The measured strength reaches a maximum followed by a decrease at higher ion fluences. Comparing the results for condensation coefficient and measured peel strength, the correlation between the adsorption probability and adhesion cannot be found, as the strength decreases at fluences where complete metal condensation and saturation in the cluster density are reached. No correlation was also found between the peel strength and the increase in the surface energy, Figures 6.22 and 6.24(b).

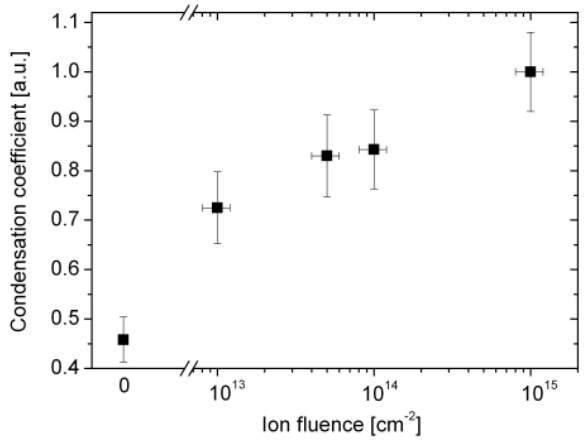

a)

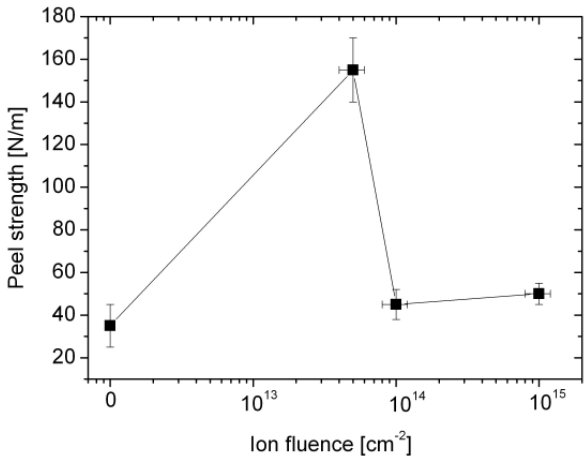

b)

Figure 6.24 *(a) Condensation coefficient and (b) peel strength of Au vs. ion fluence on argon treated PS surface.*

Figure 6.25 shows C and N_c of Cu on treated PS. It remains at ~ 42 % off all deposited metal on the pristine polymer film surface. After ion irradiation, the metal adsorption probability was enhanced up to unity. Different ions induce various chemical changes in the polymer surface, as discussed above. Nevertheless, the ion chemistry does not play a very large role in the condensation coefficient measurements. C values on surfaces treated with N_2^+ ions are larger in the fluence range of 5×10^{12} to 10^{14} cm^{-2}. At higher fluences, the difference becomes negligible as complete condensation occurs. Although, that a small variation in the adsorption probability was observed, the increase in the cluster density was found to be the

same for all treatments. Experimentally determined values of N_c are proportional to the values of the ion fluence up to 10^{14} cm^{-2} where saturation in cluster density is reached.

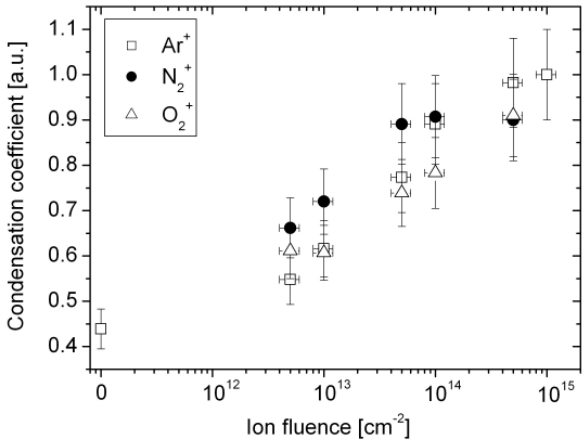

a)

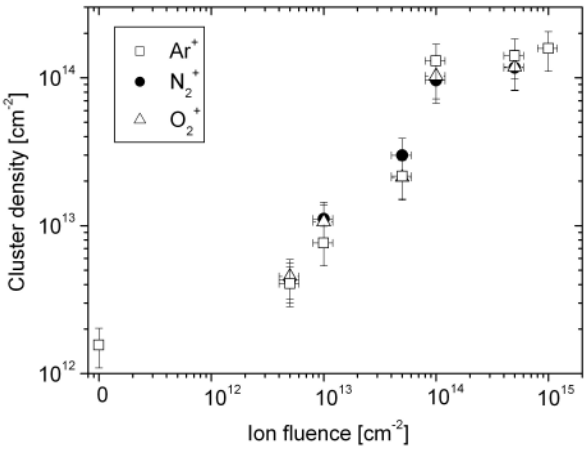

b)

Figure 6.25 *(a) Condensation coefficient and (b) cluster density of Cu on PS. The polymer surface was treated with different ions with an energy of 1 keV.*

The dependence of the condensation coefficient and the cluster density on the polymer chemistry is shown in the Figure 6.26. The number of Cu clusters and their density increases with the irradiation fluence for all polymers. PS and PαMS have the same values of C and N_c. The adsorption probability on untreated PMMA is lower by 15 % compared to the other two

polymers. After modification, this difference decreases and the condensation coefficient is close to the valued of PS and PαMS. The condensation coefficient of PP is given in Figure 6.26(c). Cu on untreated PP has the lowest adsorption probability when compared to other polymers, see Figure (a). With increasing ion fluence the value of *C* approaches unity. The cluster densities of Cu on polymers increase up to a value of 10^{14} clusters/cm^2, which remains constant at higher fluences.

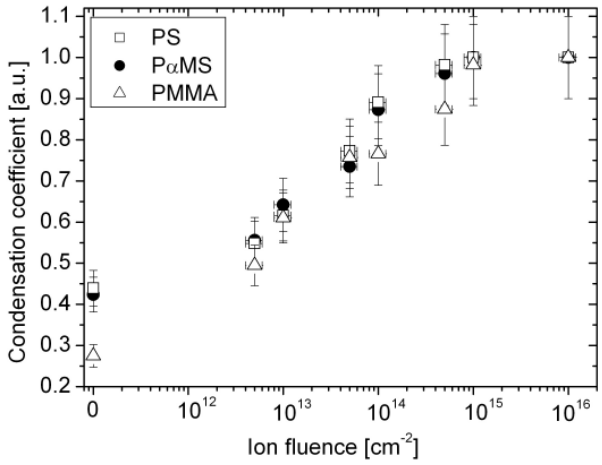

a)

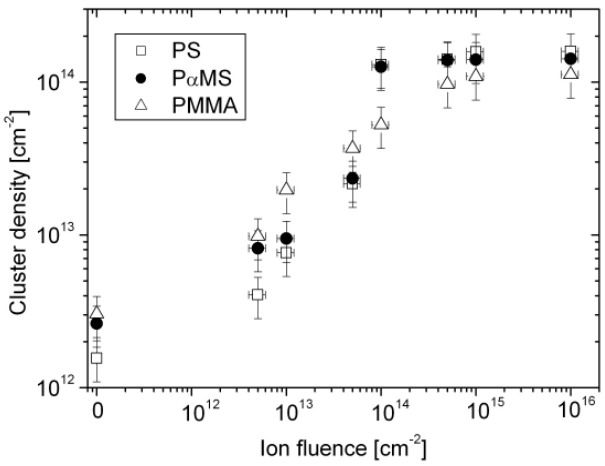

b)

Figure 6.26

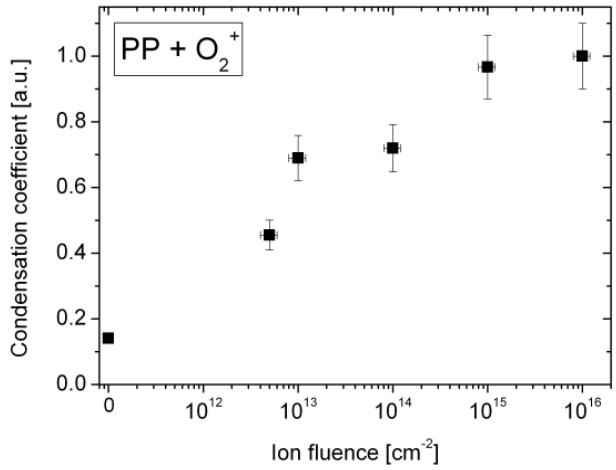

c)

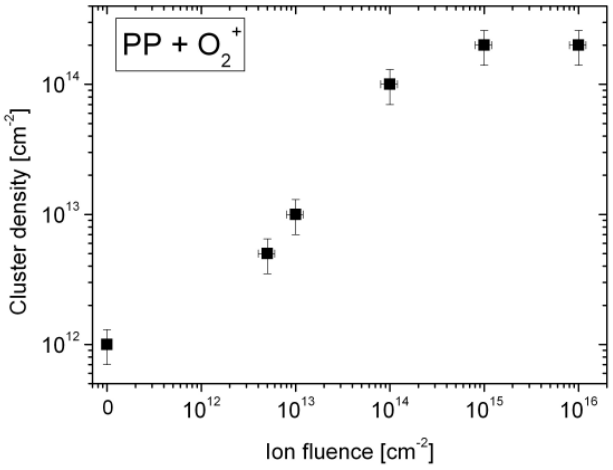

d)

Figure 6.26 (continued) *(a) Condensation coefficient and (b) cluster density of Cu on PS, PαMS and PMMA. The polymer surfaces were treated with Ar^+ ions with an energy of 1 keV. (c) and (d) condensation coefficient and cluster density of Cu on oxygen treated PP.*

6.3.2 Metal adhesion on treated polymers

The increase in condensation coefficient and cluster density indirectly shows the possible enhancement in the adhesion between metal and polymer. For the Au/PS system, Figure 6.24 only shows a correlation between the adhesion strength and the adsorption probability for low ion fluences, i.e. before the maximum was reached. However, the decrease in peel strength at higher ion fluences, where complete condensation of noble metals is observed, makes this correlation difficult to explain. In order to understand this phenomenon

the peel strength was measured for different metal/polymer systems as a function of the ion fluence and ion chemistry. The XPS analysis of the peeled-off surfaces of metal films and polymer substrates was done after the peel test experiments to determine the failure location.

6.3.2.1 Peel strength

90° peel tests (Section 5.8) were used to measure the peel strength (or adhesion strength in N/m), *P*, of metal on polymer surfaces. Figure 6.27 shows the peel strength of Cu vs. the ion fluence on PS treated with different ions with an energy of 1 keV.

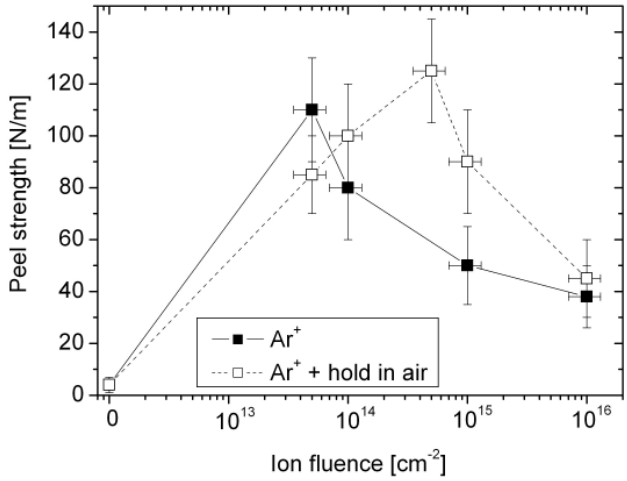

a)

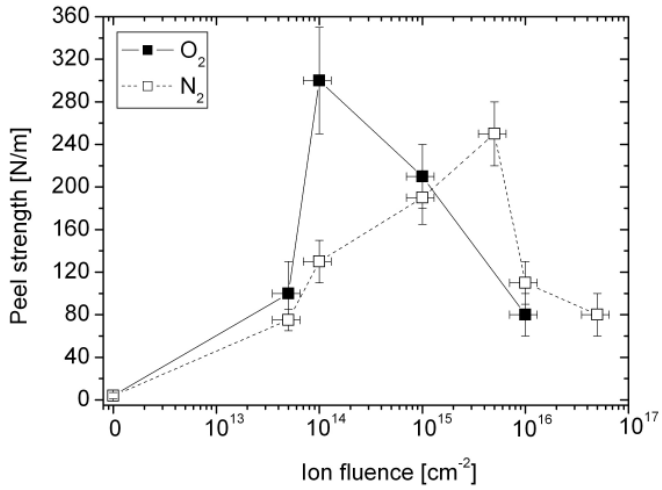

b)

Figure 6.27 *Peel strength of the Cu/PS system. PS was treated with 1 keV (a) Ar^+ ions and Ar^+ ions followed by the exposure to the air for 1 day; (b) N_2^+ and O_2^+ ions.*

The adhesion of Cu on PS increases by several orders of magnitude, reaches maximum at some ion fluence, which depends on the treatment conditions, followed by the decrease. If the polymer surface was modified with argon and afterwards exposed to air, the maximum peel strength value was shifted to a higher ion fluence compared to the pure argon treatment, Figure 6.27(a). The largest shift in the strength maximum was observed for the nitrogen treated polymer surface, Figure 6.27(b), but the highest adhesion strength is observed after irradiation of the PS surface with O_2^+ ions. The peel strength is also largest with $P \approx 90$ N/m for PS modified with O_2^+ and N_2^+ ions at ion fluence of 10^{16} cm^{-2}, while for pure argon treatment with subsequent exposure to atmosphere the peel strength value is slightly above 40 N/m at the same fluence.

The dependence of the adhesion strength on the deposited metal is given in Figure 6.28 for argon treated BPA-PC surfaces. For PS, the peel strength of Au is given in Figure 6.24 and of Cu in Figure 6.27. In the case of PS and BPA-PC, the measured adhesion strength approaches a maximum followed by a sudden decrease. In the case of polycarbonate, Cu and Au adhere with the same strength on pristine and BPA-PC treated with the lowest ion fluence. After prolonged bombardment, the difference of the peel force between the two metals becomes significant. Adhesion of Au does not show a maximum up to an ion fluence of 10^{15} cm^{-2} where the highest force is measured for Cu. It should be noted that this fluence is the last measuring point for Au. It is most probable that further treatment may leads to a decrease in the force. The ion fluence of 10^{15} cm^{-2} may be the point where the maximum value in the strength is also reached for gold.

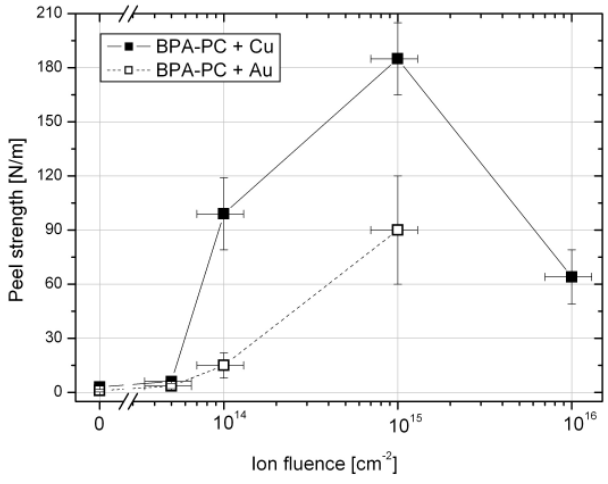

Figure 6.28 *Peel strength vs. ion fluence as a function of metal for BPA-PC treated with 1 keV Ar^+ ions.*

Figure 6.29 compares the measured peel strength of Cu on different polymers. PS and BPA-PC have maximum followed by a decrease in metal adhesion strength. PαMS and PMMA have a strength of 1 N/m and it remains constant with increasing ion fluence, Figure 6.29(a). The peel strength of Cu did not increase when these two polymers were treated with oxygen or nitrogen gas. A different behaviour was observed, when Cu was peeled-off from PP foils, Figure 6.29(b). The adhesion strength increases with increasing ion fluence and, in contrast to PS or BPA-PC case, does not fall off after the maximum was reached. Modification with oxygen showed to be an effective way to enhance the adhesion strength of Cu on PP.

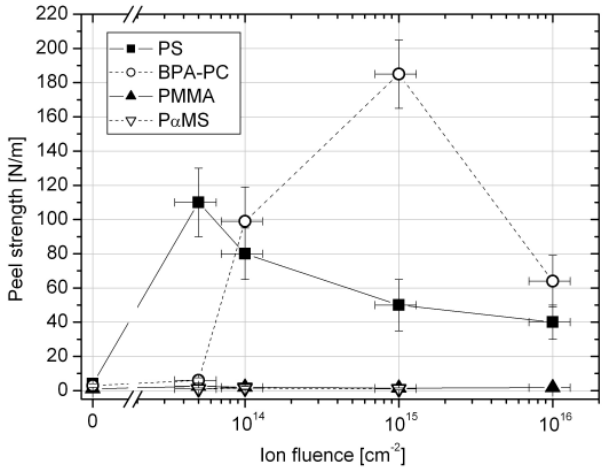

a)

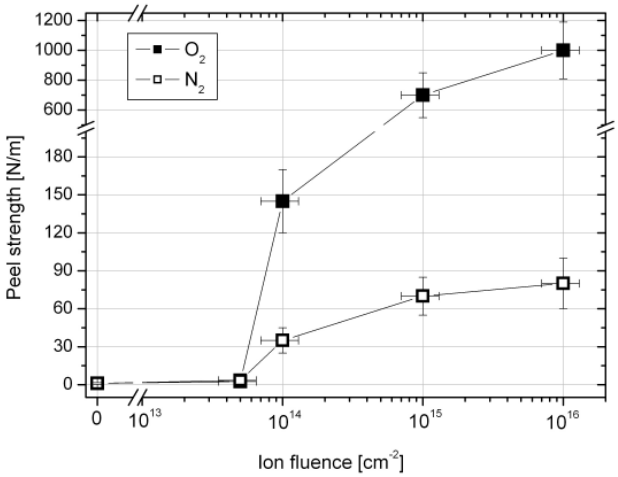

b)

Figure 6.29 *Peel strength of Cu (a) on different polymers treated with argon ions and (b) on PP treated with oxygen and nitrogen ions with an energy of 1 keV.*

The last observation, i.e. dependence of the peel strength on the polymer chemistry, showed that metal adhesion on polymers depends also on the polymer's tendency to form cross-links or to degrade under ion irradiation. PP, PS and BPA-PC are polymers that cross-link under irradiation (a detailed discussion is given in Chapter 7), and the adhesion strength increases. Even if a decrease is observed, the absolute *P* value is still larger than for the untreated polymer. PαMS and PMMA are polymers which preferably degrade, and in their case no improvement in metal adhesion was observed. On the other hand, the condensation coefficient measurements showed an enhancement in adsorption probability and cluster density for all polymers, Figure 6.26. If it is believed that the increase in *C* correlates with an indirect adhesion improvement, this is not true in the case of PαMS and PMMA. But, it should not be forgotten that the condensation coefficient is measured on the surface. However, the force obtained by the peel test measurements shows at what peel strength two surfaces are torn apart. In this case, the break may not be necessary at the interface, but in one of the materials. Therefore, it was required to determine the failure location.

6.2.3.2 Failure location

After the peel test, XPS analysis on both peeled surfaces was done. As an example, Figure 6.30 (a) shows the survey spectra for pure Cu and spectra obtained after the peel test of Cu from PS. The carbon peak intensity increased and cooper intensities decreased when peel test was done on treated polymer surfaces. It was mentioned, that the carbon C1s line is the most informative peak containing characteristic polymer features. The XPS spectra of the C1s line (Figure (b)) changed in shape when the Cu film was peeled-off from differently treated surfaces. The carbon peak recorded after the peel test from untreated PS contained some oxygen functional groups, as the envelope becomes broader on the high binding energy side (dashed line in Figure (b)), and oxygen was recorded in the XPS analysis (dashed line in Figure (a)). When Cu was peeled off from polymers treated with argon (ion fluence of 10^{14} cm^{-2}), the oxygen content decreased and the shape of C1s line was the same as for the pristine polymer containing the π-π* shake-up transition. Similar records were obtained on peeled surfaces from PS treated with other gasses, as well as on the peeled metal sides from different polymers.

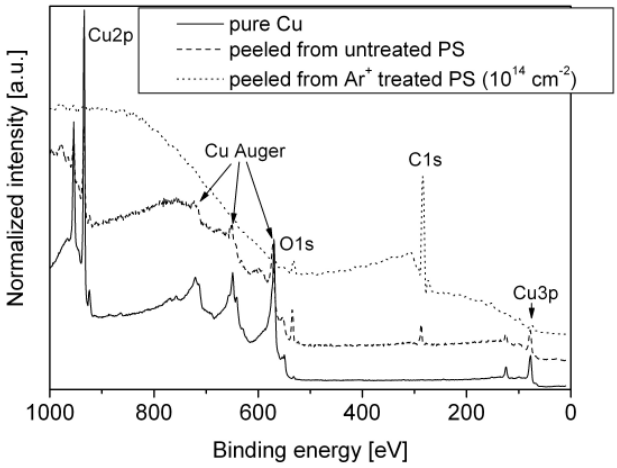

a)

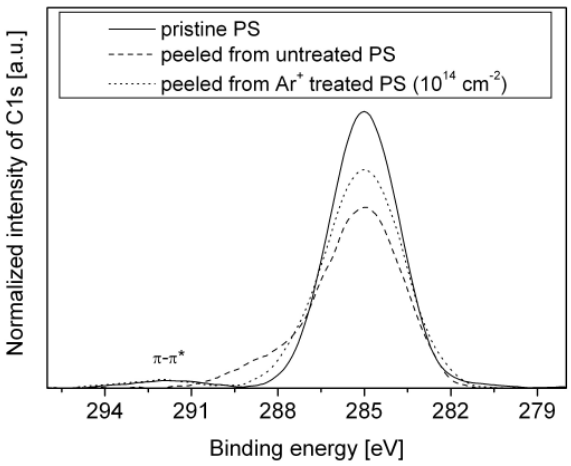

b)

Figure 6.30 *XPS spectra recorded on the peeled-off Cu side. (a) Survey spectra of pure Cu (solid line), and spectra obtained after the peel test from untreated and modified PS (dashed and dotted lines). (b) C1s peaks of pristine PS (solid line), and C1s recorded on Cu films after the peel test from untreated and treated polymer (dashed and dotted lines).*

Applying the equation 5.6 (Section 5.4.2), the thickness of the peeled-off polymer on the metal side was calculated. Figure 6.31 presents the peel strength of Cu films removed from PS, and the polymer thickness on the peeled metal side vs. ion fluence for PS treated with different gases. The thickness of the polymer removed during the adhesion measurements increased with the ion fluence for all treatments. Comparing the peel strength

values and the removed polymer layer, it could be stated that the PS layer on the metal still becomes thicker at the fluences where adhesion strength starts to decrease.

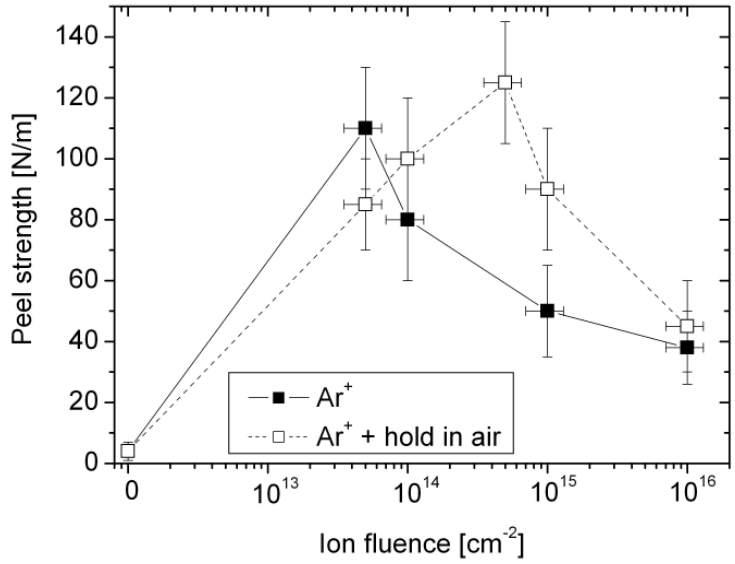

a)

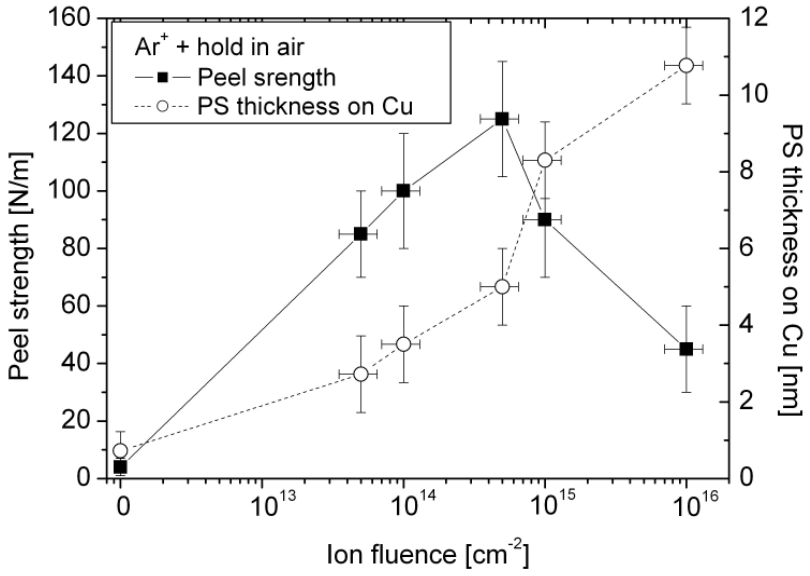

b)

Figure 6.31

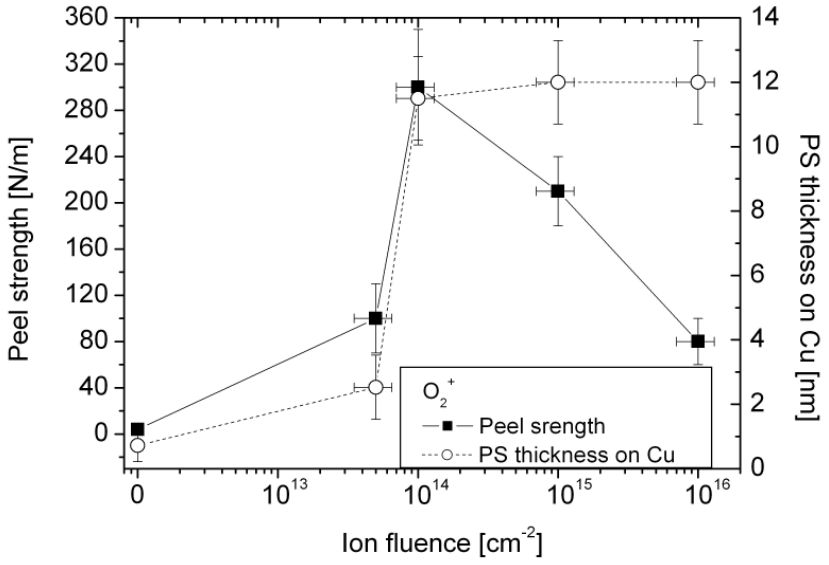

c)

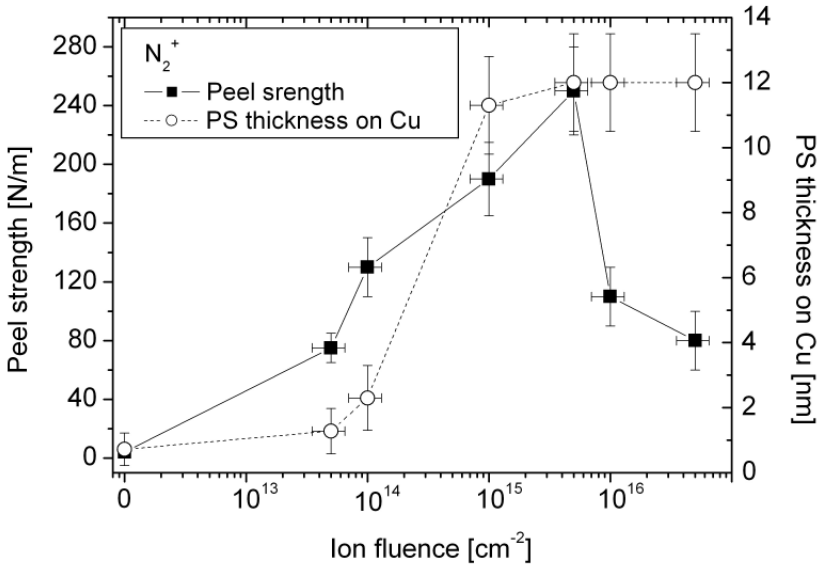

d)

Figure 6.31 (continued) *Peel strength of Cu on PS (solid squares) and the polymer thickness on the peeled metal side (open circles) vs. ion fluence for PS treated with different gases: (a) Ar; (b) Ar followed by exposure to air; (c) O_2; and (d) N_2.*

The XPS technique has limitations in determining the remained polymer layer thickness because of the attenuation length, λ, of substrate atoms through the organic layer. The maximum thickness that can be determined is 3λ [Briggs 90]. Therefore, in the case of a

polymer layer on Cu, the maximum thickness that can be determined is 10 - 11 nm, for polymer films on Au, the maximum measurable thickness is 12 -14 nm. A PS layer on a copper film removed from polymer surfaces treated with oxygen or nitrogen with an ion fluence above 10^{14} cm^{-2} becomes thicker than 10 nm, as no Cu2p or Cu3p signal was detected on the peeled metal side. In the Figures 6.31 (c) and (d), such thicknesses are denoted as 12 nm. This thickness was estimated after depth profiling of the peeled-off strips was done. A Cu signal was detected after the sputtering with 1 keV Ar^+ ions for 2 min at ion current of 137 nA which corresponds to an ion fluence of 10^{15} cm^{-2}. At this ion fluence, 2 to 3 nm of PS are removed (Section 6.1). The remaining polymer thickness was found to be about 9-10 nm.

In Table 6.6 the calculated organic layer thicknesses (in nm) on the metal (Cu or Au) side peeled off from polymers treated with 1 keV Ar^+, O_2^+, and N_2^+ ions are summarized. Treatment with O_2^+ at an ion fluence of 10^{16} cm^{-2} caused Cu to have very high adhesion strength (~ 1000 N/m) that led to the removal of a small amount of metal not suitable for the XPS analysis. The layers of other polymers on metal side increased with the ion fluence. Even for PαMS and PMMA, where the adhesion strength of 1 N/m remained constant, some polymer layer was detected on the peeled-off Cu side. In the case of PP, the polymer layer thickness removed from the oxygen treated surfaces is 1 - 2 nm up to an ion fluence of 10^{14} cm^{-2}, and only at higher fluences the removed thickness increases. After the peel test of the nitrogen treated PP surface, the peeled-off polymer layer shows a tendency to increase, but the detected layer thickness decreases above an ion fluence of 10^{15} cm^{-2}.

Table 6.6 *Thicknesses of polymer layers (in nm) on peeled-off Cu or Au sides removed from polymers treated with 1 keV Ar^+, O_2^+, and N_2^+ ions.*

	untreated	5×10^{13} cm^{-2}	10^{14} cm^{-2}	10^{15} cm^{-2}	10^{16} cm^{-2}
BPA-PC + Ar^+ + Cu	2.19	2.63	2.33	9.04	7.22
PαMS + Ar^+ + Cu	2.91	4.80	5.19	7.81	
PMMA + Ar^+ + Cu	2.07	3.34	4.48	4.84	5.24
PP + O_2^+ + Cu	1.09	1.76	0.79	6.19	
PP + N_2^+ + Cu	1.09	1.09	1.50	0.57	0.57
PS + Ar^+ + Au	1.79	4.202	9.268	> 10	
BPA-PC+ Ar^+ + Au	2.43	3.12	2.32	7.60	

In this Section, it was shown that:

1) noble metals form three dimensional clusters on polymer surfaces. The density of the clusters increased with the ion fluence because of the formation of additional adsorption sites. This resulted in an increase in the condensation coefficient. The condensation coefficient increased for all polymers;

2) the metal adhesion strength was shown to be dependent on the polymer chemistry, ion fluence and ion type. Three types of peel strength dependence were observed: (i) no improvement, (ii) the strength reached a maximum value followed by a decrease, (iii) the strength increases and reaches saturation. If polymers preferentially form degradation products under ion irradiation (PαMS, PMMA), metal adhesion did not show any dependence on the treatment time and the ion chemistry. No improvement in adhesion was observed in such cases. For cross-linking polymers (PS, BPA-PC), the peel strength increases, reaches a maximum in the fluence rage of $10^{13} - 5 \times 10^{14}$ cm^{-2} and then drops. Nevertheless, the absolute value is still larger than for the untreated polymers. O_2^+ and N_2^+ ion modification resulted in a shift of the maximum to higher ion fluences as well as to higher peel strength when compared to argon treatment results. Metal adhesion on PP increased with the ion fluence until saturation was reached;

3) the correlation between the peel strength and the condensation coefficient as well as the increase in polymer surface energy is rather very poor. In case of PS, BPA-PC, the drop in strength occurs at fluences where complete condensation and saturation in the increased surface energy were observed. For PαMS and PMMA, the peel strength remains low (1 N/m) even if improvements in adsorption and contact angle measurements were recorded. Only in the case of PP, the peel strength increased with the ion fluence and reached saturation;

4) analysis of the peeled-off side of the metal film showed that in most cases the failure location changed from interfacial for untreated polymer to cohesive failure in the polymer for treated surfaces. The maximum measured peel strength determines the adhesion force of two peeled-off polymer surfaces. Therefore, the conclusion can be drawn that adhesion at the *metal/polymer interface* was improved with increasing ion fluence, at the same time creating a weak layer in the polymer. In the case of PP, it is impossible to determine the exact location of the failure because of the controversial results.

Chapter 7

Discussion

In the introduction, it was mentioned that the goal of this research was to determine the sputter rates of different polymers as a function of the ion beam parameters; to modify the surfaces of organic films changing their chemistry, surface energy and roughness; and finally to determine the influence of the ion energy, fluence and ion chemistry on the metal condensation coefficient, nucleation, and adhesion to the polymer surface. Irradiation with ions results in polymer removal and, at the same time, surface modification. Since ion induced changes in the polymer surface layer influence the metal/polymer adhesion, this makes the discussion rather complicated, as one phenomenon cannot be explained without mentioning another one. Therefore, explanation and discussion of the results is divided into two parts. The first part (Section 7.1) deals with ion beam irradiation of polymer films. Here, the dependence of the polymer film removal as a function of the ion fluence, and the influence of the type of gas, sample temperature and polymer chemistry will be explained. The second part (Section 7.2) deals with ion beam induced modification of the metal-polymer interface formation.

7.1 Low energy ion beam irradiation of thermoplastic polymers

The effects of "conventional" ionizing radiation, like γ- and X-rays, fast electrons and neutrons, on organic substrates have been studied for many decades. Modifications under such irradiation occur not only on the surface but also in the polymer bulk due to large penetration depth of these particles. But fundamental types of radiation induced chemical modifications, established for high-energy (ionizing) irradiation, can also be applied for polymer bombardment performed with keV and MeV heavy ions. The more important chemical changes that irradiation causes in polymers are [Woods 94, Marletta 90]: formation of chemical bonds between different molecules or different parts of a macromolecule, i.e. cross-linking; irreversible cleavage of bonds within a molecule, resulting in the fragmentation of the molecule and loss of volatile species; changes in the number of unsaturated bonds, i.e. formation or disappearance of various types of double bonds between carbon atoms; the formation of intramolecular bonds – cyclization; oxidation or formation of other groups in the

presence of different gases. All of the above mentioned chemical changes influence the polymer sputter rate as well as other properties.

Up till now, a lot of investigations have been carried out on the ion irradiation of polymers with high energy (> 100 keV) ions [Fink 04, Calcagno 91, Punglisi 94, Licciardello 88] which penetrate several hundreds of nanometers and even micrometers into the bulk. Therefore, the induced processes can be compared with those obtained for ionizing radiation. However, little is known about the mechanisms of ion induced changes in polymers for low energies (1 - 5 keV), as only surface and near surface layers are involved in the process. In the following discussion, we will try to explain our results for the dependence of the polymer sputter rate on ion beam parameters like ion fluence and ion type, sample temperature and polymer chemistry, and possible sputtering mechanisms.

7.1.1 Sputter rate dependence on the ion fluence under Ar^+ irradiation

Sputter rates of polymers decrease up to an ion fluence of 5×10^{15} cm^{-2} (depending on polymer chemistry and irradiation conditions) followed by a constant removal rate (Section 6.1). This tendency was observed for all investigated polymers and all treatment gases. In Section 6.1.2, the possible reasons for the decrease in the sputter rate were discussed. Adsorbed species were removed is the first seconds of the treatment up to an ion fluence of 10^{13} cm^{-2}, and their influence on the sputter rate can be excluded. The main reason was attributed to the structural and chemical transformations that take place at the beginning of the ion irradiation, and are characteristic for each polymer. In the fluence region from 10^{13} to 5×10^{15} cm^{-2}, all polymers lose hydrogen and hydrogen-carbon molecules, as well as oxygen or nitrogen if present in the polymer. Finally, in the steady-state region the polymer surfaces are enriched with carbon.

The further discussion of polymer sputter rates obtained for argon ion bombardment will be divided into three parts, where ion irradiation mechanisms for different groups of polymers, i.e., poly(styrenes), poly(acrylates) and poly(acrylonitriles), will be analyzed.

7.1.1.1 Polystyrene and poly-α-methylstyrene

Polystyrene and poly-α-methylstyrene are structurally rather similar polymers, Table 5.1. The only difference in the structure of the two polymers is the methyl (CH_3) group at the tetra substituted carbon atom in the monomer unit. Both polymers have a phenyl ring in their structure indicated by the π-π* shake-up satellite in the C1s line of the XPS spectra. Figure 6.17 (a) shows a typical C1s peak for PS with fitted aromatic and aliphatic features. The same

shape of the carbon peak is observed for PαMS. The only difference between these two polymers in the XPS spectra is the ratio between the aromatic and aliphatic carbon features. The ratio of aromatic to aliphatic feature for PS is 3 to 1, while for PαMS this ratio is 2 to 1 because of the additional methyl group. During Ar^+ ion irradiation the carbon peak becomes broader and the π-π* feature becomes smaller until it is not detectable or is covered within the wide tail of the C1s line, Figure 6.17 (b). In relation to this, the aromatic feature will decrease and the aliphatic increase in intensity, as shown for PS in Figure 6.19 (a).

Analyzing the degradation of the phenyl ring under Ar^+ ion bombardment, it was noticed that the shake-up satellite observed with XPS decreases with increasing ion fluence for both polymers, Figure 7.1 (a). An ion fluence of 5×10^{14} cm^{-2} was the last point at which the π-π* feature was detected. The reduction rate in the satellite intensity does not differ for both polymers, as well as the change in the ratio of the aromatic and aliphatic carbon peaks, as shown in Figure 6.19 (a) for PS. The loss in the intensity of the π-π* feature may be due to the removal of the whole phenyl ring from the polymer chain. The breakage of old or the addition of new bonds to the ring may change the symmetry of the benzene molecule causing reduction in the satellite intensity as well. The emission of the rings was detected with the mass spectrometer, Figure 7.1 (b). The chemical yield (number of active species produced per 100 eV of absorbed energy) of the benzene molecule decreases under argon bombardment up to an ion fluence of 5×10^{14} to 7×10^{14} cm^{-2}. Then the constant removal rate lasts up to a fluence of 2×10^{15} cm^{-2} above which C_6H_6 molecule was not detected by our mass spectrometer anymore.

Comparing the XPS and residual gas spectra, it is obvious that the rings in PS and PαMS undergo degradation in the ion fluence range of 10^{13} to 7×10^{14} cm^{-2}. However, the yield of benzene molecule is very small compared to the yields of other molecules desorbed from polymer surfaces during the treatment, Figure 7.1 (c). Hydrogen (H_2) and acetylene (C_2H_2) molecules are the main gaseous products detected during ion irradiation. These are the main degradation products of PS and PαMS [Venkatesan 87, Calcagno 92, Wang 97, Charlesby 60]. The behaviour of H_2 and C_2H_2 molecules under ion bombardment is the same as that for ring degradation, i.e., the yields decrease with increasing ion fluence. The relative calculated yields (in mol/100 eV) for PS are $G(H_2) = 0.033$, $G(C_2H_2) = 0.008$, $G(C_6H_6) = 0.00048$, for PαMS - $G(H_2) = 0.028$, $G(C_2H_2) = 0.008$, $G(C_6H_6) = 0.00064$.

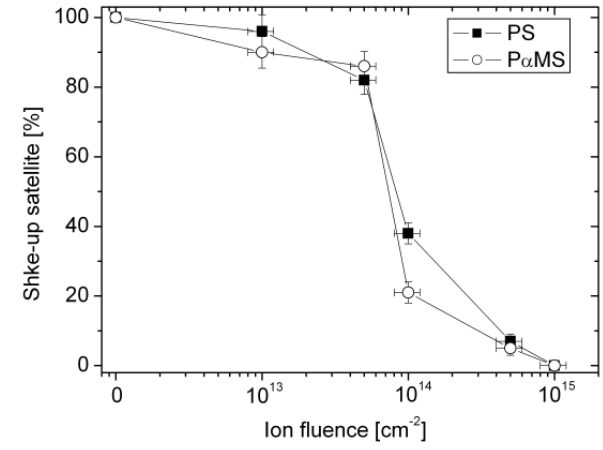

a)

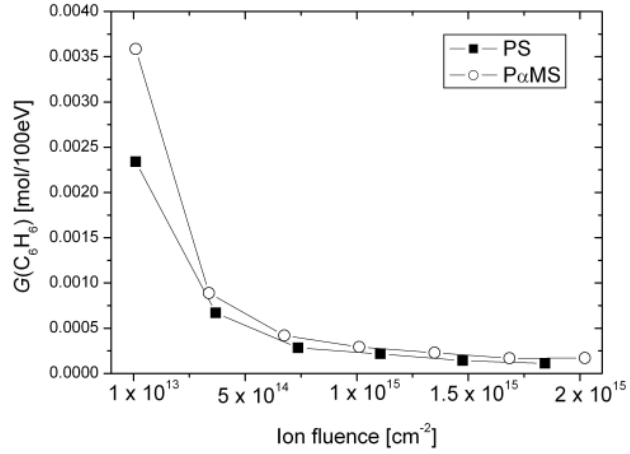

b)

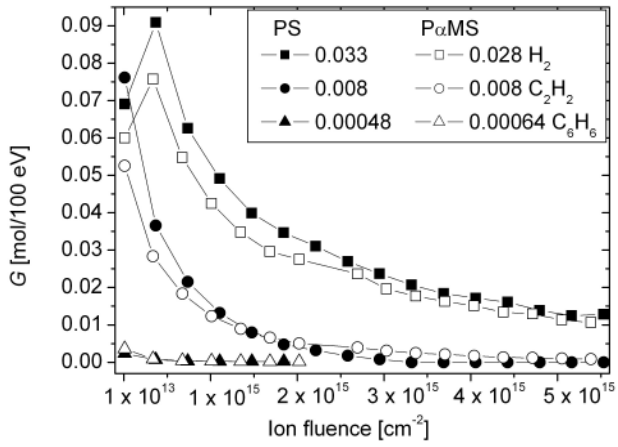

c)

Figure 7.1 *Phenyl ring degradation and molecule emission under 1 keV Ar^+ ion bombardment for PS and PαMS. (a) XPS data for the π-π* shake-up satellite vs. ion fluence. (b) Relative chemical yield of C_6H_6 (benzene molecule) vs. ion fluence. (c) Relative chemical yields of molecules emitted from PS (solid symbols) and PαMS (open symbols).*

Molecules of higher masses, such as 91 ($C_6H_5CH_2$), 104 (C_8H_8, monomer of PS), 118 (C_9H_{10}, monomer of PαMS), observed by secondary ion mass spectrometry [Briggs 82], were not detected for PS. High mass species, i.e., whole monomers, appeared for a very short time in the mass spectra when PαMS was irradiated. The maximum fluence at which these molecules were detected was 10^{13} cm^{-2}.

As smaller molecules are removed at higher rates, the reduction in the shake-up satellite cannot be only due to the desorption of the benzene molecule. A number of authors [Calcagno 92, Delcorte 04, Chapiro 62] suggests addition reactions of free radicals and hydrogen atoms with the aromatic ring leading to the change in the symmetry of the benzene molecule. This was proposed for PS, but because of the similar degradation behaviour such statements can also be applied for PαMS.

In the case of conventional ionizing irradiation, PS is a polymer with predominant formation of cross-links, while PαMS preferably degrades [Woods 94]. Indeed, α-methylstyrene has higher sputter rate than PS at the beginning of the ion irradiation, Figure6.5. However, in the steady-state region the sputter rate for argon ion bombardment of PαMS is close to that of PS (Table 6.1, Figure 6.5), and induced chemical changes as well as desorption of particular molecules is very similar for both polymers. Usually, in order to determine the yields for cross-linking and main-chain bond scissions, the techniques based on the measurements of the molecular mass of the irradiated polymer after dissolution in a suitable solvent are used. Such techniques are applied when the whole polymer film is modified uniformly. However, the ion range of 1 keV Ar^+ ions in polymers is only about 5-6 nm [Delcorte 01, Occhiello 90, Biersak 87], and the rest (~ 90 %) of the film remains unchanged making conventional techniques not applicable.

To understand the evolution in the polymer structure near the surface after irradiation of the films with low energy ions, the dependence of the surface glass transition temperature, T_{gs}, [Zaporojtchenko 01, Erichsen 04] on the ion fluence was measured. It is expected, that if a polymer is a degrading one, T_{gs} should decrease or remain unchanged for increasing ion fluence as chain scissions reduces the average molecular weight of the polymer. If the polymer preferably forms cross-links during irradiation, the increase in the molecular weight due to cross-linked chains leads to an increase in the glass transition temperature. Figure 6.20 shows the changes in the measured surface T_{gs} for PS and PαMS treated with different ions with an energy of 1 keV. The T_{gs} for PS increases monotonically with exposure, i.e. the chain mobility near the surface is reduced compared to the polymer bulk due to the formed cross-

links. The degree of cross-linking, *x*, was calculated for PS treated with Ar^+ ions applying Equation 6.3. The calculated results are given in the Table 6.3.

The value for *x* increased from ~ 2 % for an argon ion fluence of 10^{12} cm^{-2} up to ≈ 20 % for 5×10^{13} cm^{-2} [Zekonyte 03]. Using this value and taking into account that the penetration depth of the 1keV Ar^+ ions are ≈ 5 nm [Delcorte 01, Occhiello 90, Biersak 87], one can estimate the chemical yield of cross-linking *G*(X). For 1 keV energy Ar^+ ion bombardment, one obtains a value for *G*(X) = 0.3, which is approximately 10 times higher than for γ irradiation [Calcagno 92]. This higher chemical yield for low energy ions versus gamma rays is associated with the corresponding value of the ion energy loss and to the distribution of ionization along the ion track. On the other hand, the difference in the absolute value of *G*(X) between γ irradiation and ion irradiation does not change the general tendency in the ratio between cross-linking and scission processes for polymers that were found for γ or electron irradiation [Calcagno 92]. Embedding of Au nanoparticles into PS samples treated with an ion fluence of 10^{14} cm^{-2} was not observed, at least in the examined temperature range (up to 473 K). The embedding could occur at higher temperatures, or the density of cross-links formed is too high leading to the broadening of the transition region [Young 91].

It is difficult to determine the actual mechanism of the radiation cross-linking of PS due to the great variety of reactions which can in principle take place in this polymer. Because of the fact that the yield of cross-linking is higher than the chemical yield of hydrogen evolution, some authors conclude that addition reactions of free radicals and $H^{\cdot}$ atoms take place on the aromatic nucleus and consequently that the phenyl ring is involved in the cross-linking process [Chapiro 62, Woods 94, Calcagno 92]. The possible mechanism of cross-linking for PS is schematically presented in Figure 7.2. PS irradiation with noble gas ions, such as argon, helium, etc., or protons, γ- or X-rays, results in C-H bond rupture in the aromatic ring [Feldman 94, , Zezin 94, MacCallum 89, Lianos 94, Woods 94] and formation of a radical **A**, Scheme I. Such radicals may be stabilized by resonance phenomena, called benzylic carbocation [Atkins 02], and result in the formation of the benzyl-type radical **B** Scheme II. When radicals **A** and **B** combine, cross-linking occurs. Possible formation of cross-links by the combination of benzyl-type radicals is also confirmed by XPS where the intensity of the shake-up satellite is reduced with the ion fluence (Figure 7.1(a)) as new bonds produce the change in the symmetry of the phenyl ring. The loss of the satellite intensity shows that the phenyl ring is a preferred attack site under ion irradiation. Schematic diagrams given in Figure 7.2 show reactions that may occur in the polymer bulk or in the surface layer when a polymer is placed in ultra high vacuum conditions and no reactions with other species

can take place. It should not be forgotten, that oxygen was detected in the outer most surface layer (1 - 2 nm) after argon irradiation. Even if the recorded concentration is very low, some oxygen is incorporated. Possible oxygen reaction pathways are presented in Figure 7.7 and a detailed discussion is given in Section 7.1.2.

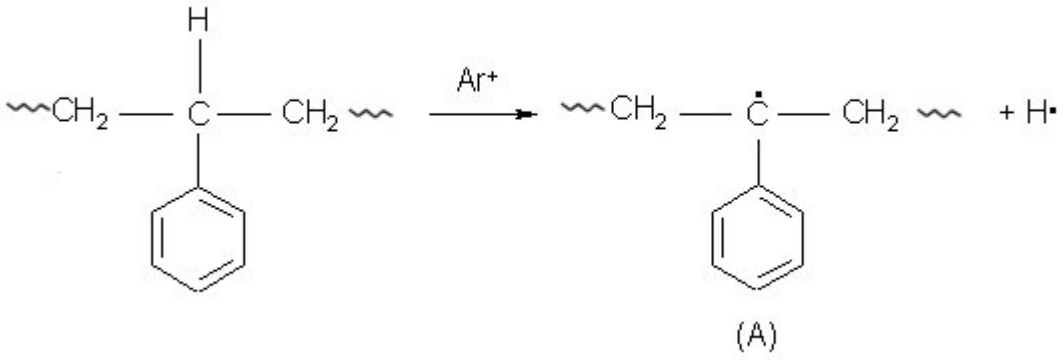

Scheme I

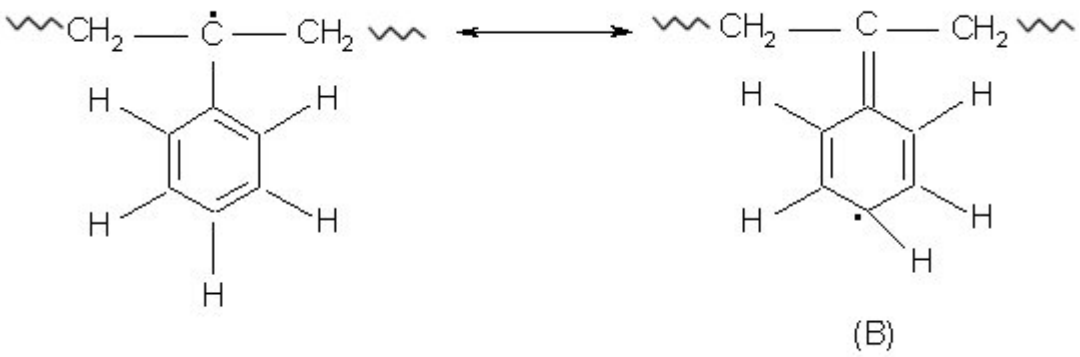

Scheme II

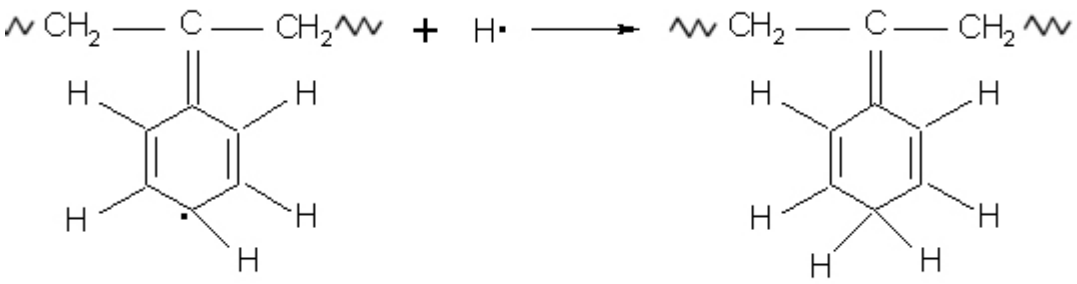

Scheme III

Figure 7.2 *Radical formation mechanisms in irradiated PS.*

The decrease in the π-π* intensity does not necessarily indicate the formation of cross-links by the ring. Aromatic polymers are known to be the most stable polymers due to the phenyl ring in which π electrons are delocalized over six carbon atoms [Akins 02]. The presence of the ring enhances the radiation stability of materials rather than an increase in the cross-linking efficiency [Feldman 94], as the yield of cross-linking for PS is rather small compared to the yields of other polymers (Table 7.1, Section 7.1.4). It was shown, that only monomeric radical cations produce the benzyl type radical which later may cause cross-linking in PS [Feldman 94, Zezin 94]. With increasing radiation dose, cyclohexadienyl radicals are formed by adding hydrogen in the para position of the phenyl ring [Delcorte 04] (see Scheme III in Figure 7.2), which also changes the symmetry in the benzene molecule and may be engaged in chemical reactions [Feldman 94, Calcagno 92, Zezin 94], including bond scission and rearrangements.

The T_{gs} measurements for poly-α-methylstyrene showed a different tendency compared to the results for PS, Figure 6.20. The temperature change between untreated and treated polymer surface is about 2 - 4 K, and this difference remains almost constant for different modification gases. T_{gs} measurements for PαMS were done up to an ion fluence of 10^{14} cm^{-2} (at this fluence no embedding of Au was observed in the case of PS). At even higher fluences, nanoclusters also did not sink in into PαMS. This may be due to the formation of a small cross-linked layer, or that the density of nuclei centres was so high and the distance between them was so close that gold clusters coalesce forming large islands resulting in a large shift in temperature at which metal clusters embeds [Erichsen 04b]. As a small change in embedding temperature was detected, the calculated cross-linking density for argon treated polymers up to an ion fluence of 10^{14} cm^{-2} is about 1 – 2.4 %. These values are much lower compared to those obtained for PS (Table 6.3), showing the accumulation of low molecular weight species on the polymer surface.

The quarternary carbon atom does not allow radical migration along the polymer chain resulting in the chain scission. Radicals formed by bond scission tend to dissociate, disproportionately, or react with a low-molecular-weight radical. PαMS under the irradiation which dissociates into a macroradical and carbocation that later will result in hydrogen abstraction, or loss of a molecule of monomer [Woods 94]. Chain scission results in the formation of monomers, dimmers, etc. with the average molecular weight is smaller than that for the pristine polymer sample resulting in an almost constant glass transition temperature for low ion fluences, see Figure 6.20. After prolonged bombardment the number of induced radicals increases. If these appear in the same position as for PS (Scheme II, Figure 7.2), these

can be resonance-stabilized resulting in an unoccupied position in the phenyl ring where cyclohexadienyl radicals may be formed. The reduction in the shake-up satellite intensity observed with XPS confirms this possibility.

In the ion fluence range of 10^{13} to 7×10^{14} cm^{-2}, in which main chemical changes take place in PS and PαMS under Ar^+ ion bombardment the removal rate of these polymers decreases, see Figures 6.3–6.5. It would be expected that polymers with preferred degradation by main chain scission, will be sputtered much faster than cross-linking polymers, because of the formation of small mass products that can desorb more easily. In this case, PαMS should be removed much faster than PS. Indeed poly-α-methylstyrene has a higher sputter rate, but only at the beginning of argon ion bombardment, Figure 6.5. At prolonged irradiation beginning at an ion fluence of 10^{15} cm^{-2}, the pristine polymer surfaces are completely modified and the rates become almost similar.

XPS analysis showed faster decomposition of the phenyl ring for α–methylstyrene in the fluence range of 10^{13} – 5×10^{14} cm^{-2}, Figure 7.1(a), which was also confirmed by mass spectra as the yield of the benzene molecule for PαMS was somewhat higher compared to the yield for PS, Figure 7.1(b). Note that the difference was observed exactly in the fluence range where the sputter rate is decreasing. However, the yield of the ring emission was much lower compared to the yields of hydrogen and acetylene which are the largest fraction of the small fragments, Figure 7.1(c), and these molecules were removed faster from PS. From another point of view, our mass spectrometer had not detected molecules having masses higher than 78 m/e (C_6H_6) when PS was sputtered with argon ions. Molecular dynamic simulations [Delcorte 00, Delcorte 04] showed that emission of PS molecules leave the surface with a rather high internal energy (0 – 40 eV). Desorbed large styrene molecules are expected to decompose into fragments before reaching the detector leading to the higher yields of small molecules. In contrast to PS, the mass spectrometer detected large PαMS fragments for very low ion fluences (up to 2×10^{14} cm^{-2}). Molecules with masses of 91 m/e (CH_2-C_6H_5), 103 m/e (C_2H_2-C_6H_5) and 118 m/e (CH_2-C_2H_3-C_6H_5, PαMS monomer) were recorded. The emission of large fragments may be the reason for higher sputter rate at the beginning of the ion bombardment. Above the fluence of 10^{14} cm^{-2}, the fragmentation of large molecules desorbed from α-methylstyrene is not excluded as only small species were recorded.

7.1.1.2 Polymethylmethacrylate and polymethylacrylate

Polymethylmethacrylate and polymethylacrylate are vinyl-type polymers containing oxygen in their chemical structure (Table 5.1). According to conventional radiochemistry PMMA preferably degrades by main chain scission while PMA undergoes cross-linking (Table 7.1, Section 7.1.4). The sputter rates of these polymers differ only up to an ion fluence of about 10^{15} cm^{-2} with PMMA having a higher rate (Figure 6.13 (b) and Figure 7.3 (a)), but the total sputter rate at an Ar^+ ion fluence of 5×10^{15} cm^{-2} is about 1.5 nm/min for both polymers.

The main chemical changes that take place in the region of decreasing rate are related to the oxygen loss (Figure 7.3 (b)), which for both polymers takes place at the same rate. However, a difference was observed in the development of some characteristic carbon features (Figure 7.3 (c)). The fitting of these functional groups is given for PMMA in Figure 6.18 (a-b). The data fitting was also done for PMA, and the same features were fitted. The difference is the ratio of these groups as no methyl is present in the PMA chemical structure. In order to make the results comparable, the intensity of carbon features had to be normalized.

The most characteristic C-O-C=O feature (marked as number 4 in the Figure 6.18 (a)) for PMMA and PMA seems to develop at different rates for these polymers. Polymethylmethacrylate loses this particular functional group faster than methylacrylate, because of the formation of less stable free radicals which prefer this group to be removed [Todd 60, Woods 94]. The C-C carbon feature remains constant up to an ion fluence of 10^{14} cm^{-2}, after which the area of the envelope increases (Figure 7.3 (c)). This feature indicates the formation of a carbon rich polymer surface with little oxygen remaining. However, small amounts of the functional group marked with the number 2 in the Figure 6.18 (a-b) may overlap with the broad C-C peak, resulting in the larger area.

XPS analysis of PMA showed slower removal of the C-O-C=O feature (Figure 7.3 (c)), but faster degradation of C-O-C groups which leads to a similar loss of oxygen for both polymers. The increase in the number of C-C bonds for PMA was rather slow, and it was not possible to fit feature 2 only at an ion fluence of 10^{16} cm^{-2}. The slower development of some features and faster degradation of other ones, may show that these groups take part in the cross-linking reactions, as the removal of side groups is not an essential feature in the polymer cross-linking [Todd 60]. It was suggested that the coupling of two polymer chains in the irradiated polyacrylates occurs via the abstraction of the α-hydrogen of the side chains and subsequent combination of the polymer free radicals [Todd 60, Chapiro 62].

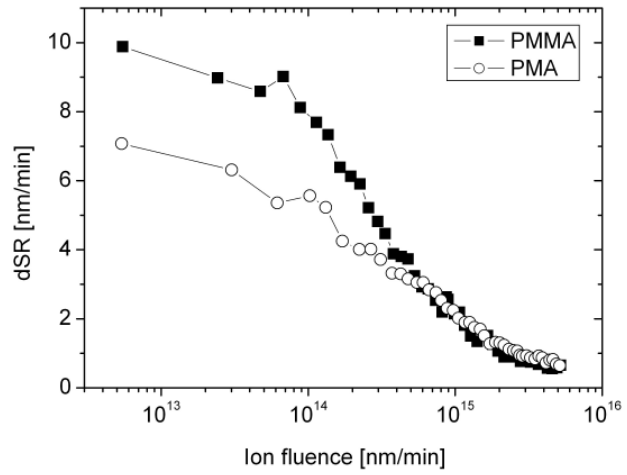

a)

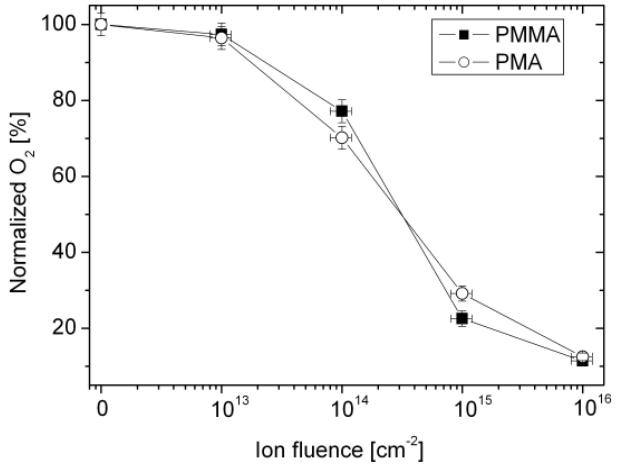

b)

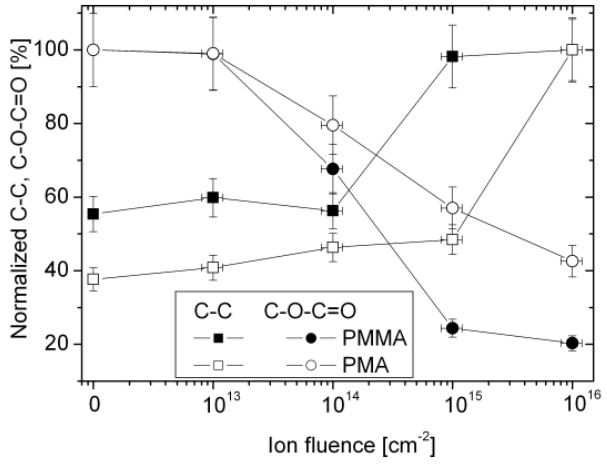

c)

Figure 7.3 *Oxygen degradation and molecule emission under 1 keV Ar^+ ion bombardment for PMMA and PMA. (a) Differential sputter rate as a function of the ion fluence. (b) XPS data of O_2 vs. ion fluence. (c) Variations of C-C and C-O-C=O features (Figure 6.18 (a-b)) under ion irradiation.*

Mass spectrum analysis of the residual gas was done while PMMA and PMA were irradiated with argon ions. No methylmethacrylate or methylacrylate monomers were detected in the mass analysis. The large fraction of H_2, CO and CO_2 molecules detected resulted from the fragmentation of $–COOCH_3$ [Fragala 98, Todd 60], proving that the ester pendent group is the primarily attacked site.

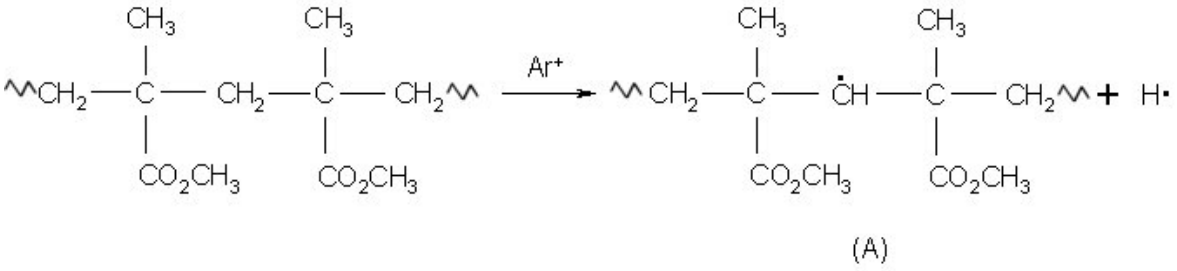

Scheme I

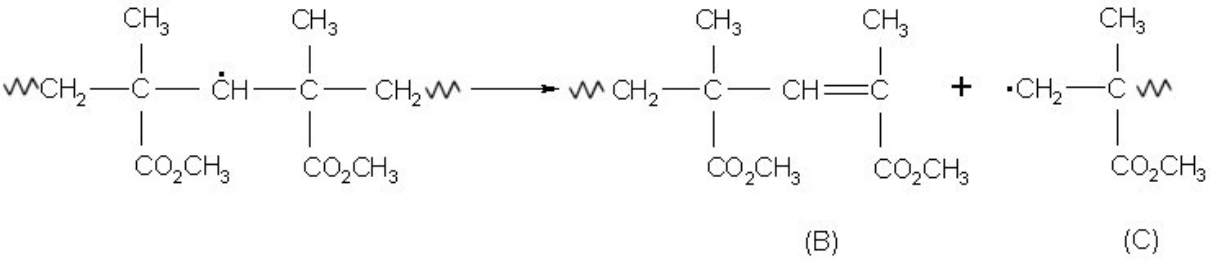

Scheme II

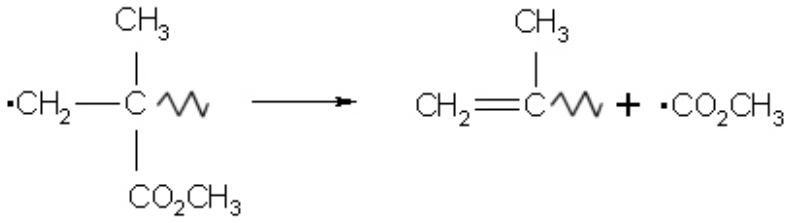

Scheme III

Figure 7.4 *Degradation mechanisms in PMMA.*

In the case of degrading polymers, it is assumed that the liberation of side groups is directly associated with main-chain scission [Todd 60]. Figure 7.4 shows possible degradation mechanisms for PMMA as proposed by a number of references [Todd 60, Woods 94, Chapiro 62, Gupta 80]. A free radical (A) (Scheme I) is formed by removal of a secondary hydrogen

atom. The radical (A) is too large to react with another radical of its kind resulting in decomposition resulting in an unsaturated polymer chain end (B) and another free radical (C), Scheme II. Radical (C) is less stable than radical (A) and so it may react in different ways [Todd 60], where the most probable results in the liberation of a $\cdot COOCH_3$ radical (Scheme III). There is also the possibility that radical (C) follows internal rearrangements to give a double bond and remove methyl radical. On the other hand, different mass spectrographic studies of the volatile products of PMMA have indicated that the CH_3 groups remain attached to the main chain [Todd 60, Lehockey 88].

Another proposed mechanism for PMMA degradation is the abstraction of the ester group occurring first [Lechokey 88]. This destabilizes the main chain resulting in its cleavage. The abstraction of one $COOCH_3$ group leads to the one backbone bond scission.

The decrease in the sputter rate is accompanied by the induced chemical changes in PMMA and PMA. The changes mostly involve loss of oxygen and formation of carbon rich polymer surfaces. As carbon is the element with the lowest sputter yield, the final removal rate of polymers is much lower compared to the initial one. The cross-linking reactions are believed to reduce the polymer removal, like in the case of PMA. PMMA undergoes preferred chain scission. However, cross-linking of PMMA through the recombination of free radicals formed by hydrogen abstraction [Chapiro 62] cannot be excluded, as some reports on PMMA network formation were published [Chapiro 62, Calcagno 92, Lechokey 88], as well as a small increase in the surface glass transition temperature was measured, Figure 6.20.

7.1.1.3 Polyacrylonitrile and polymethacrylonitrile

Polyacrilonitrile and polymethacrylonitrile belong to the group of polymers that contain nitrogen in their chains (Table 5.1). Following conventional radiochemistry and proposed empirical rules, PAN preferably cross-links, and the polymer containing CH_3 groups in the α-substituted carbon, undergoes chain scission (Table 7.1, Section 7.1.4).

Chemical changes that occur in the region of sputter rate reduction (Figure 6.13 (b)) are related mainly to nitrogen elimination and/or rearrangements (Figure 7.5 (a)). During the argon ion bombardment up to 60 % of nitrogen was removed from the polymer surfaces. In the case of polyacrylates (Figure 7.5 (b)), the removal rate of nitrogen is similar to the ones for PMAN and PAN. However, the -C≡N feature is eliminated faster for methacrilonitrile (Figure 7.5 (b)). This can be explained in the same way as for PMMA, if an unstable radical of the kind of $\cdot CH_2\text{-}CCH_3CN$ (similar to the free radical for PMMA, Figure 7.4, Schemes II and III) is formed, the side chain group -C≡N is preferentially removed.

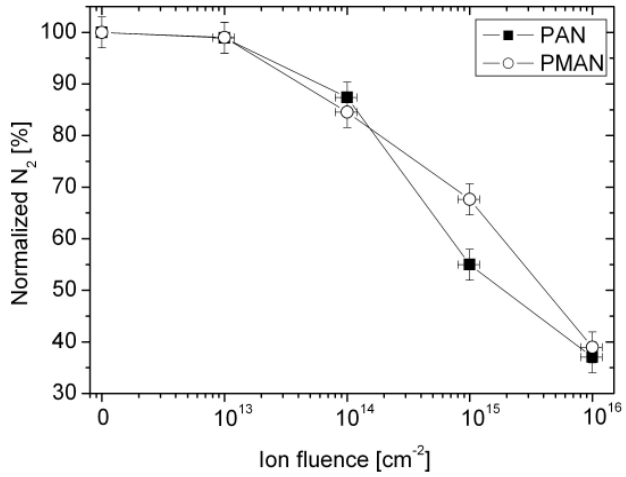

a)

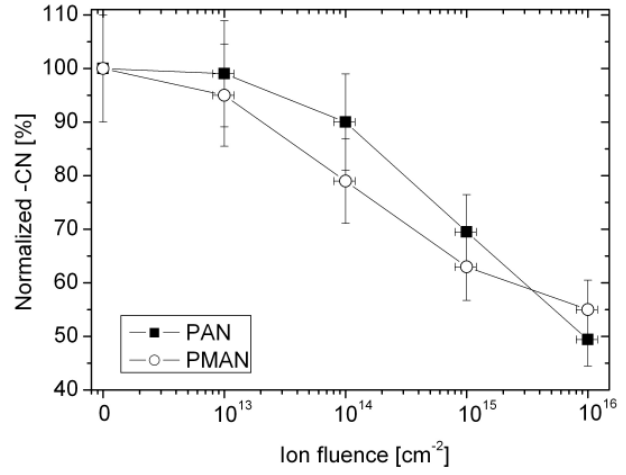

b)

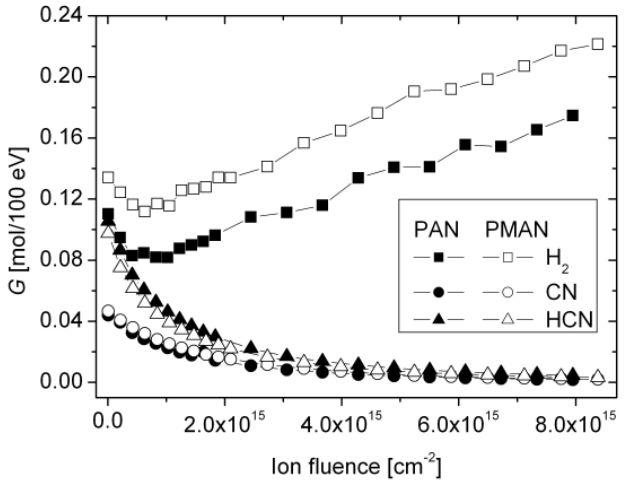

c)

Figure 7.5 *Nitrogen degradation and molecule emission under 1 keV Ar^+ ion bombardment for PAN and PMAN. (a) XPS data of N_2 degradation vs. ion fluence. (b) Variation of the -C≡N feature under ion irradiation. (c) Relative chemical yields of molecules emitted.*

Mass spectra analysis confirmed the -C≡N group removal, which reacted with eliminated hydrogen atoms to form large fractions of hydrogen cyanide (HCN), Figure 7.5 (c). CN and HCN, as well as nitrogen, decreased with the irradiation up to an ion fluence of 3 – 4×10^{15} cm^{-2}, which is approximately the same as detected with XPS.

A most interesting effect was observed for the hydrogen removal. According to the residual gas analysis, the amount of H_2 decreased up to an ion fluence of 10^{15} cm^{-2} for both polymers and then started to increase, even if degradation of CN or pure nitrogen reached the steady-state region. The reason could be the rearrangements of –C≡N side groups to –C=N– conjugated sequences resulting in polymer cyclization, as observed for thermal degradation of PMAN and PAN [McNeill 89]. The gaseous products detected in the mass spectrometer are not the result of the cyclization. These are formed by the splitting of side or end groups. The conversion of nitrile groups into conjugated bonds was also observed when PAN was irradiated with various species at high energies [Pivin 95]. The C-H peak, detected with FTIR, decreased with increasing fluence as formation of –C=N– bonds increased [Pivin 95]. The elimination of C-H bonds confirmed the degradation of H_2 molecules rather than reaction of hydrogen with other emitted species. On the other hand, according to the proposed mechanisms of cross-linking [Todd 60, Woods 94, Charlesby 60], the rupture of C-H bonds preferably leads to the formation of networks through the combination of the polymer free radicals. Breaking of such bonds will always result in the emission of hydrogen.

7.1.2 Polymer degradation under nitrogen and oxygen ions

A polymer is said to be etched if it is bombarded with nitrogen, oxygen or other ions obtained from reactive gases. Sputter or etch rate results for PS, PαMS and PMMA under 1 keV N_2^+ and O_2^+ ion irradiation are given in Figures 6.3-6.5. The removal rates of polymers obtained for nitrogen or oxygen ions show the same dependence on the ion fluence as for sputtering with argon ions: the rate decreases up to the point where a steady-state region of polymer sputtering starts. Polymers bombarded with nitrogen are etched almost at the same rate as with argon ions, while sputtering with oxygen results in the fastest polymer removal. Additional to the surface sputtering, reactions with N_2 or O_2 take place in the irradiated polymer layer. As a result carbon nitrogen or carbon oxygen groups are formed, or old functionalities are reorganized, see Figures 6.17 and 6.18 for PS and PMMA, respectively. The decrease in the rate is observed up to an ion fluence of 5×10^{14} cm^{-2} for PS and PαMS and 10^{15} cm^{-2} for PMMA. These are the fluence ranges where main chemical changes occur through the abstraction of hydrogen, but instead of one chain radical reacting with another

chain radical, oxygenation and/or nitrogen incorporation also take place [Moss 86, Idage 98, Lianos 94].

For styrene polymers, amine (C-N) and imine (C=N) functionalities are formed initially when polymers are bombarded with nitrogen. Later, above an ion fluence of 5×10^{14} cm^{-2} C-N-C and N-C-N groups are detected, Figure 6.17(e-f). Here, like for argon treated styrene polymers, a shake-up satellite, representing the phenyl ring, loses its intensity at prolonged ion irradiation suggesting that the ring is one of the primary attack sites [Idage 98]. In the case of PMMA, not only carbon-nitrogen but also nitrogen-oxygen functional groups are formed, Figure 6.18(e-f). The intensity of oxygen, recorded with XPS, decreased as the amount of nitrogen increased, finally resulting in more N_2 than O_2 on the film surface, Figure 6.14 (d). The rate at which oxygen was removed from the surface was the same as obtained for argon ion bombardment.

The removal rate of polymers for oxygen bombardment was observed to be the largest for any ion beam or plasma etching [Gokan 83, Moss 86, Eggito 90]. So called "oxidative degradation" is added to the radiation chemical events [Chapiro 88] which is the reason of the degradation events in polymers which normally cross-link. One of the primary processes of radical formation is the abstraction of hydrogen by breaking of C-H bonds. The chemical reactions take place between the molecular oxygen and free radicals resulting in peroxyradicals (COO·) (reaction (7.1a)) that in reaction with hydrogen can be stabilized by the formation of hydroperoxide (CHOO) and a new radical site that participates in further reactions (7.1b), [Moss 86, Eggito 90, Lianos 94]. When an alkoxy radical (CO·) is formed, there is large probability that chain cleavage will take place (7.1c).

$$R - C^{\cdot} - C - R + O_2 \rightarrow R - COO^{\cdot} - C - R \qquad (7.1a)$$

$$R - COO^{\cdot} - C - R + RH \rightarrow R - COOH - C - R + R^{\cdot} \qquad (7.1b)$$

$$R - COOH - C - R \rightarrow R - CO^{\cdot} - C - R + HO^{\cdot} \qquad (7.1c)$$

$$\downarrow$$

$$R - C = O + {}^{\cdot}C - R$$

$$\text{(I)} \qquad \text{(II)}$$

Cleavage product (I) (in Equation 7.1c) is stable and requires further attack on the chain before any volatile products are formed. Radical (II) should unzip along the whole chain, or if the unzipping reaction is not possible, the radical will react with another oxygen molecule leading to further reactions [Moss 86]. If the polymer is already fully oxidized, new oxidation pathways are initiated on formerly oxidized sites forming acids, esters or carbonate features, or inducing further chain decomposition [Lianos 94].

There are several mechanisms for oxidation that can take place in PMMA, since there are several potential sites for C-H bond rupture. One of the mechanisms of oxidative degradation for PMMA is schematically presented in Figure 7.6. When a $CO^{\cdot}$ radical is formed through the abstraction of OH from hydroperoxide, auto-oxidative cleavage of the main chain occurs with stable structure (I) and radical (II). The radical (II) will degrade by an unzipping and depolymerization step [Egitto 90, Moss 86]. If additional unstable radicals are formed, they undergo alternative reactions more readily forming volatile products that are desorbed from the polymer. It should be noted, that PMMA under O_2^+ irradiation loses carbon-oxygen functionalities at lower rates compared to argon and nitrogen treatments, Figure 6.14(d), indicating that some bond reorganization takes place, Figure 6.18(c-d). The rearrangements were observed to occur above an ion fluence of 10^{15} cm^{-2}, where the PMMA sputter rate was in the steady state regime and the C/O ratio remained constant, Figure 6.14(b). The intra- and inter molecular reorganization may also take place in polymethylmethacrylate, forming cycles or additional unsaturated carbon-oxygen (mostly C=O type) functional groups as proposed by Lianos et al. [Lianos 94].

PS does not contain oxygen in its initial polymer structure, therefore surface oxidation takes place at the beginning of the polymer irradiation. Oxidation is very likely to result at the tertiary carbon after the removal of the hydrogen atom, Figure 7.7 (Scheme I). Chain fragmentation occurs because of the $CO\cdot$ radical. Stable structure (I) requires additional attack on the chain to form volatile products resulting in sputtering of the polymer. Radical (II) cannot unzip, but reacts with molecular oxygen leading to the formation of another stable structure.

The radical formed at the tertiary carbon after the rupture of the C-H bond can be stabilized by the radical resonance phenomena, Figure 7.7 (Scheme II). The radical that moved to the phenyl ring may react with oxygen and after intermolecular reorganization stable structures containing oxygen in the aromatic unit may be formed [Lianos 94, Moss 86]. The existence of the oxygen reactions with the PS aromatic rings is supported by AR-XPS spectra, Figure 7.8. The figure demonstrates the normalized ratios of the shake-up/C1s (solid

symbols) and O1s/C1s (open symbols) ratios of the XPS lines vs. take-off angle for different O_2^+ ion fluences. Degradation of the aromatic ring starts at the outer-most polymer surface layer (take-off angle 50-75°), while at the same time first carbon-oxygen functional groups are formed on top of the surface. It is very probable that the π-π* satellite loses its intensity most probably because of the change in the ring symmetry due to the reactions including oxidation and cross-linking. The oxygen incorporation at the ring sites was also demonstrated by a number of authors [Lianos 94, France 98, Shard 92]. Shard and Badyal [Shard 92] concluded that C-O linkages originated from aliphatic carbon components, while unsaturated carbon-oxygen functionalities (C=O, O-C=O) resulted from the oxygen reaction with the phenyl ring.

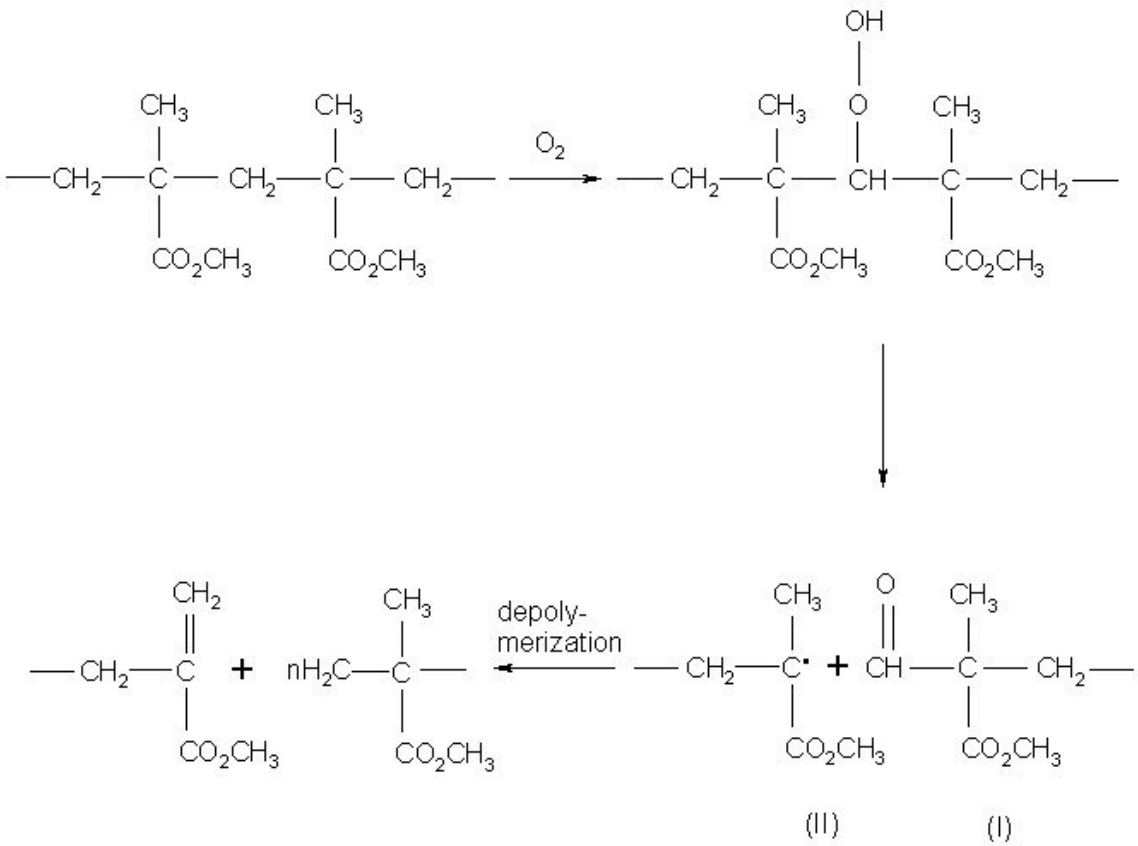

Figure 7.6 *Oxidative degradation of PMMA, [Moss 86, Eggito 90, Lianos 94].*

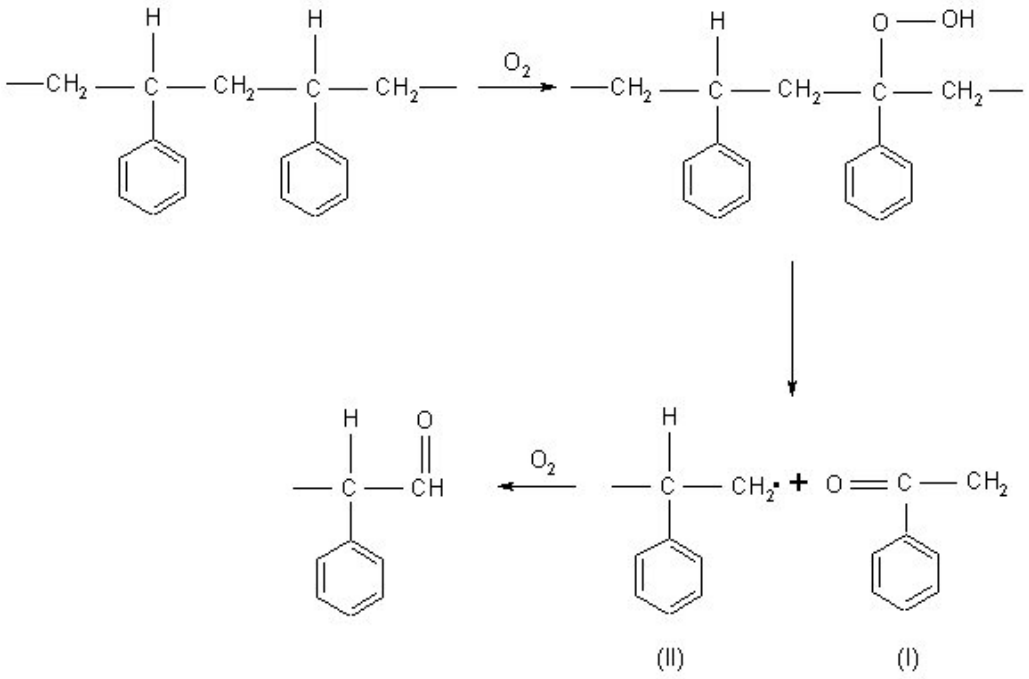

Scheme I

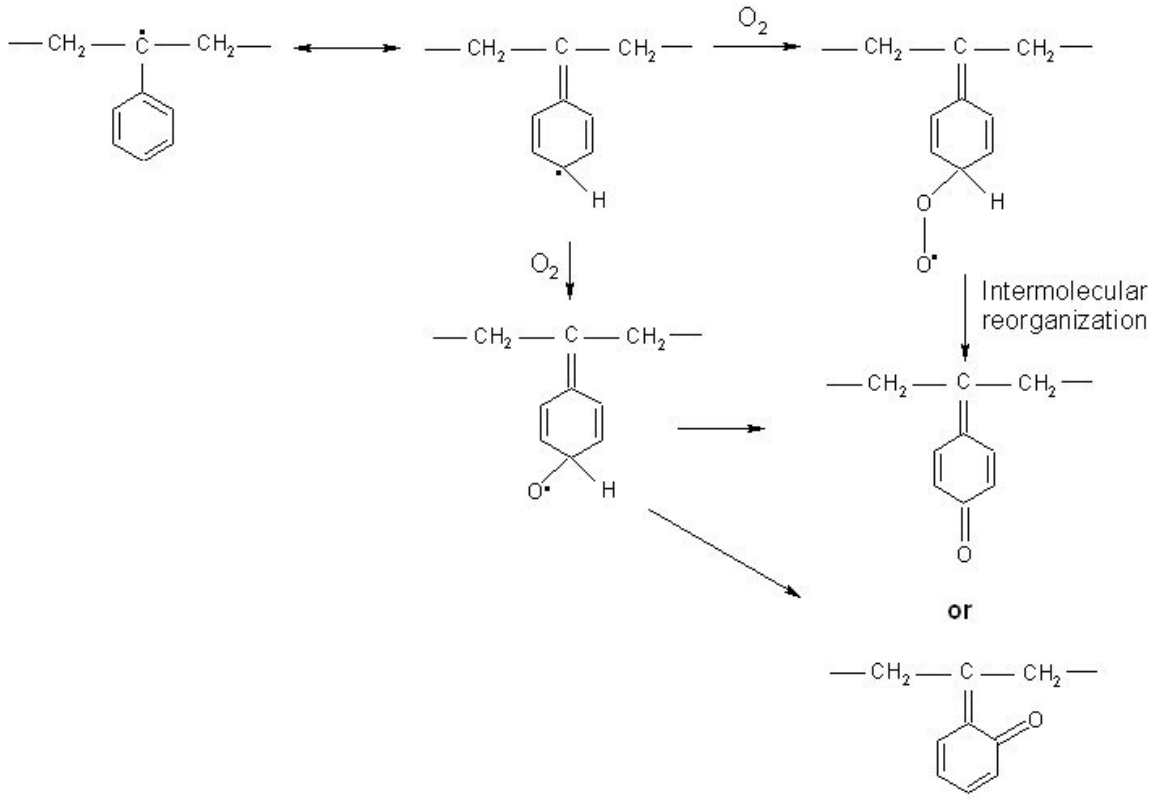

Scheme II

Figure 7.7 *Oxidative degradation of PS, [Moss 86, Eggito 90, Lianos 94].*

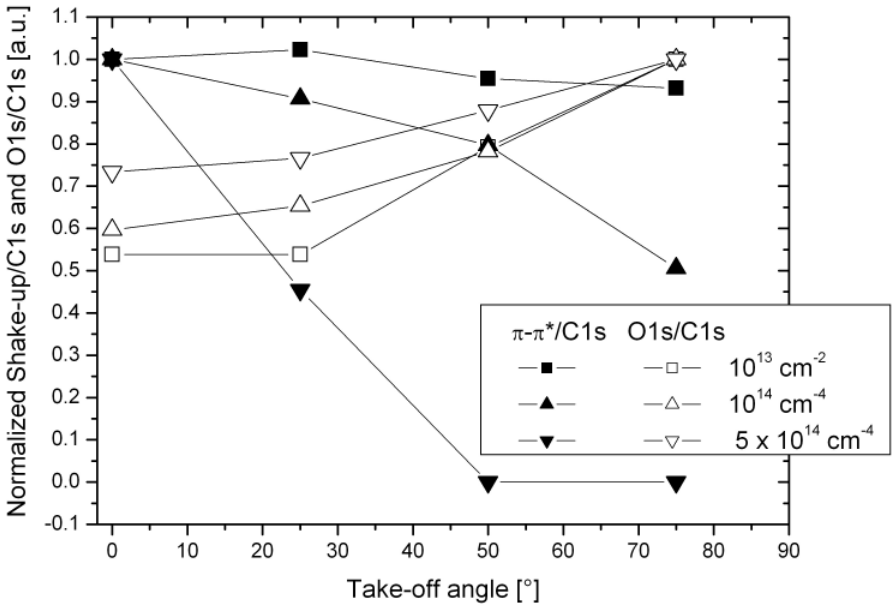

Figure 7.8 *Normalized ratios of shake-up/C1s (solid symbols) and O1s/C1s (open symbols) ratios in XPS lines vs. take-off angle for different O_2^+ ion fluences.*

PαMS preferably undergoing chain scission should also degrade by oxidation as PMMA does. However, the aromatic unit present in the polymer protects α-styrene from degradation by absorption of the energy initially transferred onto the whole polymer molecule. Reaction of oxygen with the phenyl ring is also likely as the π-π* intensity of the shake-up satellite decreased with increasing oxygen content, and carbon-oxygen functional groups similar to those fitted for PS (Figure 6.17) were obtained.

Comparing the sputter rate obtained for different ions, it is noted that polymers bombarded by nitrogen are removed at rates close to those obtained for argon sputtering, Figures 6.3 - 6.5. Nitrogen incorporation into polymers makes the polymer surfaces rather stable and less susceptible to surface reorganization [Idage 98, Gerenser 93]. Also, cross-link formation in the N_2 irradiated polymers cannot be excluded as an increase in surface T_{gs} (Table 6.3) was observed. Oxygen, on the other hand, induces oxidative degradation leading to enhanced chain scission in addition to the chemical modification. Inter- and intramolecular reorganization [Lianos 94] results in unstable polymer surfaces that may lead to the formation

of volatile products. Additionally, oxygen is highly electronegative as compared to argon and nitrogen which makes it suitable for use in fast polymer degradation.

7.1.3 Influence of the sample temperature on polymer ablation

When ions interact with a polymers surface, certain chain bonds are broken resulting in abstraction of small molecular fragments, reaction of free radicals with reactive species, macroradical formation which later can decompose forming stable structures and other radicals. The schematic diagrams of polymer decomposition under ion irradiation given in Figures 7.2, 7.4, 7.6, 7.7 are rather similar to those proposed for thermal degradation of polymers [Tsuge 97, McNeill 89]. In order to understand what mechanisms occur during ion bombardment of polymer surfaces, the ablation rate was determined as a function of the sample temperature.

Polymers that preferably cross-link or degrade were selected to demonstrate the influence of the substrate temperature on the sputter rate of organic films. The rate dependence on the sample temperature was shown in Figure 6.10 for PS and PαMS. Where polystyrene sputters at a constant rate up to 460 K, the poly-α-methylstyrene film is sputtered faster with increasing temperature. However, the tendency of the sputter rate at elevated temperatures remained the same as observed at room temperature, i.e. the rate decreases with increasing ion fluence until a steady state regime is reached, as reflected from the variation of the intensity of emitted species, Figure 6.11.

PS and PαMS undergo depolymerization (reactions that induce the reduction of macromolecular size without changing the chemical composition or altering the monomer unit structure) due to a conventional thermal decomposition process. Only, PαMS degrades by chain end scission resulting in about 100% monomer formation. For this polymer, no hydrogen transfer reactions take place and, hence, unzipping or depropagation occurs. PS undergoes random chain scission, chain end initiation, intramolecular hydrogen transfer, and bimolecular termination resulting in a lower monomer yield (~ 40 %) together with the degradation products which are a mixture of saturated and unsaturated molecules, mostly dimers and trimers [McNeill 89, Peterson 01].

When polymer films were heated only, Figure 7.9(a), some small mass molecules of PS were detected above 520 K, which included fragments like hydrogen, C_4H_3, and phenyl rings. Monomers of the PS molecule were not detected over the whole heating range (up to 573 K). Actually, main degradation products like monomers, dimers, trimers and toluene are

formed above 573 K [McNeill 89]. PαMS starts to decompose already above 230 °C (503 K), which is close to the temperature (523 K) observed by conventional pyrolysis [McNeill 89]. The mass spectrometer recorded the same volatile products as for PS including α-methylstyrene monomers. Mass analysis of some molecules for polymers that were sputtered with 1 keV Ar^+ ions at defined temperatures is shown in Figures 6.11, 6.12. Graphics (b) and (c) in the Figure 7.9 compare the phenyl ring and monomer evolution recorded for thermal treatment only and sputtering done at elevated temperatures.

Argon ion beam sputtering of PS in the temperature range of 300 – 460 K does not produce large yields of volatile products. It was observed that the emission of large molecules (51, 77, 91 m/e) increased by 40 %, while the yield of smaller molecules decreased by the same amount. Nevertheless, the total change in the emitted molecule yields remained constant in this temperature range, and so no change in the sputter rate of PS was observed up to a temperature of 460 K, above which the rate increased by three times, Figure 6.10. At this temperature, the yields of the emitted large molecules increased and were detected for higher fluences, compared with the time measured at lower temperatures, Figure 6.11 (a-b). It should be noted, that ion bombardment of heated samples resulted in monomer desorption at temperatures above 403 K, while in conventional pyrolysis monomers are formed above 573 K [McNeill 89, Schnabel 81].

When an ion impacts onto the polymer surface, energy is deposited within a small volume. As a result, this volume becomes energized and has some local temperature, *T*. What is the influence of the local temperature raised by the ion interaction with the surface on the sputter rate of the polymer? The obtained results suggest that the local temperature is not higher than the thermal degradation temperature of the polymer, as the intensities of the emitted species at room temperature are not higher than the fragment intensities obtained for thermal degradation. If the ion induced temperature was much higher than the thermal degradation temperature, there would be no influence of elevated substrate temperatures on the ablation rate, as well as no influence of the ion chemistry on the removal rate. When the polymer is heated and bombarded with ions, we assume that the local temperature has some influence on the polymer degradation.

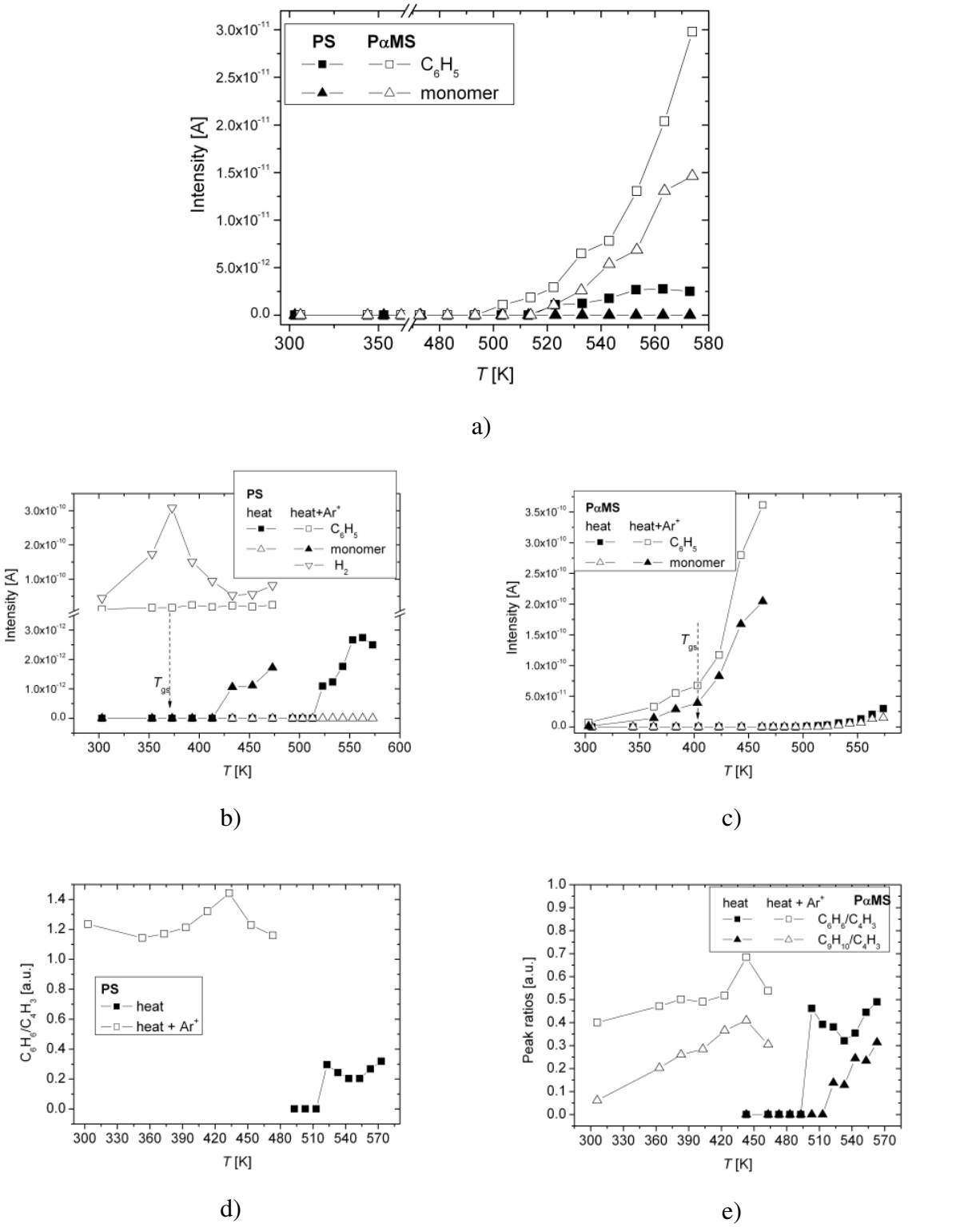

Figure 7.9 *Residual gas mass analysis of the molecule evolution as a function of temperature for PS and PαMS. (a) Molecule emission from heated polymer films. Comparison of phenyl ring and monomer intensities for heated and sputtered (b) PS and (c) PαMS. The ratios of the characteristic mass peaks as a function of the sample temperature for heated and sputtered (d) PS and (e) PαMS. Sputtered mass spectra were taken at an ion fluence of* 10^{13} cm^{-2}.

The intensities of the desorbed species increased when the polymers were sputtered at elevated temperatures. However, the detected molecules under the ion bombardment conditions are emitted at the same ratio as those obtained for pure heating in the case of PαMS, Figure 7.9(e). This suggests that polymer degradation mechanisms during sputtering are similar to those observed for thermal degradation. In the case of PS, Figure 7.9(d), the mass ratio during sputtering is much larger than that determined during heating. It should be remembered, that thermal degradation of PS starts above 573 K. And in our case, we performed heating only up to 573 K. Therefore, comparison between characteristic mass ratios cannot be done because of the missing data.

PS is a polymer with preferred cross-link formation. Ion irradiation breaks bonds resulting in formation of radical, which at elevated temperatures can easily participate in reactions with one another forming cross-link networks. This happens faster than at room temperature, due to the enhanced chain mobility. On the other hand, it is believed that in PS cross-linking takes place primarily via hydrogen abstraction [Chapiro 62]. Mass analysis showed an increase in hydrogen molecule emission up to a temperature of 373 K, which is the glass transition temperature of this polymer. Above T_g, the hydrogen intensity started to decrease. The most probable explanation is that the enhanced network formation occurs in PS sputtered at temperatures up to the glass transition temperature. Above this temperature, the viscosity of the polymer decreases, while the chain mobility and reaction rates increase. When PS is sputtered at temperatures above 380 K, free radicals can not only combine with each other forming cross-links, but also participate in intra- or intermolecular hydrogen transfer resulting in main-chain scission and formation of macroradicals. With increasing sample temperature, the cleavage of the backbone bonds should occur more often, and termination, disproportionation or recombination reactions should result in formation of monomers and/or lower or higher mass volatile molecules leading to the increase in the ablation rate of PS above 470 K. As observed in the experiments, monomer formation starts at lower temperatures compared to conventional pyrolysis. This is attributed to the ion beam induced depolymerization [Fragala 99].

When hydrogen at the tertiary carbon is substituted by a methyl group, monomer production is increased during thermal decomposition but thermal stability is reduced. Figure 7.9(a) shows monomer emission from PαMS already above 510 K, while PS does not show any styrene molecule formation during sample heating up to 573 K. Argon ion bombardment results in monomer emission at temperatures much below the depolymerization temperature (520 – 570 K) [McNeill 89]. PαMS is the only polymer that degrades by monomer emission

even at room temperature [Woods 94]. However, the yield of monomers is very low, and the main degradation products are hydrogen and acetylene molecules, see Figure 7.1. Monomer emission is enhanced by argon sputtering of heated samples. Below the surface glass transition temperature (~400 K), the changes in the yield of the α-methylstyrene molecule and the ablation rate are constant. Above T_{gs}, the sputter rate and molecule emission increases constantly up to some saturation, which can be attributed to the competition between monomer desorbtion and diffusion inside the polymer [Fragala 99]. If it is considered that thermal unzipping depolymerization of PαMS starts above 520 K, it is possible that the ion beam induced low temperature depolymerizarion is similar to that observed for PMMA [Fragala 98]. When a polymer chain is broken macroradicals are formed, end-chain initiation involves the breaking or unzipping of small units at the end of the chain resulting in the formation of monomers and radicals which further depropagate producing monomer units.

7.1.4 Sputter rate dependence on polymer chemistry

The discussion above concentrated on the dependence of the polymer sputtering rate on the ion beam parameters and the sample temperature. The removal rates of polymers showed the same tendency when the rates were analyzed as a function of the ion beam parameters. It was shown that the decrease in the polymer sputter rate is accompanied by chemical rearrangements in the polymer structure. Bombardment with reactive gases like oxygen induce oxidative degradation leading to sputter rates higher than those obtained by irradiation with argon or nitrogen ions. However, when the polymer chemistry is considered, the behaviour of the polymer rates is more complicated as shown in the experiments for the ablation rate dependence on the sample temperature. The ablation rate of PS remained constant with increasing sample temperature, while PαMS was sputtered faster when sample was heated. Therefore, the sputter rate dependence on polymer chemistry should be discussed in detail.

Ion bombardment induced chemical changes were discussed in some detail. In all cases, rearrangement of polymer bonds, loss or formation of characteristic carbon-oxygen or carbon-nitrogen functional groups, molecular emission, chain degradation and cross-linking took place in the ion fluence range of $10^{13} – 10^{15}$ cm^{-2} (depending on the polymer and the ion chemistry), where a decrease in the sputter rates of polymers is observed (Figures 6.5, 6.13). Changes for every organic film occurred individually, but at the end surfaces became enriched in carbon in the case of argon treatment, or contained additional oxygen or nitrogen. In any case, only little memory of the original polymer structure was left in the steady-state region.

The results above showed that polymers of the cross-linking type were sputtered slower than those that preferably degrade by main-chain scission. Cross-linking and degradation are non-equilibrium processes that change the structure of the polymer leading to changes in the physical properties. Cross-linking transforms a linear polymer into a three-dimensional molecule, resulting in an increase in molecular mass, lower solubility in organic solvents, and improved mechanical properties [Woods 94, Chapro 62]. Degradation results in a decrease in molecular mass, and usually has opposite effects on the physical properties. Degradation and cross-linking occur simultaneously, but the ratio of their rates depends on the chemical structure of the polymer, its physical state, and the irradiation conditions. Generally, polymers are divided into those that predominantly cross-link or undergo degradation under the bombardment with energetic particles.

A general empirical rule was derived based on the chemical structures of polymers given in the Figure 7.10. When the structure of a vinyl polymer is such that each carbon atom of the main chain caries at least one hydrogen atom and R may be H or another atom or group, the polymer cross-links, Figure 7.10 (a). Scission preferentially takes place in polymers having the structure shown in Figure 7.10 (b), where R_1 and R_2 are any atom or group but hydrogen. In this case, a tetra substituted carbon atom is present weakening the bond of the backbone chain [Woods 94, Chapro 62].

a) b)

Figure 7.10 *Chemical structures of vinyl polymers that predominantly (a) cross-link or (b) degrade under ion bombardment.*

The rule is not necessarily applicable to polymers whose backbones contain atoms other than carbon. As an example, polyisobutylene, $(\text{-}CH_2\text{-}C(CH_3)_2\text{-})_n$, and polydimethylsiloxane, $(\text{-}Si(CH_3)_2O\text{-})_n$, have two side-chain methyl groups. However, under

the irradiation only PIB predominantly degrades, while polydimethylsiloxane prefers to cross-link [Woods 94].

Following this rule and a number of literature [Woods 94, Taylor 80, Chapiro 62, Charlesby 60, Fink 04, Charlesby 87, Schnabel 81], polymers used in the experiments can be divided into those that predominantly cross-link and those that predominantly degrade, Table 7.1. An important quantitative characteristic of radiation induced cross-linking or scissioning is described by the chemical yields of cross-links, $G(X)$, and degradation, $G(S)$, that are defined as the number of cross-links or scissions, respectively, formed per 100 eV of energy absorbed. The values of $G(X)$ and $G(S)$ for the polymers used are listed in the Table 7.1. Note that these are values for polymers irradiated with γ- or X-rays at room temperature

According to the experimental observations it can be concluded that polymers with preferred cross-link formation should have a lower sputtering rate compared to the rates of polymers that predominantly degrade under irradiation. This is assumed since during preferred chain scissioning molecules of small mass are formed, and some of them can be easily ejected. But cross-linking results in an increase in molecular weight which makes it difficult to emit molecules that contain tens or hundreds of monomers. Comparing the results presented in Figure 6.13 with the dominating process listed in the Table 7.1, polymers having a tetra-substituted carbon atom (PαMS, PMAN, PMMA) are removed faster than those having no additional methyl group (PS, PAN, PMA). Additional results are presented in the Table 6.2 and repeated in Table 7.1 showing that Teflon-like polymers (PTFE, FEP, Teflon AF) are sputtered with the largest rates and these are polymers of the degrading type.

If polymers have a higher yield of chain scissioning, the sputter rate of such polymers should increase with the chemical yield, while those with a higher cross-linking yield should have lower rate. Comparing $G(S)$ values and experimental results for the sputter rate of the four polymers that degrade under conventional ionizing radiation, the sequence of increasing removal rate is PαMS → PMAN→ PMMA → PIB → PTFE → Teflon AF. The correlation agrees well with the values of $G(S)$ with one exception. According to the given data, polymethylmethacrylate has a lower chemical yield of degradation compared to PMAN, but the sputter rate under ion irradiation is higher for PMMA, Table 7.1.

Table 7.1 *Experimental values for the total sputter rate obtained for 1 keV Ar^+ ion bombardment, chemical yields of* cross-*linking and degrading polymers calculated after irradiation of γ- or X-rays at room temperature, and monomer yields by thermal degradation.*

Polymer	**Total sputter rate** [(a)], nm/min	***G*(X),** [(b)] cross-links/ 100 eV	***G*(S),** [(b)] scissions/ 100 eV	**Dominating process**	**Monomer yield,** [(c)] %
PS	0.30	0.02 – 0.2	0.01 – 0.02	cross-linking	42-45
PAN	1.04	0.59		″	5
PMA	1.53	0.5		″	0.7 – 2
BPA-PC [(d)]	0.40	0.13 – 1.34	0.17 – 0.67	″	-
PMDA-ODA [(e)]	0.128	-	-	?	-
PBO [(e)]	0.072	-	-	?	-
Nylon 11	2.51	0.5 – 1.15	0.6 – 1.4	″	-
PαMS	0.59		0.25	degrading	> 95
PMAN	1.22	< 0.05	3.3 – 3.6	″	90
PMMA	1.56	0.03	1.1 – 2.6	″	91-98
PIB	1.59		2.8 - 5	″	20
PTFE	7.36		3 – 5	″	> 95
Teflon AF	18.57		3 – 5	″	> 95

(a) Experimental results for the total sputter rate taken from Table 6.2.

(b) Values of the G(X) and G (S) are taken from [Woods 94, Brandrup 99, Calcagno 92].

(c) Monomer yields by thermal degradation were taken from [Krevelen 90].

(d) No information of a dominating process was found in the literature. But comparing the yield values, cross-linking should be preferred to chain scission.

(e) No information of chemical yield was found in the literature.

In the case of cross-linking polymers, the correlation between $G(X)$ and the sputter rate results is opposite than expected. PMA and PAN have rather high cross-linking yields compared to polystyrene. But under ion bombardment, PS has the lowest sputter rate and PMA with PAN are removed much faster, Table 7.1 and Figure 6.13. BPA-PC and Nylon 11 have similar yields of cross-linking, and compared to other values given in the table may form networks much faster. However, BPA-PC sputters faster than PS, and nylon has the highest removal rate of the investigated cross-linking polymers. When the rates of groups of polymers having a similar chemical structure are compared, the tendency is the following: acrylates are sputtered with the highest rate, then come acrylonitriles and styrenes, which have the lowest rate. This leads to the conclusion, that preferred degradation by main chain scission does not necessarily leads to high sputter rates, as well as induced cross-linking does not make polymer films more resistant to irradiation. Thus, the correlation between sputter rates and chemical yields can be applied only partially.

A partial correlation is observed between ion irradiation and thermal behaviour of the polymers, Table 7.1. Those polymers of degrading type have a high yield of monomers, and so are expected to be sputtered faster, as shown in the previous section 7.1.3 where the ablation rate of PαMS increases with increasing temperature, as the methyl groups are responsible for the depropagation reactions favouring chain degradation [Charlesby 60]. Polymers with preferred cross-linking have low yields of monomers for thermal decomposition, because of the α-hydrogen that prefers transfer reactions leading to network formation. The monomer yields of such polymers decrease with increasing $G(X)$ (Table 7.1). Fluorine containing polymers, like FEP, PTFE and Teflon AF, are resistant to transfer reactions [Krevelen 90]. Fluorine containing polymers undergo depolymerization of the radicals to monomers resulting in high monomer yields [McNeill 89]. Nevertheless, the correlation between sputter rates and monomer yields is not self explaining. When the comparison is done between the polymers of the same group, polymers of the cross-linking type are sputtered slower. However, comparing experimental sputter rates and monomer yields of cross-linking polymers only, it was observed, that the rates increased with decreasing monomer yields. The polymers with preferred chain scission have the same monomer yield, even if Teflon-like polymers are sputtered much faster than other ones.

Gokan et al. [Gokan83, Gokan 85] suggested an empirical rule, which assumed that the sputter rate of polymers is inversely proportional to the carbon content, as carbon is the main element in metal free polymers and has the lowest removal rate of all elements. Later it was noticed, that polymers containing oxygen were sputtered faster. Therefore, the statement

was corrected including the contribution of oxygen. The authors have found, that the sputter rates of polymers under argon or oxygen ion beam treatment linearly depend on the $N_T/(N_c-N_o)$ factor, where N_T is the total number of atoms in the monomer unit, N_c and N_o are the number of carbon and oxygen atoms in the monomer unit, respectively. If this dependence is true, then N, or F atoms in the polymer structure should not influence the rate, and the chemical bond strength may not be important in polymer removal, as was stated by the authors.

Figure 7.11(a) shows the dependence of the polymer sputter rate on the factor $N_T/(N_c-N_o)$ for polymers listed in Table 7.1, except PBO as the complete chemical formula was not known. The linear dependence is very weak. Polymers with the highest sputter rates, according to the assumption and experimental data obtained by Gokan, should posses the largest ratio. However, Nylon 11, and Teflon-like polymers are above the fitted line. On the other hand, the rate values given in the figure are obtained at an ion fluence above 10^{15} cm^{-2}. In this region, polymers are already in the steady-state sputtering region. The chemical structure of the virgin polymer surface is altered and enriched with carbon, with little memory of the pristine polymer. Taking this into account, experimental values of the sputter rate (from the Figure (a)) were plotted against the ratio N_T/N_c, where number of carbon atoms was taken from the monomer unit of the untreated polymer, Figure 7.11(b). At this sputter stage, the removal rate is inversely proportional to the carbon content in a unit volume, for vinyl polymers, PMDA-ODA and BPA-PC. Teflon AF, PTFE and FEP having the highest sputter rates, like in the previous figure, do not show a linear dependence on the ratio. Their rates are higher than expected from the law of linear dependence.

Experimental results presented in Table 7.1 were obtained for vapour deposited Teflon AF (in the Figure 7.11 marked Teflon AF^1). Organic films prepared by evaporation have shorter chain lengths which may lead to faster formation of small molecules that can be emitted during ion bombardment. In order to compare the sputter rate results, a spin coated fluorinated amorphous film (Teflon AF^2, open circle in figures (a) and (b)) was sputtered under the same conditions. However, the sputter rate of Teflon AF^2 does not differ too much from that of evaporated Teflon AF, showing that the chain length does not influence the polymer sputter rate.

If we plot the rate as a function of $N_T/(N_c-N_o)$ for an ion fluence of 5×10^{13} cm^{-2}, where the surface chemistry is only moderately changed, the sputter rate is expected to show a linear dependence. However, Figure 7.11(c) shows a larger scattering also for polymers that showed linear dependence for a high ion fluence (Figure 7.11(a)). The rate dependence on

N_T/N_c ratio for ion fluence of 5×10^{13} cm^{-2} shown in Figure 7.11(d) gives better agreement for the proposed correlation. Nevertheless, our experimental results do not show a linear rate dependence on the "effective" carbon content ("effective" means subtracting number of oxygen atoms from the carbon atoms) in the polymer as good as it was observed by Gokan et al. Some kind of linear enhancement vs. the ratio N_T/N_c was obtained for vinyl polymers and aromatic ring containing polymers only in the steady-state sputter regime, which is more reasonable as the polymer surfaces at such ion fluences become carbon rich with little fraction of oxygen or nitrogen. However, the sputter rates of Teflon-like polymers and Nylon are far away from ideal cases. The conclusion stated by Gokan that the chemical bond strength and different functional groups containing oxygen, nitrogen or fluorine do not play a significant role in the sputtering of polymer would not be true. Our results show that there is a large influence on the polymer removal rate depending on polymer chemistry, as well as there should be some effect of the weak and strong bonds.

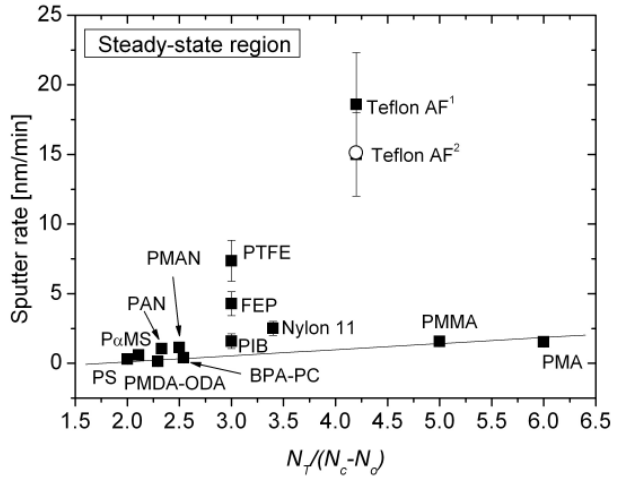

a)

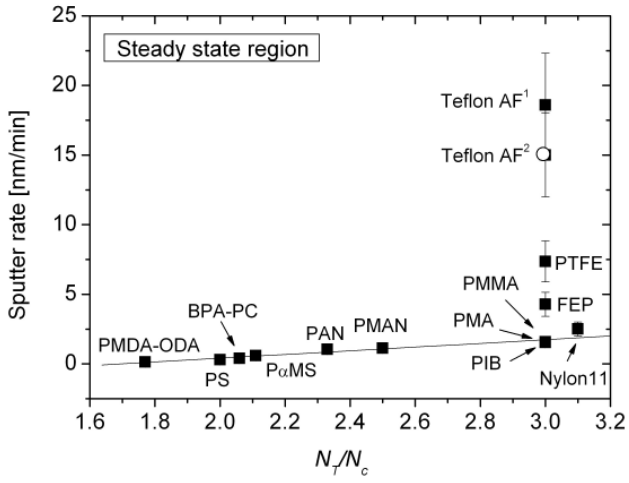

b)

Figure 7.11

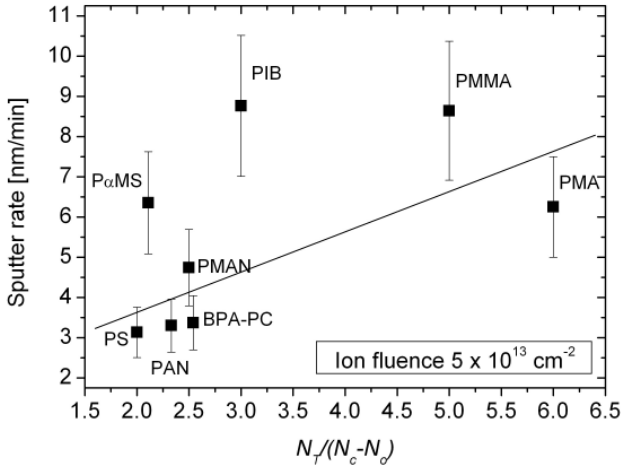

c)

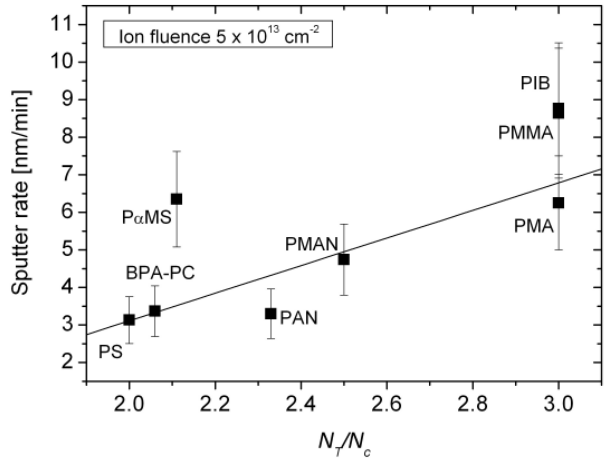

d)

Figure 7.11 (continued) *Sputter rate for 1 keV argon ion irradiation vs. (a) and (c) $N_T/(N_c-N_o)$, and (b) and (d) N_T/N_c for the steady-state region (Table 7.1) and at an ion fluence of 5 × 10^{13} cm^{-2}. Teflon AF[1] is prepared by vapour deposition, Teflon AF[2] (open circle) is spin coated.*

According to Taylor and Wolf [Taylor 80], the sputter rate determining step may be either cleavage of a backbone or of a side-chain bond which is determined by the strength of the bonds. Following this statement, strong bonds will enhance the radiation stability of polymers, weak ones enhance the degradation and activate the main chain leading to its cleavage. The rate determining step for degrading polymers is the cleavage of the main-chain bonds, as a correlation between the sputter rate and the yield of chain scission per 100 eV absorbed energy was observed [Taylor 80]. The same correlation was observed in our

experiments as was mentioned earlier in this chapter (Table 7.1). If a polymer degrades by main chain fracture, small molecules are formed with a larger probability which can be more easily desorbed from the surface, as discussed above. These molecules are usually removed side groups that are formed through the internal rearrangements of larger radicals, like in the case of PMMA, Figure 7.4.

The sputtering rates of investigated cross-linking polymers increased with the yield of cross-link formation, $G(X)$, (Table 7.1), even if it was expected that polymers with higher cross-linking formation yield should degrade slower. Taylor and Wolf suggested that the rate values should show some dependence on the strength of the main-chain side-chain bonds. In cross-linking vinyl polymers one side-chain has hydrogen, another one is connected to a benzene (C_6H_5), ester (RCOOR') or nitrile (CN) group. Therefore, the bond dissociation energies of side groups are similar, 4.4 eV for C-H and 3.4 – 3.9 eV for C-C bonds [Krevelen 90, Cottrell 58]. On the other hand, it was observed that under ion bombardment, as well as γ- or X-ray irradiation, mostly tertiary and sometimes secondary hydrogen atoms are predominantly released from polymers with a vinyl structure [Todd 60]. The combination of these radicals would produce cross-linking, or the main chain will be activated leading to rupture of the backbone bonds forming neutral molecules and radicals that can be further decomposed or can participate in other reactions, like end-linking, hydrogen addition or radical migration, etc. [Charlesby 91, Clough 91]. However, it does not answer the question why cross-linking polymers are sputtered faster than some degrading ones. One of the most important issues in polymer modification is the side chain groups that may weaken or enhance the polymer stability against any kind of irradiation. And the position of such groups, or to be more precise, the position of the weak side chain-backbone bonds was shown to be important [Taylor 80].

Aromatic rings are known to be the most effective polymer stabilizers by absorbing the excitation energy transferred to the polymers [Chapiro 62, Charlesby 60, Woods 94]. PS is the polymer that has one of the lowest $G(X)$ and at the same time one of the smallest sputter rates. The main reason is attributed to the phenyl ring that adsorbs the energy initially absorbed in the polymer. The transferred energy is dispersed in several ways without simple chemical reactions [Charlesby 91, Woods 94]. Addition of hydrogen to the aromatic unit through radical migration, as discussed above, closes the vacancy not letting it participate in other reactions. A similar effect is observed for PαMS, which from all degrading polymers has the lowest removal rate which is slightly higher than PS. Degradation by main-chain scission reduces the average number of molecules of identical molecular weight [Charlesby

91], but does not necessarily mean that every scission will form a molecule that can be desorbed from the polymer surface. Even if the backbone bonds of PαMS are broken the yield of the gas evolution is rather low proving that the presence of the aromatic rings provide the alternative pathways to bond scission for dissipation of the absorbed radiation energy. Bisphenol-A-polycarbonate has two rings in its monomer unit. However, under argon irradiation it undergoes severe bond breakage leading to the desorption of short-chain species with a rate close to styrene polymers. Weak O-CO_2 bonds attached to the main chain are the primary attack site under the Ar^+ bombardment [Gerenser 93]. The elimination of carbon-oxygen functionalities and the formation of free radicals may cause further chain scission or cross-linking. An aliphatic C_3H_6 link is expected to serve as a site for radical reaction [Clough 91], but the rings protect the polymer from complete degradation under ion bombardment. PMDA-ODA and PBO have more than two aromatic rings in their structure (Table 6.2) and have the lowest sputter rates, showing that the presence of rings protects polymers against radiation degradation even if such elements like oxygen, nitrogen or even fluorine are present.

Nitrile and ester side groups present in the polymer structures lead to higher sputter rates compared to aromatic polymers (Table 7.1, Figure 6.13). PAN and PMAN contain nitrile groups which promote the polymer stability by deactivation of reactive species [Taylor 80, Helbert 80]. Because of the triple bond (–C≡N) rearrangement to –C=N–, the possibility of cyclization on adjacent side groups of the same chain is not excluded [McNeill 89]. These reactions result in polymers to be more or less resistant to ion bombardment. In contrast to nitrile polymers, ester groups in acrylates are abstracted much faster leaving only about 10 % of all oxygen on the surface (Figure 7.3(b)). Through the abstraction of oxygen containing functional groups, the main chain is activated leading to bond scission and the formation of small molecules that may be easily desorbed, even in polymers of the cross-linking type such as PMA. The addition of phenyl rings to the methacrylate may reduce polymer degradation. This was observed when a polystyrene-polymethylmethacrylate block copolymer (PS-b-PMMA, 70 % of PS and 30 % of PMMA) was sputtered under the same conditions as respective to the homopolymers. The total rate measured at an argon ion fluence of 3×10^{15} cm^{-2} for PMMA was 2.14 nm/min, for PS-b-PMMA – 1.27 nm/min and for PS – 0.37 nm/min. It is obvious that the addition of the aromatic units reduces the sputter rate by about two times. On the other hand, when oxygen groups are added to the polymer, radiation resistance becomes weaker and the rate can be enhanced by one order of magnitude, as in the case of the PS homopolymer and PS-b-PMMA copolymer.

The highest rates were observed for fluorine containing polymers, like Teflon AF, PTFE and FEP. Teflon is known as the most inert polymer towards heat, solvents and most corrosive chemicals. However, when fluorinated polymers undergo radiation treatments, one of the highest degradation yields is observed. It was mentioned above that the C-F bond is resistant to transfer reactions, and radicals undergo depolymerization to monomers when fluorine containing polymers are heated. Degradation mechanisms by monomer depolymerization may also occur under ion irradiation, as fluorine containing organic films were successfully prepared by RF sputtering from a PTFE target [Biederman 00, Schürman 05].

7.1.5 Summary and conclusions of sputtering phenomenon of thermoplastic polymers

Various effects influencing the polymer sputter rate under low energy ion beam irradiation were discussed is the sections. It was shown that the sputter rates of polymers have a tendency to decrease with increasing ion fluence, followed by a constant removal rate in the steady-state region. The decrease is attributed to the chemical changes that occur in the ion fluence range of 10^{13} – 10^{15} cm^{-2} depending on the polymer chemistry and ion beam parameters. Large differences in the sputter rate of different polymers are observed for very low ion fluences where the main chemical modifications take place. In the steady-state region, surfaces of different polymers are enriched with carbon or similar carbon-oxygen, carbon-nitrogen functional groups leading to only small differences in the removal rate. Chemical changes involved structural rearrangements, reactions with different species, like oxygen and/or nitrogen, double bond formation, cross-linking and chain scissioning. It should be noted that, the outer most surface layer undergoes reactions with the residual oxygen, present in the vacuum chamber, even during treatment with argon gas. Therefore, post-chemical reactions should be always taken into account, when dealing with irradiation of polymer surfaces.

The tendency of the sputter rate as a function of ion beam parameters was the same for all investigated polymers. However, when the polymer chemistry was considered, the behaviour of removal rates was more complicated. A correlation between the sputter rates and the chemical yields as well as monomer yields obtained under thermal degradation was found to be partial, and applicable to small groups of polymers. A suggestion made by Gokan et al. that the sputter rates of polymers are inversely proportional to the effective carbon content in a unit volume showed good agreement only for vinyl polymers, polyimide, polycarbonate, and to some extent Nylon.

Experimental observations showed that the main factor determining the polymer removal rates organic films are bombarded at room temperature is the polymer chemistry when. Polymers containing aromatic rings were shown to have the lowest removal rates, because of the property of the ring to absorb the energy initially absorbed by the polymer in this way protecting it from degradation. Nitrogen or/and oxygen containing polymers have larger removal rates. This is because the abstraction of oxygen or nitrogen containing functional groups activates the main chain leading to the bond scission and the formation of small molecules that may be easily desorbed. It was also shown that when aromatic rings are added to polymers having high removal rates, the resistance of the polymer to ion bombardment could be increased. Teflon-like polymers were shown to have the largest sputter rates, because C-F bonds do not participate in transfer reactions, leading to radical depolymerization into monomers.

When polymers were sputtered at elevated temperatures, the observed rates were influenced by the polymer´s tendency to cross-link or degrade under the irradiation, and its thermal degradation properties. Ablation rates of PS did not change with increasing sample temperature, and only above 470 K polymer degradation increases. For PαMS ablation is much faster when the sample is heated already at temperatures below T_{gs}. Enhanced ablation of poly-α-methylstyrene is attributed to the preferential degradation by main chain scission and the ability to form large yields of monomers when the polymer is heated. Ion beam bombardment at elevated sample temperatures induced polymer depolymerization at temperatures much lower than it is observed in conventional pyrolysis leading to fast monomer emission and polymer degradation. In PS, which preferably cross-links and which's molecular yield is only 40 % under thermal degradation, ion beam induced depolymerization occurred later compared to PαMS, but still at lower temperatures than observed in conventional pyrolysis.

The energy transfer in nuclear collisions may suffice to move an atom from its initial site, which later can cause other atoms to recoil resulting in a collision cascade. Physical sputtering through the collision cascade of rigid materials is well understood. The question is, if this theory can be applied to polymer sputtering.

Experimental data, see Figure 6.8, showed that the sputter rate of polymers increases with the ion energy in the range 0.5 – 5 keV. However, this energy region is not enough to predict the tendency of the rate at higher incident energies. Because of the experimental limitations (5 keV is the maximum energy achievable with our ion gun), energy dependence calculations were done using SRIM [Ziegler 03] (commercial code of TRIM). SRIM or TRIM

codes provide accurate primary ion ranges, stopping powers, the number of displaced atoms, and are based on collision theories. In these calculations, the collision parameters of subsequent collisions are treated as uncorrelated to each other, only binary large angle collisions are regarded. The "core and bond" approach (Section 3.1.1) is included to calculate stopping powers in polymer solids [Fink 04]. Table 7.2 shows the results of the calculated sputtering yields in atoms/ion and experimental removal rates in nm/min values as a function of the Argon ion energy for PS and PMMA. In SRIM, yield values are calculated for each element present in the polymer separately. In the table there are given summed up yield values. As can be seen from the data given in the table, the differences in calculated and experimental values are very small.

Table 7.2 *Sputtering yield (calculated using SRIM) and experimental sputter rate results as a function of the Argon ion energy for PS and PMMA. Incident angle 0°.*

Ion energy, keV	Sputter yield [(a)], atoms/ion		Total Sputter rate [(b)], nm/min	
	PS	**PMMA**	**PS**	**PMMA**
0.5	0.148	0.222	0.159	0.353
1	0.29	0.424	0.284	0.458
3	0.592	0.779	0.476	0.822
5	0.876	1.027	0.754	1.353

a) In the SRIM program the yield is calculated separately for each element present in the polymer, i.e. H, C and O. Yield data given in the table are summed up.

b) Experimental rate results are taken from Figure 6.8.

Plotting the stopping power (dE/dx) vs. the energy, the polymer sputter yield or rate dependence on ion energy can be determined, Figure 7.12. Following the calculations, the broad maximum in the polymer sputter yield should be obtained at about 10 keV. At higher incident energies the decrease in the yield should follow because of the dominant electronic energy loss mechanism during which the projectile removes the electrons from the target atoms, instead of dislodging the atoms [Mahan 00]. The experimental energy dependence was shown by Delcorte et al. [Delcorte 99], who reported the decrease in the yield of large molecular fragments of PET in the energy region between 7 and 22 keV.

SRIM calculations showed a disagreement in the sputter rate dependence on the projectile's incident angle. According to the literature and calculations the yield should increase when changing the angle of incidence from 50° to 80°. According to SRIM calculations, for example, the sputter yield of PMMA for 1 keV argon ion bombardments increases from 0.42 atoms/ion at an angle of incidence of 0° to 2.19 atoms/ion at 60°. No such dependence on the sputter rate of polymers was observed in experiments, see Section 6.1.3. Disagreements between SRIM calculations and experimental data were found for the cases when sputtered with different kind of ions. Experimental results show that irradiation with oxygen induces oxidative degradation of polymers resulting in very high removal rates, while the sputtering rate obtained for nitrogen or argon ions does not differ too much. In the SRIM, no difference in the yield under argon, oxygen or nitrogen ion bombardment was calculated. Finally, a very large disagreement between SRIM calculations and the experimental sputter rate was found for the rate/yield determination as a function of the polymer chemistry. Calculated yields of PMMA, PC, and Nylon were the same. Experimental data showed, that from all three polymers, PC was sputtered with the lowest rate, and Nylon with the highest one.

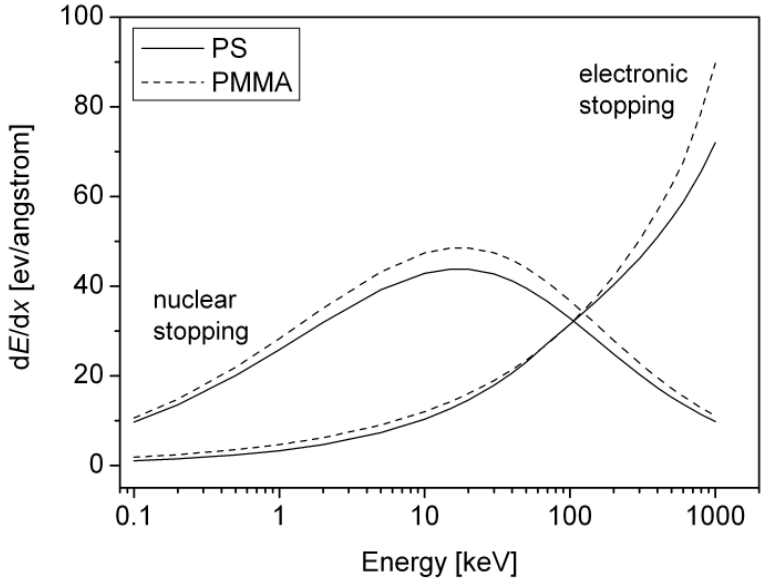

Figure 7.12 *Calculated nuclear and electronic stopping powers vs. Argon projectile energy for PMMA and PTFE, [Biersak 87, Ziegler 03].*

Experimental observations indicate that the collision cascade models are not able to explain polymer sputter rate mechanisms, as well as that the TRIM (SRIM) code is not suited to model the emission of molecules from polymers, and that more complicated molecular dynamics simulations are necessary. Recently, Delcorte and Garrison [Delcorte 04] published results based on MD simulations of molecular desorption from a PS solid under low energy argon ion beam irradiation. The authors showed that large intact molecules ranging from monomers to trimers are ejected from the polymer surface, which later are decomposed into smaller fragments. However, up to date the existent theoretical models (Section 3.2.2) cannot explain the observed dependence of the rate on ion fluence, as well as the large difference (one order of magnitude) in the rate values at the beginning and in the steady-state region, as well as the rate dependence on polymer chemistry.

7.2 Polymer-metal interface formation and adhesion after low energy ion beam irradiation

Metallized polymers are widely used for different applications from packaging to microelectronics. The metallization of polymers with noble metals is of interest in various applications as well as from a fundamental point of view [Mittal 98, Mittal 01]. In such cases, good adhesion between the polymer and the metal is required. Weak metal-polymer interactions due to the moderate activity of noble metals require a pre-treatment of one of the surfaces (usually the polymer surface) [Schonhorn 78, Baglin 87, Kinloch 94] to improve the metal/polymer adhesion.

The peel test results obtained after Cu or Au films were peeled-off from treated and untreated polymers are given in Figures 6.27 – 6.29. Three types of peel strength dependence on the ion fluence were observed, as schematically shown in Figure 7.13. For PS, BPA-PC and PP, adhesion to metal was improved by two orders of magnitude, while the Cu film on treated PMMA and PαMS was removed with the same force, i.e. no adhesion enhancement was observed. The results showed that there is no monotonous correlation between the treatment fluence and the peel strength. The observed maximum in the peel strength for PS and BPA-PC was reached in the fluence range of 5×10^{13} to 10^{15} cm^{-2} depending on the ion chemistry and the polymer/metal interface (Figures 6.24, 6.27-6.29). A decrease in the adhesion strength was recorded at higher ion fluences. Adhesion of Cu to PP reaches some kind of saturation. In contrast to the results for the peel strength measured for *plasma* treated PP reported in the literature [Friedrich 00], no maximum in strength followed by a decrease was observed in our experiments, at least not in the experimental ion fluence range.

Indirect measurements of the adhesion enhancement based on determination of the condensation coefficient (Figures 6.23-6.26) and surface tension (Figure 6.22) showed, that with increasing ion fluence the polymer surface energy increases (the contact angle decreases) and all arriving metal atoms are adsorbed on the polymer surface, indicating that metal adhesion on treated polymer improves. However, comparing these results with those obtained by peel test measurements no correlation was found: the maximum in peel strength occurred before the saturation in condensation coefficient and an increase in the surface energy (low contact angle) were reached in case of PS; for PMMA and PαMS, no enhancement in adhesion after ion treatment was observed, even if results showed an increase in the adsorption probability and surface energy. Only for PP a correlation was found, as the peel strength increases and reaches saturation with increasing ion fluence. To understand these

phenomena, the mechanisms of adhesion enhancement and reduction, as well as dependence of the adhesion on polymer chemistry had to be studied.

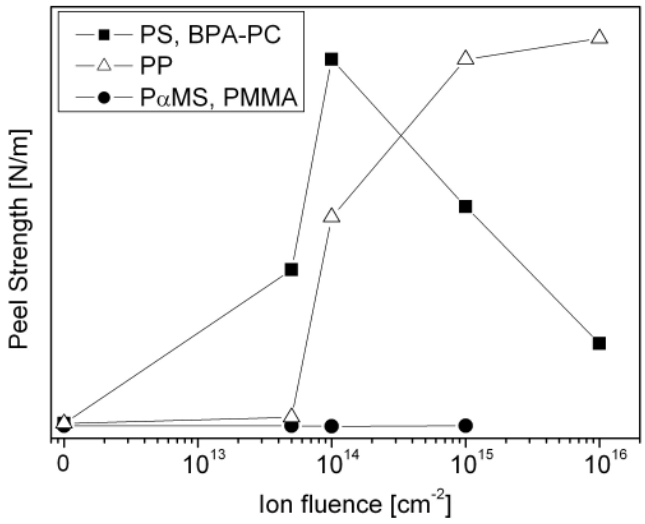

Figure 7.13 Typical peel strength dependence on ion fluence for different polymers treated with oxygen ions.

7.2.1 Adhesion improvement through mechanical interlocking

Adhesion improvement between two surfaces was explained by a number of theories shortly mentioned in Section 2.2.3 and in detail discussed by [Fourche 95, Leeden 02, Kinlock 94]. The influence of the attraction of electrostatic forces to the total work of adhesion was shown to be very small and cannot explain improvements in adhesion [Fourche 95, Garbassi 98]. The diffusion model is limited in its applicability, because the adherates must be mutually soluble, and the macromolecules must be mobile to be able to interdiffuse. This theory is usually applied to explain the enhanced adhesion between two polymer systems, but not so dissimilar systems like polymer and metal.

Mechanical adhesion or interlocking states that surface roughness or porosity increases the surface contact area leading to better adhesion. However, if there is no intimate contact between the film and the substrate, the increased roughness will result in weaker adhesion due to the uncoated areas of voids or vacancies in between the two surfaces [Mittal 76, Kinloch 94], Figure 7.14.

Changes in the surface roughness were negligible when polymers were irradiated at ion fluences in the region 10^{13} - 10^{14} cm^{-2}, where the maximum in the peel strength was observed. The root-mean-squared and average roughness of PS, PαMS and PMMA increase by two, three times at an ion fluence of 10^{15} cm^{-2} and remained in the nanometer scale region, Table 6.5. The small roughness enhancement should not have a large influence on the polymer/metal adhesion, as the peel strength of PMMA and PαMS did not change and the adhesion force for PS decreased after the maximum adhesion was reached, although the roughness increased.

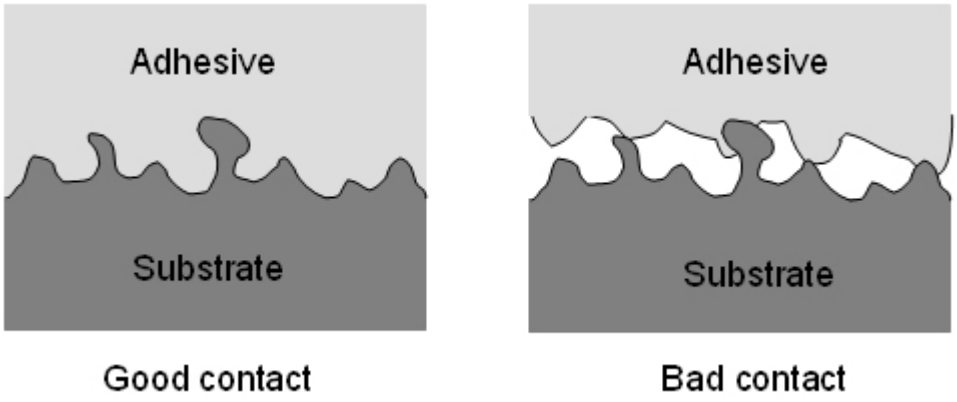

Figure 7.14 *Enhanced and diminished contact area between a rough substrate and adhesive.*

Many authors agree that mechanical interlocking is not an adhesion mechanism working at the macromolecular level [Kinloch 94, Fourche 95, Leeden 02], and the increase in adhesion is achieved only when a specific topography was obtained [Kinloch 94]. It is believed that surface roughening is merely a technical mean to increase the adsorption or wetting properties and to remove a contamination layer.

7.2.2 Influence of induced chemical changes on metal/polymer adhesion

The most widely applicable theories of adhesion are the absorption theories based on surface wetting behaviour, chemical bonding, acid-base and van der Waals interactions. The theories state that the materials will adhere because of the interatomic and intermolecular forces which are established between the atoms and molecules in the surfaces of the adhesive

and substrate provided that sufficiently intimate molecular contact is achieved at the interface [Kinloch 94, Fourche 95, Leeden 02].

It was demonstrated, that the mechanisms of adhesion in many different adhesive joints involve only interfacial secondary forces (van der Waals or hydrogen) [Kinloch 94 and references therein]. However, it was shown that when chemical bonds at the interface of adhesive and substrate are formed, the adhesive fracture energy (the energy required to propagate a crack through a unit area of interface) was higher than the thermodynamic work of adhesion (the work required to separate a unit area of a solid and a liquid phase forming an interface) [Kinloch 94]. For calculation of the values of the adhesion work it is assumed that only secondary bonds act at the interface which have much lower binding energy compared to primary chemical bonds (covalent, ionic, metallic). Adhesion by chemical bonding takes place rather frequently in the case of polymer-metal interfaces [Fourche 95]. The formation of such bonds is based on a charge transfer from the metal to the polymer. An increase in adhesion through the formation of primary bonds is obtained when special side or functional groups are introduced along the polymer chain, or new adsorption sites containing radicals, unsaturation, etc. are created.

The polymer surface chemistry was altered by ion beam modification with Ar^+, N_2^+, and O_2^+ ions at an energy of 1 keV in UHV, and exposure to air after Ar^+ bombardment. Table 7.3 shows the atomic weight percentages of oxygen and nitrogen in modified PS. Untreated PS surfaces were free from oxygen or any other species. Pronounced polymer oxidation took place after the treated polymer was exposed to atmosphere, where the detected oxygen content increased up to 17 at. %. Up to 27 at. % of oxygen was observed for the sample treated with O_2^+ ions. Treatment with pure argon and nitrogen should not lead to oxygen incorporation. However, modification with oxygen free gases can lead to the reaction of the free radicals created on the polymer surface with O_2 containing species most probably originating from the residual gas in the chamber [Idage 98, Grant 88, Chan 94].

High resolution C 1s spectra, recorded with XPS, were deconvoluted into individual peaks identifying the different functional groups as reported by [Beamson 92], Figure 6.17. The π–π^* shake-up satellite indicating polymer aromaticity is eliminated or it overlaps with the broad carbon tail, while the aliphatic carbon feature increases with increasing ion fluence. This was observed for all treatments indicating that the aromatic ring was the primary site for PS modification. Reaction with oxygen or nitrogen species resulted in the formation of carbon-oxygen or carbon-nitrogen functional groups as shown in Figure 6.17. As an example, the results obtained for oxygen treated PS are shown again in Figure 7.15(a-b).

Table 7.3 *Atomic weight percentage of oxygen and nitrogen measured in the PS after different treatments. Modification was done using the microwave IonEtch gun (Tectra).*

Gas		untreated	10^{13} cm^{-2}	10^{14} cm^{-2}	10^{15} cm^{-2}	10^{16} cm^{-2}
Ar + exposed to air		0	1	7	13	17
N_2	at % N_2	0	3.5	5.4	15.4	17.3
	at % O_2	0	-	0.6	0.7	0.9
O_2		0	13	17	24	27

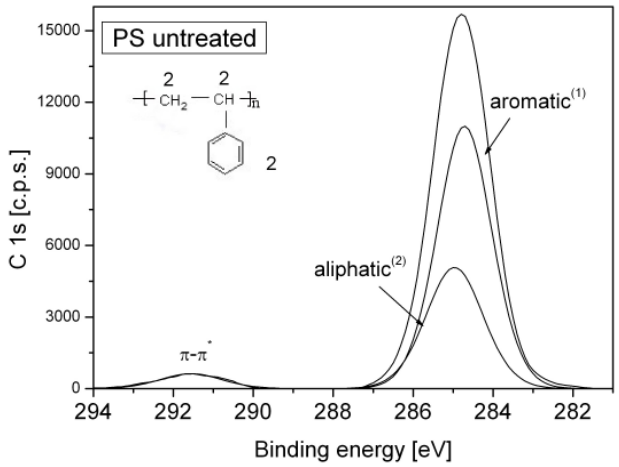

a)

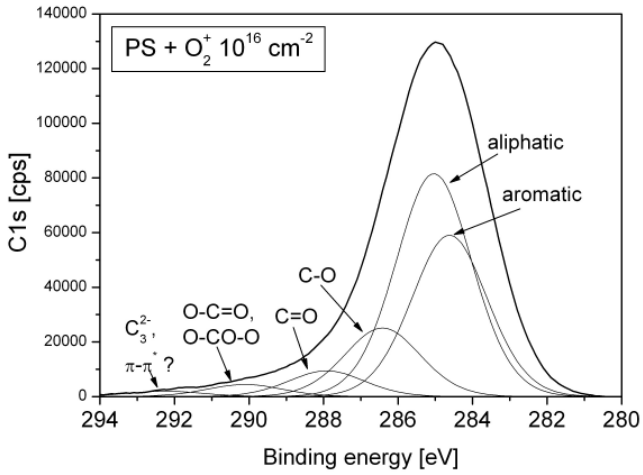

b)

Figure 7.15

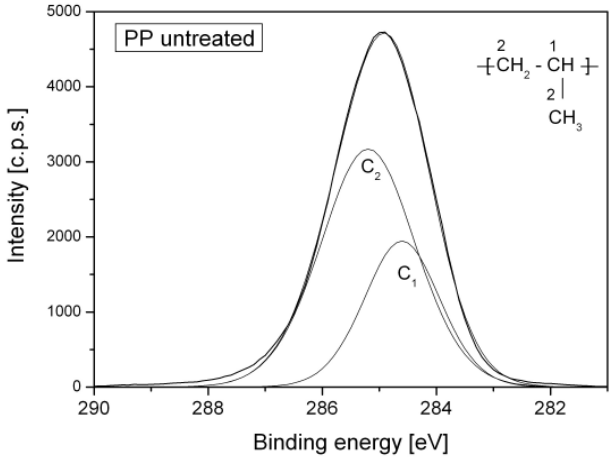

c)

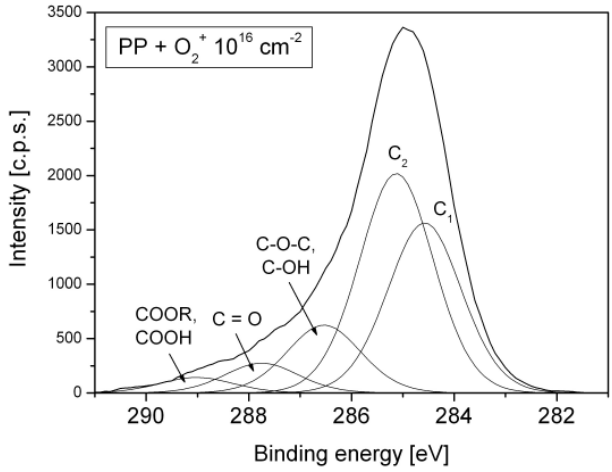

d)

Figure 7.15 (continued) *XPS spectra of Carbon C1s for (a-b) PS and (c-d) PP. The features were fitted for pristine and oxygen treated polymers. Which carbon bond corresponds to which fitted feature in the main C 1s line is indicated by the numbers in the chemical formula.*

The XPS results clearly show possible ways of O_2 incorporation into the polymer: reaction of free radicals with the residual gas in the chamber; reaction of surface radicals with atmospheric oxygen, and surface oxidation during treatment with oxygen gas itself. Carbon-nitrogen functional groups, on the other hand, were formed only after polymer irradiation with nitrogen. PS oxidizes faster in atmosphere, and during treatment with oxygen ions. If the sample is exposed to atmosphere, the long-lived free radicals formed during ion treatment react preferentially with oxygen, as no other species were detected. Even a small Ar^+ ion

fluence, 10^{13} cm^{-2}, is enough to incorporate C-O (and/or alcohol) groups into the PS surface after the modified surface was exposed to air. With increasing fluence more new oxygen containing groups are incorporated. It was observed that the more oxygen or nitrogen is built into the polymer the faster the π–π^* transition is eliminated. This leads to the conclusion that the aromatic ring is the primary site for the chemical reactions in accordance with [France 98, Shard 92]. Schematic diagrams of oxygen incorporation in PS are given in Figure 7.7.

Oxygen and nitrogen containing functional groups were found on the PP surface after treatments with one or another gas as well. Similar to PS treatment, the O_2^+ ions induced different oxygen functional groups such as C-O-C, C=O [Zekonyte 04]. N_2^+ treatment led to the incorporation of new carbon-nitrogen functionalities (C=N, C-N-C, N-C-O). Nevertheless, it seems that oxygenation and nitrogenation reactions in treated PP take place slower than in PS [Grant 88, France 98, Zekonyte 05], as was observed from the O_2 or N_2 concentrations in both films. The oxygen concentration in polypropylene was lower by 6-10% as compared to polystyrene for ion fluences of 10^{13} – 10^{14} cm^{-2}, and only above 10^{15} cm^{-2} the difference was 3%. Similar results were observed comparing the nitrogen concentration in both polymers. The example of fitted oxygen functional groups is shown in Figure 7.15(c-d). The slower formation of O_2 and N_2 species in PP can be explained in terms of the reaction pathways. PS contains phenyl rings that offer numerous reaction pathways leading to greater degree of oxidation or nitrogenation. In PP the primary attack site is the methyl group (chemical formula Table 5.1) which decreases in number with increasing modification fluence [Zekonyte 04]. The removal of this group or radical introduction offers predominant modification [France 98], however, with a rather small number of possible reaction pathways.

Treatment of PαMS, PMMA and BPA-PC with argon ions was discussed in some detail in the previous sections and will not be repeated here. As a short reminder, for poly-α-methylstyrene, similar to PS, the shake-up satellite vanishes for prolonged ion treatment (Figure 7.1). The oxygen concentration decreases with increasing ion fluence when PMMA is bombarded with different ions (Figures 6.14, 7.3). Loss of oxygen (from 20 % to 5 % in the fluence range of 0 to 10^{15} cm^{-2}) and phenyl rings was recorded for polycarbonate when it was subjected to argon treatment.

Polar and oxygenated functional groups are believed to enhance the adhesion to polymer surfaces through the strength of the chemical bonds they can form. Modified PS surfaces treated with different ions showed improved metal/polymer adhesion. Even if the adhesion decreased after a maximum was reached, the absolute values in the peel strength were larger than the values for the untreated polymer in the cases where additional oxygen

and nitrogen was incorporated, Figure 6.27. In the case of PP, modification with oxygen ions showed to be the most effective way to enhance the strength of Cu adhesion to the surface of this polymer as an extremely high peel strength was recorded, Figure 6.29(b).

Formation of new functional groups is effective when treatment is done with O_2 and N_2 gas. When the polymer is bombarded with argon ions, chemical rearrangements take place through the abstraction of particular side chain groups or oxygen containing fragments, as shown for PMMA (Figures 6.14 and 6.18). If the formation of chemical bonds between polymer and metal is important for enhancing the adhesion, the loss of reactive groups should lower the strength between these materials. The peel strength of PMMA remains unchanged with increasing argon ion fluence and, correspondingly, decreasing oxygen content, but Cu adhesion on polycarbonate is stronger than for untreated polymer, Figures 6.28, 6.29, even if carbon-oxygen functional groups are preferentially removed from the polymer. On the other hand, polycarbonate contains aromatic rings that form metal-arene sandwich complexes when metal atoms condense on ring containing polymers [Friedrich 99, Droulass 92]. PαMS also contains phenyl rings, however, no improvement in metal-polymer joint was observed. Taking this into account, it seems that the behavior of polymers under ion irradiation plays important role in metal/polymer adhesion. Experimental results lead to the conclusion that the adhesion is improved on polymers that preferentially cross-link (PS, BPA-PC, PP), while no adhesion enhancement was observed for PαMS and PMMA that undergo degradation by main chain scission under ion bombardment.

7.2.3 Adsorption of metal on treated polymer surfaces: correlation between condensation coefficient and enhancement in adhesion

In order to obtain good adhesion according to the adsorption theory, i.e. intimate contact between two materials, the adherent should wet the substrate [Fourche 95]. Good wetting is obtained when the surface energy of a substrate is greater or equal to the energy of the adherent. The polymer surface energy, and correspondingly, the wetting behavior were shown to improve after PS and PMMA were treated with Ar^+ ions, Figures 6.21, 6.22. As the measurements were done in air, the treated polymer surfaces adsorbed oxygen from the atmosphere resulting in the formation of carbon-oxygen functional groups which cause the surface to be more reactive. Wetting properties of polymers are improved through ion bombardment. As wetting is one of the most important factors for good adhesion, the interaction of metal with the polymer should also be improved leading to better adhesion between these materials.

The early stages of metallization are far from thermodynamic equilibrium conditions, since isolated metal atoms impinge on the polymer surface. Therefore, various competing processes (adsorption, surface diffusion and nucleation after encounters of metal adatoms, metal atom reemission into vacuum, etc.) have to be taken into account in order to understand how the metal-polymer interface is formed. Some details on the nucleation and growth of noble metals on non-treated polymer surfaces as well as some new techniques for investigation of these phenomena were published in several works [Zaporojtchenko 00, Thran 99]. The strong metal-polymer adhesion in the case of more reactive metals such as Cr, Al or Ni, as a rule, is accompanied by higher condensation coefficients and nucleation densities compared to noble metals. These tendencies should be taken into account when studying the influence of ion irradiation on the adhesion properties of noble metals on polymer surfaces.

Polymers and metals are very dissimilar materials, and their interaction is weak. Metals of low reactivity, especially noble metals like Cu or Au, do not wet polymer surfaces but form 3D clusters on untreated polymer surfaces. After the noble metal atoms adsorb to the polymer they will remain there and diffuse on the polymer surface for a certain time, and then desorb into the vacuum or will be trapped somewhere on or beneath the polymer surface. Only metal atoms remaining on the surface contribute to the condensation coefficient, *C*, which is defined as the ratio of the number of adsorbed metal atoms to the total number of metal atoms arriving to the surface.

There are two possibilities for metal nucleation on polymer surfaces: the so called random and preferred nucleation. For preferred nucleation, the metal atoms are trapped at some defect sites, and for random nucleation the nuclei are formed when metal atom encounter each other [Zaporojtchenko 01, Zaporojtchenko 03a]. Both cases are distinguished by examining the maximum cluster density as a function of the deposition rate. It was shown [Zaporojtchenko 00, Zaporojtchenko 03a], that noble metal atoms underwent random nucleation and complete condensation at RT on polymers with a high concentration of polar groups like PMDA-ODA polyimide.

In contrast to PMDA-ODA, incomplete condensation of Cu and Au and preferred nucleation were observed on untreated PS, as well as PMMA and PαMS. The interaction between noble metal atoms and the polymer surfaces is weak resulting in the desorbtion of metal atom before thy reach the preferred adsorption sites on the polymer surface. The condensation coefficient is lower and the cluster densities were found to be not rate dependent [Zaporojtchenko 03a]. The results for the condensation coefficients of Cu and Au on untreated and treated PS, PαMS and PMMA are presented in Figures 6.23 – 6.26. The

adsorption probability of metal on the polymer surface increases with increasing ion fluence until complete condensation (C = 1) is reached above an ion fluence of 10^{15} cm^{-2}. The same effect was observed for the PP surface, where C of Cu on the untreated surface is about 0.2. More metal is absorbed for longer treatment times and saturation is reached at an ion fluence of 10^{15} cm^{-2} [Zekonyte 04].

The metal condensation coefficient is related to the probability for a metal atom to find a preferred site which is related to the mean distance between these sites and the diffusion length of the adatoms on the polymer surface. If the distance between the nucleation centres is larger than the diffusion length of the metal adatoms, more than 50 % of all approaching metal atoms will not reach a nucleation site before desorbing from the surface resulting in a low C. Using ion-beam treatment, additional adsorption sites (defects, polar groups, unsaturations, etc.) are created on the polymer surface. Metal atoms arriving on the treated surface are likely to encounter preferred adsorption sites and to form clusters, with a distance between the clusters comparable to or even smaller than the surface diffusion length, leading to a higher cluster density and, consequently, to an increased condensation coefficient (close to 1), Figures 6.23, 6.25, 6.26.

The nature of the defects after ion bombardment can be of different kinds and depend on the ion chemistry and post chemical reactions. The adhesion centres may be terminal groups, attractive local arrangements of the polymer chains, or oxygen or nitrogen based functional groups or functionalities of other elements not previously contained in the polymer that are reactive towards a metal. When Cu, Au or other metals are evaporated onto untreated PS, the phenyl rings offer a majority of specific sites to form metal-π complexes [Droulas 92, Burkstrand 79, Gerenser 92, Friedrich 00]. As discussed in Section 2.2.4, noble metal-arene complexes are rather weakly bound (compared to complexes obtained when reactive metals (Cr, Al) are evaporated) and unstable, and for higher metal coverage the formed interfacial species disappear. The density and size of the metal clusters on polystyrene are given in Figure 6.23. TEM images of untreated PS show non-uniform Au cluster formation on the pristine polymer surface with a density of ~ 10^{12} cm^{-2} and a cluster diameter of about 3 nm. Ar^+, O_2^+ or N_2^+ ion bombardments induce additional nucleation sites resulting in a higher cluster density, more uniform metal distribution and smaller clusters (average diameter ~ 2 nm), as shown in Figure 6.26 for an argon treated PS surface. The increase in cluster density is proportional to the ion fluence (Figures 6.23 (b), 6.24 (b)), i.e. one ion creates one nucleation site until saturation is reached. Radicals created during argon irradiation can react with another radical producing unsaturation, branching or cross-linking. If the polymers

where treated at room temperature, a large number of radicals (so called long living radicals) remain unreacted and may therefore also participate in reactions with deposited metal. Treatment with O_2^+ or N_2^+ introduces functional groups, as discussed above. Incorporated oxygen or nitrogen functionalities provide a greater number of new adsorption or nucleation sites that are more reactive towards deposited metal (Cu, Au), such that metal-polymer interactions predominate over metal-metal interactions. The metal-oxygen-polymer or metal-nitrogen-polymer species were shown to be formed on different polymer surfaces [Burkstrand 78, Burkstrand 79, Gerenser 92, Droulas 92, Friedrich 00], compare Section 2.2.4. Comparing the values of the Cu condensation coefficient obtained for PS treated with different gases, it shows that N_2^+ ion treatment created a more reactive polymer surface for Cu to adsorb to, Figure 6.25 (a). Similarly, it was shown that silver preferred nitrogen treated surfaces [Gerenser 92, Burger 92]. It was concluded, that chemically more reactive metals like Al and Cr oxidize rapidly, preferentially forming strong bonds with oxygen functionalities resulting in a larger adhesion strength. Metals (Cu, Au, Ag) with lower oxidation rates are more reactive towards nitrogen containing species leading to enhanced metal-polymer interaction [Burger 92, Gerenser 92]. This tendency is observed in the condensation coefficient measurements, i.e. Cu adsorbs better on nitrogen treated PS surfaces (Figure 6.25). However, the peel test results shows that oxygen treated polymers provide better adhesion, Figures 6.27, 6.29.

Condensation coefficients of Cu for different polymers treated with argon ions are given in Figure 6.26. Cu adsorbs on untreated PαMS with the same probability as on PS. Cu on pristine PMMA, however, has a lower *C* even if oxygen functionalities are present in the polymer structure. Poly-α-methylstyrene has phenyl rings in its structure that allow formation of the same Cu-π complexes as for PS. In PMMA, the ester pendant groups are able to re-orient towards the bulk minimizing the surface energy when in contact with the apolar UHV medium [Bertrand 97]. This may lead to a lower interfacial reactivity of evaporated copper on the PMMA surface. In the case of the Cu/PMMA interface formation, the interaction of Cu with the polymer surface functionalities is low, not allowing immobilization at an adsorption site. This results in migration of the metal atoms on the surface or into the bulk until they encounter another adatom initiating cluster formation. The same Cu adsorption mechanism, i.e. pure physical interaction, is observed on untreated PP surfaces. When the surface of the polymer was irradiated with Ar^+ or other ions, new Cu nucleation with a larger density were created resulting in an increased cluster density and condensation coefficient for all polymers.

Comparing the Cu cluster density on the PS surface with the peel test results, Figures 6.23 and 6.25(b), a correlation between the maximum value in the peel strength and the saturation value of the number of metal clusters was observed.

It was interesting to determine whether the enhancement in the peel strength for most polymers is achieved through the chemical bonds between the metal and polymer or through the increased number of contact points and van der Waals forces. In order to understand this, the metallization of the polymer sample for the peel tests and the condensation coefficient measurements was done at liquid nitrogen temperature. At low temperatures, metal atoms are trapped at all nucleation sites due to little diffusion of adatoms [Zaporojtchenko 00b, Ratsch 03]. Untreated and treated PS samples for above mentioned measurements were prepared at T = -170 °C and compared with results obtained at room temperature. The results are given in Table 7.4, where condensation coefficient, cluster density and peel strength are given.

Table 7.4 *Condensation coefficient, cluster density and peel strength values for the Cu/PS system determined at room and liquid nitrogen (-170°C) temperature.*

Ion fluence,	C, a.u.		N_c, cm^{-2}		Peel strength, N/m [(b)]	
cm^{-2}	RT	-170 °C	RT	-170°C	RT	-170°C
0	0.44	0.74	10^{12}	8×10^{12}	4	45
10^{14} [(a)]	0.91	0.96	10^{14}	10^{14}	100	150

a) Treatment was done with 1 keV Ar^+ ions at room temperature. Samples were exposed to air after modification and before Cu deposition.

When metallization of untreated PS takes place at liquid nitrogen temperature (-170°C), the Cu cluster density is higher than that determined for the untreated polymer surface at room temperature. In fact, the value of N_c calculated at T = -170°C is the one that was obtained at RT after ion treatment at an ion fluence of 10^{13} cm^{-2}, Figure 6.23(b). Correspondingly, C is larger when Cu is deposited at low temperatures. If the number of nucleation sites is important for an improved metal/polymer interaction, i.e. secondary forces (van der Waals, hydrogen) play the most important role in adhesion [Kinloch 94], the peel strength should be enhanced for the system prepared at the low temperature. This was the case for untreated PS, Table 7.4.

Ar^+ ion treatment led to a larger C and N_c,in both cases with similar values. Note that the samples were exposed to atmosphere after the modification and before metal deposition, because of the sample preparation limitations. Storage in air resulted in oxygen incorporation into the polymer surface layer. As discussed above, Cu forms metal-oxygen-polymer complexes after it was evaporated. These chemical bonds are stronger than secondary bonds resulting in a higher adhesion strength. Comparing the peel test results for PS treated only with argon and argon ion modification followed by exposure to air, it was found that the adhesion strength was higher when additional oxygen was incorporated into the polymer, Figure 6.27(a).

The increased number of nucleation sites increases the metal adsorption probability as well as the adhesion strength. But the best improvement in adhesion is obtained through the addition of oxygen or nitrogen functionalities which participate in the formation of chemical bonds between the metal and the modified polymer. The improved metal interaction with the polymer surface is always attributed to the enhanced adhesion to these polymers. However, PMMA and PαMS show the opposite behaviour even if Cu adsorbs to the surface with a larger probability. For PS and BPA-PC, the decrease in the adhesion strength starts in the saturation region of the condensation coefficient. Only Cu condensation on PP increases with increasing ion fluence and therefore also does the peel strength.

The question why the peel strength decreases is still open. If improved interaction between metal and polymer influences their adhesion, it is not clear why the strength decreases after it reaches some maximum value, or why there is no improvement in adhesion at all, even if the condensation coefficient and the cluster density increase. In order to understand the adhesion mechanisms, the failure location was examined after the peel tests.

7.2.4 Failure location and mechanisms of adhesion

The peeled-off surfaces of the polymer and metal film were analyzed with XPS. The thickness of the polymer layer that remained on the Cu or Au film was calculated as described in Section 6.2.3.2, and results are given in Figure 6.31 (for Cu/PS system) and Table 6.6 (other metal/polymer systems). The calculated thickness showed that the failure mechanism changed from interfacial failure for the untreated polymer surfaces to cohesive in the polymer for the treated surfaces. The thickness of remaining polymer film in most cases increased with decreasing adhesion strength for PS and BPA-PC. While for PMMA and PαMS, the thickness of the removed layer became larger when Cu was peeled off from surfaces treated with high ion fluences. Taking this into account, it is clear that the adhesion of the metal and polymer at

the interface is improved and correlates with the increase in the condensation coefficient. On the other hand, while enhancing the adhesion at the interface, some weak layer is formed in the polymer bulk. The failure location for the Cu/PP system is difficult to determine because of the controversial results, Table 6.6.

AR-XPS analysis showed that the first reactions during ion bombardment take place in the outer-most polymer surface layer, and with increasing ion fluence the species are more evenly distributed throughout the modified layer, Figures 6.15 – 6.16. The largest reduction in the intensity of the shake-up satellite and the highest amount of O_2 or N_2 in PS are found in the first 1 - 2 nm (take-off angle of 60 – 75°). The decrease in the concentrations of different species or the increase in the intensity of the remaining satellite continues with decreasing take-off angle which corresponds to a depth of 5 – 7 nm, as was also calculated by [Tremblay 03, Paynter 02]. The calculated modification depth from the AR-XPS analysis is in good agreement with the average values of the ion penetration depth obtained by TRIM calculations reported by Biersak [Biersak 87].

Detailed spectra of the carbon C 1s line showed that the shake-up satellite (the characteristic feature of polystyrene) was detected on the removed Cu or Au film when the peeled-off polymer layer exceeded 7 nm. A PS film of this thickness was removed at or above an ion fluence 10^{14} cm^{-2}, Figures 6.31. Similar analysis was done for metal films peeled off from other polymers. The characteristic features of BPA-PC ((O-C=O)-O), PMMA (C-O-C=O) and PαMS (π-π*) where detected on metal films peeled off from polymers treated with an ion fluence of 10^{15} cm^{-2}. At these ion fluences, the failure took place in the modified polymer layer. The peel test results showed that the interfacial failure occurred when the metal film was removed from untreated polymer surfaces with very low adhesion strength. With increasing modification fluence, the crack propagated in the polymer leading to fracture mechanisms that occur between two polymer surfaces, i.e. the modified layer and the polymer bulk. To determine the failure location for the Cu/PP system is rather difficult. It seems that the tendency of the failure location with increasing ion fluence should be the same as for other polymers, i.e. the polymer thickness on peeled-off Cu film should increase with increasing ion fluence, Table 6.6. However, the calculated thickness for an nitrogen ion fluence above 10^{15} cm^{-2} and oxygen ion fluence of 10^{14} cm^{-2} showed that the fracture occurs near the metal/polymer interface. Therefore, from the available data it is difficult to draw an exact conclusion.

The work of adhesion, W_{adh}, is the work required to create two surfaces by separating them in a thermodynamically reversible way, Section 2.2.3. However, it was found that

energy required to cause a crack is much larger than the surface energy of the two surfaces [Kinloch 94, Jones 99]. It was found, that the fracture takes place under conditions far way from thermodynamic reversibility, as the crack growth in the materials necessitates rupture of strong primary bonds instead of secondary ones. In this case, the fracture toughness or fracture energy, G_c, is measured, which was found to depend on the molecular weight as shown for bulk polystyrene [Creton 99, Jones 99, Kinloch 94]. The largest value of the fracture toughness for high molecular weight (HMW) PS is around 1000 J/m^2, which is four orders of magnitude larger than the value of twice the surface energy. With decreasing molecular mass of PS, G_c decreases down to a relative molecular mass corresponding to the critical relative molecular mass for entanglement [Jones 99]. Thus in bulk glassy polymers and at the interface of two surfaces the entanglement is the main factor that determines how strong the interface is.

Ion modification of PS and BPA-PC creates radicals that participate in cross-linking reactions. An increased degree of cross-linking corresponds to an increase in the molecular weight and possibly a larger degree of entanglement, which leads to the formation of a plastic zone propagating ahead of the crack leading to the high adhesion strength values for low ion fluences. The degree of cross-linking for PS was determined by surface T_{gs} measurements, Sections 6.2.2 and 7.1.1.1. At an Ar^+ ion fluence above 5×10^{13} cm^{-2} the change in surface ΔT_{gs} was ≈ 22 K. The surface crosslink density determined at this fluence is ~ 20% and further ion bombardment increases the degree of cross-linking of the PS surface even more. In the case of N_2^+ and O_2^+ ion bombardment or after exposure to air, the surface T_{gs} was higher (ΔT_{gs} = 30 - 35 K) as compared to the PS surface treated with Ar^+ ions, (see Table 6.4) due to the formation of additional O_2 and/or N_2 containing polar groups which restrict the rotation [Young 91] together with the induced cross-links by active oxygen or nitrogen species [Lianos 94, Idage 98]. Ion beam induced cross-linking is an effective way to form a very cohesive and dense surface layer which could act as a metal diffusion barrier preventing metal migration into the bulk. As 1 keV ions penetrate up to 5 – 7 nm into the polymer, a highly modified and cross-linked layer is formed at the same depth. With increasing ion fluence the density of cross-links increases leading to the formation of a sharp interface between the treated layer and the untreated polymer bulk.

On the other hand, it should not be forgotten that additional to cross-link formation polymer degradation also takes place creating low molecular weight species. During prolonged surface modification, low molecular weight species (LMW) are formed, as was measured by size exclusion chromatography after exposure of PS to an RF discharge plasma

[Friedrich 99, Friedrich 00]. As was shown by Friedrich et al. [Friedrich 99], PS undergoes degradation by depolymerization in addition to the cross-linking reactions resulting in chains containing less monomers compared to the pristine chain. Formation of LMW species can also occur during ion bombardment. Small mass species formed on the surface are desorbed into the vacuum, while those created deeper in the polymer have a very low probability to escape. At the same time the cross-linked layer provides a diffusion barrier against migration of the degradation species, which then accumulate at the boundary between the cross-linked interface and the bulk polymer. This accumulation will lead to the formation of a weak boundary layer that causes the decrease of the metal/PS or metal/BPA-PC adhesion strength.

If LMW species are responsible for the low adhesion strength, polymers of the degrading type will form small mass molecules to an larger extent under ion irradiation resulting in low adhesion, as was shown for PαMS and PMMA. The surface glass transition temperature measurements for these two polymers did not show a large difference between treated (up to an ion fluence of 10^{14} cm^{-2}) and untreated surfaces (ΔT_{gs} = 2 - 4 K), Figure 6.20, confirming preferred degradation as dominating mechanism for these polymers. The formation of low molecular weight species in PαMS and PMMA should be the main reason for the poor metal/polymer interaction, as cross-links are formed rather slowly in such polymers compared to the production of small molecules. PαMS and PMMA degrade by main chain scission and through depolymerization reactions [Friedrich 99] and form stable small mass molecules. As discussed above, the smaller the chain size the lower is the degree of entanglement. The determined thickness of the remaining film of these polymers on the peeled off metal side increases with increasing ion fluences shows that the adhesion is improved at the metal/polymer interface due to the chemical interactions and the increased density of adsorption sites. But because of the formation of LMW species in the treated polymer layer, the entanglement is weak and therefore adhesion is poor.

For the third type of peel strength dependence on the ion fluence observed for the Cu/PP system, the adhesion increased with ongoing treatment. Our results and the results reported by Friedrich et al. [Friedrich 99] show that PP undergoes strong oxidation and cross-linking under oxygen treatment. From the failure location data it is not exactly clear where the failure occurs. But the increase in the strength measured by peel tests indicates that a strongly cross-linked layer may be the reason for the high strength, and that fracture possibly occurs in cross-linked layer.

7.2.5 Metal/polymer interface formation: summary and conclusions

The various effects of low energy ion treatment of the polymer surface discussed in the earlier sections contribute in a synergistic manner to a significant enhancement of the metal-polymer adhesion. Bombardment increased the number of nucleation sites and functional carbon-oxygen or carbon-nitrogen groups on the polymer surface leading to the enhancement of the metal adsorption probability. A partial correlation between the peel strength and the condensation coefficient as well as the increase in the polymer surface energy was found. A decrease in the measured adhesion strength (in case of PS, BPA-PC) or no adhesion improvement (for PαMS and PMMA) was recorded in the ion fluence range where complete metal condensation and saturation in the increased polymer surface energy was recorded. The exception was PP for which the peel strength increased with increasing ion fluence and reached some saturation.

XPS analysis of the fracture location showed that in most cases the failure location changed from interfacial failure for the untreated polymer to cohesive failure in the polymer for treated surfaces. These observations indicate that the adhesion is improved at the metal-polymer interface for all polymer/metal systems. The measured peel strength gives the force that is required to tear the two surfaces apart. And the fracture, as shown in the experiments, does not necessarily take place at the interface. An improvement in the metal-polymer adhesion in the ion fluence range of $10^{13} - 10^{16}$ cm^{-2} is attributed to the creation of a large density of new adsorption sites resulting in a larger contact area on the one hand, and the formation of chemically active groups on the other hand that lead to the increased interaction between metal and polymer through the formation of metal-oxygen/nitrogen-polymer species. The increase in surface roughness seen in AFM is negligible, and therefore plays little role in the adhesion.

Three types of peel strength dependence vs. ion fluence were observed, and adhesion models were suggested. The decrease in the peel strength at high ion fluences for PS and BPA-PC is attributed to the formation of a weak boundary layer that is formed between the cross-linked layer and polymer bulk, as the cohesive failure occurs deeper in the polymer with increasing ion fluence, Figure 7.16(a). The weak boundary layer is probably generated due to partial degradation of the polymer under ion bombardment and to diffusion of low molecular weight species (LMW) from the top cross-linked interface sublayer to the bulk polymer. At the same time the cross-linked layer provides a barrier against migration of the degradation species, which then accumulate at the boundary between the cross-linked interface and the bulk polymer.

For degrading polymers like PαMS and PMMA, Figure 7.16(b), LMW species are formed, which provide good interaction between the metal and the polymer at the interface, but because of the low degree of entanglement in the modified layer fracture is of the cohesive type resulting in a poor peel strength.

In the case of the Cu/PP system, a high degree of cross-linking is created under ion treatment resulting in the increased adhesion which reaches saturation at very high ion fluences. The failure location at this point cannot be identified exactly. However, excluding some of the results for the determination of the polymer thickness, the removed PP layer thickness shows a tendency to increase with increasing ion fluence. Taking this into account and paying attention to the increasing adhesion strength with increasing ion fluence, the failure may occur in the cross-linked layer.

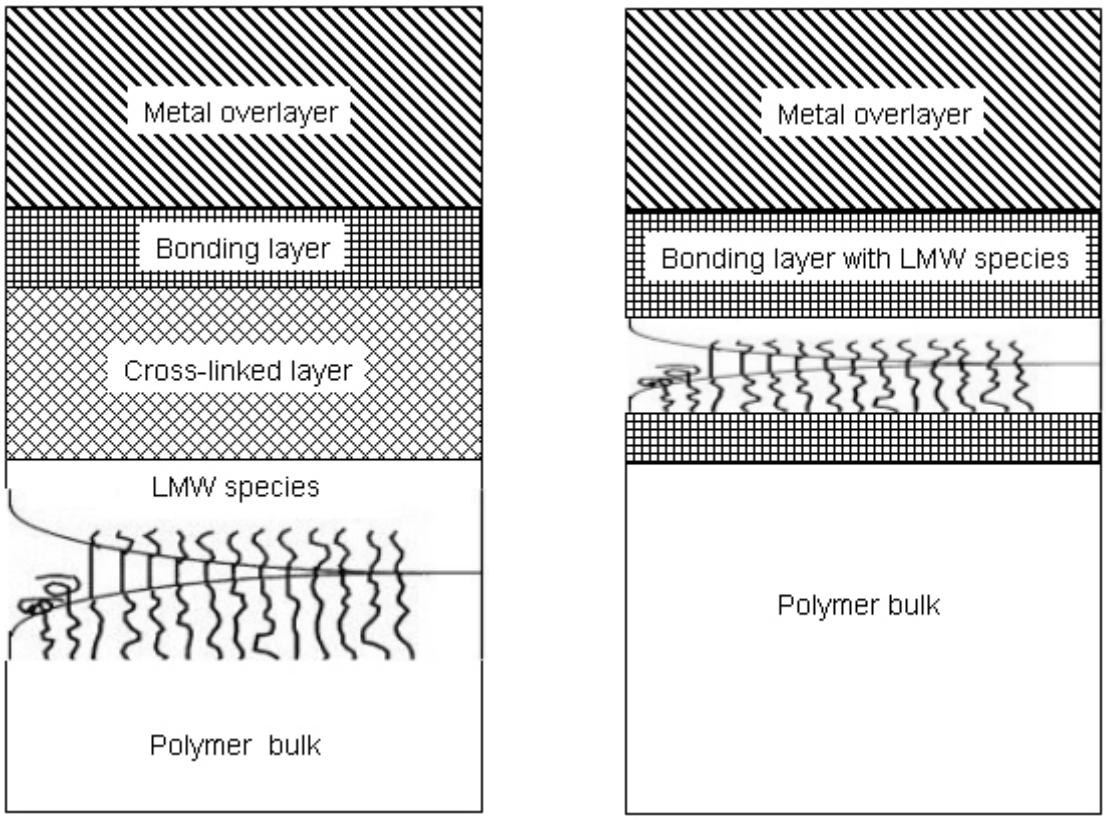

***Figure 7.16**. Multilayer models for the metal/polymer interfaces: a) PS and BPA-PC; b) PαMS and PMMA.*

Chapter 8

Summary and Conclusions

Low energy ion beam irradiation proved itself to be a suitable technique to alter the chemical and physical properties of polymer surfaces. Spin coated thin films and commercially available polymer sheets were irradiated with the ion source ISE 10 (Omicron) or a microwave ion gun IonEtch (Tectra) at ion energies of 0.5 – 5 keV in the fluence range of 10^{12} to 10^{16} cm^{-2} with argon, oxygen and nitrogen ions. The sputter rates of the different polymers were determined using three methods: step measurements with a stylus profilometer, X-ray photoelectron spectroscopy (XPS), and a quartz crystal microbalance (QCM). The QCM allowed observing the real time removal rate and the polymer sputter kinetics. The XPS method provided a good possibility to observe chemical changes that occurred in the polymer during sputtering. Step measurements with the stylus profilometer allowed us to perform quick sputter rate measurements for different polymers at defined ion fluences. A quadrupole mass spectrometer was used to perform mass analysis of the evolved gaseous species. The induced chemical changes in polymer surfaces were studied with angle resolved XPS that allowed us to determine the uniformity of the surface modification by variation of the take-off angle. Using the CASA-XPS software, data fitting was done to determine the nature and quantity of the induced new functional groups, and to monitor the removal of old functionalities. The surface glass transition temperature measurements based on the noble metal embedding method was used to determine the behaviour of the polymer under ion irradiation, i.e. cross-link formation or degradation. Atomic force microscopy was used to determine the surface roughness of thin polymer films after ion beam irradiation. The influence of the ion beam parameters and the polymer chemistry on the metal-polymer interaction was studied by measuring the metal condensation coefficient and the cluster density, polymer surface energy, and peel strength. Based on the results of the present work, the following conclusion can be drawn:

Low energy ion beam irradiation of thermoplastic polymers

- Sputter rates of various polymers differ by several orders of magnitude and showed a large dependence on the ion beam parameters and the polymer chemistry.
- The tendency of the sputter rate as a function of ion beam parameters was found to be the same for all investigated polymers. The sputter rates of the polymers decreased strongly with increasing ion fluence, followed by a constant removal rate in the steady-state region. The decrease of typically one order of magnitude was attributed to the chemical changes in the polymer structure that occurred in the ion fluence range of $10^{13} – 10^{15}$ cm^{-2} depending on the polymer chemistry, ion energy and ion type. Large differences in the sputter rate of the polymers were observed at very low ion fluences where the main chemical modifications took place. In the steady-state region, surfaces of different polymers were enriched with carbon or carbon-oxygen or carbon-nitrogen functional groups and the difference in the sputter rates were smaller, with the exception of Teflon like polymers which's removal rates remained several orders of magnitude higher compared to the other polymers. Oxygen being the most reactive gas (among those used in the experiments) caused the highest polymer removal rates compared with the rates obtained for bombardment with argon or nitrogen gas. The sputter rates of the polymers increased with increasing ion energy, while no rate dependence on different incident angles of the projectiles was observed.
- Experimental observation showed that the main factor determining the polymer removal rates of organic films bombarded at room temperature was the polymer chemistry. The rates differed by one/several orders of magnitude, as for example PS was sputtered at a rate of 0.3 nm/min, PMMA – 1.56 nm/min, and Teflon AF - 18.57 nm/min. Polymers containing aromatic rings are shown to have the lowest removal rates, as aromatic rings are known to be the most effective polymer stabilizers absorbing the excitation energy from the polymers. Nitrogen or/and oxygen containing polymers have larger removal rates, because of the abstraction of oxygen or nitrogen containing functional groups activating the main chain which led to main chain bond scission and the formation of small volatile molecules. When aromatic rings were added to polymers having high removal rates, the resistance of the polymer to ion bombardment was increased. Teflon-like polymers were shown to have the largest sputter rates.

- Chemical changes involved structural rearrangements, reactions with different species, like oxygen and/or nitrogen and led to the appearance of new functional groups, double bond formation, cross-linking and chain scissioning. The outer most surface layer underwent post-chemical reactions with the remaining active gases present in the vacuum chamber, or when subjected to reactive atmospheres. The schematic diagrams of the reaction pathways were given in the discussion. Analysis of angle resolved X-ray photoelectron spectroscopy showed that the very first changes under ion irradiation occurred in the outer most surface layer (1-2 nm), and in the saturation region the induced changes were observed in the whole penetration depth of the ions (5-7 nm for ions with an energy of 1 keV). Ion modification is a dynamical process that reaches a stationary state above an ion fluence of 10^{15} cm^{-2} and remains uniform with time.

- Polymer sputtering at elevated temperatures was influenced by the tendency of the polymers to cross-link or degrade under irradiation, and their behaviour during thermal degradation. The ability of the polymers to form cross-links or degradation products on the surface under low energy ion irradiation was confirmed by the surface glass transition measurements for PS, PαMS and PMMA. Cross-linking polymers (like PS) did not show changes in the ablation rate at elevated sample temperatures up to 470 K, while PαMS (polymer with preferred degradation) was removed much faster at elevated temperatures. In both cases, the ion beam bombardment of heated samples induced polymer depolymerization at temperatures much lower than it is observed in conventional pyrolysis leading to a large yield of monomer emission and fast polymer degradation. The ratios of the emitted species during heating and during sputtering at elevated temperatures showed that polymer degradation under ion irradiation is similar to the degradation that occurs during heating.

- There are a number of theoretical models and molecular dynamics simulations of molecular desorption mechanisms under ion bombardment. However, none of them can explain the observed rate dependence on the ion fluence, the large difference (orders of magnitude) in the sputter rate values at the beginning and in the steady-state region, and the rate dependence on the polymer chemistry. Moreover, none of the models take into account the induced post-chemical reactions that influence the polymer surface properties.

Polymer-metal interface formation and adhesion after low energy ion beam irradiation

- When polymer surfaces are treated with low energy ion beams the metallization behaviour in the early stage of metallization changes from incomplete to complete condensation. Ion bombardment increased the number of nucleation sites and functional carbon-oxygen or carbon-nitrogen groups on the polymer surface leading to an increase of the metal adsorption probability as well as an enhancement of the adhesion between the two materials.

- The condensation coefficient is related to the probability for a metal atom to reach a preferred nucleation site which in turn is related to the mean distance between these sites and the diffusion length of the adatoms on the polymer surface. Using ion-beam treatment, additional adsorption sites (terminal groups, formation of oxygen or nitrogen functional groups or functionalities of other elements not previously contained in the polymer that are reactive towards a metal) were created on the polymer surface. The increased number of clusters formed resulted in an increase in the adsorption probability.

- Only a partial correlation between the peel strength and the condensation coefficient as well as the increase in the polymer surface energy was found. A decrease in the measured adhesion strength (in case of PS, BPA-PC) or no adhesion improvement (for PαMS and PMMA) was recorded in the ion fluence range where complete metal condensation and saturation in the increased polymer surface energy were recorded. The exception was PP for which the peel strength increased with increasing ion fluence and reached some saturation.

- XPS analysis of the peeled-off surfaces showed that in most cases the failure location changed from interfacial for untreated polymers to cohesive failure inside the polymer for treated surfaces. These observations indicate that the adhesion is improved at the metal-polymer interface for all polymer/metal systems. The improvement in the metal-polymer adhesion in the ion fluence range of 10^{13} – 10^{16} cm^{-2} is attributed to the creation of a large density of new adsorption sites resulting in a larger contact area, and chemically active groups that lead to the increased interaction between the metal and the polymer by formation of metal-oxygen/nitrogen-polymer species. The influence of a large number of nucleation sites was demonstrated by the experiments done at low temperatures (-170 °C). At such temperatures the metal atoms are trapped at all nucleation sites of the untreated polymer surface due to little diffusion of

adatoms resulting in the formation of a large density of metal clusters and therefore an increased contact area. Correspondingly, an enhancement in adhesion strength by one order of magnitude was measured. The metal interaction with the polymer surface through chemically active functional groups results in strong adhesion (increase by several orders of magnitude) between two materials.

- In the literature it was stated that chemically more active metals like Al or Cr oxidize rapidly preferentially forming strong bonds with oxygen functionalities resulting in larger adhesion strengths. While metals (Cu, Au, Ag) of lower oxidation rate are more reactive with nitrogen containing species leading to enhanced metal-polymer interaction. This tendency is observed in the condensation coefficient measurements, i.e. Cu adsorbs better on nitrogen treated PS surfaces. However, the absolute values of the measured adhesion strength received for oxygen treated polymers showed better adhesion than those obtained for nitrogen treated polymers.

- Three types of peel strength behaviour vs. ion fluence were observed: the adhesion increased with increasing ion fluence until saturation was reached, which is the case for PP; the peel strength increased for low ion fluencies, reached a maximum and decreased for prolonged treatment, for PS, BPA-PC; no improvement in the peel strength for metal on treated PαMS and PMMA surfaces was recorded.

  The decrease in the peel strength for PS and BPA-PC is attributed to the formation of a weak boundary layer that is formed between the cross-linked layer and the polymer bulk, as the cohesive failure occurred deeper in the polymer with increasing ion fluence. The weak boundary layer is most probably generated due to partial degradation of the polymer by ion bombardment and diffusion of the low molecular weight species (LMW) from the top of the cross-linked interface sublayer to the bulk polymer. For degrading polymers like PαMS and PMMA, LMW species are formed, which provide good interaction between the metal and the polymer at the interface, but because of the low degree of entanglement in the modified layer fracture is of cohesive type with a poor peel strength. In the case of the Cu/PP system, a high degree of cross-linking is formed under ion treatment resulting in the increasing adhesion which reaches saturation at high ion fluences.

Chapter 9

Outlook

In this work, ion beam irradiation of different polymers was discussed with respect to the influence of the ion beam parameters, the sample temperature and the polymer chemistry. The induced alterations in the polymer surface chemistry showed to have a large influence on the surface properties like surface glass transition temperature, surface tension, metal condensation and nucleation, as well as metal-polymer adhesion. The experiments should be extended on polymers with different functional groups, like arylonitriles, acrylates, etc. The influence of the degree of crystalinity on the removal rate is also interesting.

X-ray photoelectron spectroscopy is a widely applied technique to determine the surface chemistry, and high resolution carbon spectra provided rather large information on the induced functionalities. However, performing the data fitting procedure, it was noticed that many features overlap with each other making it difficult to specify the exact functional groups that are formed. Therefore, grazing angle infrared spectroscopy would help to identify bonds and functional groups present in the polymer, as bond deformations are rather sensitive to the presence of neighbouring atoms and bonds. Chemical derivatization of ion treated polymer surfaces would also allow a more selective analysis of a particular functional group formed.

There were no investigations done on the stability of functional groups as a function of time. Contact angle measurements [Garbassi 98, Chan 94] demonstrated that the number of plasma induced polar groups decreased with time. The effect of ageing on metal adhesion on polymer surfaces should be also investigated, as it is important for technological applications.

The adhesion behaviour of more reactive metals (like Al, Ni, Cr) on treated polymer surfaces should be studied, as well as the dependence of the adhesion on the ion energy.

Superhydrophobic materials with a water contact angle larger than 150° have received a lot of attention in research. A typical procedure for the fabrication of ultrahydrophobic surfaces is to create a rough surface covered with low surface energy molecules, or to roughen the surface of hydrophobic materials. Using an ion beam it is possible to obtain well defined nanostructures on polymer surfaces by two different approaches. Firstly, because of the

difference in the sputter rates of metals and polymers, self-organized growth of metal clusters on polymer surfaces can be used to form nanomasks. As a result, the metal-free polymer surfaces will be preferentially sputtered creating needle like structures. The second approach is based on self-organized nanostructuring by using block copolymers. The removal rates differ from polymer to polymer, therefore ion irradiation of copolymers, whose blocks show a large difference in the sputter rates, will result in different patterns by preferentially removing one block. Metal nanomasks can also be used in the case of copolymers with largely differing metal condensation coefficients. Taking advantage of the different nucleation rates of noble metals on the copolymer blocks, one block can be completely covered with metal in this way be protected from ion bombardment.

Recently, first experiments were performed for polymer surface modification with relevance to cell adhesion together with the Institute of Biochemistry, Christian-Albrecht University, Kiel. It was shown, that treated PS provided good conditions for cell growth. Further research is desired to find the optimum treatment conditions for a given type of cells in order to provide good cell adhesion on a polymer surface or to prevent cell growth completely.

List of References

Adesida 84 I. Adesida, L. Karapiperis, *J. Appl. Phys*. **56**(6) (1984) 1801.

Anton 00 R. Anton, Th. Wiegner, W. Naumann, M. Liebmann, Chr. Klein, Chr. Bradley, *Rev. Sci. Instruments* **71**(2) (2000) 1177.

Atkins 02 R.C. Atkins, F.A. Carey "Organic Chemistry: A Brief Course", McGraw Hill, 2002.

Baglin 87 J.E.E. Baglin, in: "Ion-beam Modification of Insulators", P. Mazzoldi, G.W. Arnold, (eds.), Elsevier, Amsterdam, (1987), p. 585.

Beamson 92 G. Beamson, D. Briggs, "High Resolution XPS of Organic Polymers", John Wiley & Sons, Chichester, 1992.

Beardmore 95 K. Beardmore, R. Smith, *Nucl. Instrum. Meth. Phys. Res. B* **102** (1995) 223.

Beaucage 93 G. Beaucage, R. Composto, R.S. Stein, *J. Poly. Sci.; Polym. Phys. Ed.* **31** (1993) 319.

Behnke 00 K. Behnke, "Herstellung und Characterizierung von gasphasenabgeschiedenen metallhaltigen Polymerfilmen", Disertation, Technical Faculty, Christian-Albrechts University, Kiel, 2000.

Behrndt 71 K.H. Behrndt, *J. Vac. Sci. Technol*. **8**(5) (1971) 622.

Behrisch 81 R. Behrisch, "Sputtering by Particle Bombardment I", Springer-Verlag, Berlin, 1981.

Behrisch 91 R. Behrisch, K. Wittmaack, "Sputtering by Particle Bombardment III", Springer-Verlag, Berlin, 1991.

Bertrand 97 P. Bertrand, P. Lambert, Y. Travaly, *Nucl. Instrum. Meth. Phys. Res. B* **131** (1997) 71.

Bikerman 61 J.J. Bikerman, "*The Science of Adhesive Joint*s", Academic Press, New Yourk (1961).

Biederman 00 H. Biederman, *J. Vac. Sci. Technol. A* **18**(4) (2000)1642.

Biersak 80 J.P. Biersak, L.G. Haggmark, *Nucl. Instrum. Meth. Phys. Res.* **174** (1980) 257.

Biersak 87 J.P. Biersack, in: “Ion-beam Modification of Insulators”, P. Mazzoldi, G.W. Arnold, (eds.), Elsevier, Amsterdam, (1987), p. 1; p. 648.

Binning 86 G, Binning, C. Quate, Ch. Gerber, *Phys. Rev. Lett.* **56** (1986) 930.

Biswas 03 A. Biswas, Z. Marton, J. Kruse, J. Kanzow, V. Zaporojtchenko, F. Faupel, T. Strunskus, *Nano. Lett*. **3**(1) (2003) 69.

Bragg 05 W.H. Bragg, R. Kleemann, *Phil. Mag*. **10** (1905) 318.

Brandrup 99 J. Brandrup, E.H. Immergut, E.A. Grulke, “Polymer Handbook”, John Wiley & Sons, 1999.

Briggs 82 D. Briggs, A.B. Wootton, *Surf. Interface Anal.* **4**(3) (1982) 109.

Briggs 90 D. Briggs, M.P. Seah, “Practical Surface Analysis“, 2nd ed., Vol. 1, Wiley, Chichester, 1990.

Briggs 98 D. Briggs, “Surface Analysis of Polymers by XPS and SIMS“, Cambridge University Press, 1998.

Brown 04 I.C. Brown, ”The Physics and Technology of Ion Sources“, Wiley-VCH, Weinheim, 2004.

Burger 92 R.W. Burger, L.J. Gerenser, in: “Metallized Plastics 3: Fundamental and Applied Aspects”, K.L. Mittal (ed.), Plenum Press, New York, (1992), p. 179.

Burkstrand 78 J.M. Burkstrand, *Appl. Phys. Lett*. **33**(5) (1978) 387.

Burkstrand 79 J.M. Burkstrand, *Phys. Rev. B* **30**(12) (1979) 4853.

Buttry 92 D.A. Buttry, M.D. Ward, *Chem. Rev*. **92** (1992) 1355.

Calcagno 91 L. Calcagno, G. Foti, *Nucl. Instrum. Meth. Phys. Res. B* **59/60** (1991) 1153.

Calcagno 92 L. Calcagno, G. Compagnini, G. Foti, *Nucl. Instrum. Meth. Phys. Res. B* **65** (1992) 413.

Carlson 85 J.D. Carlson, J.E. Bares, A.M. Guzman, P.P.Pronko, *Nucl. Instrum. Meth. Phys. Res. B* **7/8** (1985) 507.

Chan 94 C.M. Chan, “Polymer Surface Mofication and Characterization”, Hanser Publishers, Munich, 1994.

Chapiro 62 A. Chapiro, “Radiation Chemistry of Polymeric Systems”, Interscience Publischers, New York, 1962.

Chapiro 88 A. Chapiro Nucl. Instr. Meth. Phys. Res. B 32 (1988) 111.

Chapiro 95 A. Chapiro, *Nucl. Instrum. Meth. Phys. Res. B* **105** (1995) 5.

Chapman 80 B. Chapman, “Glow Discharge Processes: Sputtering and Plasma Etching”, John Willey & Sons, New York, 1980.

Charbonnier 00 M Charbonnier, M. Romand, M. Alami, T.M. Duc, in: ″Polymer surface modification: Relevance to adhesion″, K.L. Mittal (ed.), Vol.2, (2000), p. 3.

Charlesby 60 A. Charlesby, “Atomic Radiation and Polymers”, Pergamon Press, Oxford, 1960.

Charlesby 87 A. Charlesby, in: “Radiation Chemistry: Principles and Applications”, Farhatazis, and M.A.J. Rodgers (eds.), VSH, (1987), pp. 451-476.

Charlesby 91 A. Charlesby, in “Irradiation Effects on Polymers”, D.W. Clegg, A.A. Collyer (eds.), Elsevier, (1991), p. 39.

Claybourn 98 M. Claybourn, “Infrared Reflectance Spectroscopy of Polymers”, Global Press, 1998.

Clough 91 R.L. Clough, K.T. Gillen, M. Dole, in “Irradiation Effects on Polymers”, D.W. Clegg, A.A. Collyer (eds.), Elsevier, (1991), p. 79.

Colthup 90 N.B. Colthup, L.H. Daly, S.E. Wiberley, “Introduction to Infrared and Raman Spectroscopy”, Academic Press, San Diego, 1990.

Cottrell 58 T.L. Cottrell, “The strength of Chemical Bonds”, Butterworth Scientific Publications, London, 1958.

Creton 99 C. Creton, in: “Polymer Surfaces and Interfaces III”, R.W. Richards, S.K. Peace (eds.), John Wiley& Sons, Chichester, (1999), p.101.

Dawson 76 P.H. Dawson, “Quadrupole Mass Spectrometry and its Applications”, AIP Press,Woodbury, 1976.

Delcorte 99 A. Delcorte, X. Vanden Eynde, P. Bertrand, D.F. Reich, *Intern. J. Mass Spec.* **189** (1999) 133.

Delcorte00a A. Delcorte, X. Vanden Eynde, P. Bertrand, J.C. Garrison, *J. Phys. Chem. B* **104** (2000) 2673.

Delcorte 00b A. Delcorte, B.J. Garrison, *J. Phys.Chem. B* **104** (2000) 6785.

Delcorte 01 A. Delcorte, P. Bertran, B.J. Garrison, *J. Phys. Chem. B* **105** (2001) 9474

Delcorte 04 A. Delcorte, B.J. Garrison, *J. Phys. Chem. B* **108** (2004) 15652.

Denison 73 D.R. Denison, *J. Vac. Sci. Technol*. **10**(1) (1973) 126.

Derjaguin 55 B.V. Derjaguin, *Research* **8** (1955) 70.

Dissado 92 L.A. Dissado, J.C. Fothergill, "Electrical degradation and breakdown in polymers", Peter Peregrinus, London, 1992.

Droulas 92 J.L. Droulas, Y. Jugnet, T.M. Due, in: "Metallized Plastics 3: Fundamental and Applied Aspects", K.L. Mittal (ed.), Plenum Press, New York, (1992), p. 123.

Eggito 90 F.D. Egitto, V. Vukanovic, G.N. Taylor, in: "Plasma Deposition, Treatment, and Etching of Polymers", R. d'Agostino (ed.), Academic Press, Boston, (1990), p.321.

Einstein 05 A. Einstein, *Annalen der Physik* **17** (1905) 132.

Elias 97 H.G. Elias, "Introduction to Polymer Science", VCH, Weinheim, 1997.

Elman 83 B.S. Elman, M.K. Thaker, D.J. Sangman, M.A. Newkirk, *J. Appl. Phys.* **57** (1983) 3150.

Erichsen 04a J. Erichsen, J. Kanzow, U. Schürmann, K. Dolgner, K. Günter-Schade, T. Strunskus, V. Zaporojtchenko, F. Faupel, *Macromolecules*, **37** (2004) 1831.

Erichsen 04b J. Erichsen, "Untersuchungen des Oberflächenglasüberganges von Polystyrol mittels des Einbettens von Edelmetall-Clustern", Disertation, Technical Faculty, Christian-Albrechts University, Kiel, 2004.

Faupel 02 F. Faupel, V. Zaporoftchenko, T. Satrunskus, J. Erichsen, K. Dolgner, A. Thran, M. Kiene, in: "Mettalization of Polymers 2", E. Sacher (ed.), Kluwer Academic/Plenum Publishers, New York, 2002.

Feldman 94 V.I. Feldman, F.F. Suknov, N.A. Slovokhotova, *Polym. Sci. B* **36**(3) (1994) 429.

Fink 04 D. Fink, "Fundamentals of Ion-Irradiated Polymers", Springer, Berlin, 2004.

Fischer 82 P. Fischer, in: "Electrical Properties of Polymers", D.A. Seanor (ed.), Academic Press, New York, 1982.

Flitsch 90 R. Flitsch, D.Y. Shih, *J. Vac. Sci. Technol. A* **8** (3) (1990) 2376.

Forrest 96 J.A. Forrest, K. Dalnoki-Veress, J.R. Stevens, R.J. Dutcher, *Phys. Rev. Lett*. **77** (1996) 2002.

Forrest 00 J.A. Forrest, R.L.A. Jones, in: "Polymer Surfaces, Interfaces and Thin Films", A. Karim, S. Kumar (eds.), World, Scientific, Singapore, (2000), p. 251.

Fourche 95 G. Fourche*, Polym. Eng. Sci*., **35** (1995) 957.

Fragala 98 M.E. Fragala, G. Compagnini, L. Torrisi, O. Puglisi, *Nucl. Instrum. Meth. Phys. Res. B* **141** (1998) 169.

Fragala 99 M.E. Fragala, G. Compagnini, O. Puglisi, *J. Mater. Res.* **14** (1999) 228.

France 98 R.M. France, R.D. Short, *Langmuir* **14** (1998) 4827.

Friedrich 99 J.F. Friedrich, W.E.S. unger, A. Lippits, I. Korpinarov, G. Kühn, St. Weidner, L. Vogel, *Surf. Coat. Technol.* **116-119** (1999) 772.

Friedrich 00 J.F. Friedrich, W.E.S. Unger, A. Lippitz, R. Giebler, I. Koprinarov, St. Weidner, G. Kühn, in: ″Polymer surface modification: Relevance to adhesion″, K.L. Mittal (ed.), Vol.2, (2000), p. 137.

Fuchs 90 E. Fuchs, H. Oppolzer, H. Rehme, "Particle Beam Microanalysis", VCH, Weinheim, 1990.

Galuska 92 A. Galuska, in: ″Metalized Plastics 3: Fundamental and Applied Aspects″ K.L. Mittal (ed.), Plenum Press, New York, (1992), p. 267.

Garbassi 98 F. Garbassi, M. Morra, E. Occhiello, "Polymer Surfaces: from Physics to technology", John Wiley& Sons, Chichester, 1998.

Garrison 00 B.J. Garrison, A. Delcorte, K.D. Kratzmann, *Acc. Chem. Res*. **33** (2000) 69.

Gent 77 A.N. Gent, G.R. Hamed, *Polym. Eng. Sci.* **17** (1977) 462.

Gerenser 92 L.J. Gerenser, K.E. Goppert-Berarducci, in: ″Metalized Plastics 3: Fundamental and Applied Aspects″ K.L. Mittal (ed.), Plenum Press, New York, (1992), p. 163.

Gerenser 93 L.J. Gerenser, *J. Adhesion Sci. Technol*. **7**(10) (1993) 1019.

Gokan 83 H. Gokan, S. Esho, Y. Ohnishi, *J. Electrochem. Soc.* **130**(1) (1983) 143.

Gokan 84 H. Gokan, M. Itoh, S. Echo, *J. Vac. Sci. Technol. B* **2**(1) (1984) 34.

Gokan 85 H. Gokan, K. Tanigaki, Y. Ohnishi, *Solid State Technol*. **28** (1985) 163.

Goldstein 96 E. Goldstein, *Berl. Ber.* **39** (1896) 691.

Golser 91 R. Golser, D. Semrad, *Phys. Rev. Lett*. **66** (1991) 1831.

Grant 98 J.L. Grant, D.S. Dunn, D.J. McClure, J. Vac. Sci. Technol. A 6 (1998) 2213.

Grest 71 G.S. Grest, H.H. Cohen, *Adv. Chem. Phys*. **4** (1971) 21.

Grove 52 W.R. Grove, *Phil. Trans. R. Soc. Lond*. **142** (1852) 87.

Gupta 80 A. Gupta, R. Liang, F.D. Tsai, J. Moacanin, *Macromolecules* **13** (1980) 1696.

Haring 87 R.A. Haring, H.E. Roosendal, P.C. Zalm, *Nucl. Instrum. Meth. Phys. Res.* **B 28** (1987) 205.

Helbert 80 J.N. Helbert, M.A. Schmidt, J.H. Lai, *Organic Coatings and Plastics Chemistry* **43** (1980) 258.

Hertz 87 H. Hertz, *Ann. Phys*. **31** (1887) 938.

Hnatowizc 93 V. Hnatowicz, V. Havranek, J. Kvitek, V. Perina, V. Svorcik, V. Rybka, Jpn. J. Appl. Phys. 32 (1993) 1810.

Hoogebrugge 87 R. Hoogebrugge, P.G. Kistermaker, *Nucl. Instrum. Meth. Phys. Res.* **B 21** (1987) 37.

Idage 98 S.B. Idage, S. Badrinarayanan, Langmuir 14 (1998) 2780.

Israelachvili 91 J. Israelachvili, “Intermolecular and surface forces”, Academic Press, San Diego, 1991.

Johnson 87 R.E. Johnson, B.U.R. Sundqvist, A. Hedin, D. Fenyö, *Phys. Rev.* **B 40** (1989) 49.

Jones 99 R.A.L. Jones, R.W. Richards, “Polymers at Surfaces and Interfaces”, Cambridge University Press, 1999.

Kanzow 04 J. Kanzow, “Structur, Vernetzung und Metallisierung duroplastischer Polymere”, Disertation, Technical Faculty, Christian-Albrechts University, Kiel 2004.

Katz 68 R. Katz, *Nuclear Track Detection* **2** (1968) 1.

Keddie 94 J.L. Keddie, R.A.L. Jones, R.A. Cory, *Europhys. Lett*. **27** (1994) 59.

Kelly 90 R. Kelly, *Nucl. Instrum. Meth. Phys. Res. B* **46** (1990) 441.

Kim 01 H.J. Kim, K.J. Lee, Y.Seo, S.Kwak, S.K. Koh, *Macromolecules* **34** (2001) 2546.

Kinloch 81 A.J. Kinloch, S.J. Shaw, *J. Adhesion* **12** (1981) 59.

Kinlock 94 A.J. Kinloch, “Adhesion and Adesives: Science and Technology”, Chapman & Hall, London, 1994.

Krevelen 90 D.W. van Krevelen, “Properties of Polymers”, Elsevier, Amsterdam, 1990.

Landau 59 L.D. Landau, E.M. Lifschitz, “Fluid Mechanics”, Reading, Massachussetts, 1959.

Langmuir 25 I. Langmuir, K.H. Kingdon, *Proc. R. Soc. London A* **107** (1925) 61.

Lee 91 L.H. Lee (ed.), “Fundamentals of adhesion”, Plenum Press , New York, 1991.

Leeden 02 M.C. van der Leeden, G. Frens, *Adv. Eng. Mat*., **4**(5) (2002) 280.

Lehokey 88 E.M. Lehokey, I. Reid, I. Hill, *J. Vac. Sci. Technol. A* **6**(4) (1988) 2221.

Lianos 94 L. Lianos, D. Parrat, T.Q. Hoc, T.M. Duc, *J. Vac. Sci. Technol. A* **12**(4) (1994) 2491.

Licciardello 88 A. Licciardello, O. Puglisi, L. Calcagno, G. Foti, *Nucl. Instrum. Meth. Phys. Res. B* **32** (1988) 131.

Lu 72 C.S. Lu, O. Lewis, *J. Appl. Phys*. **43**(11) (1972) 4385.

Lu 75 C.S. Lu, *J. Vac. Sci. Technol*. **12**(1) (1975) 578.

Lucchese 87 R.R. Lucchese, *J. Chem. Phys.* **86** (1987) 443.

MacCallum 89 J.R. MacCallum, in: "Comprehensive Polymer Science: Polymer Reactions", Volume 6, G.C. Eastmond, A. Ledwith, S. Russo, P. Sigwalt (eds.), Pergamon Press, (1989), Chapter 18, p. 529.

Magonov 96 S.N. Magonov, M.-H. Whangbo, "Surface Analysis with STM and AFM", VSH, Weinheim, 1996.

Mahan 00 J.E. Mahan, "Physical Vapour Deposition of Thin Films", Willey, (2000), Chapter VII.

March 95 R.E. March, J.F.J. Todd, "Practical Aspects of Ion Trap Mass Spectrometry", CRC Press, Boca Raton, 1995.

Marletta 90a G. Marletta, *Nucl. Instrum. Meth. Phys. Res. B* **46** (1990) 295.

Marletta 90b G. Marletta, S. M. Catalano, S. Pignataro, *Surf. Interface Anal*. **16** (1990) 407.

Mattox 98 D.M. Matox, "Handbook of Physical Vapour Deposition Processing", Noyes Publications, New Jersey, 1998.

McNeill 89 I.C. McNeill, in: "Comprehensive Polymer Science: Polymer Reactions", Volume 6, G.C. Eastmond, A. Ledwith, S. Russo, P. Sigwalt (eds.), Pergamon Press, (1989), Chapter 15, p. 471.

Menges 90 G. Menges, "Werkstoffkunde Kunstoffe", Hanser, München, (1990).

Meyerhofer 78 D. Meyerhofer, *J. Appl. Phys*. **49**(7) (1978) 3993.

Michael 86 R. Michael, D. Stulick, *J. Vac. Sci. Technol. A* **4** (1986) 1861.

Mittal 76 K.L. Mittal, *J. Vac. Sci. Technol.* **13**(1) (1976) 19.

Mittal 98 K.L. Mittal (Ed.), Metallized Plastics 5&6: Fundamental and Applied Aspects, VSP, Utrecht, 1998.

Mittal 01 K.L. Mittal (Ed.), Metallized Plastics 7: Fundamental and Applied Aspects, VSP, Utrecht, 2001.

Morra 90 M. Morra, E. Occiello, R. Marolly, F. Garbassi, P. Humphrey, D. Johnson, *J. Colloid Interface Sci*. **137** (1990) 11.

Moss 86 S.J. Moss, A.M. Jolly, B.J. Tighe, *Plasma Chemistry and Plasma Processing*, **6**(4) (1986) 401.

Moulder 92 J.F. Moulder, W.F. Stickle, P.E. Sobol, K.D. Bomben, "Handbook, of X-ray Photoelectron Spectroscopy", Perkin-Elmer Corporation, 1992.

Occhiello 90 E. Occhiello, F. Garbassi, in: "High Energy Density Technologies in Material Science", F. Garbassi, E. Occhiello (eds.) Kluwer, (1990), p. 105.

Ohring 92 M. Ohring, "The Materials Science of Thin Films", Academic Press, San Diego, 1992.

Paynter 02 R.W. Paynter, *Surf. Interface Anal.* **33** (2002) 14.

Peterson 01 J.D. Peterson, S. Vyazovkin, C.A. Wight, *Macromol. Chem. Phys.* **202** (2001) 775.

Pivin 95 J.C. Pivin, P. Viel, G. Zalczer, G. Marletta, *Nucl. Instrum. Meth. Phys. Res. B* **105** (1995) 192.

Puglisi 88 O. Puglisi, A. Licciardello, L. Calcagno, G. Foti, *J. Mater. Res*. **3**(6) (1988) 1247.

Puglisi 94 O. Puglisi, A. Licciardello, *Nucl. Instrum. Meth. Phys. Res. B* **91** (1994) 431.

Ratsch 03 C. Ratsch, J.A. Venables, *J. Vac. Sci. Technol. A* **21**(5) (2003) S96.

Reimann 93 C.T. Reimann, *Mat. -Fys. Medd. K. Dan. Vidensk. Selks*. **43** (1993) 351.

Reimer 84 H. Reimer, "*Transmission Eletron Microscopy*", Springer Verlag, Berlin, 1984.

Reiter 94 G. Reiter, *Macromolecules* **27** (1994) 3046.

Sabbatini 93 L. Sabbatini, P. G. Zambonin, ”Surface Characterization of Advanced Polymers”, VSH, Weinheim, 1993.

Sauerbey 59 G. Sauerbey, *Z. Phys*. **155** (1959) 206.

Schnabel 81 W. Schnabel, „Polymer Degradation: Principles and Practical Applications“, Hanser International, München, 1981.

Schonhorn 78 H. Schonhorn, in: “Polymer Surfaces”, D.T. Clark, W.J. Feast (eds.), Wiley, (1978), p. 213.

Schürmann 05 U. Schürmann, W. Hartung, H. Takele, V. Zaporojtchenko, F. Faupel, *Nanoletters*, 2005, in press.

Seah 80 M.P. Seah, *Surf. Interface Anal.* **2** (1980) 222.

Shard 92 A.G. Shard, J.P.S. Badyal, *Macromolecules* **25** (1992) 2053.

Sigmund 81 P. Sigmund, in: ”Sputtering by Particle Bombardment I”, R. Behrisch (ed.), Springer-Verlag, Berlin, (1981), p. 9.

Strobel 89 M. Strobel, C.Dunatov, J.M. Strobel, C. S. Lyons, S. J. Perron, M. C. Morgen, *J. Adhesion Sci. Technol.* **3**(5) (1989) 321.

Strobel 03 M. Strobel, C.S. Lyons, *J. Adhesion Sci. Technol.* **17**(1) (2003) 15.

Strunskus 98 T. Strunskus, M. Kiene, R. Willecke, A. Thran, C.v. Bechtolsheim, F. Faupel, *Materials and Corrosion* 49 (1998) 180.

Sundquist 91 Bo U.R. Sundquist, in: ”Sputtering by Particle Bombardment III”, R. Behrisch, K. Wittmaack (eds.), Springer-Verlag, Berlin, (1991), p. 256.

Sunner 88 J. Sunner, A. Morales, P. Kebarle, *Int. J. Mass Spectr. and Ion Proc*. **86** (1988) 169.

Tanuma 93 S. Tanuma, C.J. Powell, D.R. Penn, *Surf. Interf. Anal*. **21** (1993) 165.

Taylor 80 G.N. Taylor, T.M. Wolf, *Polym. Engineering Sci.,* **20**(16) (1980) 1087.

Thran 99 Thran, M. Keine, V. Zaporojtchenko, F. Faupel, *Phys. Rev. Lett.,* **82** (1999) 1903.

Todd 60 A. Todd, *J. Polym. Sci*. **42** (1960) 223.

Tremblay 03 M.C. Tremblay, R.W. Paynter, *Surf. Interface Anal*. **35** (2003) 502.

Tsuge 97 S. Tsuge, H. Ohtani, *Polymer Degradation and Stability* **58** (1997) 109.

Urbassek 91 H.M. Urbassek, K.T. Waldeer, *Phys. Rev. Lett*. **67** (1991) 105.

Venkatesan 83 T. Venkatesan, S.R. Forrest, M.L. Kaplan, C.A. Murray, P.H. Schmith, B.J. Wilkens, *J. Appl. Phys.* **54** (1983) 3150.

Venkatesan 87 T. Venkatesan, L. Calgano, B.S. Elman, G. Foti, in: "Ion-beam Modification of Insulators", P. Mazzoldi, G.W. Arnold, (eds.), Elsevier, Amsterdam, (1987), p. 301.

Voyutskii 49 S.S. Voyutskii, Y.L. Margolina, *Uspechi Khimi*. **18** (1949) 449; *Rubber Chem. Technol.* **30** (1957) 531.

Wang 93 Y.Q. Wang, R.E. Giedd, L.B. Bridwell, *Nucl. Instrum. Meth. Phys. Res. B* **79** (1987) 659.

Wang 97 Y.Q. Wang, L.B. Bridwell, R.E. Giedd, in: "Desk Reference of Functional Polymers: Syntheses and Applications", R. Arshady (ed.), American Chemical Society, Washington, 1997, Chapter 2.5, p. 373.

Wilson 93a R.G. Wilson, *J. Appl. Phys*. **73**(5) (1993) 2215.

Wilson 93b R.G. Wilson, G.E. Lux, C.L. Kirschbaum, *J. Appl. Phys*. **73**(5) (1993) 2524.

Woods 94 R.J. Woods, A.K. Pikaev, "Applied Radiation Chemistry: Radiation Processing", John Wiley & Sons, New York, 1994.

Wolf 95 B. Wolf, "Ion Sources", CRS Press, Boca Raton, 1995.

Young 91 R.J. Young, P.A. Lovell, "Introduction to Polymers", Chapman & Hall, London, 1991.

Zaporojtchenko 00a V. Zaporojtchenko, K. Behnke, T. Strunskus, F. Faupel, *Surf. Interface Anal*. **30** (2000) 439.

Zaporojtchenko 00b V. Zaporojtchenko, K. Behnke, T. Strunskus, F. Faupel, *Surf. Sci*. **454-456** (2000) 412.

Zaporojtchenko 01 V. Zaporojtchenko, T. Strunskus, J. Erichsen, F. Faupel, *Macromolecules* **34**(5) (2001) 1125.

Zaporojtchenko 02 V. Zaporojtchenko, J. Erichsen, J. Zekonyte, A. Thran, T. Strunskus, F. Faupel, in: "Mettalization of Polymers 2", E. Sacher (ed.), Kluwer Academic/Plenum Publishers, New York, 2002, p. 107.

Zaporojtchenko 03a V. Zaporojtchenko, J. Zekonyte, A. Biswas, F. Faupel, *Surface Science* **532-535** (2003) 300.

Zaporojtchenko 03b V. Zaporojtchenko, J. Zekonyte, J. Erichsen, F. Faupel, *Nucl. Instrum. Meth. Phys. Res. B* **208** (2003) 155.

Zaporojtchenko 05 V. Zaporojtchenko, J. Zekonyte, S. Wille, U. Schuermann, F. Faupel, *Nucl. Instrum. Meth. Phys. Res. B* (2005) **236** (2005) 95.

Zel'dovich 67 Ya.B. Zel'dovich, Yu. P. Raizer, in: "Physics of Shock Waves and High-temperature Hydrodynamic Phenomena", W.D. Hayes, R.F. Probstein (eds.) Academic Press, New York, 1967.

Zekonyte 03 J. Zekonyte, J. Erichsen, V. Zaporojtchenko, F. Faupel, *Surface Science* **532-535** (2003) 1040.

Zekonyte 04 J. Zekonyte, V. Zaporojtchenko, S. Wille, U, Shuermann, F. Faupel, in: K.L. Mittal (Ed.), Polymer Surface Modification: Relevance to Adhesion, Vol. 3, VSP, (2004), p. 243.

Zekonyte 05 J. Zekonyte, V. Zaporojtchenko, F. Faupel, *Nucl. Instrum. Meth. Phys. Res. B* **236** (2005) 241.

Zezin 94 A.A. Zezin, V.I. Feldman, F.F. Sukhnoy, *Polym. Sci. A* **36**(6) (1994) 763.

Ziegler 88 J.F. Ziegler, J. Manoyan, *Nucl. Instrum. Meth. Phys. Res.* **B 35** (1988) 215.

Ziegler 03 J.F. Ziegler, J.P.Biersak, SRIM version 2003.26, http://www.srim.org.

Symbols and Abbreviations

A	Hamaker constant
A_F	aperture area of a Faraday cup
AES	Auger electron emission
AFM	Atomic force microscopy
ARXPS	angle-resolved XPS
CC	condensation coefficient
d	removed amount of material (in sputter rate measurements)
e	electron charge
E_k	electron kinetic energy
E_p	electron pass energy
ECR	electron cyclotron resonance
FTIR	Fourier transform IR
G	Chemical yield of active species
G(S)	chemical yield of chain scission
G(X)	chemical yield of cross-links
G_c	fracture energy (toughness)
IF	ion fluence
IR	infrared spectroscopy
j	ion current
LMW	low molecular weight species
MD	molecular dynamics simulation
MS	magnetron sputtering
N_c	metal cluster density
P	peel strength
PVD	physical vapour deposition
QCM	quartz crystal microbalance
QMS	quadrupole mass spectrometry
R	range of the projectile in a material
R_{ave}	average surface roughness
R_{rms}	root-mean-squared roughness
S	relative sensitivity factor
dSR	differential sputter rate
SR	polymer sputter rate
t_s	sputter time
T_g	polymer glass transition temperature
T_{gs}	surface glass transition temperature of a polymer
T_m	polymer melting temperature
TEM	transmission electron microscopy
V_f	free volume of a polymer
V_R	retarding voltage
W_{adh}	work of adhesion
XPS	X-ray photoelectron spectroscopy
XRF	X-ray fluorescence
γ	interfacial tension
Y	sputtering yield

Publication List

1. V. Zaporojtchenko, J. Erichsen, **J. Zekonyte**, A. Thran, T. Strunskus, F. Faupel, Adsorption of noble metal atoms on polymers, in: “Mettalization of Polymers 2”, E. Sacher (ed.), Kluwer Academic/Plenum Publishers, New York, 2002, p. 107.

2. V. Zaporojtchenko, **J. Zekonyte**, A. Biswas, F. Faupel, Controlled growth on nano-size metal clusters on polymers by VPD method, *Surface Science* **532-535** (2003) 300-305.

3. **J. Zekonyte**, J Erichsen, V. Zaporojtchenko, F. Faupel, Mechanisms of argon ion-beam surface modification of PS, *Surface Science* **532-535** (2003) 1040-1044.

4. V. Zaporojtchenko, **J. Zekonyte**, J. Erichsen, F. Faupel, Etching rate and structural modification of polymer films during low energy ion irradiation*, Nuclear Instruments and Methods in Physics Research B* **208** (2003) 155-160.

5. **J. Zekonyte**, V. Zaporojtchenko, S. Wille, U. Schuermann, F. Faupel, Structural and chemical surface modification of polymers by low-energy ions and influence on nucleation, growth and adhesion of noble metals, in: “Polymer Surface Modification: Relevance to Adhesion”, K.L. Mittal (ed.), VSP, vol. 3, (2004), pp. 243-261

6. V. Zaporojtchenko, **J. Zekonyte**, S. Wille, U. Schuermann, F. Faupel, Tailoring of the PS surface with low energy ions: relevance to growth and adhesion of noble metals*, Nuclear Instruments and Methods in Physics Research B* **236** (2005) 95.

7. **J. Zekonyte**, V. Zaporojtchenko, F. Faupel, Investigation of the drastic change in the sputter rate of polymers at low ion fluence*, Nuclear Instruments and Methods in Physics Research B* **236** (2005) 241.

8. **J. Zekonyte,** V. Zaporojtchenko, F. Faupel, in: “Polymer Surface Modification: Relevance to Adhesion”, K.L. Mittal (ed.), (2005), submitted.

Publications not related to the present theses

1. S.-J. Ding, V. Zaporojtchenko, J. Kruse, **J. Zekonyte**, F. Faupel, Investigation of the interaction of evaporated aluminium with vapour deposited Teflon AF films via XPS, *Applied Physics A* **76** (2003) 851-856.

2. S.K. Sharma, V. Zaporojtchenko, **J. Zekonyte**, S. Deki, F. Faupel, Effects of thermal annealing of thin Au films on $Fe_{40}Ni_{38}Mo_4B_{18}$, *Materials Science and Engineering A* **351** (2003) 316-324.

3. S.K. Sharma, V. Zaporojtchenko, **J. Zekonyte**, A. Buettner, S. Deki, F. Faupel, Effects of thermal annealing of thin Au films on $Fe_{40}Ni_{38}Mo_4B_{18}$ in ultrahigh vacuum, *Journal of Materials Science* **39** (2004) 6291-6297.

4. S. Yakovlev, **J. Zekonyte**, C.-H. Solterbeck, M. Es-Souni, Interfacial effects on the electrical properties of multiferroic $BiFeO_3$/Pt/Si thin film heterostructures, *Thin Solid Films* (2005) in press.

Acknowledgements

I express my deep gratitude to many people who contributed through their support, experience and friendship to this work.

I thank Prof. Dr. Franz Faupel for giving me the opportunity to work in his group, and allowing me to perform interesting research.

Particular thanks to Dr. Vladimir Zaporojtchenko for his supervision, confidence, support, helpful discussions, and shearing his experience. This work would not have been done without you. Thank You!

I want to thank Dipl.-Ing. Stefan Rehders for the help with our experimental devices, for the construction of metal deposition chamber and all technical contributions to our researches. Dipl.-Ing. Rainer Kloth for fast computer problem solving.

Special thanks to Dr. Jörn Erichsen for teaching me to prepare polymer thin films, to do surface glass transition temperature measurements, and for his friendship.

Hearty thanks to M. Sc. Michael Scharnberg for his patience while reading and checking the English of my thesis.

Thanks to Dipl.-Min. Ulrich Schürmann for TEM and Dipl.-Ing. Henry Greve for the help to perform TEM experiments.

Thanks to Dipl.-Ing. Sebastian Wille who did hundreds of peel test measurements (also required for his student project). Thanks also to the master student Weinan Wang for the second half of the peel strength measurements.

Many thanks to Dr. Klaus Rätzke, Dr. Rainer Adelung, Dr. Jörn Kanzow, Dipl.-Ing. Alexander Bartsch, Dr. Angela Büttner, Dipl.-Phys. Rainer Kunz, Dipl.-Chem Kai Dolgner, Dipl.-Ing. Jan Kruse, M. Sc. Haile Takele, Dipl.-Ing. Christian Pochstein, M. Sc. Mady Elbahri, our secretary Beata Minten for their help, scientific discussions, relaxing talks during our lunch breaks friendship, and being the best colleagues anyone could wish.

Dr. D.K. Avasthi for reading the manuscript and his valuable suggestions.

Finally I express my deep gratitude to my parents, sisters Ruta and Ieva, and friends, especially Marina Kovaleva, for their support over the years.

Hearty thanks to Sergey Yakovlev for his support, trust and love.